

Spin States and Efficiency-Limiting Pathways in Optoelectronic Materials and Devices

Dissertation zur Erlangung des
naturwissenschaftlichen Doktorgrades
der Julius-Maximilians-Universität Würzburg



vorgelegt von

Jeannine Grüne

aus Jena

Würzburg, 2022



Eingereicht am: 19.05.2022
bei der Fakultät für Physik und Astronomie

1. Gutachter: Prof. Dr. Vladimir Dyakonov
2. Gutachter: Prof. Dr. Volker Christian Behr
der Dissertation.

Vorsitzende(r):

1. Prüfer: Prof. Dr. Vladimir Dyakonov
2. Prüfer: Prof. Dr. Volker Christian Behr
3. Prüfer: Prof. Dr. Johanna Erdmenger
im Promotionskolloquium.

Tag des Promotionskolloquiums: 16.11.2022

Doktorurkunde ausgehändigt am:

Contents

1	Introduction	7
2	Organic Semiconductors	11
2.1	Fundamentals of Organic Semiconductors	11
2.1.1	Molecular Orbitals	11
2.1.2	Electron Configuration	13
2.1.3	Jablonski Diagram	14
2.2	Transition Rates	16
2.2.1	Optical Transitions	17
2.2.2	(Reverse) Intersystem Crossing	18
2.3	Optoelectronics	21
2.3.1	Organic Light Emitting Diode	21
2.3.2	Organic Photovoltaic	24
3	Electron Paramagnetic Resonance	29
3.1	Electron Spin States	29
3.2	Spin Hamiltonian	32
3.2.1	Electron Zeeman Interaction	32
3.2.2	Zero-Field Splitting	33
3.2.3	Exchange Interaction	36
3.3	Spin Polarization	37
3.3.1	Transitions between Triplet Sublevels	38
3.3.2	Spin Polarization by SOC-induced ISC	40
3.3.3	Spin Polarization by Geminate Back Charge Transfer	41
4	Experimental Section	45
4.1	Materials	45
4.1.1	Thermally Activated Delayed Fluorescence	45
4.1.2	Organic Photovoltaic	46
4.2	Sample Preparation	49
4.2.1	OLED Fabrication	49
4.2.2	Thin Film Samples	50

4.3	Experimental Methods	51
4.3.1	Transient Electron Paramagnetic Resonance (trEPR)	51
4.3.2	Photoluminescence Detected Magnetic Resonance (PLDMR)	53
4.3.3	Transient Photo-/Electroluminescence Detected Magnetic Resonance (trPLDMR, trELDMR)	54
4.3.4	Transient Electroluminescence (trEL)	54
4.3.5	Transient Absorption (TA) Spectroscopy	55
5	Kinetic Modeling of Transient Electroluminescence reveals Efficiency-Limiting Process in Exciplex-Based TADF OLEDs	57
5.1	Introduction	58
5.2	Kinetic Model	60
5.3	Results	62
5.3.1	Temperature Dependent trEL	62
5.3.2	Dominant Annihilation Effect	64
5.3.3	Fit Results	66
5.4	Discussion	69
5.4.1	Depopulation of Triplet States	70
5.4.2	Contribution to EL	71
5.5	Conclusion	73
6	Detecting Triplet States in Optoelectronic Materials and Devices by Transient ODMR	75
6.1	Introduction	76
6.2	Method of Transient ODMR	77
6.3	Optically- and Electrically-Induced Triplet States	80
6.3.1	Organic Photovoltaics	80
6.3.2	Organic Light Emitting Diodes	83
6.3.3	Spin-Spin Interactions	87
6.4	Conclusion	89
7	Triplet States and their Generation Pathways in (Non-) Halogenated PBDB-T:Y-Series	91
7.1	Introduction	92
7.2	Probing Triplet Excitons with Magnetic Resonance	94
7.2.1	Detecting Triplet Excitons with Spin-Sensitive Photoluminescence	95
7.2.2	Probing Triplet Pathways with trEPR	98

7.3	Studying Influence of Halogenation on Excited State Kinetics	101
7.3.1	Hole Transfer Kinetics by Transient Absorption	101
7.3.2	ISC Rates in (Non-) Halogenated Y-Series	104
7.3.3	Impact of Halogenation on ISC and HT Yield	105
7.4	Discussion	106
7.5	Conclusion	110
7.6	Additional Information	111
8	Experimental Framework for Probing Triplet Recombination Pathways in Organic Solar Cells	113
8.1	Introduction	114
8.2	Geminate and Non-Geminate Pathways for Triplet Exciton Formation . . .	115
8.2.1	Photoluminescence Detected Magnetic Resonance	117
8.2.2	Transient Electron Paramagnetic Resonance	121
8.2.3	Transient Absorption Spectroscopy	125
8.3	Complementarity of PLDMR, trEPR and TA	128
8.4	Conclusion	130
8.5	Additional Information	131
9	Summary	133
10	Appendix	141
	Bibliography	148
	Publications	183
	Danksagung	185

1 Introduction

Je suis de ceux qui pensent que la science est d'une grande beauté. Un scientifique dans son laboratoire est non seulement un technicien: il est aussi un enfant placé devant des phénomènes naturels qui l'impressionnent comme des contes de fées.

Marie Curie, 1933

Marie Curie is one of the most famous physicists and is best known for her groundbreaking research in the field of radioactivity.^[1] In addition, the discoveries made in her laboratory also laid the foundation for research in another field: Electroluminescence (EL). In 1936, EL was first investigated by Georges Destriau in Marie Curie's laboratory in Paris on zinc sulfide (ZnS) phosphor powder.^[2] About 27 years later, in 1963, EL was also observed for the first time in organic materials by Pope et al.^[3] For this purpose, they applied over 400V to an anthracene single crystal using a small silver electrode in order to investigate this effect.^[3] With these findings, the foundation was laid for organic electronics, which is even nowadays still a topic of high interest both in academic research and in technology. Today, the range of applications for organic electronics is broad, reaching from light-emitting diodes over photovoltaics to field-effect transistors.^[4–6] The rapid progress in their performance in recent years has led to the commercialization of optoelectronic devices, in particular organic light-emitting diodes (OLEDs) have become indispensable in modern display technology. Given its promising chemical and mechanical advantages for potential applications, organic optoelectronics remain a highly interesting research topic, leading to the emergence of the present thesis. The two main areas of optoelectronics explored are thereby OLEDs and organic photovoltaics (OPV), both combining semiconductor electronics with optics by the interconversion of electric current and light.

The first OLED was built in 1987 by the group of Tang and VanSlyke based on tris(8-hydroxyquinoline)aluminum (ALQ₃) with an external quantum efficiency of 1%.^[7] Using vapor-deposited organic thin films between electrodes of indium tin oxide (ITO) and manganese:silver (Mg:Ag), their work came remarkably close to modern OLEDs. Three years later, in 1990, Burroughes et al. developed the first solution-processed polymer-based OLED, employing poly(p-phenylene-vinylene) (PPV), which laid the foundation for a rapidly growing research field.^[8] These research works provided the basis for the so-called first generation of OLEDs, using fluorescent emitters and achiev-

ing a maximum internal quantum efficiency of 25% through the radiative recombination of singlet excitons. The second generation of OLEDs was introduced in 1998 by Baldo et. al. by presenting the first phosphorescent OLED, capable of achieving an internal quantum efficiency of 100%.^[9] This family of OLEDs employs heavy metal atoms to enhance the spin-orbit coupling that drives radiative phosphorescent emission in organic materials. Although they perform well in terms of brightness and efficiency, resulting in their current application in commercial technology, the necessity of heavy metal atoms has always been a significant drawback. This concern was finally overcome by the development of OLEDs based on thermally activated delayed fluorescence (TADF) by Endo et al..^[10] These TADF OLEDs introduced the third generation and gained great scientific success by achieving high efficiencies in the absence of the source-limited rare metal complexes. Research on this type of OLEDs has expanded considerably in terms of materials, donor/acceptor types, emission color and purity, and still remains the major area of current OLED research.

In parallel, OPV research has also made remarkable progress. Starting from 1986, C. W. Tang reported the first bilayer device based on copper phthalocyanine and a perylenetetracarboxylic acid derivative, which exhibited an power conversion efficiency of 1%.^[11] A subsequent major step was made by the observation of ultrafast electron transfer after photoexcitation at the interface between conjugated polymers and fullerenes.^[12] This finding could be directly incorporated into the work of Yu et al. in 1995, who allowed the efficiency of dissociation of polymer excitons at the interface to be increased remarkably by the introduction of the bulk heterojunction (BHJ).^[13] For this purpose, they used a bulk mixing of polymer donor and fullerene acceptor with phase-separated domains sized to match the exciton diffusion length. The success of these BHJ further emerged with the simultaneous development of [6,6]-phenyl-C61-butyric acid methyl ester (PC₆₀BM)^[14], whose side chains provide higher solubility while also exhibiting better electron transport than its fullerene predecessor C₆₀, and remains still of interest in current OPV research. For more than two decades, fullerenes were the state-of-the-art acceptors until they were outperformed by non-fullerene acceptors (NFAs). The great success of NFAs is based not only on better absorption in the visible and near-infrared (NIR) wavelength regions their energy-level tunability, but also on outstanding improvements in the development of new polymer donors.^[15–17] Several NFAs have exceeded each other' maximum efficiencies, among three are discussed in the scope of this thesis, leading to an efficiency record of currently 19%.^[18]

Given the similarities in fundamentals and research goals, an increasing number of groups have combined the research areas of OLEDs and OPV. There have also been first ideas to combine both topics in one device to minimize non-radiative loss, e.g.,

solar cells based on OLED materials or utilizing TADF emitters as acceptors in OPV devices.^[19] The general research goals are similar for both optoelectronic topics, especially in the area of performance and stability. In particular, efficiency lags strongly behind current commercially employed devices, whereby the origins of loss processes for both device types are similar. One major impact in this context are triplet states, as they are able to cause annihilation effects, provide non-radiative loss channels and reduce stability by interaction with oxygen.^[20–22] The aim of this work is to identify and study the triplet states, their kinetics and their contribution to loss pathways utilizing different spin-sensitive techniques. In addition to purely optical techniques, the paramagnetic property of triplet states is exploited by applying methods based on the principle of electron paramagnetic resonance (EPR). The combination of EPR with optical detection leads to optically detected magnetic resonance (ODMR), while the combination of all-optical and magnetic resonance techniques allows a deeper understanding of the important processes in optoelectronic materials and devices. First, the theoretical background about organic semiconductors (ch. 2) and EPR (ch. 3) as well as an introduction into the material systems and experimental techniques (ch. 4) are given. Subsequently, the results of this thesis (ch. 5 - 8) are divided into four topics as follows:

Kinetic Modeling of Transient Electroluminescence reveals Efficiency-Limiting Process in Exciplex-Based TADF OLEDs

(published in *J. Phys. Chem. C*^[23])

Chapter 5 characterizes the excited state kinetics of donor:acceptor based OLEDs by the use of transient EL (trEL), providing a foundation for identifying considerable loss processes in these types of OLEDs. By developing and applying a suitable kinetic model, the impact of efficiency-limiting processes associated with triplet states can be quantified.

Detecting Triplet States in Optoelectronic Materials and Devices by Transient ODMR

(published in *Mater. Horiz.*^[24])

Chapter 6 continues by gaining a deeper understanding of the role of triplet states not only in the already introduced OLED devices but also in OPV systems. For this purpose, it introduces a newly developed method of transient ODMR (trODMR), whose advantages are presented in the application of thin films, emitting photoluminescence (transient photoluminescence detected magnetic resonance, trPLDMR) and devices emitting EL (transient electroluminescence detected magnetic resonance, trELDMR).

Triplet States and their Generation Pathways in (Non-) Halogenated PBDB-T:Y-Series

(*under review*. Preprint available^[25])

Chapter 7 continues the study on OPV materials by investigating the role of triplet states, their associated kinetics and pathways in state-of-the-art donor and acceptor combinations. In particular, the three spin-sensitive techniques PLDMR, transient EPR (trEPR), and transient absorption (TA) help to provide a comprehensive picture of the excited states processes and the eventual dependence on different material combinations.

Experimental Framework for Probing Triplet Recombination Pathways in Organic Solar Cells

(published in *Adv. Energy Mater.*^[26])

Chapter 8 completes the studies of the previous chapters by the investigation of fullerene-based systems. It additionally presents the strengths and limitations of the three spin-sensitive techniques with a focus on triplet research, whereby the combination proves to be very valuable for the future research goal of triplet loss prevention.

2 Organic Semiconductors

Organic materials consist mainly of carbon and hydrogen atoms with some heteroatoms such as sulfur, oxygen or nitrogen. Thereby, they possess semiconductor properties as absorption and emission in the ultraviolet (UV), visible or near-infrared (NIR) wavelength range and conductivities suitable for semiconducting devices, e.g., organic light-emitting diodes (OLEDs), organic photovoltaics (OPVs) or organic field-effect transistors (OFETs). The following chapter provides fundamentals of organic semiconductors, including the formation of molecular orbitals, electron configurations, excited states and their transitions (ch. 2.1), followed by quantum-mechanical analysis of the most important transition rates (ch. 2.2). In addition, ch. 2.3 addresses functionalities of the optoelectronic materials and devices important for this theses, i.e., principles of OLED and OPV operation.

The information in this chapter is based, unless otherwise noted, on textbooks by A. Köhler and H. Bässler^[27], W. Tress^[28] and W. Brütting^[29] and reviews by M. J. Griffith et al.^[30], C. Deibel et al.^[31], and W. Brütting et al.^[32]

2.1 Fundamentals of Organic Semiconductors

2.1.1 Molecular Orbitals

An essential requirement for electrical conductivity is the presence of delocalized electrons, which is realized in organic materials by conjugated π -systems, the origin of which is explained in the following. A single carbon atom in the ground state with six electrons has an electronic configuration of $1s^2 2s^2 2p^2$: The two s orbitals in the first and second shells are fully occupied, with the two remaining electrons residing in the degenerate $2p$ orbitals $2p_x$, $2p_y$ and $2p_z$. When attempting to bond with adjacent atoms, the $2s$ and $2p$ orbitals can hybridize into more energetically favorable configurations by maximizing the spatial separation of the electrons, resulting in more possible covalent bonds. Depending on the $2p$ orbitals involved, the mixing leads to sp^3 , sp^2 , or sp hybrid orbitals. To understand the semiconducting properties in conjugated organic systems, we have to examine the sp^2 hybridization as in the example of ethene. In this molecule, three sp^2 orbitals are formed by mixing the $2s$ orbitals and two $2p$ orbitals, e.g., $2p_x$ and $2p_y$. The hybridized orbitals are aligned in a plane (xy -plane) in an

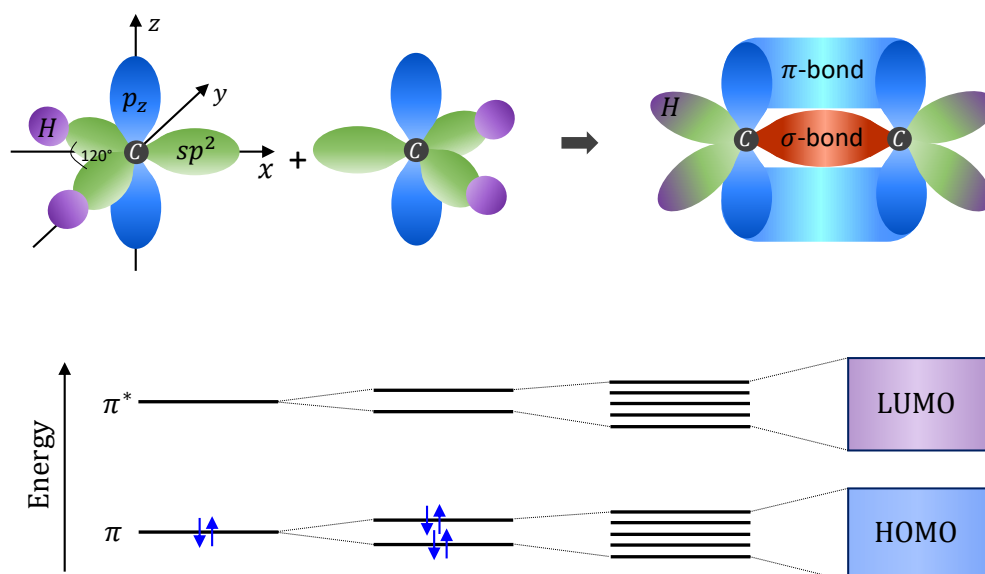


Figure 2.1: Schematic formation of molecular orbitals. Top: Schematics of sp^2 hybridization of two carbon atoms to yield ethene. The sp^2 orbitals form σ -bonds whereas the pairing of the electrons in the p_z orbitals results in a π -bond. Bottom: Starting from π and π^* orbitals for ethene, the extension of carbon atoms leads to longer π -conjugated chains, resulting in the formation of a HOMO and LUMO π -band. Adapted from^[30]

approximately equilateral triangle, with the remaining, non-hybridized, $2p_z$ orbitals oriented perpendicularly to the plane. The electrons in the three sp^2 orbitals of the carbon atoms can form σ -bonds with neighboring atoms. Figure 2.1 (top) shows the example of ethene, where two σ -bonds are formed with hydrogen and one with the second carbon atom. The pairing of electrons in the $2p_z$ orbitals forms a π -orbital or π -bond with spatial probability density above and below the molecular axis.^[27,30]

Molecular orbitals can be derived by the linear combination of atomic orbitals (LCAO) theory. Thereby, bonding and antibonding molecular orbitals with different energies can be obtained, with the energy difference depending on the resonance interaction. For instance, as can be found in ethene, the $2sp^2$ hybrid orbitals have a large charge overlap along the internuclear axis, leading to bonding σ and antibonding σ^* -orbitals with a large energy splitting. In contrast, the interaction of the p_z orbitals occurs over larger distances, resulting in a smaller splitting between the bonding π - and antibonding π^* -orbital. In organic molecules, this splitting is often in the energy range of the UV, visible or NIR spectrum. Considering the number of valence electrons in ethene, the π -orbital represents the highest occupied molecular orbital (HOMO), while the π^* -orbital is empty in the ground state and is called the lowest unoccupied molecular orbital (LUMO). In molecules with an increasing number of carbon atoms, the number of π - and π^* -orbitals increases. The resulting closely spaced energy levels form a band-

like structure, as shown in Figure 2.1 (below). In analogy to inorganic semiconductors, the HOMO corresponds to the valence band, while the LUMO is the analog to the conduction band. The linear superposition of the overlapping p_z orbitals forms a single molecular π -orbital with delocalized electron density across the conjugated π -system, determining the electronic properties of OSCs.^[27,30]

2.1.2 Electron Configuration

When addressing the fundamentals in organic semiconductors, typically three fields are relevant: orbitals (e.g., HOMO, LUMO), electron configuration, and electronic states (e.g., singlet/triplet states). Having clarified the formation of molecular orbitals when several atoms are combined, we can now address the occupation of these orbitals. The electron configuration describes the filling of the orbitals by means of energy minimization. The so-called *Aufbau principle* thereby describes the occupation of the states with the lowest energy first. For degenerate orbitals, *Hund's rule* specifies the most stable molecular configuration when the orbitals are initially occupied by a single electron.^[28]

For an illustrative purpose, a molecule with four π -electrons can be considered. Electrons are fermions and possess a spin angular momentum with spin quantum number $S = 1/2$, occupying a *spin-up* or *spin-down* state (detailed explanation in ch. 3.1: Electron Spin States). This additional quantum number can be considered, in terms of the Pauli principle, as an additional degree of freedom that an electron can adopt. Accordingly, in the absence of degenerate energy levels, all electrons exist in pairs in the lowest possible orbitals. The molecule then has the lowest possible energy, i.e., it is in the ground state.^[28,33]

If an electron is removed (or added), a half-filled molecular orbital is created and the molecule becomes a radical cation (or anion). This electronic state is referred to as *spin-doublet* (ch. 3.1) because it can exhibit two states depending on the spin configuration. As molecules strive to reach closed-shell formation, i.e., completely filled shells, this configuration is usually chemically reactive. An alternative approach to deviate from the stable ground state, with constant number of electrons, is realized by raising an electron from the π -orbital (i.e., HOMO) to the π^* -orbital (i.e., LUMO). For instance, this excitation can be achieved upon light absorption in the UV, visible or NIR wavelength ranges, matching the HOMO - LUMO difference in many organic semiconductors. Since the molecule is no longer in the lowest energy state, it is called an excited state, which will relax back into the ground state with a certain transition rate, discussed in the next sections.^[27,28]

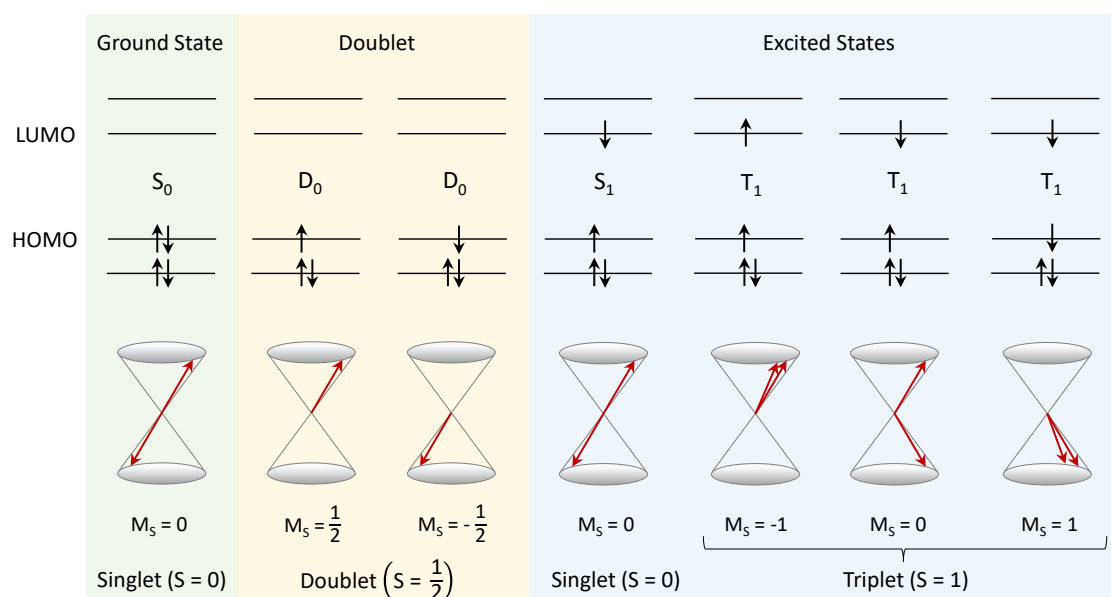


Figure 2.2: Electron configuration describing singlet, doublet, and triplet states. Top: electron configuration of S_0 with fully occupied HOMO, doublet D_0 with half-filled HOMO and excited states S_1 and T_1 with one electron in HOMO and one in LUMO. Arrows indicate the orientation of the electron spin (without phase). Bottom: Relative orientation of two spin angular momenta of the electrons with magnetic field in z -direction. Singlet states: antiparallel and 180° out of phase, triplet state: parallel or 180° in phase. Quantum mechanical derivation in ch. 3.1.

In contrast to the radical case, this excitation results in the creation of two half-filled orbitals. As each electron possesses two possible spin configurations, there are four possible eigenstates of the two particle system. The quantum mechanical derivation of these spin states will be discussed in ch. 3.1. In short, they can form one singlet state (spin quantum number $S = 0$) or one of three triplet states (spin quantum number $S = 1$). Semiclassically described, singlet states (S_0 , S_1) are two-particle systems with antiparallel spin (180° out of phase) in the π/π^* -orbital, while the spin configuration in triplet states (e.g., T_1) is parallel or in phase, as shown in Figure 2.2. The spin quantum number M_S is thereby the projection of the spin angular momentum along the z -axis, see ch. 3.1. [27,28,34]

2.1.3 Jablonski Diagram

If the energies required to transfer a molecule to an excited state are drawn with respect to the ground state, the corresponding representation is called a Jablonski diagram. Figure 2.3 shows the Jablonski diagram for a valence electron of a molecule including the most important transition pathways between the electronic states. As all orbitals up to the HOMO are occupied in the ground state by paired electrons, the ground state

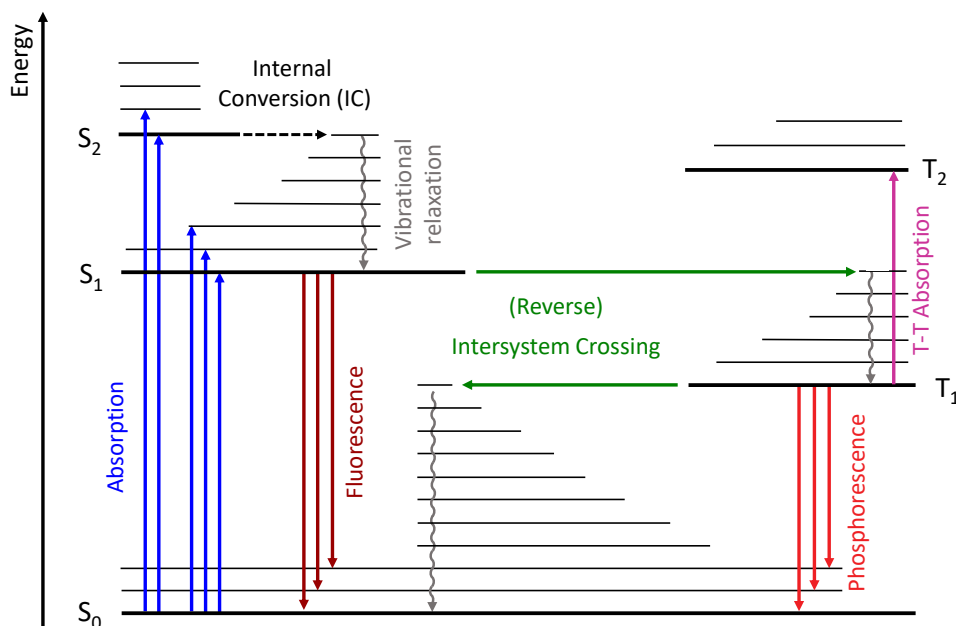


Figure 2.3: Jablonski diagram with ground state S_0 and excited singlet states S_1 , S_2 and triplet states T_1 , T_2 (thick lines) with their respective vibrational levels (thin lines). Transitions between electronic states are indicated as (colored) arrows. Radiative processes are fluorescence and phosphorescence, while vibrational relaxation, internal conversion (conversion of excited state to vibrational levels of next lower excited state) and (reverse) intersystem crossing between excited states (e.g. $S_1 \leftrightarrow T_1$) are non-radiative. Adapted from^[28]

is of singlet character S_0 . As discussed in the last section, the excited states (solid lines) are either singlet (S_1 , S_2) or triplet states (T_1 , T_2). Singlet and triplet states are energetically split by the exchange integral ($J < 0$ in most organic molecules, i.e., $E(S_1) > E(T_1)$), further discussed in the context of the spin Hamiltonian in ch. 3.2.3.^[28,34]

A photon can raise an electron from the π -orbital into the π^* -orbital, this process is referred to as *absorption*. In context of electronic states, the molecule is transferred from the ground state S_0 into an excited state S_n (thick lines) or one of its vibrational levels (thin lines). This transition is followed by *vibrational relaxation* to the lowest vibrational level within the same electronic state. Higher excited states (e.g., S_2) have short lifetimes and relax on fast timescales (ps) to the vibrational levels of the next lower electronically excited state by *internal conversion* (IC). Vibrational relaxation and IC are non-radiative while, according to *Kasha's rule*, the radiative transition always occurs from the lowest electronic state of the given multiplicity, e.g., the S_1 state. *Fluorescence* thereby describes the fast (spin-allowed) radiative transition between $S_1 \rightarrow S_0$. If the exciton in the excited state is created by optical excitation, i.e., light absorption, the emitted luminescence is denoted as photoluminescence (PL). In an electrically driven

device, as organic light emitting diodes (OLED), radiative recombination of injected charges is denoted as electroluminescence (EL).^[27,28]

While IC takes place between states of the same spin manifold (e.g., $S_2 \rightarrow S_1$), *inter-system crossing* (ISC) involves a spin-flip and causes transitions between singlet and triplet states (e.g., $T_1 \rightarrow S_0$). The radiative slower (spin-forbidden) transition from the lowest triplet states T_1 to the ground state S_0 is denoted as *phosphorescence*. ISC can also occur non-radiatively between excited states (e.g., $S_1 \rightarrow T_1$), whereby the opposite direction is referred to as reverse ISC (e.g., $T_1 \rightarrow S_1$). As direct and reverse ISC are one of the essential topics in this thesis, the theoretical background of these transitions will be discussed in more detail in chapter 2.2.2.^[28,42]

2.2 Transition Rates

Fermi's Golden Rule:

Transitions between electronic states (e.g., between excited states or ground and excited state) change the total energy of the molecule or the system. In terms of quantum mechanics, perturbation theory can describe the probabilities of these transitions. In this context, the Hamilton operator \hat{H} of the perturbed system can be described as the sum of the unperturbed Hamilton operator \hat{H}_0 and the Hamilton operator \hat{H}' of the corresponding physical interaction:^[27]

$$\hat{H} = \hat{H}_0 + \hat{H}' \quad (2.1)$$

Since the unperturbed operator \hat{H}_0 has no impact on the mixing of the electronic states, the transition rate k_{if} between initial state with wavefunction Ψ_i and final state Ψ_f can be determined by *Fermi's golden rule*:^[28]

$$k_{if} = \frac{2\pi}{\hbar} |\langle \Psi_f | \hat{H}' | \Psi_i \rangle|^2 \rho \quad (2.2)$$

Here, ρ represents the density of the final states and \hbar the reduced Planck's constant. $|\Psi\rangle = |\Psi_{el}\rangle |\Psi_{vib}\rangle |\Psi_{spin}\rangle$ presents the total molecular wavefunction as a product of electron wavefunction $|\Psi_{el}\rangle$ (i.e., function of electron's spatial coordinates and the positions of the nuclei), vibrational wavefunctions $|\Psi_{vib}\rangle$ (i.e., vibrational motion of the nuclei) and spin wavefunction $|\Psi_{spin}\rangle$ (electron spin eigenstates, i.e., singlet or triplet wavefunction from ch. 3.1).

2.2.1 Optical Transitions

The rate for optical transitions, i.e., emission or absorption of photons, can be derived by using the dipole operator $\hat{\mu}_{\text{dip}} = e\hat{r}$ as perturbation Hamiltonian operator, acting on the total molecular wavefunction $|\Psi\rangle = |\Psi_{\text{el}}\rangle|\Psi_{\text{vib}}\rangle|\Psi_{\text{spin}}\rangle$:^[27]

$$k_{\text{if}} = \frac{2\pi}{\hbar} \left| \langle \Psi_{\text{el},f} \Psi_{\text{spin},f} \Psi_{\text{vib},f} | e\hat{r} | \Psi_{\text{el},i} \Psi_{\text{spin},i} \Psi_{\text{vib},i} \rangle \right|^2 \rho \quad (2.3)$$

Eq. 2.3 can be simplified by applying the Born-Oppenheimer approximation and the Franck-Condon principle (also called Condon approximation). The former allows the separation of nuclear and electron motion while the latter assumes electronic transitions to occur on time scales much faster than nuclear motions, i.e., the nuclei are too heavy to respond to electronic oscillations. Thus, the contributions can be separated with the vibrational wavefunction $|\Psi_{\text{vib}}\rangle$ being insensitive to the dipole operator. Since the spin wavefunction $|\Psi_{\text{spin}}\rangle$ is also mostly independent on electric and magnetic fields of the absorbed/emitted photon, the Hamilton operator can be assumed to only act on the electronic wavefunction $|\Psi_{\text{el}}\rangle$:^[28]

$$k_{\text{if}} = \frac{2\pi}{\hbar} \left| \langle \Psi_{\text{el},f} | e\hat{r} | \Psi_{\text{el},i} \rangle \right|^2 \left| \langle \Psi_{\text{vib},f} | \Psi_{\text{vib},i} \rangle \right|^2 \left| \langle \Psi_{\text{spin},f} | \Psi_{\text{spin},i} \rangle \right|^2 \rho \quad (2.4)$$

Electronic Factor: The matrix element $\left| \langle \Psi_{\text{el},f} | e\hat{r} | \Psi_{\text{el},i} \rangle \right|^2$ determines if a transition is dipole-allowed ($\neq 0$) or dipole-forbidden ($= 0$). The value of the matrix element scales on the one hand with the electronic wavefunction overlap of initial and final state, i.e., $\pi - \pi^*$ transitions on the same part of the molecule have a higher rate. On the other hand, the probability of the transition scales with the dipole operator $\hat{\mu}_{\text{dip}}$. Since the dipole operator depends on the displacement vector \vec{r} between the charges, the participation of larger, more extended orbitals increases the absorption and emission intensity.^[27]

Vibrational Factor: The vibrational factor $\left| \langle \Psi_{\text{vib},i} | \Psi_{\text{vib},f} \rangle \right|^2$ is also referred as *Franck-Condon factor* FC and depends on the overlap of vibrational wavefunctions of the lower (e.g., S_0) and the upper (e.g., S_1) electronic state.^[35,36] In case of absorption, it gives the probability/strength of the transition from a particular vibrational eigenstate in the lower electronic state (e.g., 0th vibrational level of S_0) to the vibrational eigenstate of the excited state (e.g., nth vibrational level of S_1). The Franck-Condon factor can also be expressed by the *Huang-Rhys-parameter* S_{HR} , which is related to the change in the

equilibrium nuclear coordinate of the lower and upper electronic states and will be addressed further below:^[27,35]

$$FC_{f,i} = |\langle \Psi_{\text{vib},i} | \Psi_{\text{vib},f} \rangle|^2 = \frac{S_{\text{HR}}^n}{n!} \exp(-S_{\text{HR}}) \quad (2.5)$$

Spin Factor: Besides the electronic and vibrational elements, the rate of a transition depends on the involved spin. Thereby, the transition depends on the difference in spin multiplicity: $|\langle \Psi_{\text{spin},i} | \Psi_{\text{spin},f} \rangle| = 1$ for transitions between state with the same spin quantum number S ("spin-allowed"), whereby $|\langle \Psi_{\text{spin},i} | \Psi_{\text{spin},f} \rangle| = 0$ for different spin quantum number S ("spin-forbidden"), resulting in the selection rule $\Delta S = 0$ for electronic transitions. Nevertheless, also spin-forbidden transitions between singlet ($S = 0$) and triplet ($S = 1$) states are experimentally observed, as intersystem crossing between excited states (e.g., $S_1 \rightarrow T_1$) or phosphorescence ($T_1 \rightarrow S_0$). This "spin-forbidden" transition of intersystem crossing needs an additional perturbation Hamiltonian, mostly driven by spin-orbit coupling (SOC) in organic molecules. As ISC is one of the most important transitions for the scope of this thesis, the fundamentals will be explained in more detail in the following.^[27,42]

2.2.2 (Reverse) Intersystem Crossing

As explained in the previous section, transitions between singlet and triplet states are generally spin-forbidden with $|\langle \Psi_{\text{spin},i} | \Psi_{\text{spin},f} \rangle|^2 = 0$. However, spin-forbidden transitions are possible when perturbations are considered, which lead to the intermixing of the wavefunction contributions from triplet and singlet states. A dominant mechanism in organic semiconductors driving this spin transition is spin-orbit coupling (SOC), which describes the interaction of the magnetic moment of the electron (ch. 3.2.1) with the magnetic field generated by the orbital angular momentum. The principle is based on the coupling between the spin angular momentum \hat{S} with the orbital angular momentum \hat{L} to form the total angular momentum \hat{J} :^[37]

$$\hat{J} = \hat{L} + \hat{S} \quad (2.6)$$

Since spin conservation is only required for the total angular momentum \hat{J} , a change in spin angular momentum \hat{S} can be compensated by an opposite change in orbital angular momentum \hat{L} . In the context of perturbation theory, the effect of SOC will mix

the pure triplet state wavefunction $|\ ^3\Psi_1^0\rangle$ (here for the first excited triplet state T_1) with a small amount of the wavefunction $|\ ^1\Psi_k^0\rangle$ of a pure higher lying singlet state S_k :^[27]

$$|\ ^3\Psi_1'\rangle = |\ ^3\Psi_1^0\rangle + \sum_k \frac{\langle\ ^1\Psi_k^0|\hat{H}_{\text{SOC}}|\ ^3\Psi_1^0\rangle}{E(T_1) - E(S_k)} |\ ^1\Psi_k^0\rangle \quad (2.7)$$

Where $|\ ^3\Psi_1'\rangle$ represents the wavefunction of the mixed triplet state and \hat{H}_{SOC} the perturbing spin-orbit coupling Hamilton operator. The mixing furthermore depends on the energy gap of the triplet $E(T_1)$ and the respective k^{th} singlet state $E(S_k)$. Analogously, the wavefunction of a mixed singlet state, e.g., $|\ ^1\Psi_1'\rangle$, can be expressed as:^[27]

$$|\ ^1\Psi_1'\rangle = |\ ^1\Psi_1^0\rangle + \sum_k \frac{\langle\ ^3\Psi_k^0|\hat{H}_{\text{SOC}}|\ ^1\Psi_1^0\rangle}{E(S_1) - E(T_k)} |\ ^3\Psi_k^0\rangle \quad (2.8)$$

The amount of the mixing therefore depends on both the energetic gap between the respective singlet and triplet states as well as the magnitude of the SOC matrix element. The spin-orbit coupling Hamiltonian can be conveniently written as an interaction term between the orbital angular momentum \hat{L} and the spin angular momentum \hat{S} , mediated by the atomic nuclei of the molecule:^[38]

$$\hat{H}_{\text{SOC}} = \alpha_{\text{fs}}^2 \sum_{\mu} \sum_i \frac{Z_{\mu}}{r_{i\mu}^3} \hat{L}_i \hat{S}_i \quad (2.9)$$

Here, $r_{i\mu}$ describes the distance of electron i to nucleus μ , Z_{μ} the effective nuclear charge and α_{fs} the fine structure constant. Thus, the strength of SOC also depends on the atomic charge, with a correlation of $\hat{H}_{\text{SOC}} \propto Z^4$ found for atoms and $\hat{H}_{\text{SOC}} \propto Z^4 - Z^5$ for molecules. As a result, ISC is more pronounced when atoms of a high atomic charge are embedded in the molecule, also known as *heavy atom effect*.^[27,38]

Direct ISC Rate:

Having clarified how the SOC mechanism affects the singlet and triplet wavefunction and enables their admixture, we can now address the calculation of the ISC rate. We consider here a transition between excited states, e.g., S_1 and T_k with corresponding wavefunctions $|\ ^1\Psi_1\rangle$ and $|\ ^3\Psi_k\rangle$. The rate can be represented by Fermi's golden rule (eq. 2.2) with \hat{H}_{SOC} as the perturbation operator. In addition to the SOC matrix element $|\langle\ ^3\Psi_k|\hat{H}_{\text{SOC}}|\ ^1\Psi_1\rangle|$ between singlet and triplet states, we further consider the

Franck-Condon-weighted density of states FCWD, i.e., the density of vibrational states in the triplet manifold multiplied by the Franck-Condon vibrational overlap:^[38]

$$k_{\text{ISC}} = \frac{2\pi}{\hbar} |\langle {}^3\Psi_k | \hat{H}_{\text{SOC}} | {}^1\Psi_1 \rangle|^2 \text{FCWD} \quad (2.10)$$

The FCWD can thereby be evaluated in the framework of different theories. In the calculations presented in ch. 7, the FCWD is calculated in the context of the Marcus-Levich-Jornter-Theory, which can be derived from the semi-classical Marcus expression by involving the intramolecular vibrational modes assisting the ISC:^[39]

$$\text{FCWD} = \sqrt{\frac{1}{4\pi\lambda_S k_B T}} \sum_n \exp(-S_{\text{HR}}) \frac{S_{\text{HR}}^n}{n!} \exp\left[-\frac{(-\Delta E_{\text{ST}} + \lambda_S + n\hbar\omega)^2}{4\lambda_S k_B T}\right] \quad (2.11)$$

λ_S represents the external reorganization energy, k_B the Boltzmann constant, ΔE_{ST} the gap between the respective singlet and triplet states and $\hbar\omega$ the energy of an effective high-frequency intramolecular vibrational mode that assists ISC. The second exponential term can be seen as a transition probability whereby the prior term presents the Franck Condon factor (eq. 2.5). The effective Huang-Rhys-parameter S_{HR} for this mode can be further expressed by $S_{\text{HR}} = \frac{\lambda_i}{\hbar\omega}$; with the inner reorganization energy λ_i corresponding to the energy required to accommodate the nuclear rearrangements between the two electronic states. The sum in equation 2.11 considers the overlapping wavefunctions of the singlet state with all possible vibrational modes of the triplet state ($n = 0, 1, 2, \dots$).^[21,39]

Reverse ISC Rate:

While transitions from singlet to triplet states are normally referred to as ISC, *reverse intersystem crossing* (RISC) denotes the opposite pathway. If the respective triplet state T_k is energetically below S_1 , ISC is called a downhill process whereby RISC represents an uphill process. The rate is thereby analogous to 2.11, whereby the wavefunctions of initial and final state change and the positive sign in front of ΔE_{ST} accounts for the uphill mechanism:^[40,41]

$$k_{\text{RISC}} = \frac{2\pi}{\hbar} |\langle {}^1\Psi_1 | \hat{H}_{\text{SOC}} | {}^3\Psi_k \rangle|^2 \text{FCWD} \quad (2.12)$$

$$\text{FCWD} = \sqrt{\frac{1}{4\pi\lambda_S k_B T}} \sum_n \exp(-S_{\text{HR}}) \frac{S_{\text{HR}}^n}{n!} \exp\left[-\frac{(\Delta E_{\text{ST}} + \lambda_S + n\hbar\omega)^2}{4\lambda_S k_B T}\right]$$

RISC is the central mechanism for systems based on *thermally activated delayed fluorescence* (TADF), whereby a small singlet-triplet gap ΔE_{ST} is used to efficiently harvest triplet excitons by thermal upconversion to the singlet states. Since RISC rates are typically in the orders of $10^5 - 10^7 \text{ s}^{-1}$, the subsequently radiative emission from the singlet states is called delayed fluorescence. According to eq. 2.12, efficient RISC requires a sizable SOC matrix element as well as a small singlet triplet gap ΔE_{ST} . This thesis deals with intermolecular TADF systems, with RISC acting on charge transfer (CT) states spread over separated donor and acceptor molecules. The spatially separated wavefunctions reduce the exchange interaction (see ch. 3.2.3), favorable for efficient RISC. However, if singlet and triplet states have the same spatial orbital occupation, i.e., same orbital type as here both of CT nature, the SOC coupling is significantly reduced because the change in spin cannot be compensated by the corresponding change in orbital angular momentum. Consequently, the goal in TADF research is to find a good trade-off between a small ΔE_{ST} and simultaneously sizable SOC matrix element to realize an efficient RISC process.^[40–42]

2.3 Optoelectronics

Optoelectronics by definition describes the combination of optics with semiconductor electronics. These devices are designed for generating light from electric current or vice versa. The most common organic optoelectronic devices are organic light-emitting diodes (OLEDs) and organic photovoltaic (OPV). Both devices are in principle constructed similarly, with an organic layer (multiple layers in real devices) sandwiched between two electrodes. While a voltage is applied to an OLED to inject charge carriers that eventually recombine radiatively, OPV works in the reverse direction by absorbing light and generating excitons that eventually dissociate into free charge carriers. The OLED mechanism to create excitons and the principle of OPV to form free charge carriers are the main topics of this work and will be discussed in more detail below.^[27,29,32]

2.3.1 Organic Light Emitting Diode

Fig. 2.4 schematically shows the structure of a multilayer OLED. It basically consists of two electrodes (anode and cathode), injection and transport layers for electrons and holes, respectively, and an emission layer. When a voltage is applied, the positively biased anode injects holes into the HOMO of the hole injection/transport layer (HIL, HTL). On the other side, the negatively biased cathode injects electrons into the LUMO of the electron injection/transport layer (EIL, ETL). Given the different work functions

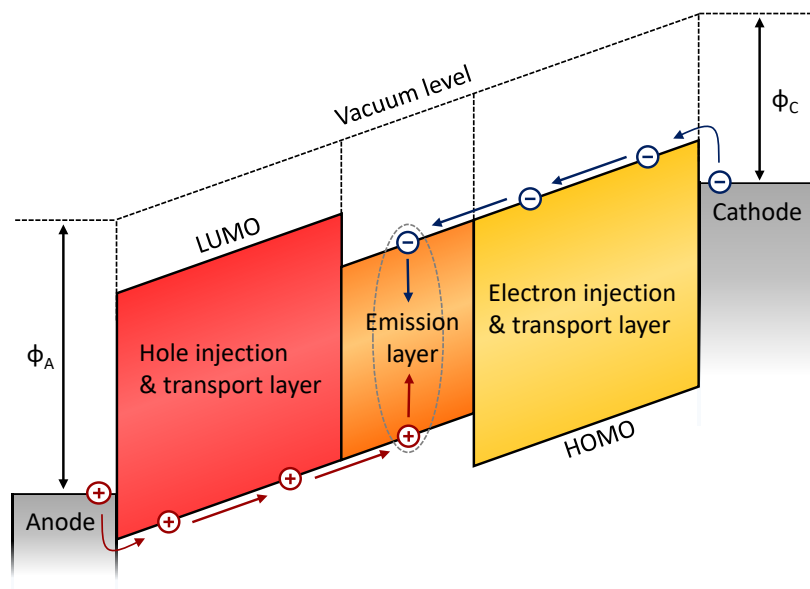


Figure 2.4: Schematic energetic structure of a multilayer OLED. The OLED consists of electrodes (anode and cathode) and organic layers, here hole injection- and transport layers (HIL, HTL), emission layer and electron injection- and transport layer (EIL, ETL). Upon applying a voltage, electrons (holes) are injected from the cathode (anode) into the LUMO (HOMO) of the EIL/ETL (HIL/HTL). Electrons and holes will, with properly chosen materials, accumulate in the emission layer and recombine. Adapted from^[32]

of the anode and cathode (Φ_A and Φ_C), a build-in voltage (also called turn-on voltage) Φ_{BI} must first be exceeded. Once the voltage is sufficiently high to overcome the build-in voltage, the carriers diffuse through the respective transport layers and meet in the emission layer. The energetically higher LUMO or lower HOMO level (or additional barrier layers with suitable energetics) further accumulates the charge carriers in the emission layer. When the electron and hole meet in the emission layer, they can form a strongly bound e-h pair (Frenkel exciton, see ch. 2.3.2) which can decay radiatively. However, it is possible for a leakage current to occur, in which the charge carrier leaves the device at the opposite electrode. The processes in an operating OLED can be divided into three main steps:^[29,32]

Injection of Charge Carriers at the Electrodes

Metal-semiconductor interfaces present an energy barrier that must be overcome by the charge carriers to be injected. In the case of an OLED, the critical parameter for the injection of electrons and holes is the energy difference between the transport states and the electron work function. One model for overcoming this barrier is Fowler-Nordheim tunneling.^[43] It is based on a high electric voltage that tilts the potentials

allowing electrons to tunnel from the electrode through the triangular barrier into the HOMO or LUMO of the organic layer. Another approach is the Richardson-Schottky thermionic injection model.^[44] It is based on charge carriers using thermal energy to be injected into the semiconductor from the Fermi level of the electrode. The combination of both models is called thermionic field emission and is based on the thermal excitation of the charge carriers and the subsequent tunneling through the energy barrier.^[45]

Charge Transport

The charge transport in disordered organic semiconductors, covered in this thesis, is governed by phonon-assisted tunneling of charge carriers from one occupied state to the next unoccupied state, also called *hopping* transport. The hopping rate thereby depends on the tunneling between sites and the thermal activation. Miller-Abrahams proposed a model that describes the hopping rate:^[31]

$$v_{ij} = v_0 \exp(-2\gamma r_{ij}) \begin{cases} \exp\left(-\frac{\Delta E_{ij}}{k_B T}\right) & \Delta E_{ij} > 0 \\ 1 & \Delta E_{ij} \leq 0 \end{cases} . \quad (2.13)$$

Here, the first part describes the tunneling contribution, where v_0 is the maximum hopping rate, γ is the inverse localization radius (proportional to the transfer integral, i.e., the wavefunction overlap between locations i and j), and r_{ij} is the distance between sites. The second part, on the other hand, describes the thermal activation. Thereby, the model assumes that the Boltzmann factor for downward jump is equal to 1, whereby thermal activation is required for the jump to a site higher in energy with energy gap ΔE_{ij} . The charge carriers additionally collide with nucleus or defects and produce scattering events that slow down the charge transport in organic semiconductors. Thus, in contrast to band transport in inorganic semiconductors, the mobilities of organic materials are generally lower with values in the range of $10^{-6} - 10^1 \text{ cm}^2 \text{ V}^{-1} \text{ s}^{-1}$.^[30,31]

Exciton Formation and Recombination

If the injected positive and negative charge carriers collide and recombine, it is called *non-geminate recombination*. As previously explained, charge transport is of the hopping type, whereby the free mean path length of the charge carriers is comparable to the intermolecular distance. When the electron and hole approach each other in the Coulomb capture radius (also called Onsager radius) R_{e-h} , they recombine to form an

exciton. The radius depends on the thermal energy $k_B T$ and the relative permittivity ϵ_r of the material:^[30]

$$R_{e-h} = \frac{e^2}{4\pi\epsilon_r\epsilon_0 k_B T} \quad (2.14)$$

Here, e represents the elementary charge and ϵ_0 the vacuum permittivity. Together with the Einstein relation $eD = \mu k_B T$ (with diffusion coefficient D and mobility μ), the recombination rate λ of electron and hole can be derived:^[30]

$$\lambda = 4\pi R_{e-h} (D_e + D_h) = \frac{e(\mu_e + \mu_h)}{\epsilon_r\epsilon_0} \quad (2.15)$$

Equation. 2.15 is also known as the Langevin recombination rate and is part of ch. 5. Since electron and hole generally have independent spin orientations, recombination of electrons and holes leads to 25% occupations of singlet and 75% triplet states (see ch. 3.1). The formed excitons can decay radiatively or non-radiatively to the ground state or undergo transitions between electronic states, as already explained in ch. 2.1.3.

2.3.2 Organic Photovoltaic

While the main process in OLEDs relies on generating light from injected charge carriers, organic photovoltaic is based on the reverse principle: the generation of free charge carriers from absorbed light. After absorption of photons on donor or acceptor, there exist different pathways, with multiple spin states involved, before free charge carriers can be collected as photo current. Figure 2.5a shows the three different main steps to generate photocurrent in a bulk heterojunction, while Figure 2.5b shows the associated spin states and pathways in a Jablonski diagram. Here, Figure 2.5b shows the example of an energetically lower singlet state of the acceptor as found in modern non-fullerene acceptors (NFAs). In blends with fullerene acceptors, the relative energies of the donor and acceptor can be reversed. The three steps to generate free charge carriers are as follows:^[28,31]

Molecular Excitation

In donor:acceptor solar cells, the absorbed photon mainly generates excitons on the donor or on the acceptor. NFA-based blends cover most of the visible spectrum given the energetically low singlets states of the acceptor. In fullerene-based blends, the donor, i.e., polymer, mostly absorbs the photons due to the energetically high acceptor singlet states. In contrast to electrical injection, spin conservation results in the formation of only excited singlet states. Given the low dielectric constant and large screening length, the binding energy of these excitons is significantly larger than the thermal en-

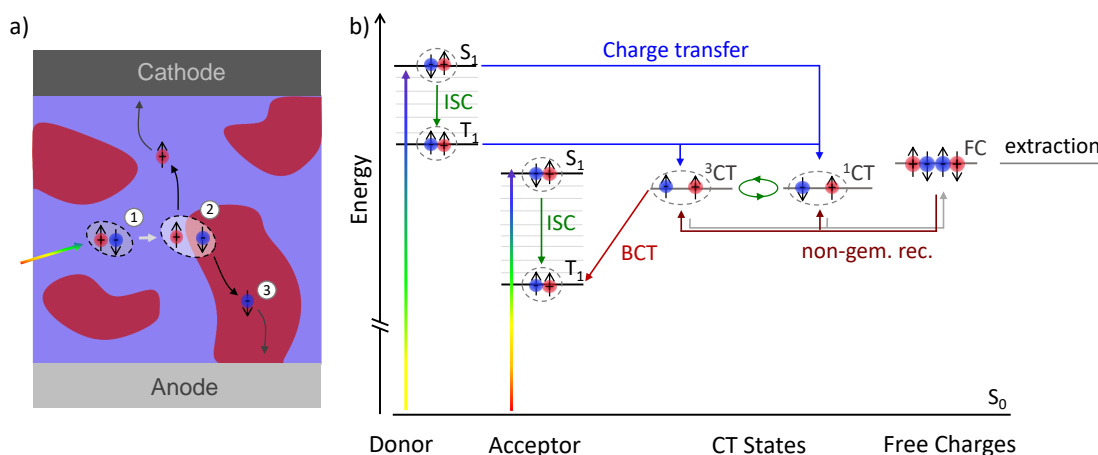


Figure 2.5: Schematic formation of free charge carriers from absorbed light in a bulk hetero-junction. a) Molecular exciton is formed upon light absorption (1). After diffusion to the donor:acceptor interface, a charge transfer (CT) takes place (2). CT excitons can separate into free charge carriers which can be extracted at the electrodes (3). Adapted from^[31] b) Jablonski diagram showing the processes between electronic states. Light absorption generates excitons on the singlet states S_1 , which can undergo ISC to T_1 or charge transfer to CT states 1CT . Triplet CT states 3CT can be occupied from the 1CT or from higher lying T_1 . 3CT can undergo back charge transfer (BCT) to lower lying T_1 states. If CT excitons dissociate, free charge carriers (FC) are formed which can be extracted at the electrodes or recombine non-geminately.

ergy, also called *Frenkel exciton*. There are three possible pathways from the excited singlet state: with certain probabilities (rates) the singlet exciton decays back to the ground state, it undergoes ISC to the triplet state or it diffuses to the donor:acceptor interface to undergo a charge transfer (CT). If the triplet state is higher in energy than the CT state (donor T_1 in Figure 2.5b), the formed triplet exciton can also undergo CT to the lower lying CT states. In contrast, if the triplet state is lower (acceptor triplet in Figure 2.5b), the triplet excitons are energetically trapped, as it is investigated in more detail in ch. 7 and ch. 8.^[30,31]

Charge Transfer

The charge transfer represents the transition of the electron from the LUMO of the donor to the LUMO of the acceptor or hole transfer from the HOMO of the acceptor to the HOMO of the donor. For this process to occur, the exciton first has to diffuse to a donor:acceptor interface within its lifetime to prevent premature recombination. Efficient organic solar cells have an active layer processed as a so-called bulk hetero-junction, i.e., a mixed donor:acceptor structure. A good trade-off is required between sufficient intermixing to facilitate charge transfer and a certain domain size to enable

charge transport to the electrodes. If the exciton reaches a donor:acceptor interface, the difference in LUMO offset (electron transfer) or HOMO offset (hole transfer) between donor and acceptor gives the charge transfer a driving force. The resulting CT exciton is still coulombically bound and is the intermediate step from exciton to free charge carriers. As long as the exciton originates from the same primary photoexcitation, it is also called a *geminate* pair. Besides the CT singlet states ^1CT , there are also three possible triplet states ^3CT , energetically degenerate without an external magnetic field. The singlet and triplet CT states can be described in the context of a so-called *spin-correlated radical pair* (SCRPs) or *spin-correlated polaron pair* (SCPP), further explained in the next chapter. The ^3CT states can thereby be occupied by spin mixing of the singlet and triplet SCRPs states. Furthermore, if the donor (acceptor) triplet state T_1 is higher lying in energy, ^3CT states can be occupied by spin-allowed charge transfer. If the acceptor (donor) triplet T_1 is energetically below the ^3CT states, back charge transfer (BCT) from these geminate ^3CT to molecular T_1 states eventually occurs, referred to as *geminate BCT*. This pathway represents a considerable triplet loss channel especially in fullerene-based OSC and is further addressed in ch. 8. [31,46,47]

Dissociation into Free Charges

Once a charge transfer exciton, also referred to as polaron pair, is formed, it has to be separated to gain free polarons or charge carriers. A polaron is by definition a charge (i.e., electron or hole) in combination with distortion of the environment. In organic semiconductors, the charge can thereby deform the whole molecule, lowering the charge carrier mobility. The most common description of polaron pair separation is the Braun-Onsager model: The polaron pair can either recombine in the polaron pair lifetime τ_{PP} with rate k_f or it can dissociate to free charge carriers with rate k_d . The electric field dependent dissociation probability is thus given by: [48]

$$P(E) = \frac{k_d(E)}{k_d(E) + k_f} \quad (2.16)$$

The dissociation rate k_d is hereby dependent on the electric field E . Free charges can either dissociate to the respective electrodes (electrons to anode, holes to cathode) or they encounter and recombine non-geminately. The non-geminate recombination was already discussed within the electrical injection in OLED devices, resulting in 25% singlet and 75% triplet CT states due to spin statistics in the donor:acceptor blend. If only the bulk-heterojunction as thin film without electrodes instead of an optoelectronic device is investigated, all free charge carriers have to recombine non-geminately again. If the ^3CT excitons formed via non-geminate recombination un-

dergo spin-allowed transition to molecular T_1 states, it is referred to as *non-geminate BCT*. This pathway represents a dominant loss process in all studied OSC blends and is further discussed in ch. 7 and ch. 8.^[31,49]

3 Electron Paramagnetic Resonance

Electron paramagnetic resonance (EPR) spectroscopy is a useful technique for studying the characteristics of paramagnetic samples, i.e., species with unpaired electrons. The method is based on the interaction of the electron's magnetic moment with an external magnetic field, whereby microwave irradiation induces transitions between spin sublevels. EPR spectroscopy can provide insight into the character of paramagnetic species and reveal information about their environment and the interactions involved. This chapter gives the theoretical background for EPR, starting with the definition of electron spin and the formation of spin states, the interaction of electron spins described by the spin Hamiltonian, and finishing with the presentation of characteristic spin polarizations, i.e., unequally occupied spin sublevels. The explanations in this chapter are based, unless otherwise noted, on EPR textbooks of J. A. Weil, J. R. Bolton and J. E. Wertz^[34], M. Brustolon and E. Giamello^[33], P. G. Baranov, H. J. v. Bardeleben, F. Jelezko and J. Wachtrup^[37], Daniella Goldfarb and Stefal Stoll^[50] as well as the articles by S. Richert et al.^[51] and T. Biskup^[52].

3.1 Electron Spin States

Electrons are elementary particles and characterized by an intrinsic angular momentum. The angular momentum of interest in EPR spectroscopy is the spin angular momentum \hat{S} , also denoted as electron spin. Mathematically, it is a quantum mechanical property and is described in the algebra of angular momentum theory. Physically, the angular momentum is usually represented in the units of the reduced Planck constant \hbar with $\hat{G}_S = \hbar\hat{S}$, whereby the dimensionless spin angular momentum operator \hat{S} will be used in the following. The eigenstates (also eigenfunctions, eigenvectors) of the spin angular momentum can be described using Dirac's notation to be eigenfunctions for the total angular momentum \hat{S}^2 and one component of \hat{S} , here \hat{S}_Z :^[34,37]

$$\hat{S}^2 |S, M_S\rangle = S(S+1) |S, M_S\rangle \quad (3.1)$$

$$\hat{S}_Z |S, M_S\rangle = M_S |S, M_S\rangle \quad (3.2)$$

With $S(S+1)$ and M_S being the eigenvalues of \hat{S}^2 and \hat{S}_Z , respectively. S can be considered as the quantum number for the total spin angular momentum while M_S is the spin quantum number for the projection of the spin angular momentum along the

z -axis (by convention the direction of the external magnetic field). As a result of the angular momentum algebra, M_S can take values from $-S$ to $+S$ in unit increments, resulting in $2S + 1$ possible projections of \hat{S} in z direction. This quantity of possible spin states projected in a selected direction (here z -axis) for a given spin quantum number S is called multiplicity. In the following, the most important electronic states, already addressed in ch. 2, will be described quantum-mechanically.

Doublet

For a free electron, the spin quantum number is $S = \frac{1}{2}$, resulting in $M_S = \pm\frac{1}{2}$. Due to the multiplicity of $2S + 1 = 2$, these states are referred to as *doublet states*. These two eigenstates $|S, M_S\rangle$ for the one-electron system are denoted by the following common convention (also called 'spin-up' and 'spin-down'):^[34]

$$\text{Doublet } (S = \frac{1}{2}): \quad \begin{cases} |\frac{1}{2}, \frac{1}{2}\rangle = \alpha \\ |\frac{1}{2}, -\frac{1}{2}\rangle = \beta \end{cases} \quad (3.3)$$

Singlet/Triplet

In the case of two electrons, a coupling of the individual spin angular momenta has to be taken into account. In this coupled representation, the total spin angular momentum can be defined by the addition of the uncoupled spin operators:^[34]

$$\hat{S} = \hat{S}_1 + \hat{S}_2 \quad (3.4)$$

The coupling results in the formation of four spin states with spin quantum number $S = 0$ and $S = 1$. The spin quantum number $S = 0$ leads to a multiplicity of $2S + 1 = 1$, referred to as *singlet states*. The spin quantum number $S = 1$ results in a multiplicity of $2S + 1 = 3$, also called *triplet states*. The triplet states thus possess spin quantum numbers in z -direction of $M_S = -1, 0, +1$. The four new collective eigenstates $|S, M_S\rangle$ of the two-electron system can be represented by linear combination of spin eigenfunction from the one-electron systems:^[27,34]

$$\begin{aligned} \text{Singlet } (S=0): \quad & |0, 0\rangle = \frac{1}{\sqrt{2}} [\alpha(1)\beta(2) - \beta(1)\alpha(2)] \\ \text{Triplet } (S=1): \quad & \begin{cases} |1, 1\rangle = \alpha(1)\alpha(2) \\ |1, 0\rangle = \frac{1}{\sqrt{2}} [\alpha(1)\beta(2) + \beta(1)\alpha(2)] \\ |1, -1\rangle = \beta(1)\beta(2) \end{cases} \end{aligned} \quad (3.5)$$

The three triplet eigenstates are also denoted as $|1, 1\rangle = |T_+\rangle$, $|1, 0\rangle = |T_0\rangle$ and $|1, -1\rangle = |T_-\rangle$ according to their spin quantum number M_S . These coupled spin eigenstates are either symmetric (triplet) or antisymmetric (singlet) regarding the exchange of the electrons. The occupation of both electrons in the same spatial orbital results in singlet states obeying the Pauli principle (antisymmetric coupling of spin eigenfunctions). As a consequence, the ground state in closed-shell organic molecules always exhibit singlet character. In contrast, electrons occupying different molecular orbitals, e.g., in excited states where an electron of the HOMO has been raised to an energetically higher molecular orbital, can exhibit both singlet and triplet character.^[28,34]

Spin-Correlated Radical Pair

A more complex situation of coupling occurs when photoexcitation, producing an excited singlet state, is followed by, e.g., electron transfer from a donor to an acceptor molecule. As this process is in general spin conserving, the final state of this transition is still a coupled spin system, generating a *spin-correlated radical pair* (SCRPA), or also called *spin-correlated polaron pair* (SCPP) in terms of OPV. These SCRPA are referred to as intermediate charge transfer (CT) states between strongly coupled excitons (i.e., singlet/triplet) and fully separated polarons (i.e., doublets). The SCRPA is characterized by a set of four eigenstates, two of which are pure triplet states, while the singlet state $|0, 0\rangle$ and the triplet sublevel $|T_0\rangle = |1, 0\rangle$ are being mixed. The four spin eigenstates of a SCRPA with singlet-triplet mixing ratio ϕ are then given by:^[46,53]

$$\begin{aligned}
 |1\rangle &= |1, 1\rangle \\
 |2\rangle &= \cos\phi |0, 0\rangle + \sin\phi |1, 0\rangle \\
 |3\rangle &= -\sin\phi |0, 0\rangle + \cos\phi |1, 0\rangle \\
 |4\rangle &= |1, -1\rangle
 \end{aligned}
 \tag{3.6}$$

Due to angular momentum conservation, only a mixing of the spin states with singlet content, $|2\rangle$ and $|3\rangle$ states, occur. The singlet-triplet mixing ratio depends on $\tan 2\phi = \left(\frac{\frac{1}{2}\Delta\omega}{J + \frac{1}{2}d}\right)$. The individual contributions of this term are explained in the following sections in the context of the electron interactions described by the spin Hamiltonian. In short, it depends on the dipolar coupling constant $d = D(3\cos^2\Theta - 1)$ (with ZFS parameter D and Θ describing the angle between spin-spin vector and magnetic field axis, see ch. 3.2.2), the difference in Zeeman interaction (see ch. 3.2.1, given as frequency $\Delta\omega = \Delta E/\hbar$) and the exchange interaction J (see ch. 3.2.3).^[46,54]

3.2 Spin Hamiltonian

The interaction of an electron spin in a system can be described by a spin Hamiltonian. The total electron spin Hamiltonian operator \hat{H} of a system including all relevant interactions reads:^[52]

$$\hat{H} = \hat{H}_{EZ} + \hat{H}_{NZ} + \hat{H}_{ZFS} + \hat{H}_{HFI} + \hat{H}_{EX} \quad (3.7)$$

The most known interaction is the **electron Zeeman interaction** \hat{H}_{EZ} of the electron spin with an external magnetic field. The corresponding **nuclear Zeeman interaction** \hat{H}_{NZ} of the nuclear spin with the external magnetic field is usually weak and therefore typically negligible. When considering a system with $S \geq 1$, the **zero-field splitting** operator \hat{H}_{ZFS} gets important. It consists of a spin-orbit term and a dipolar coupling term, whereby the former one can be neglected here as further elaborated below. The **exchange interaction** \hat{H}_{EX} describes the quantum mechanical interaction between two electrons enforced by the Pauli principle and produces the energetic splitting between singlet and triplet states in organic molecules. Lastly, the **hyperfine interaction** \hat{H}_{HFI} is based on the interaction of an electron spin with surrounding nuclear spins. In the investigated systems, hyperfine couplings are rarely resolved and hidden in the inhomogeneous line broadening, thus can be considered as minor perturbations. In the following sections, the interaction terms most relevant to the organic systems studied in this thesis are described in more detail. These include the electron Zeeman interaction \hat{H}_{EZ} , the zero-field splitting \hat{H}_{ZFS} and the exchange interaction \hat{H}_{EX} .

3.2.1 Electron Zeeman Interaction

The spin angular momentum \hat{S} , discussed in sec. 3.1, can be associated with a magnetic moment $\hat{\mu}$ using the following relation:^[33,37]

$$\hat{\mu} = -\mathbf{g}\mu_B\hat{S} \quad (3.8)$$

\mathbf{g} is the g-tensor, which can be assumed to be isotropic due to a small spin-orbit coupling in organic molecules with light atoms. For a free electron without interaction with the environment, the g-factor possesses a value of $g_e = 2.002319$. μ_B is the Bohr magneton with $\mu_B = 9.27410^{-24} \text{ J T}^{-1}$. Eq. 3.8 defines that the spin angular momentum \hat{S} and the magnetic moment $\hat{\mu}$ have opposite directions.

The interaction of the magnetic moment $\hat{\mu}$ with an external magnetic field \vec{B} leads to an energetic separation of the electron's eigenstates possessing different spin quantum

numbers M_S . This interaction, named after the physicist Pieter Zeeman who discovered this splitting in 1896, is determined by the following Hamilton operator:^[37]

$$\hat{H}_{EZ} = -\hat{\mu} \vec{B} = g\mu_B \hat{S} \vec{B} \quad (3.9)$$

When choosing the z -axis along the external magnetic field \vec{B} with magnitude B_0 , the scalar product simplifies to:^[34]

$$\hat{H}_{EZ} = g\mu_B \hat{S}_Z B_0 \quad (3.10)$$

The quantized energy level of the systems are then given by the eigenvalues of the Hamiltonian operator:^[37]

$$\hat{H}_{EZ} |S, M_S\rangle = E_{EZ} |S, M_S\rangle \quad (3.11)$$

With the eigenvalues of the \hat{S}_Z operators from eq. 3.1, the energy level can be determined as:^[34]

$$\hat{H}_{EZ} |S, M_S\rangle = g\mu_B B_0 \hat{S}_Z |S, M_S\rangle = g\mu_B B_0 M_S |S, M_S\rangle \quad (3.12)$$

For triplet states with spin quantum numbers $S = 1$ and $M_S = -1, 0, +1$, eq. 3.12 results in an energetic splitting into three triplet sublevels $|T_-\rangle$, $|T_0\rangle$ and $|T_+\rangle$ with an energy difference of $\Delta E_{EZ} = g\mu_B B_0$, as shown in Figure 3.1.

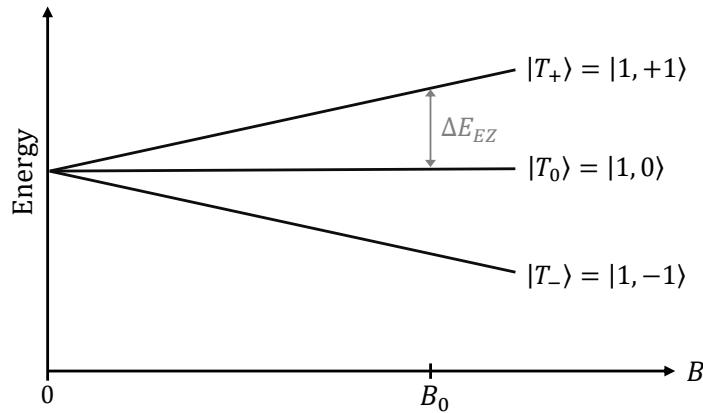


Figure 3.1: Zeeman splitting for triplet sublevels $S = 1$ and $M_S = -1, 0, +1$ with magnetic field dependent energetic splitting ΔE_{EZ} . According to the spin quantum number M_S , the triplet sublevels are denoted as $|T_-\rangle$, $|T_0\rangle$ and $|T_+\rangle$.

3.2.2 Zero-Field Splitting

If the total spin quantum number of a system is $S \geq 1$, the description has to account for spin-spin interactions, for instance between two unpaired spins of an excited state or coexisting spins in different orbitals. The coupling between the electrons' magnetic

moments leads to the removal of the degeneracy even in zero magnetic field, also referred to as zero-field splitting (ZFS). In organic molecules, it is reduced to the dipolar coupling, describing the interaction of the magnetic moment of one magnetic dipole with the magnetic field generated by the other magnetic dipole at the location of the first dipole. The corresponding Hamiltonian \hat{H}_{ZFS} can be derived as the product of the spin angular momentum \hat{S} of the coupled system with the zero-field tensor \mathbf{D} :^[51]

$$\hat{H}_{\text{ZFS}} = \hat{S}^T \mathbf{D} \hat{S} \quad (3.13)$$

For randomly selected axes, eq. 3.18 can be written in the general matrix form:^[55]

$$\hat{H}_{\text{ZFS}} = \begin{pmatrix} \hat{S}_x & \hat{S}_y & \hat{S}_z \end{pmatrix} \begin{pmatrix} D_{xx} & D_{xy} & D_{xz} \\ D_{yx} & D_{yy} & D_{yz} \\ D_{zx} & D_{zy} & D_{zz} \end{pmatrix} \begin{pmatrix} \hat{S}_x \\ \hat{S}_y \\ \hat{S}_z \end{pmatrix} \quad (3.14)$$

When choosing the coordinate frame along suited symmetry directions of the molecule, i.e., the principal axes, the tensor \mathbf{D} can be simplified to its diagonal form:^[51]

$$\hat{H}_{\text{ZFS}} = \begin{pmatrix} \hat{S}_x & \hat{S}_y & \hat{S}_z \end{pmatrix} \begin{pmatrix} D_x & 0 & 0 \\ 0 & D_y & 0 \\ 0 & 0 & D_z \end{pmatrix} \begin{pmatrix} \hat{S}_x \\ \hat{S}_y \\ \hat{S}_z \end{pmatrix} = D_x \hat{S}_x^2 + D_y \hat{S}_y^2 + D_z \hat{S}_z^2 \quad (3.15)$$

Since the trace of \mathbf{D} only shifts the total energy of the spin sublevels and is irrelevant for EPR, the trace $D_x + D_y + D_z$ is set to zero. Thus, two independent scalar parameters D and E can describe the zero-field interaction:^[51]

$$\hat{H}_{\text{ZFS}} = D \left(\hat{S}_z^2 - \frac{1}{3} S(S+1) \right) + E \left(\hat{S}_x^2 - \hat{S}_y^2 \right) \quad (3.16)$$

Here, $D = \frac{3}{2} D_z$ describes the axial symmetry and $E = \frac{1}{2} (D_x - D_y)$ the deviation from the axial symmetry, i.e., the rhombicity.

The energetically splitted zero-field sublevels are denoted as $|X\rangle$, $|Y\rangle$ and $|Z\rangle$ according to the principal axes of the ZFS tensor, whose energies are given by:^[51,52]

$$\begin{aligned} \varepsilon_{|X\rangle} &= -D_x = \frac{1}{3} D - E \\ \varepsilon_{|Y\rangle} &= -D_y = \frac{1}{3} D + E \\ \varepsilon_{|Z\rangle} &= -D_z = -\frac{2}{3} D \end{aligned} \quad (3.17)$$

As described above, the ZFS operator carries both, contributions from dipolar coupling as well as SOC. Given the light atoms in organic molecules, the dipolar coupling ex-

ceeds the the spin-orbit contribution, thus, the interaction can be derived only considering the former. Expressing the ZFS Hamiltonian analogous to the dipolar interaction, the parameters D and E can be written as follows: [34,51]

$$D = \frac{3}{4} \frac{\mu_0 (\mu_B g)^2}{4\pi} \left\langle \frac{r^2 - 3z^2}{r^5} \right\rangle = \frac{3}{4} \frac{\mu_0 (\mu_B g)^2}{4\pi} \left\langle \frac{1 - 3\cos^2\Theta}{r^3} \right\rangle$$

$$E = \frac{3}{4} \frac{\mu_0 (\mu_B g)^2}{4\pi} \left\langle \frac{y^2 - x^2}{r^5} \right\rangle$$
(3.18)

Thereby, r represents the distance between the unpaired spins and Θ the angle between the spin-spin vector and the principal z -axis. Thus, D is a value for the average inter-spin distance and is usually decisive for the width of the triplet EPR spectrum (ch. 3.3.1). The sign of D thereby depends on $1 - 3\cos^2\Theta$ and differs between oblate ($D > 0$) and prolate ($D < 0$) spin distributions. The ZFS parameters D and E describe energies, the units of which depend on the definition of the spin Hamiltonian. In organic semiconductor research, the SI unit Joule is common, hence the interactions are defined in the same units. The Zeeman energy has already been defined in $[E_{EZ}] = J$ with the introduction of $[\mu_B] = J T^{-1}$. However, according to EPR convention, which is often specified in units of frequency, the ZFS values are usually shown in MHz. To stay with this convention, the determined values of the ZFS parameters D and E will be given in the following divided by the Planck constant h as $[D/h]$, $[E/h] = \text{MHz}$. The influence of ZFS parameters D and E on the zero-field sublevels is shown in Figure 3.2. [34,50,51]

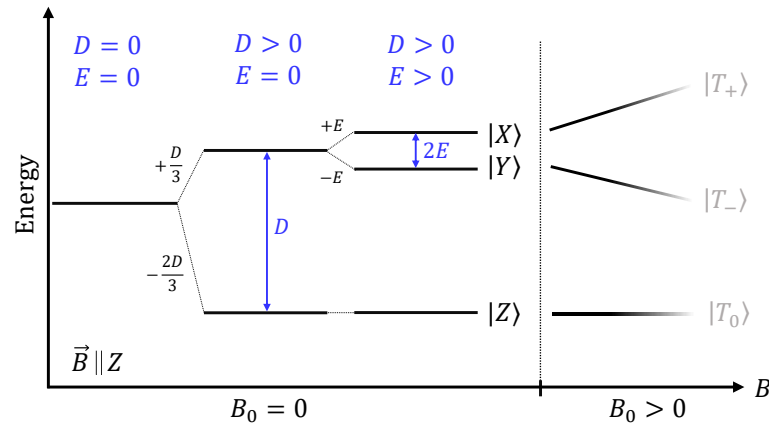


Figure 3.2: Zero-field splitting (ZFS) of triplet sublevels. Axial ZFS parameter D lifts the degeneracy between zero-field states $|Z\rangle$ and $|Y\rangle/|X\rangle$. The rhombic ZFS parameter E further splits the zero-field sublevels $|Y\rangle$ and $|X\rangle$. With the application of an external magnetic field, the triplet sublevels split according to the Zeeman splitting. Energetics are shown for $\vec{B} \parallel Z$.

3.2.3 Exchange Interaction

Usually, the exchange interaction is described as a pure quantum mechanical effect without a real classical analogue and is a direct consequence of the indistinguishability of electrons and the Pauli principle. In the simplest case, considering a pair of electrons forming a strongly bound state, the exchange interaction can be understood as the Pauli principle forcing the electrons to adopt antisymmetric spin states, while the symmetric case is split off by an energetic offset. The exchange interaction thus leads to an energetic splitting of singlet and triplet states, as will be explained in the following.^[56]

Since excitons consist of two electrons carrying a fermionic character, the total wavefunction of this quasiparticle must be antisymmetric with respect to the exchange of these two electrons. This constraint can be directly applied to the respective spin and orbital parts of the total wavefunction. An antisymmetric spin wavefunction (singlet) must be coupled with a symmetric orbital function, whereby a symmetric spin wavefunction (triplet) must be coupled with an antisymmetric orbital function. Given this direct coupling between the orbital and spin wavefunctions, the exchange interaction operator can be expressed by the spin wavefunction of the single electron only.^[34]

$$\hat{H}_{\text{EX}} = \hat{S}_1^T \mathbf{J} \hat{S}_2 \quad (3.19)$$

\hat{S}_1 and \hat{S}_2 are the individual electron spin angular momentum operators for electron 1 and 2 and \mathbf{J} as the exchange tensor. As in the last chapter for the ZFS Hamilton operator, eq. 3.19 can be written in the matrix form:^[55]

$$\hat{H}_{\text{EX}} = \begin{pmatrix} \hat{S}_x & \hat{S}_y & \hat{S}_z \end{pmatrix} \begin{pmatrix} J_{xx} & J_{xy} & J_{xz} \\ J_{yx} & J_{yy} & J_{yz} \\ J_{zx} & J_{zy} & J_{zz} \end{pmatrix} \begin{pmatrix} \hat{S}_x \\ \hat{S}_y \\ \hat{S}_z \end{pmatrix} \quad (3.20)$$

The term of most relevance to the description is the isotropic part of the exchange interaction operator, as it removes the degeneracy of the eigenvalues of S^2 , i.e., singlet and triplet state. It can be described with the isotropic electron-exchange coupling constant $J_0 = \frac{1}{3} \text{tr}(\mathbf{J})$, whereby eq. 3.19 simplifies to:^[34,56]

$$\hat{H}_{\text{EX, iso}} = J_0 \hat{S}_1^T \hat{S}_2 \quad (3.21)$$

The constant J_0 carries the information about the orbital component of the wavefunction and can be expressed as the exchange integral between the individual orbital parts as^[34]

$$J_0 = -2 \langle \Psi_a(1)\Psi_b(2) | \frac{e^2}{4\pi\epsilon_0 r} | \Psi_a(2)\Psi_b(1) \rangle \quad (3.22)$$

in a first approximation. Here $\Psi_{a,b}(1,2)$ denotes the spatial orbital wavefunctions on the sites a and b populated with electron 1 and 2, respectively. r is the inter-electron distance, e the electron charge and ϵ_0 the vacuum permittivity. In the case of organic semiconductors, $\Psi_{a,b}$ denotes the molecular orbital wavefunctions, i.e., HOMO and LUMO, respectively. Given the fundamental difference in orbital symmetry between triplet and singlet states, this exchange integral typically induces an energetic splitting ΔE_{ST} , equally to description of J_0 in eq. 3.22. In organic systems, the exchange integral carries a negative sign, leading to triplet states, which are energetically lower than the singlet states. The energetic splitting thereby strongly depends on the overlap wavefunction, as seen from eq. 3.22. Thus, molecular states with large HOMO-LUMO wavefunction overlap possess a larger energetic splitting between singlet and triplet state, while CT states with HOMO and LUMO wavefunction located on different molecules reveal a smaller energetic splitting.^[34,42,56]

3.3 Spin Polarization

Spin polarization is the unequal population of paramagnetic states, e.g., by different population of triplet sublevels upon photoexcitation. This unequal population of triplet states is fundamental for EPR experiments, since microwave radiation is absorbed/emitted only in a spin polarized system. There are several processes that lead to spin polarization, whereby those most relevant to this work are discussed below. The resulting unequal population is compensated either by spin-lattice interactions to achieve Boltzmann conditions, or by microwave-induced transitions under magnetic resonance conditions with the aim to achieve an equal distribution between triplet sublevels. This section first discusses microwave-induced transitions before explaining the origin of spin polarization by SOC-induced ISC and geminate BCT. The information is, additionally to the sources mentioned at the beginning of the chapter, based on articles from F. Kraffert et al.^[46], Y. Hou et al.^[57], and C. D. Buckley et al.^[53].

3.3.1 Transitions between Triplet Sublevels

Full-Field Transitions

This work mainly covers EPR research on triplet states ($S = 1$) in organic systems. The relatively short distance between the spins leads to the exchange interaction exceeding the dipolar interaction. Therefore, the triplet sublevels are separated from the singlet state and the EPR triplet spectra are mainly determined by Zeeman and ZFS interactions. The energetic splitting of the high-field triplet states $|T_-\rangle$, $|T_0\rangle$ and $|T_+\rangle$ depends on the orientation of the external magnetic field \vec{B} with respect to the principal axes X , Y and Z of the ZFS tensor. In the canonical orientation, the external magnetic field is aligned with one of the principal axes and the energy of the corresponding state is independent of B . While its energy is equal to the energy in the zero-field, the energies of the other two states increase and decrease, respectively, as a function of B . For the case of $\vec{B} \parallel Z$, the energies of the triplet substates are given by:^[51]

$$\begin{aligned}\varepsilon_+ &= \frac{1}{3}D + \sqrt{E^2 + (g\mu_B B)^2} \\ \varepsilon_0 &= -\frac{2}{3}D \\ \varepsilon_- &= \frac{1}{3}D - \sqrt{E^2 + (g\mu_B B)^2}\end{aligned}\quad (3.23)$$

Analogously, the energies of the sublevels for the other two canonical orientations $\vec{B} \parallel X$ and $\vec{B} \parallel Y$ can be calculated. Microwave irradiation with $E = h\nu_{\text{MW}}$ can induce spin-allowed transitions of $\Delta M_S = \pm 1$ between triplet sublevels. The magnetic field component of the electromagnetic microwave irradiation is denoted by B_1 . Only

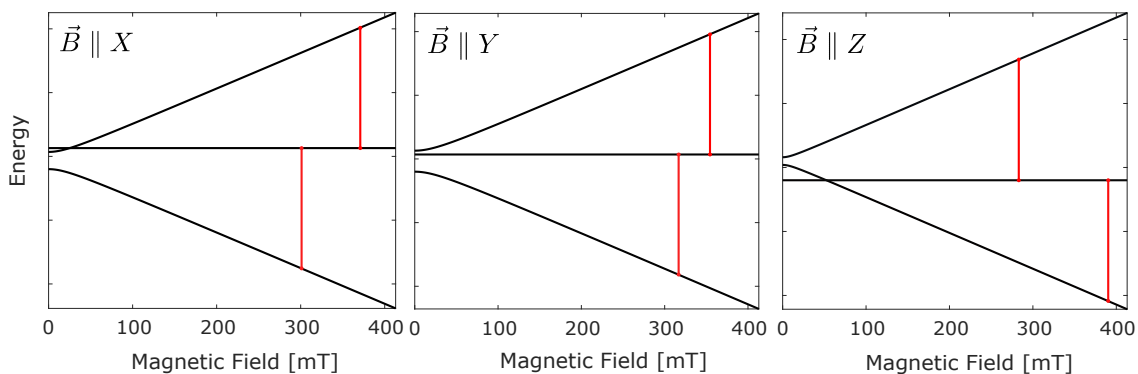


Figure 3.3: Energetics of triplet sublevels for all canonical orientations $\vec{B} \parallel X$ (left), $\vec{B} \parallel Y$ (middle) and $\vec{B} \parallel Z$ (right) with exemplary values of $D/h = 1500\text{MHz}$, $E/h = 150\text{MHz}$ and $\nu_{\text{MW}} = 9.43\text{GHz}$. The spin allowed transitions $\Delta M_S = \pm 1$ are shown in red. Energy levels and transitions determined with MATLAB toolbox EasySpin.^[58]

the B_1 contribution oscillating in the xy plane, i.e., perpendicular to the static Zeeman field B_0 in the z direction, enables effective interaction between electron spin and microwave irradiation. Figure 3.3 shows the triplet sublevel energy splitting for all canonical orientations with exemplary values, realistic for organic polymers studied in the X-band region, of $D/h = 1500$ MHz, $E/h = 150$ MHz, and $\nu_{\text{MW}} = 9.43$ GHz. It also depicts the spin-allowed $\Delta M_S = \pm 1$ transitions (red) between $|T_-\rangle \leftrightarrow |T_0\rangle$ and $|T_0\rangle \leftrightarrow |T_+\rangle$, so called *full-field* (FF) transitions. Here, the distance between transitions depends on the canonical orientation and is proportional to $|D| + 3|E|$, $|D| - 3|E|$ and $|2D|$ for $\vec{B} \parallel X$, $\vec{B} \parallel Y$, and $\vec{B} \parallel Z$, respectively. Therefore, the total width of an EPR spectrum can be directly correlated with the ZFS parameter D , making it an direct indicator of spin density delocalization (eq. 3.18) in a given material.^[51,52,59]

Half-Field Transitions

In addition to the spin-allowed $\Delta M_S = \pm 1$ transitions, first-order spin-forbidden $\Delta M_S = \pm 2$ transitions can also be observed in systems with strong dipolar coupling. Since these transitions occur at $g \approx 4$, i.e., at half the resonant magnetic field, they are referred to as *half-field* (HF) transitions. In the S-, X-, and Q-band regions (i.e., $\nu_{\text{MW}} = 2 - 50$ GHz), the relative intensity of the HF signal to the FF signal scales with the interspin distance r between the two electron spins:^[60]

$$I_{\text{HF}} = \frac{A}{r^6} \left(\frac{9.1}{\nu_{\text{MW}}} \right)^2 \quad (3.24)$$

Here, ν_{MW} represents the applied microwave frequency and A a prefactor. Based on eq. 3.24, HF transitions predominantly occur for short interspin distances ($r < 1$ nm), i.e., molecular triplet excitons. The position B_{min} of the HF signal depends on the ZFS parameters D and E :^[60,61]

$$B_{\text{min}} = \frac{1}{2g_e\mu_B} \left[(h\nu_{\text{MW}})^2 - 4 \left(\frac{D^2}{3} + E^2 \right) \right]^{\frac{1}{2}} \quad (3.25)$$

With microwave frequency ν_{MW} , g value of the free electron g_e and Bohr magneton μ_B . Eq. 3.25 demonstrates that molecular excitons with different ZFS parameters possess different HF positions. Thus, the HF signal can be used as an additional characteristic to distinguish the molecular affiliation of the observed triplet excitons.

3.3.2 Spin Polarization by SOC-induced ISC

Having clarified the transitions in a spin polarized triplet system, the main processes leading to an unequal population of triplet sublevels are explained in the following. According to the selection rules, photoexcitation can only result in excited singlet excitons, whereby subsequently ISC leads to population of the triplet states. As already discussed in ch. 2.2.2, SOC is the dominant mechanism driving ISC in small molecules. SOC-induced ISC thereby acts on the zero-field triplet states $|X\rangle$, $|Y\rangle$, and $|Z\rangle$, whose populations can be transferred to populations of the high-field states $|T_-\rangle$, $|T_0\rangle$, and $|T_+\rangle$. As already mentioned in sec. 3.3.1, the energetics of triplet sublevels depends on the canonical orientation. The populations p_- , p_0 , and p_+ for the respective triplet

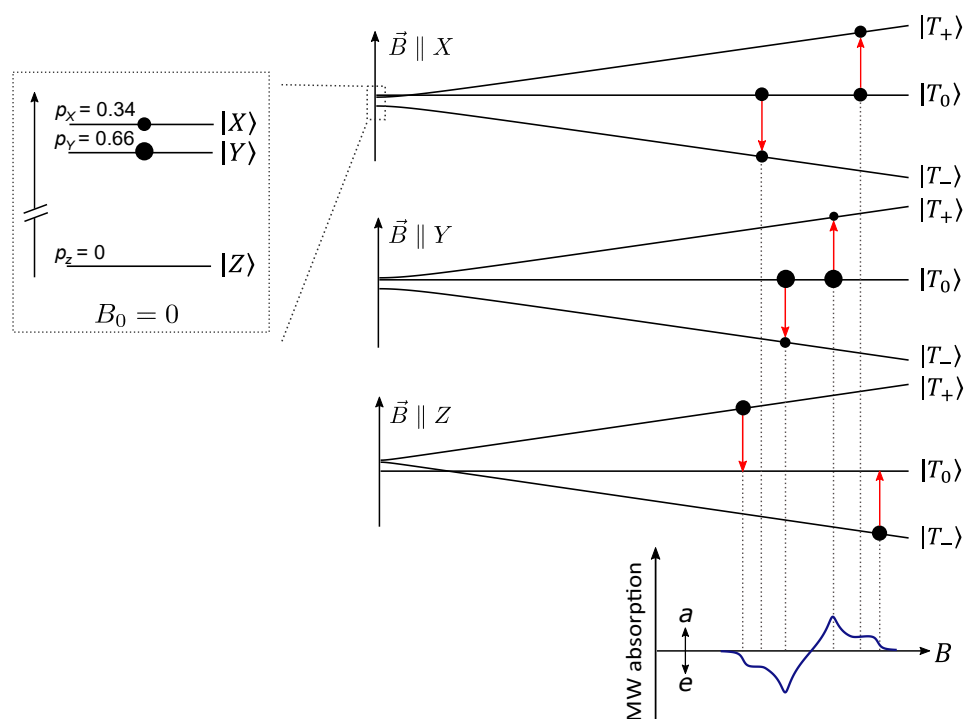


Figure 3.4: Polarization pattern, observable with trEPR, of a spin polarized triplet state formed by SOC-induced ISC. SOC-induced ISC leads to characteristic population of the zero-field triplet states $|X\rangle$, $|Y\rangle$, and $|Z\rangle$. The zero-field population is transferred to population of high-field states $|T_-\rangle$, $|T_0\rangle$ and $|T_+\rangle$ depending on the canonical orientation, i.e., orientation of the external magnetic field to the principal axis X, Y, Z of the ZFS tensor. Resonant microwave irradiation induces absorption or emission, whereby disordered samples exhibit transitions from all canonical orientations. Here shown for exemplary values of ZFS parameters $D/h = 1500$ MHz, $E/h = 150$ MHz and relative zero-field population $[p_x, p_y, p_z] = [0, 0.66, 0.34]$. Energy levels determined with MATLAB toolbox EasySpin.^[58] Adapted from^[59]

sublevels in the high field can be derived from the populations p_x , p_y , and p_z in the zero-field as follows:^[51,59]

$$\begin{aligned}\vec{B} \parallel X: p_0 &= p_x, p_{\pm} = \frac{1}{2}(p_y + p_z) \\ \vec{B} \parallel Y: p_0 &= p_y, p_{\pm} = \frac{1}{2}(p_x + p_z) \\ \vec{B} \parallel Z: p_0 &= p_z, p_{\pm} = \frac{1}{2}(p_x + p_y)\end{aligned}\tag{3.26}$$

These non-Boltzmann populations of triplet sublevels for all canonical orientations lead to absorbing (*a*) or emitting (*e*) transitions under resonance conditions, depending on the relative population of these sublevels. In this context, transient EPR (ch. 4.3.1) can distinguish between population pathways by directly measuring microwave emission and absorption, while optically detected magnetic resonance (ch. 4.3.2) measures spin polarization indirectly by coupling the spin polarized triplet states to luminescence (a detailed comparison of these methods can be found in ch. 7 and ch. 8). In a disordered sample, the transitions for all canonical orientations add up to a characteristic polarization pattern, exemplified in Figure 3.4 for the relative zero-field population $[p_x, p_y, p_z] = [0.34, 0.66, 0]$. Considering all possible spin polarizations, trEPR spectra of triplet states populated by SOC-induced ISC can exhibit *aaaaee*, *eeeeaa*, *eeaeaa*, *aaeeae*, *aeaeae*, or *eeaeae* patterns.^[51,59]

3.3.3 Spin Polarization by Geminate Back Charge Transfer

If the photoexcited singlet states do not undergo SOC-induced ISC, they may dissociate at the donor:acceptor interface and undergo charge transfer, as discussed already in ch. 2.3.2. CT states can be described in the context of SCRP (eq. 3.6), with only spin mixing between spin states with singlet fraction, i.e., $|2\rangle$ and $|3\rangle$, owing to angular momentum conservation (ch. 3.1). Thus, photoexcitation and subsequent charge transfer result in an overpopulation of $|2\rangle$ and $|3\rangle$, while the pure triplet states $|1\rangle$ and $|4\rangle$ are not populated. This spin polarization leads to absorbing transitions to $|1\rangle$ and emitting transitions to $|4\rangle$, as shown in Figure 3.5. Depending on the energetic splitting of $|2\rangle$ and $|3\rangle$, the CT states after optical excitation exhibit a *aeae* or *eeae* polarization pattern in trEPR.^[46,53]

Ch. 2.3.2 also explained the emergence of geminate BCT, i.e., spin-allowed relaxation from CT states to energetically lower molecular triplet states. This triplet population pathway can be directly distinguished from triplet formation by SOC-induced ISC via a different polarization pattern. Here, only BCT from CT states formed by gem-

inate e-h pairs, i.e., electron-hole pairs originating from the same primary photoexcitation, exhibits significant characteristic spin polarization.^[62] The spin polarization of geminate-formed CT states is preserved when transferred spin-allowed to triplet states with shorter spin-spin distance, i.e., molecular triplet states. Thus, triplet formation via back charge transfer of geminate-formed CT leads to a selective population of the high-field spin states $|T_{-}\rangle$, $|T_0\rangle$, and $|T_{+}\rangle$, as shown in Figure 3.5. The ensuing overpopulated $|T_0\rangle$ state results in an *aeaeae* pattern, whereas overpopulated $|T_{\pm}\rangle$ states would result in an *eeaeae* pattern in the trEPR when considering transitions in all canonical directions. These patterns can only be obtained by selective population of high-field spin states and can be clearly distinguished from triplet excitons by SOC-induced ISC.^[51,57]

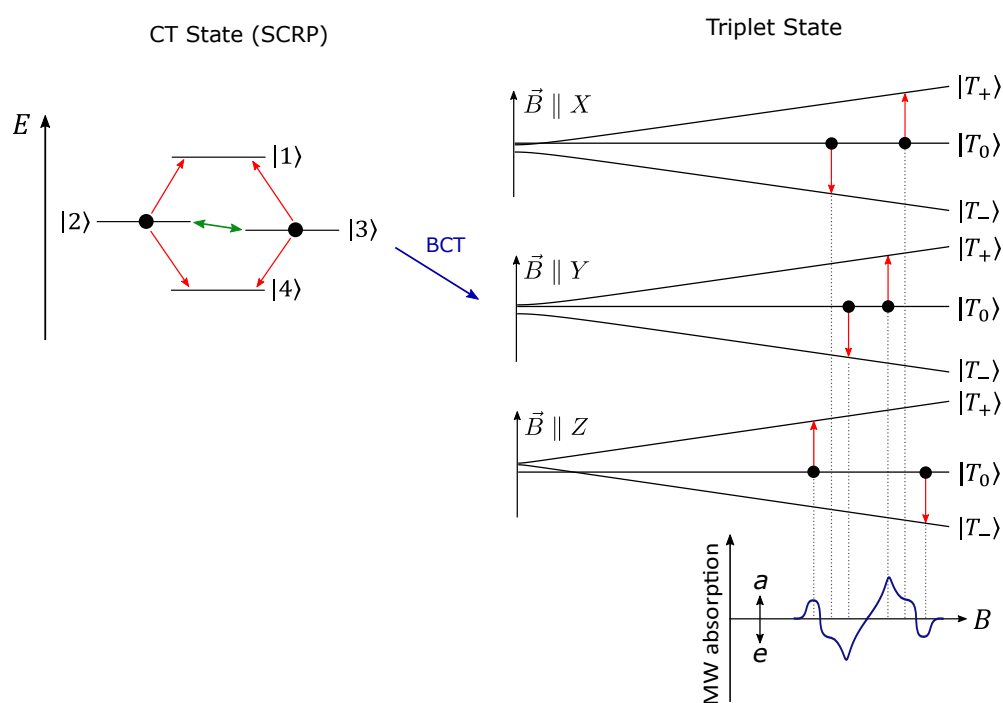


Figure 3.5: Polarization pattern, observable with trEPR, of a spin polarized triplet state formed by geminate BCT. Spin-mixing in the CT states (also referred as SCRPs) of $|2\rangle$ and $|3\rangle$ leads to a selective population, while $|1\rangle$ and $|4\rangle$ are not populated. During BCT, the spin polarization is preserved, resulting in an overpopulation of high-field state $|T_0\rangle$. Resonant microwave irradiation induces absorption or emission, whereby disordered samples exhibit transitions from all canonical orientations. Here shown for exemplary values of ZFS parameters $D/h = 1500\text{MHz}$ and $E/h = 150\text{MHz}$. Energy levels determined with MATLAB toolbox EasySpin.^[58] Adapted from^[57]

Non-Geminate Recombination

In contrast to CT states formed by geminate pairs, triplet CT states formed by non-geminate recombination are more difficult to detect with magnetic resonance techniques. Non-geminate recombination occurs when free charge carriers of different photoexcitations recombine, or in electrically driven OLEDs where excitons are generated exclusively by non-geminate recombination of electrically injected charge carriers. Recombining free charge carriers recombine spin-statistically into 25% singlet and 75% triplet states. In this process, the triplet sublevels exhibit equal occupancy, resulting in initially no spin polarization. Considering only spin-lattice relaxation, the triplet sublevels establish thermal equilibrium according to Boltzmann statistics. However, processes such as (reverse) ISC, non-radiative decay, and annihilation effects, e.g., triplet-triplet annihilation (TTA), will further enhance the spin polarization. A distinction must be made between steady-state optical/electrical excitation (as in ODMR) and a short laser pulse (as in trEPR). Steady-state excitation leads to an accumulation of charge carriers, which increases the probability of annihilation effects and further enhances spin polarization. Together with the increased sensitivity of optical detection, ODMR can usually detect non-geminate pathways. Although trEPR only detects highly spin polarized triplet states, as formed by SOC-induced ISC or geminate BCT, it can directly determine spin polarization and distinguish between geminate triplet formation pathways.^[52,63]

4 Experimental Section

The previous chapters gave an overview about the fundamentals of organic semiconductors and the principle of EPR. This chapter specifies the chosen organic material systems, the sample preparation for measurements based on electrical (devices) and optical excitation (thin films) as well as gives information about the most important methods in this thesis: transient EPR (trEPR), continuous-wave photoluminescence-detected magnetic resonance (cwPLDMR), transient electroluminescence and photoluminescence detected magnetic resonance (trELDMR, trPLDMR), transient electroluminescence (trEL) and transient absorption (TA).

4.1 Materials

4.1.1 Thermally Activated Delayed Fluorescence

On the one hand, this thesis studies organic material systems for the application in OLEDs based on the principle of TADF (ch. 5, ch. 6). To reduce ΔE_{ST} in TADF systems, HOMO and LUMO are spatially separated, resulting in donor:acceptor configuration.

The separation can be achieved by intramolecular approach, where the emitter exhibits separated donor and acceptor moieties, e.g., through molecular twist.

This approach forms an intramolecular CT state between the HOMO on the donor and LUMO on the acceptor unit. Another approach are intermolecular TADF systems, whereby the spatial separation is achieved by HOMO and LUMO located on two different molecules. The formed CT state between the donor and acceptor molecule is also called an exciplex (excited complex). Figure 4.1 shows the intermolecular TADF system, studied in this work, consisting of **m-MTDATA** (4,4',4''-tris[(3-methylphenyl)phenylamino]triphenylamine) as donor and **3TPYMB** (tris(2,4,6-trimethyl-3-(pyridin-3yl)phenyl)borane) as acceptor. While the

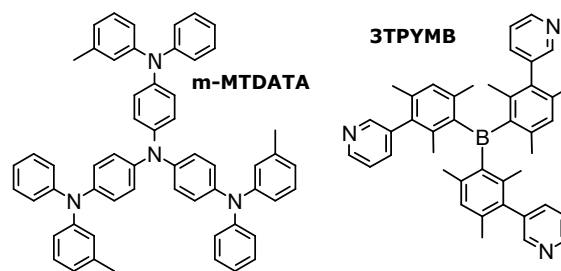


Figure 4.1: Molecular structure of intermolecular TADF system, employing m-MTDATA as donor and 3TPYMB as acceptor.

donor m-MTDATA contains triphenylamines as electron-donating moieties, the acceptor 3TPYMB possesses triarylborane as electron-withdrawing moieties.^[42]

4.1.2 Organic Photovoltaic

Besides donor:acceptor based TADF systems, this thesis also studies donor:acceptor systems for the application in OPV (ch. 6, ch. 7, ch. 8). The different donor and acceptor materials studied are described in the following.

Donor Materials

Donor materials used in this work are **PBDB-T** (poly[[4,8-bis[5-(2-ethylhexyl)-2-thienyl]benzo[1,2-b:4,5-b]dithiophene-2,6-diyl]-2,5-thiophenediyl[5,7-bis(2-ethylhexyl)-4,8-dioxo-4H,8H-benzo[1,2-c:4,5-c]dithiophene-1,3-diyl]]) as well as its fluorinated version **PM6** (also called PBDB-T-2F, poly[[4,8-bis[5-(2-ethylhexyl)-4-fluoro-2-thienyl]benzo[1,2-b:4,5-b]dithiophene-2,6-diyl]-2,5-thiophenediyl[5,7-bis(2-ethylhexyl)-4,8-dioxo-4H,8H-benzo[1,2-c:4,5-c]dithiophene-1,3-diyl]]) and chlorinated version **PM7** (also called PBDB-T-2Cl, poly[[4,8-bis[5-(2-ethylhexyl)-4-chloro-2-thienyl]benzo[1,2-b:4,5-b]dithiophene-2,6-diyl]-2,5-thiophenediyl[5,7-bis(2-ethylhexyl)-4,8-dioxo-4H,8H-benzo[1,2-c:4,5-c]dithiophene-1,3-diyl])). These molecules mainly consist of 2-alkylthiophene-substituted benzo [1,2-b:4,5-b0] dithio-phenene (BDT) core with conjugated side chains and 1,3-bis(thiophen-2-yl)-5,7-bis(2-ethylhexyl)benzo-[1,2-c:4,5-c0]dithiophene-4,8-dione (BDD) units^[64]. These donor materials are well suited for NFA-based OSCs due to their high absorption coefficient, medium band gap, deep-lying HOMO and high carrier mobilities.^[64] The halogenation substitution on the thiophene conjugated side chain of the BDT unit further down-shifts the HOMO level to reduce energy loss in NFA-based OSC.^[65,66]

As further donor material, the polymer **PTB7-Th** (poly([2,6-4,8-di(5-ethylhexylthienyl)benzo[1,2-b;3,3-b]dithiophene]3-fluoro-2[(2-ethylhexyl)carbonyl]thieno[3,4-b]thiophenediyl)) is employed. It is a PBDDT-type low-bandgap polymer with an additional 2-ethylhexyl-thienyl group in the BDT unit to further increase the absorption wavelength, up to nearly 800nm in contrast to the previous used PTB7. Thus, it is a likely used acceptor for fullerene-based OSC as it compensates the high band gap of fullerenes. Together with the fluorine-substituted TT (thieno[3,4-b]thiophene) moiety (FTT), the HOMO is also downshifted for better light harvesting.^[67-69]

The chemical structures of all OPV donor materials are shown in Figure 4.2, the HOMO and LUMO level are given in Figure 4.4.

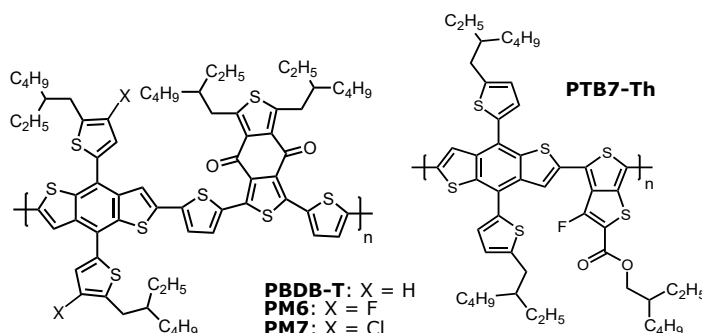


Figure 4.2: Molecular structures of donor materials for studies on OPV systems. Left: PBDB-T, PM6, and PM7. PM6 and PM7 are produced upon replacing the H atom with fluorine (F) or chlorine (Cl) at the "X" positions. Right: PTB7-Th.

Acceptor Materials

The most frequently studied acceptors for OSCs are based on either fullerenes or non-fullerenes, while the acceptors studied in this thesis are described below.

Non-Fullerene Acceptors

Non-fullerene acceptors (NFAs) proved themselves due to a high and broad optical absorption from UV-vis to NIR, increasing the efficiencies up to 19%.^[5,18,64] Moreover, they possess easily tunable molecular energy levels, low-cost fabrication, and low energy losses in combination with previously described polymers PBDB-T, PM6, and PM7.^[64,70] NFAs are built of intramolecular D-A structures with aromatic cores (D unit), end-capping group (A unit) and alkyl side chains, whereby the A units are especially important for molecular packing, electronic structures and carrier mobilities.^[71]

Studied NFAs in this thesis is the A-D-A type acceptor **ITIC** (3,9-bis(2-methylene-(3-(1,1-dicyanomethylene)-indanone))-5,5,11,11-tetrakis(4-hexylphenyl)-dithieno [2,3-d':2',3'-d']-s-indaceno[1,2 b:5,6-b']dithiophene) as well as the newest NFAs with A-D-A-D-A structure **Y6** (also called **BTP-2F**, 2,2'-((2Z,2'Z)-((12,13-bis(2-ethylhexyl)-3,9-diundecyl-12,13-dihydro-[1,2,5]thiadiazolo[3,4-e]thieno[2",3":4',5']thieno[2',3':4,5]pyrrolo[3,2-g]thieno[2',3':4,5]thieno[3,2-b]indole-2,10-diyl)bis(methanylylidene))bis(5,6-difluoro-3-oxo-2,3-dihydro-1H-indene-2,1-diylidene))dimalononitrile) and **Y7** (also called **BTP-4Cl**, 2,2'-((2Z,2'Z)-((12,13-bis(2-ethylhexyl)-3,9-diundecyl-12,13-dihydro-[1,2,5]thiadiazolo[3,4-e]thieno[2",3":4',5']thieno[2',3':4,5]pyrrolo[3,2-g]thieno[2',3':4,5]thieno[3,2-b]indole-2,10-diyl)bis(methanylylidene))bis(5,6-dichloro-3-oxo-2,3-dihydro-1H-indene-2,1-diylidene))dimalononitrile).

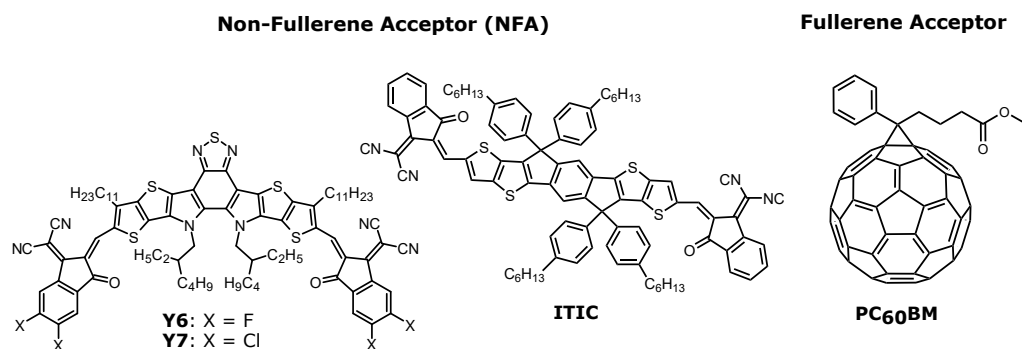


Figure 4.3: Molecular structures of acceptor materials for studies on OPV systems. Left: Non-fullerene acceptors Y6, Y7 and ITIC. Y6 and Y7 are produced upon replacing the H atom with flourine (F) or chlorine (Cl) at the "X" positions. Right: Fullerene acceptor PC₆₀BM.

Fullerene Acceptor

Prior to NFAs, fullerenes were popular acceptors for the application in OSCs, given their high electron affinity and potential for effective charge transport.^[72] One of the most famous fullerene is C₆₀, forming a stable molecule consisting of 60 carbon atoms.^[73] PC₆₀BM ([6,6]-phenyl-C61-butyric acid methyl ester) has proven to be superior to C₆₀ fullerene in that side chains on the fullerene have resulted in better solubility for processing from solution.^[14] However, the relatively high optical band gap of fullerenes and the resulting inferior absorption let plateauing the fullerene-based OSC efficiencies. Nevertheless, PC₆₀BM is still used in state-of-the art research, as in ternary blends for OPV devices, as electron transport layer in perovskite solar cells, or, as in this thesis, as a model system to develop new experimental frameworks.^[74–76]

The chemical structures of all OPV acceptor materials are shown in Figure 4.3, the HOMO and LUMO level are given in Figure 4.4.

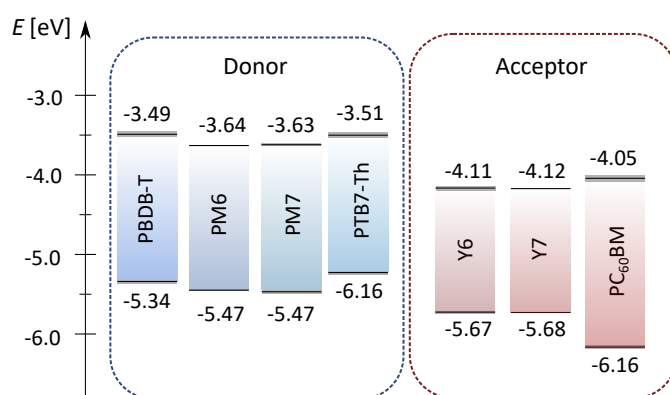


Figure 4.4: HOMO and LUMO level of studied donor and acceptor materials. Mean value (black line) including standard error (gray box). Values taken from literature for donors PBDB-T^[65,77–79], PM6^[65,78–81], PM7^[80–83], PTB7-Th^[84–87] and acceptors Y6^[88–92], Y7^[93,94] and PC₆₀BM^[95–99].

4.2 Sample Preparation

4.2.1 OLED Fabrication

The electrical measurements in this thesis (trEL, trELDMR) were performed on OLED devices. In the current research, physical vapor deposition (PVD) is a widely used method for device fabrication with small molecules, as the here used m-MTDATA and 3TPYMB. In general, OLEDs were fabricated on indium-tin-oxide (ITO) pre-coated glass substrates (1.62 cm²), consisting of a mixture of indium-oxide In₂O₃ and tin-oxide SnO₂ and characterized by transparency and charge carrier densities of about $10^{21} \frac{1}{\text{cm}^3}$ [100]. After cleaning the ITO

coated substrates, they are exposed to an oxygen plasma for 30 s to improve the stoichiometry of the surface and enhance the workfunction. [101,102] In order to facilitate the hole injection, a composition of the two polymers PEDOT:PSS (poly(3,4-ethylenedioxythiophene):polystyrene sulfonate, in a ratio of 1:6) is spin-coated as hole injection layer (HIL) onto the anode. The substrates are subsequently annealed at 130°C for 10 min to remove the residual water of the PEDOT:PSS solution. The active semiconductor layer is composed of the already described organic materials m-MTDATA, as donor and 3TPYMB, as acceptor. While m-MTDATA is used as hole transport layer (HTL), 3TPYMB is used as electron transport layer (ETL). The emission layer consists of a blend of both materials, due to the similarity in charge carrier concentration and charge carrier mobility used in a ratio of 1:1. The evaporation rate is thereby 1 Å/s for all three organic layers. A co-evaporation of the emission layer with adjusted rates ensures the mentioned ratio of the materials of 1:1. Lastly, the cathode is made up of aluminum (2 - 3 Å/s) whereby an electron injection layer (EIL) of calcium (0.1 - 0.3 Å/s) adapts the work function. The latter, together with the organic materials, are evaporated in a vacuum chamber with $p \leq 1.0 \cdot 10^{-6}$ mbar. The device structure of the produced OLEDs is ITO/PEDOT:PSS/m-MTDATA(30nm)/m-MTDATA:3TPYMB(70nm,1:1)/3TPYMB(30nm)/Ca(5nm)/Al(120nm), displayed in Figure 4.5.

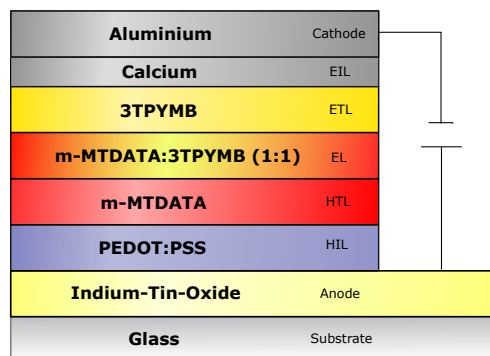


Figure 4.5: Device structure of the OLEDs used in this thesis. On an ITO-coated glass substrate, PEDOT:PSS is spin-coated as HIL. Organic layers (HTL, EL and ETL) and cathode (calcium, aluminum) are deposited, with the emission layer of m-MTDATA and 3TPYMB coevaporated in a 1:1 ratio.

4.2.2 Thin Film Samples

Measurements based on optical excitation (trEPR, trPLDMR, cwPLDMR, PL, PLE and TA) were performed on thin films. The samples can be prepared either by spin-coating the solution onto glass substrates or by drop-casting the solution into an EPR tube and subsequent evaporation of the solvent. Both preparation methods and the corresponding recipes are described below.

Spin-Coated Samples

Solutions for spin-coated samples were produced by optimized recipes for the respective studied systems:

- Neat PM-series, neat Y-Series: 18 mg/ml, anhydrous chloroform, 3000 rpm
- PM:Y-series: 18 mg/ml, 1:1.2, anhydrous chloroform, 0.5% v/v 1-chloronaphthalene, 3000 rpm
- Neat PTB7-Th: 20 mg/ml, anhydrous chlorobenzene, 2000 rpm
- Neat PM6: 18 mg/ml, anhydrous chloroform, 3000 rpm
- PTB7-Th:PCBM: 20 mg/ml, 1:1.5 anhydrous chlorobenzene, 3% v/v 1,8-diiodooctane (DIO), 2000 rpm
- PM6:PCBM: 18 mg/ml, 1:1 anhydrous chloroform, 0.5% v/v 1-chloronaphthalene, 3000 rpm

The solutions are spin-coated on glass substrates with the given parameters and annealed for 10 min at 110°C. PLDMR and trEPR samples possess (20x20x0.2) mm size whereby TA/PL samples use (15x15x1) mm substrates. PLDMR and trEPR glass substrates are cut into thin strips (2 mm width) whereby around 10 strips are filled into a standard EPR tube (Wilmad) with ≈ 2.8 mm inner diameter. To ensure oxygen free atmosphere, the EPR tube is vacuumed and, after repeated flushing with gaseous helium, sealed under the helium atmosphere with $\approx 10^{-2}$ mbar. TA samples were encapsulated with (20x20x0.2) mm cover slips (with spacer between the two glasses) and epoxy glue (Loctite 9340, Hysol).

Drop-Cast Samples

For samples prepared by drop-casting, the respective materials are dissolved in anhydrous chlorobenzene, and measurements on blends are performed on a subsequent mixture of the original solutions. Since signal intensities scale with the concentration

of the material in the solution in EPR, while optical transparency must be maintained in PLDMR, trEPR samples use 20 mg/ml, while PLDMR samples exhibit 5 mg/ml. A small amount ($\approx 100\mu\text{l}$) of these compositions are filled into an EPR tube. Evaporation of the solvent produces a thin film on the wall of the EPR tube. An oxygen-free atmosphere is ensured by flushing the EPR tube several times with helium and subsequent sealing under a helium atmosphere.

4.3 Experimental Methods

The following section contains information about the experimental techniques used in this work. The focus is thereby on the setup specifications, while the principles of the techniques are explained in the following chapters in combination with the respective experimental results.

4.3.1 Transient Electron Paramagnetic Resonance (trEPR)

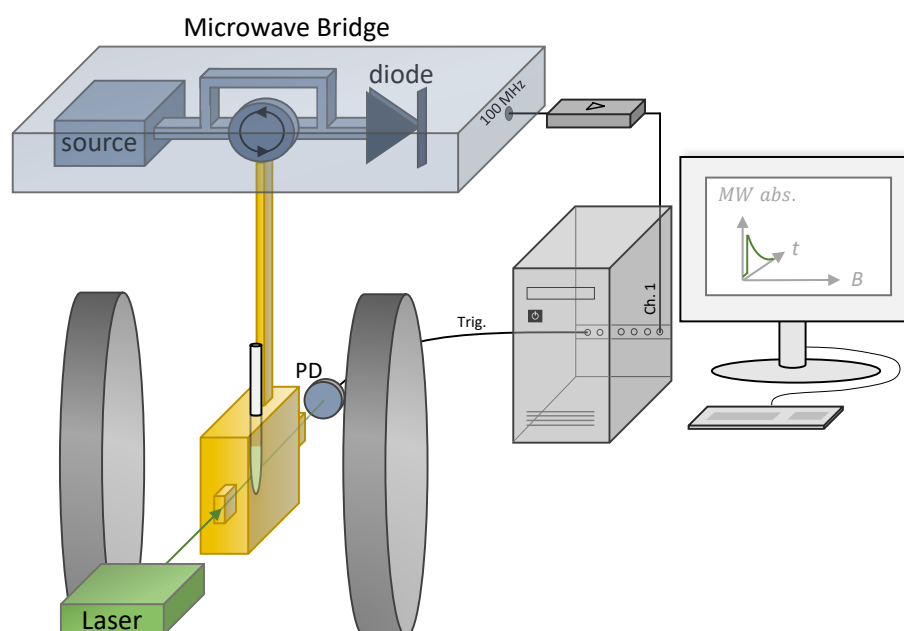


Figure 4.6: Setup for trEPR using a microwave (MW) bridge (blue) including source, circulator and detector diode. The generated microwaves are guided into the resonator (gold) with openings for optical excitation by a pulsed 532 nm laser (green). The reflected microwaves are detected by the detector diode, whose signal is amplified and recorded by a digitizer card. A photodiode (PD) on the other side opening is used as a trigger for the digital oscilloscope. Two magnetic coils (gray) produce the external magnetic field.

Figure 4.6 shows the setup scheme for trEPR measurements. It includes a modified X-band spectrometer (Bruker ESP300) equipped with two magnetic coils for the generation of an external magnetic field, a microwave bridge (Bruker ER 047 MRP) and a resonator (Bruker ER4104OR) with optical access. The electromagnet consists of two copper coils, enabling a magnetic field up to $\approx 1.4\text{T}$ via a controllable current. The resonator is placed in the center of the electromagnet with a resonance frequency of around $\nu_{\text{res}} = 9.43\text{GHz}$ (X-band regime). The microwave bridge essentially consists of a microwave source, a circulator and a microwave detector diode (attenuators and phase shifters are not shown for simplicity). The microwave irradiation with a maximum power of 200 mW is partially guided into the resonator via the circulator. Thereby, the resonator should be critically coupled, i.e., the microwave frequency ν_{MW} should be adjusted in a manner that no microwaves are reflected in non-resonant conditions. An internal automatic frequency control (AFC) locks the frequency ν_{MW} . In magnetic resonance conditions, the critical coupling is disturbed, resulting in reflection of the microwave irradiation. The reflected microwaves pass the circulator in the microwave bridge to the internal detector diode. The microwave bridge has an output with an amplifier of 100 MHz bandwidth for transient recording. A voltage amplifier (Femto DHPVA-200) further enhances the detector signal before it is recorded by a digitizer card (GaGe Razor Express 1642 ComptuScope) with a bandwidth of 125 MHz.

A Nd:YAG laser, whose second harmonic of 532 nm is used, provides short excitation pulses (Amplitude Minilite II: 5 ns pulselength, 15 Hz repetition rate, 5 mJ pulse energy. Ekspla PL2210: 80 ps pulselength, 1 kHz repetition rate, 100 μJ pulse energy), which are guided into the resonator through one optical window to photoexcite the thin film in the EPR tube. A photodetector (Hamamatsu Si photodiode S2281) on the opposite optical window is used to produce a trigger signal for the digitizer card to ensure the synchronization of the measured transients. The EPR tube is placed inside the resonator in a helium-flow cryostat (Oxford Instruments ESR900) with temperature range of 3.4 K – 300 K, adjustable by a temperature controller (Lakeshore 335).

All components and data processing are controlled by Labview softwares. For recording a 2D plot, averaged EPR transients are recorded at discrete B values while automatically increasing the magnetic field in adjustable ΔB values. trEPR spectra are averaged from 0.5 – 1.5 μs after laser excitation. The maximum time resolution is limited by the Q -factor of the resonator of around 3000. With resonator response time of $\tau_{\text{res}} = Q/(\pi\nu_{\text{res}})$, the time resolution is $\approx 100\text{ns}$.

4.3.2 Photoluminescence Detected Magnetic Resonance (PLDMR)

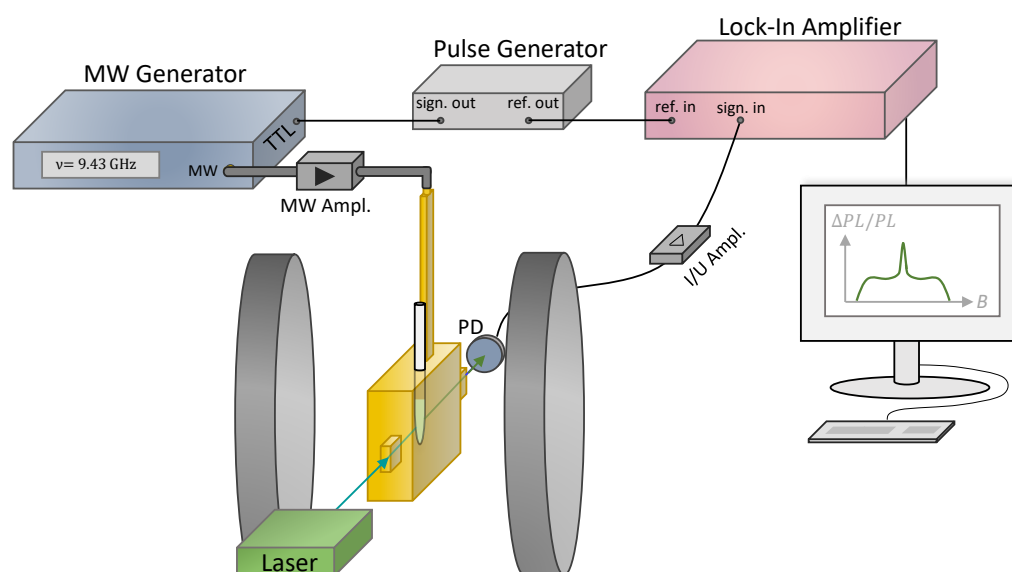


Figure 4.7: Setup for PLDMR using a microwave (MW) generator (blue), whose output is subsequently amplified to 3 W. MW are guided into the resonator (gold) with openings for optical excitation by a 473 nm laser (green) and PL detection. PL is amplified and recorded by a lock-in-amplifier (red). A pulse generator provides a TTL signals that is used as modulation for the microwaves as well as reference signal for the lock-in-amplifier. Two magnetic coils (gray) produce the external magnetic field.

Optically detected magnetic resonance (ODMR) can be applied by recording photoluminescence, i.e., PLDMR, or electroluminescence, i.e., ELDMR, under magnetic resonant conditions. Figure 4.7 shows the setup scheme for continuous-wave (cw) PLDMR. The electromagnet, the resonator and the cryostat are identical with the setup for trEPR in ch. 4.3.1. Other components have to be changed to enable PLDMR measurements: Continuous optical excitation is provided by a monochromatic light source represented either by an UV LED with 365 nm wavelength (for TADF materials) or a laser with 473 nm wavelength (for OPV materials). The silicon photodiode (Hamamatsu Si photodiode S2281) on the opposite opening of the cavity detects the resulting PL, using a long-pass filter (409 nm for TADF, 561 nm for OPV) to reject the excitation wavelength. A current/voltage amplifier (Femto DHPKA-100) amplifies the generated photocurrent with gain level up to 10^7 V/A. For cwPLDMR (Figure 4.7), a lock-in detector (Ametek SR 7230) records the PL signal from the photodetector, referenced by a TTL (transistor-

transistor-logic) signal with variable modulation frequency ν_{mod} . The TTL signal is provided by a pulse generator (Keithley 3390), whereby the microwave irradiation are modulated with the same TTL signal and frequency ν_{mod} . The microwave irradiation is produced by a microwave generator (Anritsu MG3694C), whereby a microwave amplifier (Microsemi) allows powers of up to 3W. The microwave irradiation is guided into the resonator, also in the critical coupling regime. In magnetic resonant conditions, the modulated microwaves induce a complementary oscillation in the PL between $\text{PL}_{\text{MW-off}}$ and $\text{PL}_{\text{MW-on}}$, whereby $\text{PL}_{\text{MW-on}} = \text{PL}_{\text{MW-off}} + \Delta\text{PL}$. Since the reference of the lock-in detector and the PL signal exhibit the same modulation frequency, only the component with the same frequency ν_{mod} is amplified. Assuming pink noise (proportional to $1/\nu$), the selection of a higher modulation frequency leads to a noise reduction and thus to an increase in the signal-to-noise ratio.

4.3.3 Transient Photo-/Electroluminescence Detected Magnetic Resonance (trPLDMR, trELDMR)

In addition to continuous-wave mode, ODMR can also be performed with transient recording, so called transient PLDMR (trPLDMR) or transient ELDMR (trELMDR). In contrast to continuous-wave detection, the transient recording offers on the one hand the advantage of obtaining time-resolved ODMR spectra, allowing additionally the deconvolution of overlapping signals. On the other hand, the absence of a lock-in detector allows the sign of the ODMR signal to be determined unambiguously, whereby the ODMR signal can reach its full amplitude in absence of a modulation frequency. Since this measurement method was developed within the framework of this thesis, the method will be explained in detail in ch. 6: Detecting Triplet States in Optoelectronic Materials and Devices by Transient ODMR. Additionally, the advantages of this technique are demonstrated by exemplary applications on two case studies of optoelectronic materials and devices for the application in OPV and OLEDs.

4.3.4 Transient Electroluminescence (trEL)

Figure 4.8 shows the setup scheme for performing trEL measurements. For trEL measurements, the OLED is supplied with a voltage pulse of several milliseconds, ensuring the EL to reach its steady-state. In particular, the switch-off behavior of the EL is investigated in order to study the kinetics of the material system within the electrically driven device. For voltage pulses, the OLED is connected to a function generator (Agilent Technologies 81150 A), providing voltages up to 5V for a set pulse length. For higher voltages, a voltage amplifier (Tabor Electronics A10150) with a gain of 5

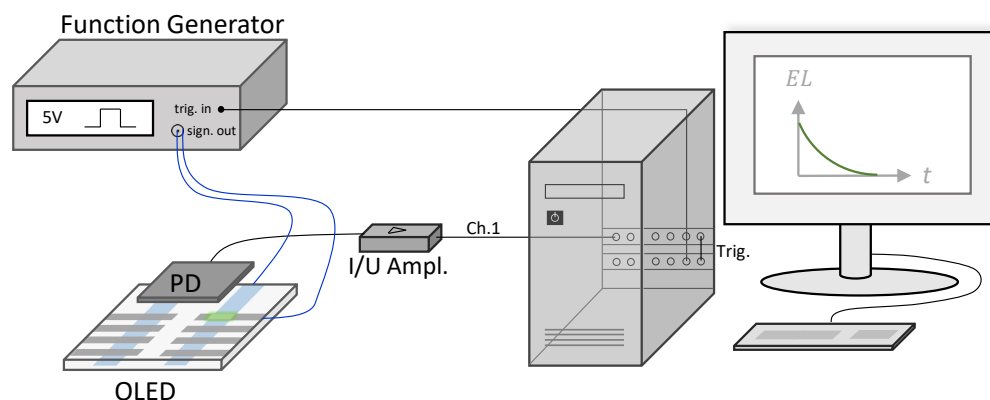


Figure 4.8: Setup for trEL using a function generator for pulsed OLED operation. A photodiode (PD) detects the emitted light, whose photocurrent is amplified and recorded by a digitizer card. A pulse blaster card triggers the digitizer card as well as the function generator.

is available. The emitted EL is detected by a photodiode (Hamamatsu Si photodiode S2387-66R). A current-voltage amplifier (Femto DHPA-100) amplifies the light-induced photocurrent, which is recorded with by a digitizer card (GaGe Razor Express 1622 CompuScope). The response time of the setup is determined by the bandwidth of the current-voltage amplifier of 1 MHz at a gain level of 10^6 V/A. To receive a defined sample data count, the step-size of the transient EL measurements is interpolated to this time resolution. Furthermore, a pulse blaster card (PulseBlasterESR-PRO) triggers the function generator and the digitizer card simultaneously to ensure synchronization of the measured transients. For temperature control and an oxygen free atmosphere, the OLED is placed in a nitrogen flow cryostat (Oxford 935).

4.3.5 Transient Absorption (TA) Spectroscopy

TA spectroscopy in this thesis (ch. 7 and ch. 8) were performed by Dr. A. J. Gillett at the Cavendish Laboratory at the University of Cambridge. The following describes the setups used for TA spectroscopy, more specifics can be found in Ref. ^[25,26,103] The TA principle is explained in ch. 7.3.1.

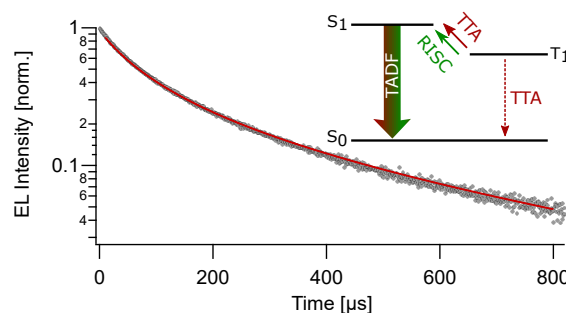
TA spectroscopy allows insight into the evolution of optically bright and dark spin states within femtoseconds after photoexcitation, enabling investigation of ultrafast excited state kinetics. This method is based on the transient pump-probe technique, whereby the pump pulse creates short-living excited states while the time-dependent evolution of these states is probed by a second pulse after different time intervals. The investigation of these short living states requires a short pump pulse ($\approx 100 - 200$ fs).

Here, a Yb amplifier (PHAROS, Light Conversion) generates 200 fs pulses ($\nu_{\text{rep}} = 38 \text{ kHz}$) centered at 1030 nm or a Ti:Sapphire amplifier (Spectra Physics Solstice Ace) generates 100 fs pulses ($\nu_{\text{rep}} = 1 \text{ kHz}$) centered at 800 nm, while an optical parametric amplifier (ORPHEUS, Light Conversion; TOPAS) provides tuneable pump wavelengths. The probe pulse should cover a wider spectral wavelength range in the visible or NIR wavelength range. For white light, a small portion of the fundamental Yb beam is focused into a YAG (yttrium aluminum garnet) crystal while NIR probe pulses are produced by a broadband non-collinear optical parametric amplifier (NOPA), running by the Ti:sapphire laser. After transmitting the sample, the probe is imaged using a silicon photodiode array (Stresing S11490) or a InGaAs dual-line array detector (Hamamatsu G11608-512DA), respectively. The probe pulse thereby passes an optical chopper (at half or quarter of the laser output) to calculate differential transmission $\Delta T/T$ spectra with and without pump pulse (see ch. 7.3.1). Measurement in ch. 7 were performed on the setup powered by the Yb amplifier, while measurements in ch. 8 used the setup powered by the Ti:Sapphire amplifier.^[25,26,103]

5 Kinetic Modeling of Transient Electroluminescence reveals Efficiency-Limiting Process in Exciplex-Based TADF OLEDs

ABSTRACT

Organic light emitting diodes (OLEDs) based on thermally activated delayed fluorescence (TADF) show increased efficiencies due to efficient upconversion of non-emissive triplet states to emissive singlet states via reverse intersystem crossing (RISC). To assess the influence of the characteristic efficiency-enhancing RISC process as well as possible efficiency-limiting effects in operational OLEDs, this chapter presents temperature-dependent measurements of transient electroluminescence (trEL). Establishing a suitable kinetic model thereby quantifies and separates the impact of different temperature-dependent depopulation processes and contributions to EL in the established donor:acceptor model system m-MTDATA:3TPYMB. The underlying rate equations adapted for EL measurements on TADF systems include radiative and non-radiative first- and second-order effects. The simulations enable the evaluation of non-radiative recombination and annihilation processes with respect to their efficiency-limiting effects on these OLEDs. On the one hand, the depopulation of intermolecular exciplex triplet states via non-radiative direct triplet decay, RISC and triplet-triplet annihilation (TTA) can be evaluated. On the other hand, the contribution to the EL by the formation of singlet exciplex states via polarons, RISC, and TTA is investigated. The results show that TTA accounts for a significant part to triplet depopulation and contributes to EL while limiting the overall device performance.



This chapter is based on: J. Grüne, N. Bunzmann, M. Meinecke, V. Dyakonov and A. Sperlich. Kinetic Modeling of Transient Electroluminescence reveals TTA as Efficiency-Limiting Process in Exciplex-Based TADF OLEDs. *J. Phys. Chem. C*, 124, 47, 25667-25674 (2020).^[23]

5.1 Introduction

Organic light emitting diodes (OLEDs) based on thermally activated delayed fluorescence (TADF) exhibit high potential due by their ability to achieve 100% internal quantum efficiency in absence of the expensive and source-limited rare metal complexes.^[10] The underlying mechanism is based on harvesting the non-emissive triplet states and upconvert them to emissive singlet states via reverse intersystem crossing (RISC), as explained in more detail in ch. 2.2.2.^[104,105] Since this mechanism is driven by thermal energy, a necessary molecular property for this purpose is a small energy gap ΔE_{ST} between the first excited singlet and triplet states, e.g., by minimizing the overlap of involved HOMO and LUMO orbitals (see eq. 2.12 for the RISC rate and eq. 3.22 for the exchange integral).^[106] Several promising concepts are under consideration to realize efficient TADF: either by combining donor and acceptor molecules that can share an intermolecular exciton at their interface, also called exciplex^[4,107], or alternatively by designing molecules that incorporate donor and acceptor moieties, enabling intramolecular excitons.^[108,109] However, a small energy gap ΔE_{ST} is not the only requirement for efficient TADF devices.^[110] The efficiency-increasing RISC rate must be large enough to outperform efficiency-reducing non-radiative recombination and annihilation processes.

This chapter focuses on a model system for the investigation of exciplex-based OLEDs employing the donor m-MTDATA and the acceptor 3TPYMB, the full molecule names and chemical structures are given in ch. 4.1.1. This material combination still attracts a lot of attention in literature^[111-113], however, according to reports, it never achieved an external quantum efficiency (EQE) higher than 12.9%^[113]. Since intermolecular donor:acceptor systems are generally characterized by a small singlet-triplet gap ΔE_{ST} , the limitation in efficiency is surprising. One indication for lower EQE could be the comparatively low photoluminescence quantum yield (PLQY) of 45%^[112]. However, exciplex states are non-absorbing, thus requiring a previous optical excitation of the donor/acceptor molecules, as further discussed below.^[114] Intermediate transitions to exciplex states and associated loss mechanisms on the pristine molecules can lower the PLQY without involvement of the exciplex states. In contrast, electrical excitation directly occupies exciplex states. Thereby, second-order processes, such as annihilation effects, are able to reduce EQE significantly, which impacts increase through the higher triplet density in electrical operation. Thus, temperature-dependent transient electroluminescence (trEL) measurements, probing the exciplex state exclusively, are thereby well suited to investigate the influence of the characteristic RISC process as well as possible efficiency-limiting effects on device performance. Therefore, a suit-

able kinetic model is adapted for EL measurements on TADF devices in order to identify loss processes. The underlying rate equations for singlets, triplets and polarons include second-order terms to consider annihilation processes.

The new kinetic model addresses all relevant processes involved in an operating OLED device, since previous research either refers to modeling of transient photoluminescence (trPL) on TADF materials^[110,115,116], transient EL of TADF devices without considering annihilation effects^[117] or on transient EL of non-TADF devices considering for second-order processes^[20,118–120]. However, as shown in the following, it is especially important in TADF devices to account for annihilation effects. One reason is that annihilation effects are often based on interactions with triplet excitons and are therefore more influential with increasing triplet density in the OLED device. In TADF-based OLEDs, the RISC process positively counteracts the impact of annihilation effects as it reduces the triplet density by upconverting triplet excitons to the singlet state. Thus, the magnitude of the RISC rate and the resulting effective triplet density are important factors determining the influence of efficiency-limiting processes.^[121] Another reason is the higher triplet generation in electrical excitation due to spin-statistical recombination in contrast to optical excitation, making the consideration of second-order effects especially important for electrically driven devices. Due to their long lifetime, triplet excitons accumulate, facilitating the influence of annihilation processes.^[122] However, a difficulty in transient EL modeling is that the OLED first reaches an equilibrium state, determined by all present rates, before the transient EL decay is recorded at the time of switching off the applied voltage. As will be shown in this chapter, the population ratio of triplets to singlets in the operational steady state amounts to 67:1, differing significantly from the spin-statistical generation ratio of 3:1. Therefore, a suitable kinetic model has to determine the population number in the operational steady-state as starting parameters for the transient EL decays.

This chapter presents adequate kinetic modeling of temperature-dependent transient EL measurements to quantify efficiency-increasing and efficiency-limiting first- and second-order processes. First, it demonstrates a rate equation based fit procedure, accurately reproducing transient EL measurements and providing required first- and second-order rates. The procedure is especially advantageous for exciplex-based systems, since rate extraction by transient PL is significantly complicated due to non-absorbing exciplex states, as further discussed below. Ultimately, the results enable quantifying the impact of efficiency-limiting processes in operational devices and to determine the contribution of relevant processes to the steady-state EL.

5.2 Kinetic Model

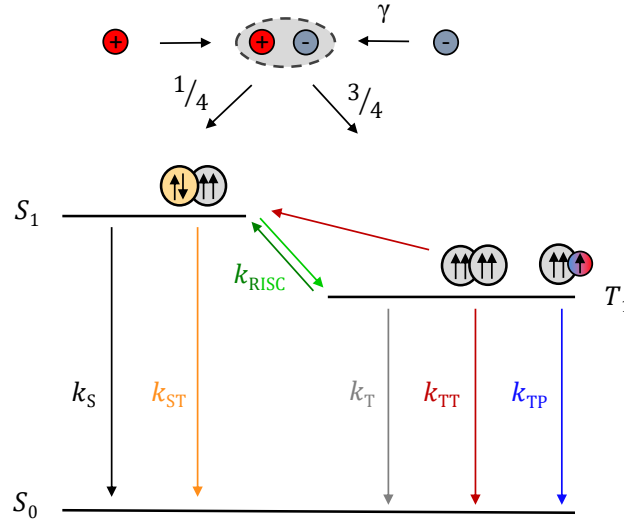
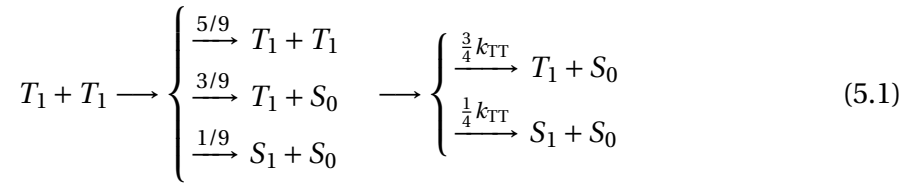


Figure 5.1: Kinetic model of a three-level system for transient EL. Injected charge carriers form excitons with the Langevin recombination rate γ . Excitons populate singlet and triplet states according to 1:3 spin statistics. Possible first-order processes include singlet decay rate k_S , (reverse) intersystem crossing rate $k_{(R)ISC}$ and non-radiative decay rate k_T . Second-order processes are considered with singlet-triplet annihilation rate k_{ST} , triplet-triplet annihilation rate k_{TT} and triplet-polaron annihilation rate k_{TP} .

Figure 5.1 schematically illustrates the kinetic model including all of the considered processes for the analysis of electrically driven TADF OLEDs. In EL measurements, the excitation is given by electrical injection. The injected charge carriers thereby form excitons, assuming Langevin recombination with rate γ (see eq. 2.15), populating continuously the singlet states S_1 and triplet states T_1 in a 1:3 ratio according to spin statistics.^[123,124] Subsequently, the excitons undergo transitions with rate-dependent probabilities. After a certain time of continuous OLED operation, an equilibrium of singlet, triplet and charge carrier densities, determined by all present rates, is achieved. At this point, the OLED has reached the steady-state of EL operation. The first-order processes in this kinetic model include the decay rate k_S of the S_1 states, the direct intersystem crossing (ISC) rate k_{ISC} as well as the reverse ISC rate k_{RISC} for transitions between S_1 and T_1 and the non-radiative decay rate k_T of the T_1 states. For the sake of simplicity, the singlet decay rate k_S considers both, the radiative and non-radiative decay.^[20,120] Density-dependent second-order processes involve all relevant annihilation effects that are considered in literature in relation to TADF.^[111,113,125,126] In particular, these are effects involving interactions with triplet excitons, for two main reasons: Regarding the long lifetime of triplet excitons, the probability of annihilation processes is expected to be higher for triplet excitons than for singlet excitons.^[122] Furthermore,

the triplet density in electrically driven devices is significantly higher than in optical excitation due to their generation ratio. Therefore, the kinetic model considers the processes with according rates for triplet-triplet annihilation k_{TT} , triplet-polaron annihilation k_{TP} and singlet-triplet annihilation k_{ST} . These processes are further explained in the following.

Triplet-triplet annihilation (TTA) is based on the interaction of two triplet excitons. Their encounter leads to an intermediate compound or scatter state ($T_1 T_1$) which, according to spin statistics, will be transformed into a singlet, triplet or quintet state.^[127,128] Since the quintet state reforms back into two triplet states, the rate k_{TT} can effectively be transformed into $\frac{1}{4}k_{TT}$ for the singlet and $\frac{3}{4}k_{TT}$ for the triplet states (see Appendix for transformation):



Triplet-polaron annihilation (TPA) is mainly a Förster-type transfer and can be described as an annihilation process of triplet excitons with the spin state of the polaron, resulting in the transfer of the polaron in the ground state n to an excited state n^* .^[120,122,129]



Based on the long-living triplet states, singlet-triplet annihilation (STA) can also become a significant loss channel at high triplet densities.^[20] STA is a spin-allowed Förster-type energy transfer, whereby the triplet exciton will be raised to a higher triplet state T_n with relaxation of the singlet exciton into the ground state S_0 .^[120]



Considering these second-order effects in combination with the linear first-order processes mentioned above, the kinetics of the excited states in an operating OLED can be described with a set of rate equations, which will be introduced in the following. The polaron density n can be derived by the injected charge carriers per volume, which recombines with the Langevin recombination rate γ to excitons:^[20,120,121,130]

$$\frac{dn}{dt} = \frac{j}{ed} - \gamma n^2 \quad (5.4)$$

While $\frac{j}{ed}$ describes the polaron generation within the emissive layer with thickness d by injected current density j , divided by the elementary charge e , the second term γn^2 subtracts the exciton formation.^[118,129] The Langevin recombination rate is given by $\gamma = e(\mu_e + \mu_h)/(\epsilon_0 \epsilon_r)$ (see eq. 2.15) with $\mu_e = 10^{-4} \text{ cm}^2\text{V}^{-1}\text{s}^{-1}$ and $\mu_h = 10^{-5} \text{ cm}^2\text{V}^{-1}\text{s}^{-1}$ representing the mobilities of electrons and holes in the emission layer; ϵ_0 and $\epsilon_r = 2.9$ are the vacuum and emission layer permittivity, respectively.^[20,111,120,131]

A quarter of the created excitons ($\frac{1}{4}\gamma n^2$) contributes directly to the population of the singlet states. The first-order processes populating (positive sign) and depopulating (negative sign) the singlet states are intersystem crossing ($k_{\text{ISC}}S_1$), reverse intersystem crossing ($k_{\text{RISC}}T_1$) and the singlet decay ($k_S S_1$). Based on equations 5.1 and 5.3, the annihilation processes affecting the singlet states are triplet-triplet annihilation ($\frac{1}{4}k_{\text{TT}}T_1^2$) and singlet-triplet annihilation ($k_{\text{ST}}T_1 S_1$). The resulting rate equation for the kinetics of the singlet states can therefore be written as:

$$\frac{dS_1}{dt} = -k_S S_1 - k_{\text{ISC}}S_1 + k_{\text{RISC}}T_1 + \frac{1}{4}k_{\text{TT}}T_1^2 - k_{\text{ST}}T_1 S_1 + \frac{1}{4}\gamma n^2 \quad (5.5)$$

The triplet states are directly populated by the other three quarters of initial excitons ($\frac{3}{4}\gamma n^2$). The first-order processes are analogous to the singlet state with intersystem crossing ($k_{\text{ISC}}S_1$), reverse intersystem crossing ($k_{\text{RISC}}T_1$) and the triplet decay ($k_T T_1$). Annihilation processes interfering with the triplet states are triplet-triplet annihilation ($\frac{5}{4}k_{\text{TT}}T_1^2$) and triplet-polaron annihilation ($k_{\text{TP}}T_1 n$), based on equation 5.1 and 5.2. The resulting rate equation for the kinetics of the triplet states is therefore:

$$\frac{dT_1}{dt} = -k_T T_1 + k_{\text{ISC}}S_1 - k_{\text{RISC}}T_1 - \frac{5}{4}k_{\text{TT}}T_1^2 - 2k_{\text{TP}}T_1 n + \frac{3}{4}\gamma n^2 \quad (5.6)$$

The pre-factor for TTA ($\frac{1}{4}$ or $\frac{5}{4}$) is obtained from the different cases of eq. 5.1 (see derivation in eq. 10.1 in Appendix). The pre-factor for TPA (2) is based on the assumption of balanced electron and hole density in the emissive layer, which is discussed in more detail below.

5.3 Results

5.3.1 Temperature Dependent trEL

Having established a suitable kinetic model for the system under investigation, we can turn to experimental data and the respective fitting procedure. Figure 5.2 shows transient EL measurements of the reported system in semi-logarithmic representation for temperatures from 200 K to 300 K in 20 K steps. On the one hand, the transient EL traces

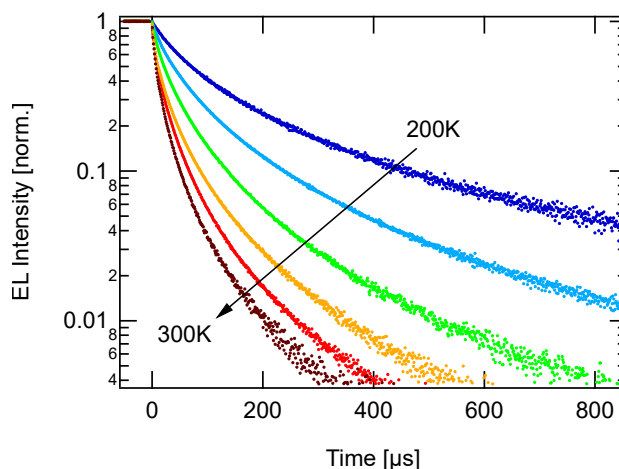


Figure 5.2: Temperature-dependent transient EL decays for an OLED with emission layer of m-MTDATA:3TPYMB. The traces show a temperature-activated behavior, but deviate from a biexponential decay. The curved shape indicates involvement of second-order processes in the kinetic model.

show a temperature-activated process since the decays become faster with increasing temperature. On the other hand, the shape of the transients deviates from the expected biexponential decay by prompt and delayed fluorescence, typically describing the kinetics of a TADF OLED. A deviation from linear traces in semi-logarithmic presentation indicates the influence of second-order processes, i.e., annihilation effects. Murawski et al. and Baldo et al. reported deviations from mono-exponential decay in transient EL measurements of phosphorescent OLEDs and both attributed this effect to TTA.^[118,122] However, to account also for the other annihilation effects mentioned, the behavior, i.e., the solution, of the rate equations 5.4 - 5.6 is examined in regard of STA, TPA and TTA to find the dominant second-order process that is responsible for the shape of the traces in Figure 5.2. But before investigating the influence of these annihilation rates on the transients, we first have to clarify how to solve the given rate equations and how to simulate or fit them to the measured trEL data.

Fit Procedure

The procedure of trEL modeling differs from the commonly known transient PL modeling. While trPL uses a short pulsed laser excitation that generates an initial population of the singlet states $S_1 = 1$, measuring trEL first runs the OLED to a steady-state before the current is switched off. Thus, the population of the OLED's steady-state has first to be simulated based on the rate equations 5.4 – 5.6 and the injected current density. This population number is important as it characterizes the initial state of the transient decay. Since this population ratio is determined by an equilibrium of all rates present during OLED operation, it is different from the generation ratio of 1:3. In order to pro-

duce the subsequent transient EL decay, the current density j in equation 5.4 is set to zero, which is equivalent to turning off the OLED.

The set of rate equations 5.4 – 5.6 for polarons, singlets and triplets are not analytically resolvable. Therefore, the numerical solution of the rate equation set is established by using an iterative procedure (forward Euler method), in which the rate equations are solved by stepwise integration by a timestep Δt , small enough to properly model the data. The fitting can then be realized by a standard Levenberg-Marquardt-Algorithm, implemented in the Scipy library (v. 1.1.0) in Python (v. 3.7.6), using the simulated rate equation model as fitting function. The script used for the iterative solution of the rate equations including calculation of loss processes and contribution to EL (shown in the discussion) can be found in the Appendix, ch. 10.

5.3.2 Dominant Annihilation Effect

Before fitting the numerical solution of the rate equation set to the transient EL decays from Figure 5.2, the dominant annihilation effect, determining the shape of the transients, should be identified to reduce the rate model to the most important rates. Therefore, the reduced rate equations 5.4 – 5.6 are analyzed with one annihilation effect, respectively. By producing the numerical solution of the reduced rate equations and varying the annihilation rate, we can investigate the influence of the respective rate on the trEL decay shape.

To visualize the influence of the different annihilation effects on the transient EL decay, Figure 5.3 shows the numerical solution of the reduced rate equations 5.4 – 5.6 with the variation of one annihilation rate, respectively. Figure 5.3a presents simulated transient EL traces with different STA rates. In Figure 5.3b, the TPA rate was varied and Figure 5.3c shows the influence of different TTA rates. For comparison with experimental data, the gray curve always displays the experimental EL transient recorded at 200 K. The simulation method described above, based on the established kinetic model, only provides reasonable fits for the case of TTA as annihilation effect. Therefore, TTA can be assumed to be the dominant second-order effect, as verified in the following.

The influence of STA depends on the product of singlet and triplet population densities. Due to the smaller density and shorter lifetime of singlet excitons, STA does not have a relevant influence. At lower values of STA, the modeled traces (Figure 5.3a) are still approximately linear in the semi-logarithmic presentation. At higher orders of magnitude, the influence can be observed mainly at the beginning of the transient. Overall, this annihilation effect cannot reproduce the shape of the measured trEL traces. Furthermore, the measured transient EL decays were shown to be current dependent, which contradicts the dominance of STA.^[23,122] The influence of the TPA rate on EL

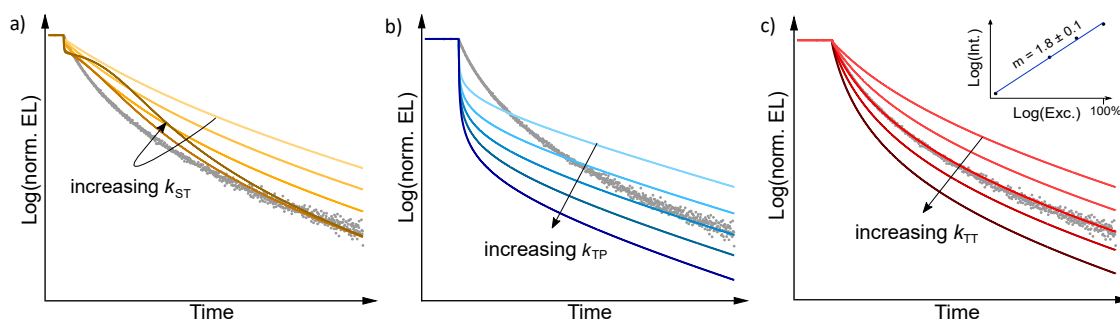


Figure 5.3: Influence of different annihilation processes on the transient decay. Colored transients show the numerical solutions of reduced rate equations 5.4 – 5.6 with varying annihilation rates of a) singlet-triplet annihilation, b) triplet-polaron annihilation, c) triplet-triplet annihilation. The gray curve always displays the experimental EL transient recorded at 200K. Only a dominant TTA mechanism can reproduce the experimental transient EL curve accurately. Inset: Excitation power-dependent PL measurements verifies TTA with a slope of $m = 1.8 \pm 0.1$.

transients (Figure 5.3b) is particularly strong shortly after switching off the OLED, i.e., during the first microseconds. The reason for this is the finite transit time of polarons in the device active layer after the voltage turn-off, determining the time scale in which TPA can occur. After this transit time, the traces follow a mono-exponential decay. In operational OLEDs, the presence of majority charge carriers is often discussed to promote TPA while minority charge carriers are used for exciton formation.^[129] However, the influence of these majority carriers would also be negligible beyond the transit time of a few microseconds and can therefore not be responsible for the shape of the transient at later times. In contrast, TTA is present during a longer time span of the decay. Certainly, the influence of TTA is higher at the beginning of the transient, since most triplet excitons are present there. Nevertheless, TTA influences the EL decay as long as triplet excitons are existent, therefore the influence of TTA is present over the whole decay. Figure 5.3c confirms that considering TTA in the rate equations 5.4 – 5.6 matches the measured transient EL trace almost perfectly.

Comparing the behaviors of the modeled traces of Figure 5.3, TTA can be identified as the mechanism, which is responsible for the characteristic shape of the transient EL traces. On the one hand, this result is consistent with the already mentioned statements of Murawski et al. and Baldo et al., who explained deviations in EL transients from linear progressions with TTA.^[118,122] On the other hand, excitation power-dependent PL measurements (inset in Figure 5.3c) give the order of the process from the slope when plotted in a double logarithmic representation. The slope of nearly two implies the requirement of two triplet excitons for the radiative decay and is a commonly used evidence for the presence of TTA.^[132] The fact that this effect can be de-

tected even under optical excitation with lower triplet density further demonstrates the impact of TTA in this system.

5.3.3 Fit Results

Having identified the dominant annihilation effect, we can fit the reduced rate equations to the trEL curves. This can be accomplished with the previously explained fit procedure in Python, using the reduced rate equations 5.4 – 5.6 with considering the dominant annihilation effect TTA. In order to avoid distorting the fit by too many free parameters, the singlet decay rate k_S is set to values according to literature.^[133] Therefore, the fit procedure determine the ISC rate k_{ISC} , the RISC rate k_{RISC} , the non-radiative decay rate k_T and the TTA rate k_{TT} , whereby k_{ISC} is assumed to be temperature-independent as commonly done for TADF emitters in this temperature range.^[104] Typically, transient PL measurements or sometimes also PL quantum yield measurements are used to provide fundamental rates such as k_S , $k_{(R)ISC}$ and k_T .^[110,115,134] However, the kinetics in PL and EL are different in intermolecular/excimer-based systems in contrast to intramolecular emitters: Figure 5.4 shows the photoluminescence (PL)/-excitation (PLE) and electroluminescence (EL) spectra of m-MTDATA:3TPYMB. Comparing PL and EL spectra reveals that the same emissive state is emitting, while PLE spectra identify the exciplex system to be non-absorbing. Excimer systems are defined by linear combination of the excited states of the donor and acceptor molecules whereby optical excitation can only generate an intramolecular exciton on the donor or acceptor molecule.^[114] The subsequent charge transfer creates an intermolecular exciton at the interface, i.e., excimer state. Considering the initial excitation via an intramolecular excitation complicates the rate equations for trPL in contrast to directly absorbing

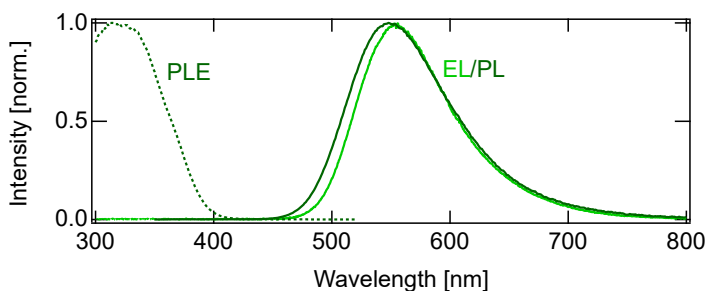


Figure 5.4: Optical spectra for excimer system m-MTDATA:3TPYMB. Photoluminescence (PL, dark green, solid) and electroluminescence (EL, light green, solid) spectra overlap, showing that the same spin state is emitting. However, the photoluminescence excitation (PLE, dark green, dotted) spectrum shows that optical excitation does not excite the excimer state directly, i.e., primary excitation occurs on donor and acceptor molecules. PL (PLE) measurement used excitation (emission) wavelength of 365 nm (540 nm).

CT states. Electrical excitation (EL), however, populates exciplex states directly, which simplifies the system to a three-level system. Therefore, transient EL measurements are particularly appropriate (compared to PL) for the determination of the RISC rate in these exciplex systems.

Numerical Fit at 200 K

Figure 5.5a shows the resulting fit (red) of the transient EL measurement at 200 K. The RISC rate was determined to be $k_{\text{RISC}} = 4.7 \cdot 10^4 \text{ s}^{-1}$ which corresponds to a RISC time of about 21 μs . The order of magnitude of this rate is consistent with reports from this or similar donor:acceptor TADF systems.^[104,133] At the same time, the RISC rates in these intermolecular exciplex systems are smaller than for state-of-the-art intramolecular TADF emitters due to the similarity in orbital types of singlet and triplet states, as further explained in ch. 2.2.2. Hence, the depopulation of triplet states by RISC proceeds slower and the long-living triplet excitons accumulate in an operating OLED, enhancing the influence of TTA.^[122] The fit determines a TTA rate of $k_{\text{TT}} = 1.4 \cdot 10^{-14} \text{ cm}^3 \text{ s}^{-1}$, whereby this rate is multiplied by the squared triplet density in the rate equations, increasing the impact of this rate. Baldo et al., Kasemann et al. and Murawski et al. reported TTA rates from transient EL measurements on phosphorescent OLEDs of the same orders of magnitude.^[20,118,122] Niwa et al. determined a TTA rate of about $10^{-18} \text{ cm}^3 \text{ s}^{-1}$ by steady-state PL measurements of intramolecular TADF emitters at liquid helium temperatures.^[126] However, since the TTA rate is highly temperature dependent (Table 4.1), the fitted TTA rates agree very well with previously discussed rates. The ISC rate was determined to be $k_{\text{ISC}} = 3.4 \cdot 10^6 \text{ s}^{-1}$ which is consistent with reports for this material system.^[4,133] The non-radiative decay rate k_{T} is with a value of $k_{\text{T}} =$

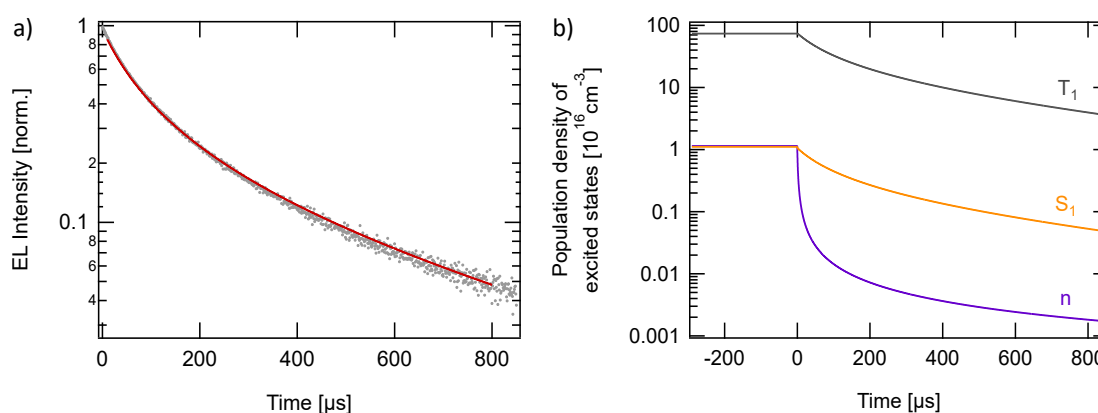


Figure 5.5: Results of the fit procedure for 200 K. a) Fit (red) of the iterative numerical solution of equations 5.4 – 5.6 with considering TTA as the dominant annihilation mechanism. b) Time-dependent population density of polarons n (purple), singlet states S_1 (orange) and triplet states T_1 (gray).

$1.0 \cdot 10^2 \text{ s}^{-1}$ about two orders of magnitude smaller than the RISC rate, implying that the long EL decay is not effectively shortened by non-radiative triplet decay. Therefore, the depopulation by non-radiative triplet decay plays a minor role, which will be discussed in more detail below.

To quantify the density and lifetime of the excited states, Figure 5.5b shows the time-dependent population density of polarons (n), first excited singlet states (S_1) and first excited triplet states (T_1) slightly before and after switching off the OLED at time $t = 0$ s for 200 K. The simulations for the population density are based on the fit results in Figure 4a and the rate equations 5.4 – 5.6. On the one hand, the simulations show the disappearance of the polarons within a few microseconds. This observation agrees well with the results shown in Figure 5.3b, suggesting that TPA only affects the beginning of the EL transients as there are negligibly few free polarons available in the device after several microseconds. On the other hand, Figure 5.5b shows that the steady-state triplet density ($t < 0 \mu\text{s}$) is with a ratio of 67 : 1 significantly higher than the singlet density, facilitating annihilation processes such as TTA.^[121] The actual triplet-to-singlet ratio when the OLED is switched off therefore does not match the electrical occupation of the states with the ratio of 3:1 according to simple spin statistics. In fluorescent OLEDs, when only considering the non-radiative decay rate, Shinar et al. showed that the triplet density can be up to 10^5 times higher than the singlet density.^[135] However, they assumed a relatively high ratio of triplet-to-singlet lifetime of $10^5 : 1$ and included no depopulation of the triplet states by annihilation processes or RISC mechanism in their estimation. Since the ratio of triplet-to-singlet lifetime in the present system is smaller and RISC and TTA processes both play a significant role in the depopulation of triplet states, the triplet-to-singlet population ratio is reduced. Nevertheless, the significant deviation of the steady-state ratio (67:1) from the occupation ratio (3:1) shows the considerable accumulation of triplet excitons in these systems.

Temperature Dependent Fit Results

Before discussing the impact of efficiency-limiting processes on the overall device performance, the excited state kinetics are evaluated for all temperatures from Figure 5.2. The fit results up to 300 K are shown in Table 4.1. The RISC rate k_{RISC} is determined for 200 K as this temperature possesses with the longest decay the smallest fit inaccuracy. The singlet-triplet gap ΔE_{ST} is then evaluated by fitting the transient EL measurement at 220 K and assuming a Boltzmann-activated process from 200 K. The fit procedure delivers a singlet-triplet energy gap of $\Delta E_{\text{ST}} = 23 \text{ meV}$, which is comparable with previous reports for this material system and underlines the small energy gap in intermolecular systems.^[112,133] Since the rates to be fitted are not entirely independent from each

other and the transient decay become faster, i.e., less data points are available, physically reasonable boundary conditions are set to ensure reliable fitting results. Besides the assumption of a temperature independent ISC rate k_{ISC} , as often used for TADF modeling in this temperature range, the RISC rate is modeled according to Boltzmann behavior based on the determined ΔE_{ST} :

$$k_{\text{RISC},T} = k_{\text{RISC},200\text{K}} \cdot \exp\left(\left(\frac{1}{T_{200\text{K}}} - \frac{1}{T_x}\right) \cdot \frac{\Delta E_{\text{ST}}}{k_{\text{B}}}\right) \quad (5.7)$$

The determined k_{RISC} rates are displayed in Table 4.1 and further discussed below. The TTA annihilation rate k_{TT} and non-radiative triplet decay rate k_{T} could then be fitted without boundary conditions.

Table 4.1: Temperature-dependent fit results (\pm fit error) for m-MTDATA:3TPYMB OLEDs. The measurements were performed at a current density of 10 mA cm^{-2} and the singlet decay rate k_{S} was taken from literature.^[133]

T [K]	k_{TT} [$10^{-14} \text{ cm}^3 \text{ s}^{-1}$]	k_{T} [10^3 s^{-1}]	k_{RISC} [10^4 s^{-1}]	k_{ISC} [10^6 s^{-1}]	k_{S} [10^5 s^{-1}]	j [mA cm^{-2}]
200	1.432 ± 0.015	0.1 [1]	4.7	3.4	1.0	10
220	3.706 ± 0.011	2.3	5.3 [2]	3.4	1.0	10
240	9.995 ± 0.027	4.846 ± 0.023	5.9	3.4	1.0	10
260	19.766 ± 0.097	8.368 ± 0.061	6.4	3.4	1.0	10
280	40.07 ± 0.24	9.30 ± 0.10	6.9	3.4	1.0	10
300	67.29 ± 0.50	11.91 ± 0.16	7.4	3.4	1.0	10

[1] Fit with boundary conditions for 200 K and 220 K ($k \geq 0$) \rightarrow no realistic fit error computable

[2] $\Delta E_{\text{ST}} = 22.7 \text{ meV}$ follows from fitting k_{RISC} at 220 K

5.4 Discussion

Having solved the set of rate equations 5.4 – 5.6 of the established kinetic model in a temperature-dependent manner for the present TADF system, the influence of the involved processes on OLED performance will be discussed in the following. On the one hand, the contribution of TTA, RISC and non-radiative triplet decay on the depopulation of triplet states will be addressed. On the other hand, the contribution of the processes populating the singlet states, i.e., TTA, RISC and exciton formation, to the EL of the OLED can be determined. This evaluation allows a complete picture of the first- and second-order processes involved in the OLED and their impact to be drawn.

5.4.1 Depopulation of Triplet States

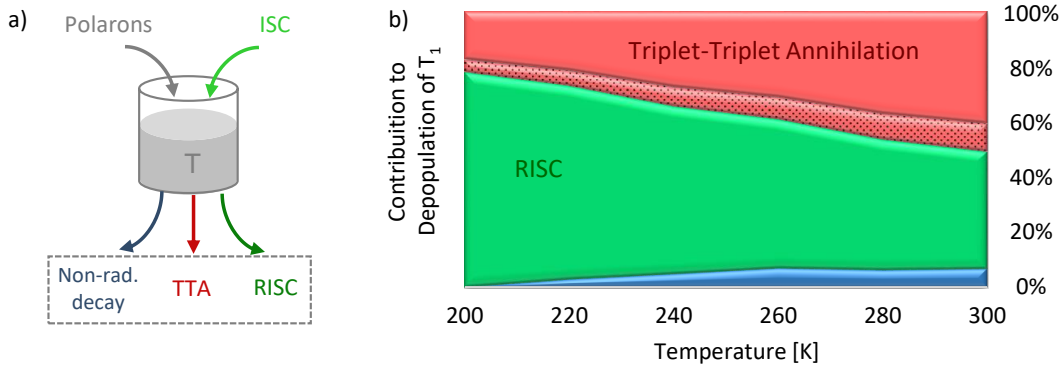


Figure 5.6: Schematic bucket model (de-)populating the triplet state and temperature-dependent impact of the three different depopulation processes. a) The triplet states are populated by free charge carriers (polarons) and ISC from the singlet state. Depopulation processes are non-radiative decay, TTA and RISC to singlet states. b) Relative contribution to depopulation of triplet state T_1 : non-radiative decay (blue), RISC (green), and TTA with creation of a singlet state (red, dotted) or a triplet state (red).

Figure 5.6 shows a scheme of the processes that contribute to the population (polarons, ISC) and depopulation (non-radiative decay, TTA, RISC) of the triplet states. To assess the influence of the processes depopulating the triplet states, the impact of the respective depopulation channels (gray framed rates in Figure 5.6a) has to be investigated. Reviewing equation 5.6, the triplet states are depopulated by TTA ($\frac{5}{4} k_{TT} T_1^2$), by RISC ($k_{RISC} T_1$) and by the non-radiative decay ($k_T T_1$). The diagram in Figure 5.6b represents the temperature-dependent contributions of these individual depopulation processes of the triplet states in operational conditions (in a relative manner, added up to 100%). The data set is derived from the fit results of the measured EL transients (Table 4.1), which are used to calculate the steady-state conditions with equations 5.4 – 5.6. In other words, this calculation considers the rates (including prefactors) times the (squared) triplet density T_1 to account for the total number of triplet excitons depopulated by these processes (detailed computation can be found in the Python code in Appendix, ch. 10). The results show that the first-order non-radiative decay process of the triplet states (blue) slightly increases with temperature but overall plays a minor role in the depopulation of the triplet states. Therefore, TTA and RISC are primarily responsible for the depopulation of the triplet states. As already discussed, the fit procedure determined a singlet-triplet energy gap of $\Delta E_{ST} = 23 \text{ meV}$ on the basis of an exponentially increasing RISC rate according to the Boltzmann factor. However, the impact of RISC on the depopulation of the triplet states T_1 decreases with increas-

ing temperature. The reason for the decline is the proportion of TTA, which is also temperature-activated.

The measurements were performed at the same current density for each temperature, thus, an excess of injected charge carriers cannot cause this effect. Actually, in contrast to the RISC rate which is increasing following a Boltzmann factor $\exp(-c_1/T)$, the TTA rate increases exponentially given the relation $\exp(c_2 \cdot T)$, with constants $c_1, c_2 > 0$ (Table 4.1). Consequently, the proportion of TTA in triplet density depopulation increases with temperature towards exceeding depopulation via RISC at room temperature. This observation is remarkable since at relatively high temperatures, the triplet lifetime is significantly reduced by the fast phonon-assisted decay, normally overcoming TTA.^[136,137] The fact that the proportion of TTA nevertheless increases indicates the enormous influence of TTA in this system. TTA has already been detected in other TADF systems.^[126,138] However, the proportion of TTA in these exciplex-based OLEDs is significantly higher. One factor is the investigation of operational OLEDs, since a higher triplet density is present in electrical than in optical excitation. But even more influential is the moderate RISC rate on the order of 10^4 s^{-1} in exciplex-based systems. This slowed depopulation by RISC allows an accumulation of triplet excitons, enhancing the probability of annihilation effects. As a result, about 50% of the triplet depopulation is caused by TTA and only 44% by the - for TADF specific - RISC mechanism at room temperature. Since one TTA event results in the loss of at least one triplet exciton, this annihilation effect provides a strong efficiency-limiting decay channel in these OLEDs.

Naturally, in contrast to the RISC process, TTA is a population density dependent process and thus scales with the injected current density. In order to assess this dependency, the same measurements and evaluation procedure was applied for two further current densities: 5 mA/cm^2 and 20 mA/cm^2 . The results reveal that the influence of TTA at room temperature is, as expected, increasing with current density. While at the lower current density of 5 mA/cm^2 , 47% of the triplet excitons are depopulated by TTA at room temperature, this value increases to 55% for a current density of 20 mA/cm^2 .

5.4.2 Contribution to EL

A quarter of the discussed TTA events produces singlet excitons (equation 5.1), which is represented by the red, dotted area in Figure 5.6b. Reviewing equation 5.5, the singlet states are populated by this quarter of TTA events ($\frac{1}{4} k_{\text{TT}} T_1^2$) as well as by triplet excitons upconverted by RISC ($k_{\text{RISC}} T_1$) and by polarons that directly recombine to singlet excitons ($\frac{1}{4} \gamma n^2$). These processes are summarized in Figure 5.7a, illustrating the mentioned population channels (TTA, RISC, polarons) together with depopulation

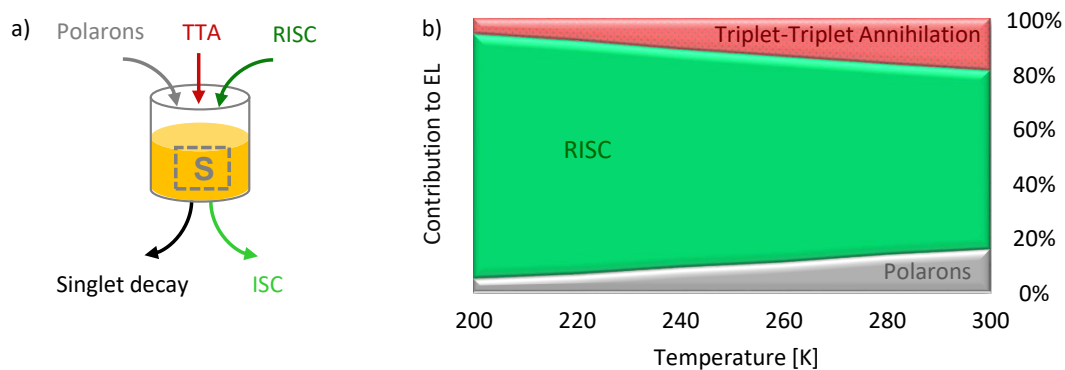


Figure 5.7: Schematic bucket model of processes (de-)populating the singlet state and temperature-dependent impact of contribution to EL. a) The singlet states are populated by free charge carriers (polarons), TTA and RISC from the triplet states. Depopulation processes are singlet decay and ISC to the triplet states. b) Relative contribution of the processes contributing to EL: singlet excitons formed via polarons (gray), RISC (green), and TTA (red, dotted).

channels (singlet decay, ISC) of the singlet states. To investigate the influence of the different population processes of the singlet state by polarons, RISC and TTA on the EL, the amount of excitons present in the singlet state (gray box) initially populated by the mentioned processes are analyzed (depopulation processes from the singlet states are included iteratively). In order to quantify the influence of these population processes on the EL, the diagram in Figure 5.7b illustrates the contributions of singlet excitons generated via polarons, RISC and TTA to the actual light emission (in a relative manner, added up to 100%, see also Python code in Appendix for detailed computation). As discussed in the previous section, the impact of TTA leads to an increasing loss of triplet excitons with increasing temperature (Figure 5.6b). Analogously, as also shown in Figure 5.6b, the proportion of triplet excitons that are depopulated by RISC decreases with temperature. Accordingly, the number of singlet excitons created by RISC in Figure 5.7b follows the same trend (the green part in Figure 5.7b also counts singlet excitons, which are formed from polarons, subsequently undergo ISC and are again upconverted by RISC). This also leads to the result that, while the total number of polarons remains the same given constant current density, the percentage in the EL of singlet excitons formed directly by polarons increases with temperature. The interesting fact is that TTA events, whereof only 25% generate singlet excitons (equation 5.1), also contribute to the EL (red, dotted part). Since this path of producing singlet excitons requires twice as many triplet excitons as RISC and only takes place in a quarter of the occurring TTA events, it represents a by far less efficient way of triplet harvesting.

5.5 Conclusion

This chapter presented a kinetic model for electrically driven TADF OLEDs that includes first- and second-order radiative and non-radiative effects and accurately reproduced transient EL measurements. A suitable fitting procedure thereby enabled the analysis of the kinetic processes and the investigation of the influence of efficiency-limiting processes in operational OLEDs. This method is especially advantageous for exciplex-based systems, since rate extraction with transient PL is considerably complicated by non-absorbing exciplex states and the associated requirement for initial optical excitation of the donor/acceptor molecules. In the exciplex-based TADF model system m-MTDATA:3TPYMB, triplet-triplet annihilation (TTA) could be revealed as the dominant second-order effect. Remarkably, TTA accounts for a significant part to triplet depopulation as a result of a moderate RISC rate and a high triplet density, especially in electrical excitation. Since one TTA event results in the loss of at least one triplet exciton, this is an important quantum efficiency-limiting loss channel for this type of OLEDs. Moreover, since the influence of TTA has been shown to increase with temperature, TTA is limiting the overall performance of OLEDs, especially at room temperature. Consequently, the EL does not only consist of prompt and delayed constituents due to RISC, it also contains a contribution of emissive excited states formed via TTA. Since TTA is a less efficient triplet harvesting mechanism in contrast to RISC, these results represent an important insight for research on exciplex-based TADF OLEDs.

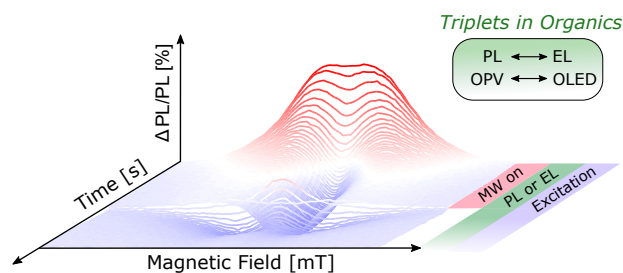
Copyright Clearance

Content of this chapter is reprinted/adapted with permission from *J. Phys. Chem. C* 2020, 124, 47, 25667–25674. ^[23] Copyright 2020 American Chemical Society.

6 Detecting Triplet States in Optoelectronic Materials and Devices by Transient ODMR

ABSTRACT

Optically detected magnetic resonance (ODMR) is a widely used technique to probe paramagnetic spin states associated with luminescence. On the one hand, ODMR can be implemented as a continuous wave (cw) method based on lock-in detection, which, however, makes it difficult to determine the correct sign of the effect, signal amplitude and in general to separate superimposed signals. On the other hand, pulsed techniques such as pulsed EPR or pulsed ODMR are used to study coherent properties of optically accessible spin centers. This chapter presents an intriguing intermediate case for the study of luminescent materials, where coherent spin manipulation is not readily applicable due to a rapid spin decoherence. The application of "long" microwave pulses over milliseconds allows the ODMR intensities to reach equilibrium conditions, while signal formation and decay can be observed with an excellent signal-to-noise ratio. The recording of time-dependent spectra enables the deconvolution of temporally superimposed contributions with correct amplitudes, signal signs and time constants. This chapter demonstrates the setup, principle and analysis of this method on optically- and electrically-generated excited triplet states and presents the advantages within two case studies of molecular donor:acceptor systems for OPV and OLED applications. The implementation of this technique thereby unravel the role of intermediate excited spin states and reveal fundamental differences in recombination pathways in optically-excited thin films and electrically driven devices.



This chapter is based on: J. Grüne, V. Dyakonov and A. Sperlich. Detecting triplet states in opto-electronic and photovoltaic materials and devices by transient optically detected magnetic resonance. *Mater. Horiz.*, 8, 9, 2569-2575 (2021).^[24]

6.1 Introduction

The most common form of electron paramagnetic resonance (EPR) spectroscopy is detecting the interaction of microwave irradiation with electron spins in a magnetic field (see ch. 3).^[139] There are several different implementations of EPR, such as continuous wave (cw) EPR^[140], pulsed EPR^[141], transient (tr) EPR^[51,59], double electron-electron resonance (DEER)^[142] equivalent to pulsed electron electron double resonance (PELDOR)^[143] and a number of others. When applied to luminescent materials or optoelectronic devices, the primary interest is on the paramagnetic species that directly affect the optical properties. Therefore, the focus is to probe only those spin states that are directly related to luminescence without measuring the background of unrelated paramagnetic radicals or charge traps.^[139] For this purpose, optically detected magnetic resonance (ODMR) is a well-known and widely used technique that combines spin-sensitive and optical spectroscopy and has been performed since 1950.^[144] Apart from the crucial advantage that ODMR only examines the paramagnetic species directly associated with luminescence or absorption, optical detection allows to study short-lived photoexcitations not detectable in cwEPR and yields a higher sensitivity than transient EPR.^[145] The spin states to be investigated with ODMR can be related to the analyzed luminescence in various ways: either they are directly influencing the luminescence or the paramagnetic spin states are indirectly correlated. The former is exemplified by phosphorescent materials^[146–150] or photoluminescence of defect centers, e.g., NV centers in diamond^[151]. The latter is represented by (reverse) intersystem crossing of non-emissive triplet states to fluorescent singlet states. This mechanism is often employed for triplet systems in organic semiconductors, such as in organic photovoltaic (OPV)^[22,152,153] or, as shown in the previous chapter, in organic light emitting diodes (OLEDs)^[112,154]. Applying resonant microwave irradiation disturbs the steady-state equilibrium of the triplet sublevels. This change in spin polarization leads to a change in luminescence, which is detectable with high sensitivity via ODMR.

Pulsed techniques, such as pulsed EPR or pulsed ODMR^[155,156], are used to determine spin relaxation times or study coherent spin effects by applying short, high-power microwave pulses.^[157] However, these techniques require a certain coherence time to build up a detectable alignment of the involved spins. Therefore, organic systems, in particular with short T_2 coherence times in the range of up to or less than hundreds of nanoseconds^[158–161], often prevent the retention of the required spin coherence beyond the dead-time of the spectrometer and are thus difficult to study.^[157]

This chapter presents a transient ODMR technique, that employs “long” microwave pulses up to milliseconds and uses, in contrast to cwODMR, direct detection of the

luminescence.^[162–165] The aim is not to build up coherent spin alignment, but to manipulate spin polarization between the triplet sublevels with simultaneous recording of the PL/EL change. Therefore, this technique can display processes that occur on longer timescales and boost signal intensities with the long pulses to achieve a good signal-to-noise ratio. By sweeping the magnetic field, time-dependent ODMR spectra are recorded, which yields reliable absolute signal intensities and sign in contrast to lock-in detection. Applying a two-dimensional (time and magnetic field) global fit enables the separation and identification of superimposed spin-dependent contributions to luminescence or possible exciton loss processes of the system. Thereby, the application of this method is not limited to optically-induced spin states only, but also electrically excited states represent an interesting application. This approach reveals a detailed insight into the excitation pathways, which differ substantially for optically excited thin films and electrically driven devices.

The following chapter demonstrates transient ODMR on materials emitting photoluminescence (transient photoluminescence detected magnetic resonance, trPLDMR) or electrically driven devices producing electroluminescence (transient electroluminescence detected magnetic resonance, trELDMR), such as OLEDs or reverse operated solar cells. The method is, in contrast to pulsed ODMR, chosen to be based on continuous optical or electrical excitation since the envisioned optoelectronic device applications are also based on continuous operation. In pulsed optical or electrical excitation mode, the densities of charge carriers or triplet excitons, as well as their interaction rates would differ decisively, limiting the usefulness of pulsed techniques. This chapter is structured as follows: First, the setup and pulse sequence used for this technique are introduced to record two-dimensional PLDMR and ELDMR spectra. Subsequently, the application on two case studies of OPV and OLED demonstrates the advantages and usefulness of this technique for research on optoelectronic materials and devices.

6.2 Method of Transient ODMR

This chapter addresses the development of trODMR in the scope of this thesis, hence, the setup and pulse sequence will be explained in the following. Figure 6.1 depicts the components that basically constitute a modified pulsed EPR spectrometer whereby luminescence transients are recorded instead of microwave echoes. Most of these elements are already known from the experimental chapter (ch. 4.3), as this setup represents a combination of trEPR, trEL (or trPL) and cwODMR. The specific components for the setup composition of trODMR are outlined in the following, whereby these elements for trELDMR and trPLDMR are identical:

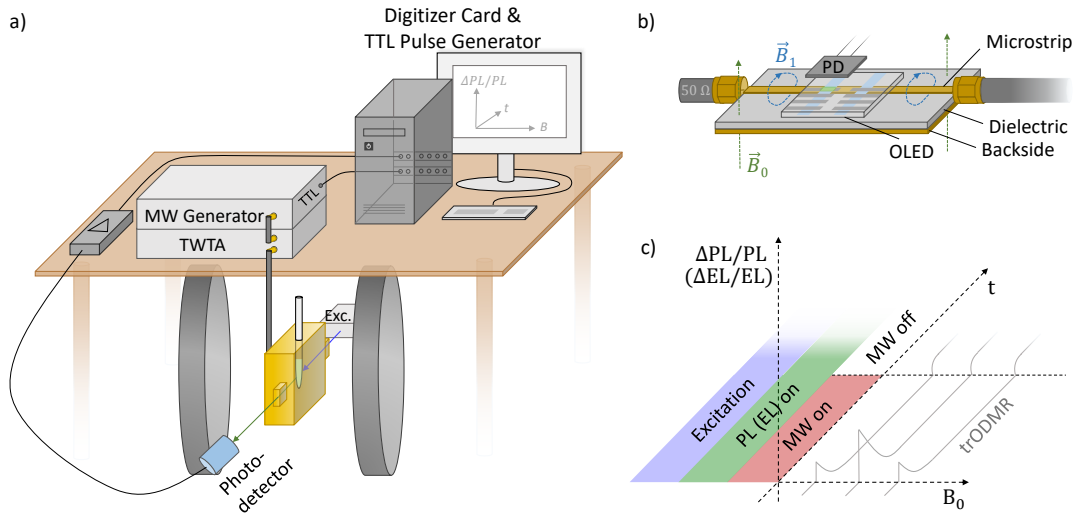


Figure 6.1: Experimental details of transient ODMR. a) Setup for trPLDMR using a microwave resonator (gold) with openings for optical excitation and detection. PL is first amplified and then recorded by a digitizer card. A TTL pulse generator triggers the MW generator whose output is amplified by a traveling wave tube amplifier (TWTA) and guided into the resonator. b) Microwave transmission line for trELDMR of electrically driven devices (here OLED) with photodetector (PD) for light detection. The oscillating B_1 MW-field crosses the device placed on top. c) Pulse and detection sequence of trODMR. Continuous optical or electrical excitation (blue) results in continuous PL or EL (green), respectively. ODMR transients of relative change in PL or EL (gray) are recorded while microwave pulses are applied (MW on, red). The external magnetic field B_0 is incrementally increased to record a two-dimensional data set.

- i. Photodetector (Hamamatsu Si photodiode S2387-66R) behind a long-pass filter that blocks excitation light.
- ii. Current/voltage amplifier with bandwidth suitable for the time resolution of the system (Femto DHP-100) amplifies the photocurrent.
- iii. 16-bit digitizer card records the photocurrent transients in DC coupling mode (GaGe Razor Express 1642 CompuScope).
- iv. TTL pulse sequence generator (SpinCore PulseBlasterESR-PRO) triggers digitizer and microwave generator.
- v. Microwave generator (Anritsu MG3694C) produces pulses of a set length, amplified up to 44 W (53 dB gain) with a subsequent solid-state or traveling wave tube amplifier (TWTA: Varian VZX 6981 K1ACDK).
- vi. Electromagnet for external magnetic field B_0 .

At this point, trPLDMR and trELDMR setups differ: trPLDMR (Figure 6.1a) uses a thin film sample in an EPR tube that are inserted into a microwave resonator (9.43 GHz, Bruker ER4104OR) with optical access and a helium cryostat insert (Oxford ESR900). A cw excitation source (laser or LED) on one side opening of the resonator illuminates the sample. A photodetector on the opposite opening collects the continuous PL emission with a suitable long pass filter to block residual excitation light.

To perform ODMR on optoelectronic devices, either very thin substrates for cavity use are required, or a microwave transmission line is utilized to generate the B_1 field. Figure 6.1b shows schematically the structure of such a microwave transmission line, with an OLED placed on top, used for trELDMR. It consists of a metallic microstrip on a dielectric substrate with a conducting backside.^[166] Similar to a coaxial cable, the electromagnetic waves propagate in the dielectric with the oscillating magnetic field component B_1 crossing the EL-emitting devices that is placed directly on top. This construction gives the device a high architectural flexibility and is also not limited to a unique microwave resonance frequency such as with typical EPR resonators. A source-measuring unit (Keithley 236) operates the device with a constant current to ensure continuous EL emission that is detected by a photodetector placed on top. Additionally, a nitrogen-flow cryostat (Oxford 935) offers temperature control and ensures an oxygen-free atmosphere.

In order to record a two-dimensional data set, Figure 6.1c shows the corresponding pulse and detection sequence for trODMR: Continuous optical (or electrical) excitation produces continuous PL (or EL). At a set magnetic field, microwave pulses are applied for a defined duration (MW on/off) resulting in a spin-dependent change of luminescence $\Delta\text{PL}/\text{PL}$ ($\Delta\text{EL}/\text{EL}$). In contrast to pulsed ODMR or EPR with the intention of coherent spin manipulation, the microwave pulse duration is longer to allow resonant effects to reach equilibrium intensities. After the microwave pulse, the system relaxes back to its previous equilibrium state of $\Delta\text{PL}/\text{PL} = 0$ ($\Delta\text{EL}/\text{EL} = 0$). Incrementally increasing the external magnetic field B_0 between ODMR transients results in two-dimensional data sets providing time-dependent ODMR spectra. Due to direct recording of the optical signal, the spectra obtain the correct signs and amplitudes. These information are valuable, i.e., when identifying exciton loss processes or comparing spin polarization.^[167] This is in stark contrast to cw techniques that usually employ lock-in detection with microwave on/off or magnetic field modulation, which results in time-averaged spectra with ambiguous signal signs and amplitudes depending on modulation frequency and lock-in phase.^[167] The possible time-resolution of the implemented technique is limited by either the optical detection, the bandwidth of the current-voltage amplifier or the quality factor of the microwave resonator, allowing

time resolutions down to tens of nanoseconds. The microwave magnetic field strength B_1 is determined by the conversion factors of the used cavity ($C_{\text{cav}} = 0.1 \text{ mT W}^{-1/2}$) and transmission line ($C_{\text{tl}} \approx 0.01 \text{ mT W}^{-1/2}$).

6.3 Optically- and Electrically-Induced Triplet States

The following demonstrates trODMR on two organic optoelectronic donor:acceptor systems, whose operating principles strongly depend on excited triplet states: First, OPV systems based on state-of-the-art non-fullerene acceptors (NFA) and, second, the newest generation of OLEDs based on thermally activated delayed fluorescence (TADF), as already introduced in the previous chapter. For both systems, ODMR spectra can be used as “fingerprint” for the triplet states participating in the luminescence generating mechanism.^[22]

6.3.1 Organic Photovoltaics

Triplet exciton formation is crucial for OPV as triplet states present exciton loss mechanisms or trap states, as already explained in ch. 2.3.2.^[168,169] Furthermore, they can result in singlet oxygen formation and are in general involved in material degradation.^[22,170,171] Triplet states are commonly difficult to detect, whereby cwODMR has already proven to be well suited to study excited triplet states in such systems, and will also be employed in the next chapters.^[22,169] However, in some cases, the application of trODMR is advantageous, which is demonstrated in the context of OPV on the state-of-the-art donor:acceptor system containing the donor polymer PM6 and the acceptor ITIC. The full molecule names and chemical structures are given in ch. 4.1.2.

trPLDMR on PM6:ITIC and pristine NFA ITIC

Figure 6.2a shows a two-dimensional (time vs. magnetic field) trPLDMR plot of a PM6:ITIC thin film at $T = 10 \text{ K}$ and excitation wavelength of 473 nm. Microwave pulses are applied from $t = 0 - 10 \text{ ms}$ at a MW frequency of $\nu_{\text{MW}} = 9.43 \text{ GHz}$. The PLDMR transient on the right ($B = 336.5 \text{ mT}$) clearly reveals the luminescence response ($\Delta\text{PL}/\text{PL}$) to magnetic resonance conditions. A spectral slice is extracted at the end of the MW pulse at $\Delta t = 9 - 10 \text{ ms}$, resulting in a so-called full field (FF) spectrum. It reveals a broad, wing-like signal of almost 100 mT width, corresponding to close-by spins with a zero-field splitting of $D/h = 1300 \text{ MHz}$.^[172] This signal is

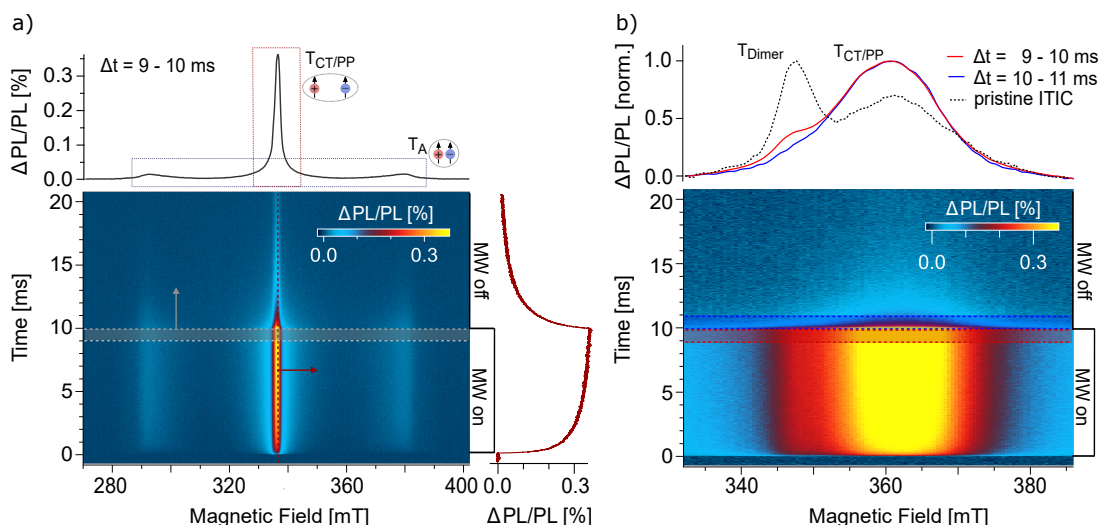


Figure 6.2: trPLDMR of the OPV donor:acceptor system PM6:ITIC at $T = 10\text{K}$. a) Two-dimensional full field (FF) plot. A horizontal slice from $\Delta t = 9 - 10\text{ms}$ (gray spectrum, top) shows a PLDMR spectrum with contributions of a broad wing-like feature due to ITIC triplets (T_A) and a central peak due to charge transfer states or polaron pairs ($T_{CT/PP}$). The PLDMR transient (red trace, right) for $B = 336.5\text{mT}$ is recorded when the resonant MW pulse is switched on and off. b) Central $T_{CT/PP}$ peak with higher spectral resolution. An additional shoulder at $B = 334.8\text{mT}$ (red spectrum, top, $\Delta t = 9 - 10\text{ms}$) is revealed that is separable from the CT/PP peak, since this signal vanishes quickly after the MW pulse (blue spectrum, top, $\Delta t = 10 - 11\text{ms}$). This contribution (T_{Dimer}) is also observed for pristine ITIC (black, dashed spectrum, top, $\Delta t = 9 - 10\text{ms}$ from Figure 6.3).

assigned to triplet excitons located on ITIC acceptor molecules (T_A) as discussed in the following: First, the same zero-field splitting value is extracted for trPLDMR measurements of pristine ITIC (Figure 6.3a), i.e., the same width of the broad triplet feature in the FF signal. Second, the half field (HF) signal (see ch. 3.3.1) of PM6:ITIC and pristine ITIC are identical in shape and position, as visible in Figure 6.3b. Since the intensity of the HF signal is strongly dependent on the inter-spin distance r of the two charges bound in the triplet state ($I_{HF} \sim r^{-6}$, see eq. 3.24), it is evident that the HF signal originates from the broad feature in the FF spectrum. The HF and the broad FF signal in PM6:ITIC can thus be assigned to triplet excitons on ITIC molecules.

Signal Sign with trPLDMR

The narrow (\approx few mT) central peak in the blend originates from charge transfer (${}^3\text{CT}$) states, also considered as spin-correlated radical pairs, and non-geminate recombination of distant polaron pairs (PP).^[22,47] The PLDMR transient on the right at $B = 336.5\text{mT}$ shows the temporal response of the narrow peak during the MW pulse and, most importantly, the sign of the PLDMR signal. The positive sign ($\Delta\text{PL}/\text{PL} > 0$) reveals higher population of the light-emitting channel in resonant conditions. The

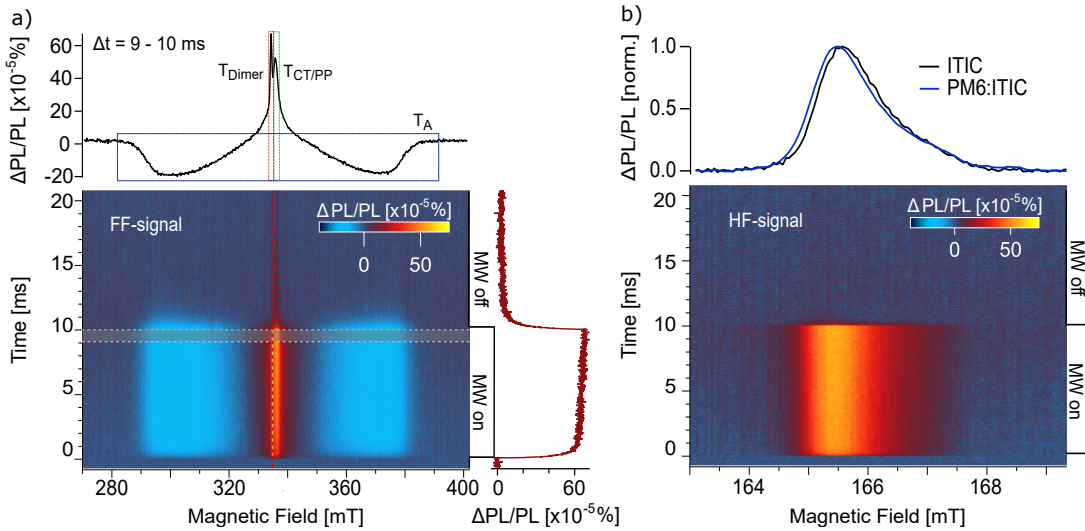


Figure 6.3: trPLDMR of the NFA ITIC at $T = 10\text{K}$. a) Two-dimensional full field (FF) signal. A horizontal slice from $\Delta t = 9 - 10\text{ms}$ (black spectrum, top) shows a PLDMR spectrum with contributions of a broad molecular triplet feature T_A (blue box), polaron pair peak T_{PP} (green box) and an additional peak due to dimer triplet excitons T_{Dimer} (red box). The PLDMR transient (red trace, right) for $B = 334.8\text{mT}$ shows the associated positive PL response in resonant condition of the dimer contribution. b) Two-dimensional half field (HF) signal. A horizontal slice from $\Delta t = 9 - 10\text{ms}$ (black spectrum, top) shows the HF spectrum of pristine ITIC (black) in normalized manner together with the HF signal of PM6:ITIC (blue). Both signals have the same spectral position (g-factor), shape and comparable intensities.

most common mechanism, producing a positive PLDMR signal in OPV blends, is triplet polaron annihilation (TPA) and represents a central bimolecular process in state-of-the-art OSC.^[49,135,173] Thereby, the triplet ($S = 1$) – polaron ($S = \frac{1}{2}$) pair can either result in a quartet manifold ($S = \frac{3}{2}$) or a doublet manifold ($S = \frac{1}{2}$).^[174] Since TPA results in a final state consisting of a singlet ($S = 0$) and a polaron ($S = \frac{1}{2}$), the initial state must also exist in the doublet manifold due to spin conservation.^[135] Magnetic resonance condition leads to a mixing of the doublet and quartet manifold (i.e., transition of the spin-allowed doublet state into the spin-forbidden quartet state), causing a net change in the recombination (i.e., reduced TPA). Thus, after 10ms of MW irradiation, a new equilibrium PL intensity is reached with enhanced emission. After switching off the MW irradiation, the PL intensity relaxes back into its previous steady-state. Given the long time constants to build up the ODMR signal, high modulation frequencies ($\nu_{\text{mod}} > 100\text{Hz}$) in cwODMR would accordingly misrepresent the measurement result, as the full signal amplitude cannot be reached within the modulation time.

Signal Separation with trPLDMR

Time-dependent ODMR spectra are also useful for separating superimposed signals. Figure 6.2b shows the narrow $^3\text{CT/PP}$ peak with higher spectral resolution. Additional to the main central peak ($T_{\text{CT/PP}}$), there is a discernible shoulder at around $B = 334.8\text{mT}$ (red normalized spectrum, averaged over $\Delta t = 9 - 10\text{ms}$). This signal is separable from the $^3\text{CT/PP}$ peak itself, since it vanishes quickly after microwave switch off (blue normalized spectrum, averaged over $\Delta t = 10 - 11\text{ms}$). This analysis is corroborated by detecting the same spectral contributions in pristine ITIC in Figure 6.3a: besides the contributions of a broad molecular triplet feature T_{A} , and a polaron pair peak T_{PP} , there is an additional contribution at 334.8mT . In previous research, the shoulder could be tentatively assigned to an additional triplet exciton delocalized over ITIC dimers (T_{Dimer}).^[175] The PLDMR transient (red trace, right) for $B = 334.8\text{mT}$ shows the associated positive PL response in resonant condition of the dimer contribution. Returning to Figure 6.2b (normalized spectrum of pristine ITIC as dashed line), the dimer formation is not as pronounced in the blend PM6:ITIC, since additional donor:acceptor ^3CT states contribute to the $^3\text{CT/PP}$ peak at 336.5mT . Furthermore, blend mixing decreases the impact of ITIC dimers on the overall signal in a bulk heterojunction. Nevertheless, this additional contribution is conclusively detectable and separable by means of trODMR.

6.3.2 Organic Light Emitting Diodes

In the trODMR spectra of the above-discussed OPV systems, the $^3\text{CT/PP}$ peak is quite narrow ($D \rightarrow 0$) and easily distinguishable from the broad ($D/h = 1300\text{MHz}$) molecular triplet feature. In other systems, the involved triplet species do not exhibit such a significant difference in zero-field splitting D , making their separation more challenging due to significant overlap. trODMR enables to separate spectral and temporal behavior of these different spin species, as demonstrated in the following on a TADF OLED system. In addition to trPLDMR of optically excited films, trELDMR on electrically driven devices is used to reveal crucial differences in the spin states involved and thus the importance of spin-sensitive spectroscopy for both PL and EL simultaneously.

Global Fitting of Time-Dependent trODMR Spectra

Evaluation of trPLDMR

As already addressed in the previous chapter, the newest generation of OLEDs is based on harvesting non-emissive triplet excitons using thermal energy to overcome the small energy gap ΔE_{ST} to the emissive singlet states.^[4,104] Subsequently, the thermally acti-

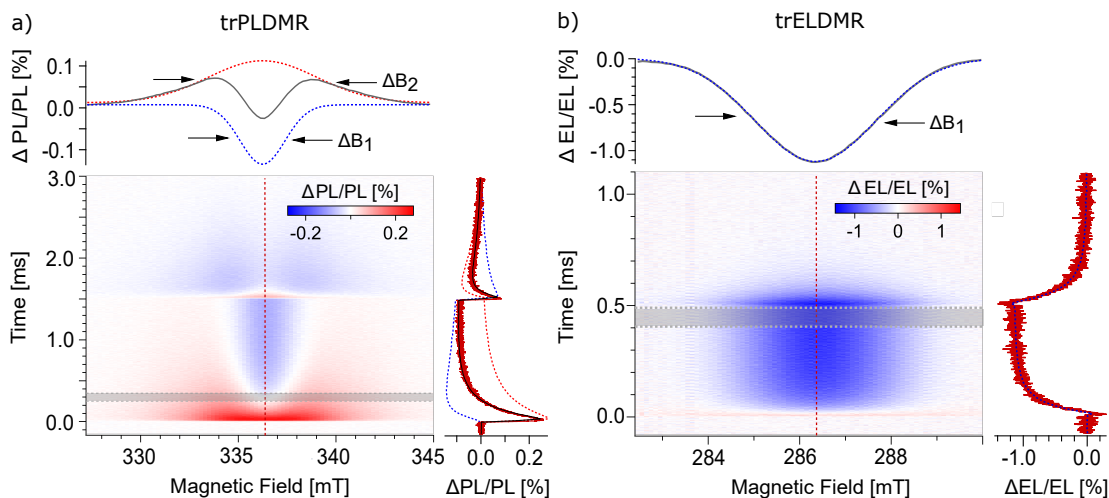


Figure 6.4: Transient ODMR of the OLED donor:acceptor system m-MTDATA:3TPYMB. a) Two-dimensional trPLDMR plot of an optically excited thin film sample at $T = 50$ K. A PLDMR spectrum averaged from $\Delta t = 0.25 - 0.35$ ms (gray trace, top) and a PLDMR transient at $B = 336.5$ mT (red trace, right) reveal two superimposed signals. By applying a global fit of two Gaussian linewidths, a narrow (ΔB_1 , blue dotted) and broad (ΔB_2 , red dotted) spectrum with their temporal contributions (dotted lines, right) can be distinguished. b) Two-dimensional trELDMR plot of an electrically driven OLED device at $T = 200$ K. An ELDMR spectrum averaged from $\Delta t = 0.4 - 0.5$ ms (gray trace, top) and an ELDMR transient at $B = 286.3$ mT (red trace, right) reveal just one Gaussian signal (ΔB_1), supported by the results of the global fit (blue dotted lines, top/right).

vated triplet excitons contribute with delayed fluorescence to luminescence, enhancing the quantum efficiency significantly. For the demonstration of trODMR, the TADF donor:acceptor combination, employing m-MTDATA as donor and 3TPYMB as acceptor, is chosen (full molecule names and chemical structures are given in ch. 4.1). The previous chapter already showed the involvement of triplet excitons in luminescence for this TADF combination, making this material system highly suitable for the present investigation. In addition, there is a variety of measurement techniques on this system in literature, including magnetic field-dependent studies of triplet states, whereby trODMR now extends this experimental toolkit.^[111,176,177] Figure 6.4a shows the two-dimensional trPLDMR plot of the donor:acceptor blended thin film with 365 nm optical LED excitation at $T = 50$ K. Microwave pulses are applied from $\Delta t = 0 - 1.5$ ms, which is sufficient to reach equilibrium intensities. An in-resonance transient is shown on the right (red, $B = 336.5$ mT). It reveals a fast rising (≈ 0.1 mT), positive ($\Delta\text{PL}/\text{PL} > 0$) peak, followed by an exponential decay to reach equilibrium with negative intensity ($\Delta\text{PL}/\text{PL} < 0$). This behavior already indicates superimposed signals with opposite sign of different spin states involved in PL. The spectrum on the top (gray) shows a slice of the 2D data set, averaged between $\Delta t = 0.25 - 0.35$ ms. This spectrum emphasizes the

observation of two superimposed signals by revealing a broad positive and a narrow negative signal with the same center magnetic field.

The width of the spectrum contains information about the delocalization of the spin species ($D \sim r^{-3}$, see ch. 3.2.2).^[22,172] Consequently, the broad signal represents a more localized while the narrow signal represents a more delocalized triplet state, further discussed below. The 2D data set shows the temporal development of these two signals: the broad signal is predominantly present at the beginning of the microwave pulse while the narrow, negative signal dominates at later times. After switching off the microwave irradiation at 1.5 ms, both signals relax with different time constants and opposite sign back to their previous stationary state.

Hereby, trODMR shows its strength by giving access to a range of spectra for different points in time. An appropriate two-dimensional analysis is used to deconvolute the superimposed spectra and determine the individual transient intensities, i.e., signal contributions. Therefore, the following assumptions are made: The signal origins, e.g., the triplet states ($\hat{=}$ linewidths) remain identical over time, only the contributions ($\hat{=}$ amplitudes) change. These assumptions allow to apply a global fit with two Gaussian line shapes (which represent the envelopes of inhomogeneously broadened spectra) to these time-dependent PLDMR spectra. The top graph of Figure 6.4a shows the superimposed spectra, consisting of a narrow spectrum with a linewidth (FWHM) of $\Delta B_1 = 2.7$ mT (blue dotted line) and a broader contribution with $\Delta B_2 = 6.6$ mT (red dotted line). The deconvoluted temporal amplitudes of these two triplet states are shown on the right: The narrow signal rises slowly to a negative value of about 0.1% (blue dotted line), while the broad signal presents a steep rising peak followed by a slow decay (red dotted line). The sum of these amplitudes (black line) fits the in-resonant transient. Thus, the PL on TADF-based thin films exhibits two triplet contributions: one localized triplet state whose luminescence is enhanced under resonant conditions at 50 K, and a more delocalized triplet state with reduced PL emission.

Evaluation of trELDMR

PL-based measurement methods are well suited to obtain valuable information about the material systems themselves. However, OLED materials are intended to be used in electrically driven devices where electric fields and injected charge carriers may result in very different conditions than optical excitation. Therefore, the following demonstrates trELDMR on operational OLED devices (layer structure given in ch. 4.2.1).

Figure 6.4b presents the two-dimensional trELDMR result at $T = 200$ K. The MW pulse is applied from $t = 0$ – 0.5 ms to reach equilibrium signal intensities. The use of a microwave transmission line makes the choice of the resonant frequency variable.

Therefore, this measurement uses $\nu_{\text{MW}} = 8\text{GHz}$ due to good signal intensities, leading to a spectral shift in the resonance magnetic field in contrast to trPLDMR. The extracted in-resonance transient on the right (red) reveals just one negative signal with exponentially decaying intensity upon microwave pulse start/end. The spectrum on the top (gray) is averaged between $\Delta t = 0.4 - 0.5\text{ms}$ and displays also only one Gaussian line shape with negative sign. In order to directly compare the result with the trPLDMR measurements from Figure 6.4a, the responsible triplet state is investigated by the already described two-dimensional analysis with one single Gaussian fit function. The resulting linewidth of $\Delta B_1 = 3.0\text{mT}$ (top, blue dotted line) is almost identical to the narrow linewidth from the trPLDMR analysis. Furthermore, the temporal amplitude of this signal (right, blue dotted) matches with the measured in-resonance transient which proves that just one triplet state is probed. This delocalized triplet state (narrow signal) is thus involved in both, electrically driven OLED systems and optically excited thin films, while possessing the same sign, i.e., luminescence quenching in resonant conditions. trPLDMR, however, exhibits a second more localized (broad signal) triplet state, as further discussed below.

Temperature Dependence of Optically Induced Triplet States

To access whether the different spin states in thin films and OLED devices is not attributable to temperature difference (since proper OLED operation is not possible below 200K based on the temperature-activated injection and hopping process, see ch. 2.3.1), Figure 6.5 shows the temperature-dependent trPLDMR measurements on m-MTDATA:3TPYMB thin films in direct comparison for up to 200K in 50K steps. The global fit analysis described above was again used to precisely deconvolute the involved triplet states for all temperatures: Both contributions, the narrow triplet signal (ΔB_1 , blue), i.e., delocalized triplet state, and broad triplet signal (ΔB_2 , red), i.e., more localized triplet state, are present for all temperatures up to 200K. Thereby, the PLDMR sign for the narrow triplet signal is always negative, i.e., PL quenching under resonance conditions. In contrast, the broad triplet signal exhibits a positive sign at low temperatures, while it becomes negative at higher temperatures, indicating a difference in temperature activation, as discussed further below. More importantly, the measurement at 200K proves that the localized triplet state (broad signal) is still significantly involved in PL even at this temperature, while it is absent in OLED devices.

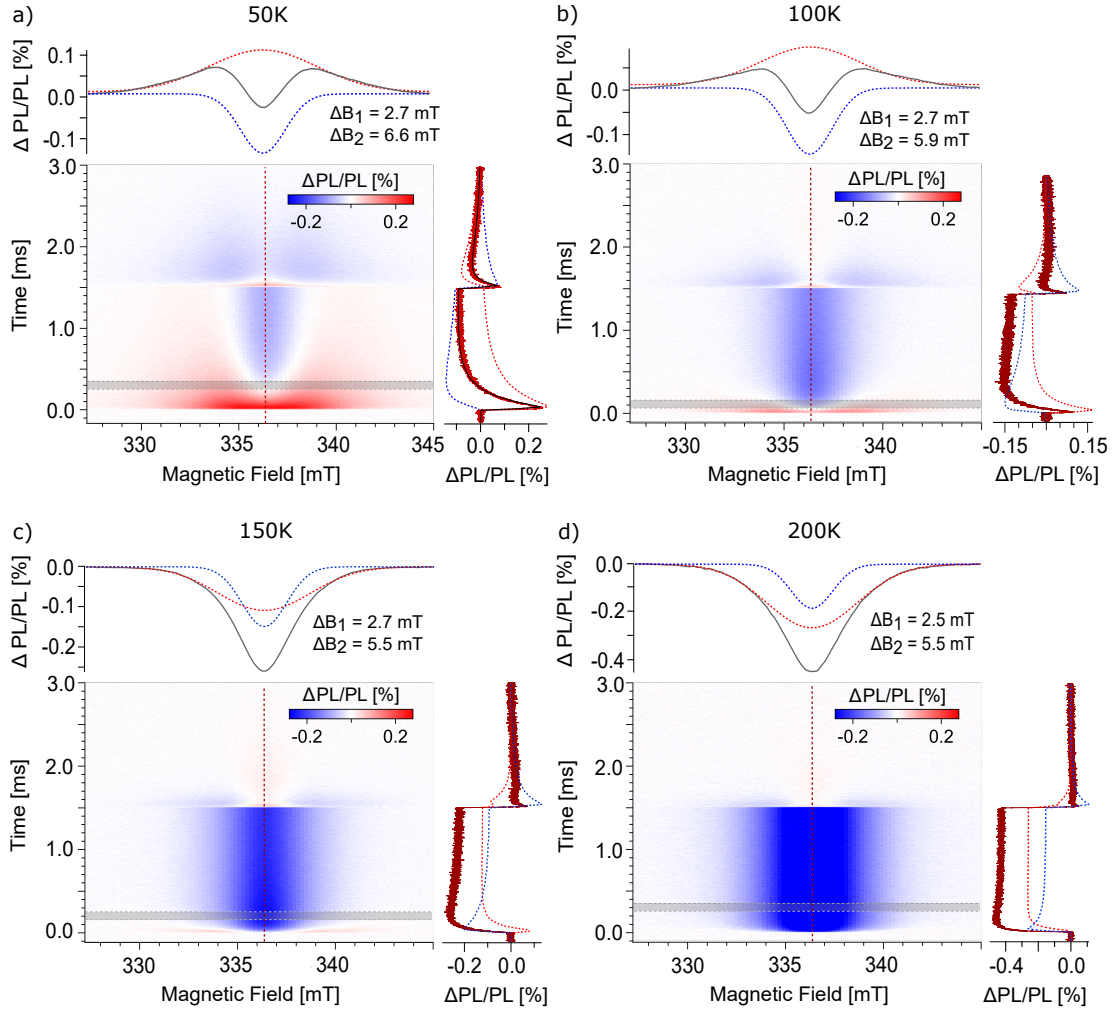


Figure 6.5: Transient PLDMR of m-MTDATA:3TPYMB blended thin film for 50 K, 100 K, 150 K and 200 K. PLDMR spectra extracted from 2D plot (gray traces, top), averaged at different time intervals, and PLDMR transients at $B = 336.5$ mT (red traces, right) exhibit two superimposed signals at all temperatures. Global fit analysis reveal contribution of the narrow signal (ΔB_1 , blue) and broad signal (ΔB_2 , red). The PLDMR signal of the narrow signal remains negative in resonant conditions for all temperatures, while the sign of the broad signal changes upon temperature increase. Measurements performed with $\lambda_{\text{ex}} = 365$ nm excitation.

6.3.3 Spin-Spin Interactions

ODMR spectra are a useful tool for monitoring spin-spin interactions and thus provide information about the spin states involved along with their localization. As described in ch. 3.2.2 and ch. 2.1.3, the width of the PLDMR spectrum correlates with the ZFS parameter D (width $\sim \frac{|2D|}{g\mu_B}$), which in turn is an indicator of the delocalization of the spin distribution ($D \sim r^3$, eq. 3.18). The nearly 100 mT wide PLDMR spectrum of PM6:ITIC corresponds to a ZFS value of $D/h = 1300$ MHz (Figure 6.2), indicating spin-spin inter-

actions of molecular excitons.^[22] By comparison with pristine ITIC (Figure 6.3), these molecular excitons can be assigned to the population of triplet states on the acceptor molecule. As discussed in more detail in the next chapter, OPV blends based on NFA acceptors usually possess a NFA triplet state below the CT states owing to the energetically low-lying NFA singlet states.^[49,178,179] Thus, these triplet states can be occupied by back charge transfer (BCT) from CT states or intersystem crossing (ISC) from singlet states (see ch. 2.3.2) and are visible in PLDMR.^[26] In contrast, CT triplet states exhibit a more delocalized spin distribution, leading to a narrow spectrum, as also visible in PM6:ITIC blends as a middle peak ($\Delta B = 2.5$ mT).

In comparison to the OPV blends in this or in the following chapters, trPLDMR and trELDMMR on the TADF system (Figure 6.4) only exhibit signals with smaller linewidth ($\Delta B = 2.7 - 6.6$ mT). As the used donor and acceptor molecules of m-MTDATA and 3TPYMB are even smaller than NFAs (Figure 4.1 and Figure 4.3), the D value of molecular excitons would most probably be higher, suggesting the signals' origin to interaction of CT states. As explained in the previous chapter, electrical excitation in m-MTDATA:3TPYMB results in the direct formation of exciplex states, whereby triplet states are occupied in a singlet:triplet ratio of 1:3. Exciplex states are non-absorbing CT states, wherefore they will be also referred to as CT states in the following to provide comparable notation.^[114] Electrical injection can be described by the recombination of non-geminate charge carriers, recombining to excitons within the Onsager radius (eq. 2.14). Thus, this excitation form results in more delocalized 3 CT states (narrow linewidth $\Delta B = 2.7 - 3.0$ mT), e.g., distributed over multiple small molecules. trPLDMR spectra exhibit a second signal contribution with larger spectral width, caused by the stronger spin-spin interaction of more localized states, however, still small compared to molecular states. Optical excitation initially leads to the formation of geminate e-h pairs and most likely involves additional, more localized 3 CT states, e.g., distributed over the nearest neighbor small molecules (broader linewidth $\Delta B = 6.6$ mT).^[62] The simultaneous presence of the narrow signal in the PL suggests the separation of geminate pairs into free charge carriers and subsequent non-geminate recombination, as also known from OPV blends discussed in the next chapters.

Additionally, delocalized spins (i.e., narrow signal in trELDMMR and trPLDMR in m-MTDATA:3TPYMB) exhibit a smaller exchange interaction (see eq. 3.22), making RISC possible at 200K as also verified in the trEL measurements from the previous chapter. A negative ODMR signal has been assigned to the RISC process in TADF-based OLED systems in literature, suggesting similar emergence of the negative signal in the present TADF system.^[178] Spatially closer spins (i.e., broader signal of trPLDMR in m-MTDATA:3TPYMB) exhibit a larger exchange interaction, suggesting efficient triplet

harvesting only at higher temperatures and producing the change in the PLDMR sign upon temperature increasing.

Overall, experiments based on optical excitation must be treated with special caution: The emitting final state may be identical (see EL and PL spectra in Figure 5.4 from previous chapter), but there may be different intermediate excited states and recombination pathways that are absent for electrical excitation. However, due to the variety of time-dependent ODMR spectra, the presented method offers the possibility to precisely deconvolute the different spin states in PL from those accessible in current-driven devices. Aside from advantages of separating signals by the additional time component, trODMR is able to unambiguously determine the actual sign and amplitude of the luminescence response under magnetic resonance conditions, allowing additional conclusions of the involved mechanisms.

6.4 Conclusion

This chapter presented a new method of transient optically detected magnetic resonance (trODMR). It is a spectral and time-resolved technique that directly probes the spin-carrying excited states participating in photo- or electroluminescence. This technique allows the deconvolution and identification of superimposed spectral components occurring on different time scales with the enhanced sensitivity of optical detection. The method can be applied to all materials with spin-dependent luminescence, including systems with fast spin-spin relaxation times and especially operating optoelectronic devices. In two case studies, this technique proved its advantageous application to molecular donor:acceptor systems widely used in organic photovoltaics based on non-fullerene acceptors (NFA) and OLEDs based on thermally activated delayed fluorescence (TADF). A global fit analysis of the time-dependent ODMR spectra provides the exact spectral contributions with absolute sign and amplitude and thus reveals the individual spin-dependent radiative recombination paths. In particular, different intermediate triplet states were found to be involved in optically excited films and electrically driven devices, which decisive difference is often undetectable with spin-insensitive methods.

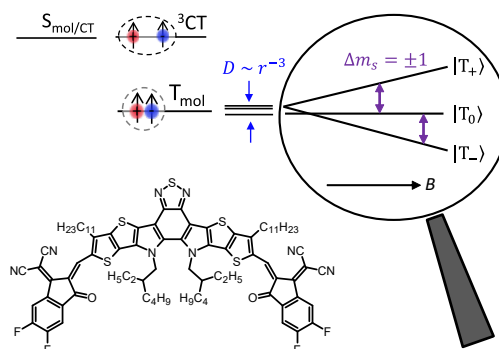
Copyright Clearance

Content of this chapter is reproduced from *Mater. Horiz.*, 2021, **8**, 9, 2569-2575^[24] with permission from the Royal Society of Chemistry.

7 Triplet States and their Generation Pathways in (Non-) Halogenated PBDB-T:Y-Series

ABSTRACT

The great progress in organic photovoltaics (OPV) over the past few years has been largely achieved by the development of non-fullerene acceptors (NFAs), with power conversion efficiencies now approaching 20%. To achieve this result and further improve device performance, loss mechanisms must be identified and minimized. Triplet states are known to adversely affect device performance, since they can form energetically trapped excitons on low-lying states that are responsible for non-radiative losses or even device degradation. Halogenation of OPV materials has long been employed to tailor energy levels and to enhance open circuit voltage. However, the influence on recombination to triplet excitons is still largely unexplored. Using the complementary spin-sensitive methods of photoluminescence detected magnetic resonance (PLDMR) and transient electron paramagnetic resonance (trEPR) corroborated by transient absorption (TA) and quantum-chemical calculations, this chapter unravels exciton pathways in OPV blends employing the polymer donors PBDB-T, PM6 and PM7 together with NFAs Y6 and Y7. All blends reveal triplet excitons on the NFA populated via non-geminate hole back transfer and, in blends with halogenated donors, also by spin-orbit coupling induced intersystem crossing. Identifying these triplet formation pathways in all tested solar cell absorber films highlights the untapped potential for improved charge generation to further increase plateauing OPV efficiencies.



This chapter is based on: J. Grüne, G. Londi, A. J. Gillett, B. Stähly, S. Lulei, M. Kotova, Y. Olivier, V. Dyakonov and A. Sperlich. Energetically Trapped Triplet Excitons and their Generation Pathways in (Non-) Halogenated PBDB-T:Y-Series. *under review*. Preprint [arXiv:2204.14088](https://arxiv.org/abs/2204.14088).^[25]

7.1 Introduction

Organic solar cells (OSC) based on non-fullerene acceptors (NFAs) have attracted much attention due to their strong absorption in the visible and near infrared (NIR) spectral regions and their energy-level tunability, in contrast to fullerene acceptors.^[17] However, despite the great success of OSC development to power conversion efficiencies (PCE) up to 19%^[18], there is still untapped potential for further improvement. One limiting factor is the total voltage loss ($\Delta V_{\text{loss}} = e^{-1}E_{\text{g}} - V_{\text{OC}}$), defined as the difference between the optical band gap (E_{g}) times the elementary charge e and the open-circuit voltage (V_{OC}).^[49,180–182] Thereby, ΔV_{loss} is composed of losses due to radiative (ΔV_{r}) and non-radiative (ΔV_{nr}) recombination.^[179,180] According to the Shockley-Queisser limit, an ideal solar cell possesses only radiative recombination, making this contribution unavoidable.^[183,184] Non-radiative recombination processes have the highest impact on reduction of V_{OC} and the short-circuit current J_{SC} and are therefore of great interest for OSC research.^[49,181] Furthermore, after optical excitation of donor (D) or acceptor (A) singlet states, charge transfer (CT) at the interface is expected to reduce the photovoltage due to the difference in the donor or acceptor band gaps and the energy of CT states ($E_{\text{g}} - E_{\text{CT}}$).^[182,185,186] However, in state-of-the-art D:A combinations, such as PM6:Y6, this difference is almost negligible, making the non-radiative processes the most dominant in terms of efficiency losses.^[179] Due to the close energetic alignment between singlet states of NFA and the CT states, especially in the PBDB-T:Y-series, NFA triplet states are energetically located below the CT states and represent a significant non-radiative decay channel for excitons.^[187] This chapter shows that preventing the population of these triplet states is extremely difficult, even in state-of-the-art blends. Direct intersystem crossing (ISC) from optically-excited donor or acceptor singlet states to molecular triplet states is one of the possible triplet formation mechanisms.^[188] The yield of this geminate pathway depends on the number of optically-generated singlet excitons not reaching the D:A interface to undergo charge transfer within their exciton diffusion length.^[189] Another loss pathways are triplet CT states (^3CT) that relax spin-allowed to energetically lower molecular triplet states, also called back charge transfer (BCT), as already explained in ch. 2.3.2.^[179,190] BCT can be further subdivided into back transfer of electrons to the donor (electron back transfer, EBT) and back transfer of holes to the acceptor (hole back transfer, HBT), respectively, with the pathway emerging depending on the energies of the triplet states. Thereby, HBT to NFA triplet T_{NFA} from ^3CT formed via non-geminate recombination was shown to have a considerable impact on V_{OC} reduction in NFA-based OSC.^[49] All mentioned triplet formation mechanisms can lead to excitons, localized on the lowest-lying molecu-

lar triplet states, i.e., energetically trapped. These excitations therefore increase non-radiative recombination, resulting in a reduction of PCE.

The present chapter sets the focus on the impact of donor and acceptor halogenation on the formation of triplet excitons and associated excited state kinetics. Halogenation of, e.g., donor polymers can improve device efficiencies, as shown for fluorination and chlorination of PBDB-T to yield PM6 and PM7, respectively.^[191–193] Thereby, halogenation is beneficial in terms of fill factor and V_{OC} and thus the PCE, whose reasons lie among others in downshifted highest occupied molecular orbital (HOMO) energy levels (see Figure 4.4 in experimental chapter), resulting in higher V_{OC} .^[194,195] However, the question arises if the reduced HOMO offset impacts the driving force of the, in NFA blends, important hole transfer (HT). Another advantage is observed for morphology, since halogenation increases aggregation, leading to a rise in charge carrier dissociation and therefore in fill factor.^[196] However, ISC rates of organic semiconductors can also be enhanced by halogenation as has been shown for organic light-emitting diodes (OLEDs) employing thermally activated delayed fluorescence (TADF), where bromination and iodination increase reverse ISC rates due to the heavy atom effect.^[195] In this context, it remains to be clarified whether fluorination and chlorination of OPV materials also have an impact on ISC and HT kinetics or overall on triplet exciton formation.

Since formation of long-lived triplet states results in a loss of OSC performance and can exacerbate device degradation, studying the presence of triplet excitons and their generation mechanisms is essential. For their investigation, this chapter describes two complementary methods, which are highly sensitive to triplet excitons: photoluminescence detected magnetic resonance (PLDMR) and transient electron paramagnetic resonance (trEPR). Both methods were already applied independently of each other in the past to investigate triplet formation in OSCs.^[22,24,49,169,175] The combination of both techniques is especially powerful, as exploited in this and in the following chapter: trEPR probes triplet excitons directly by the detection of microwave absorption between triplet sublevels and reveals geminate triplet exciton formation pathways, such as ISC or geminate HBT.^[26] In contrast to that, PLDMR probes triplet states indirectly with the higher sensitivity of optical detection and thus revealing especially those spin states that are associated with luminescence, e.g., via triplet-triplet annihilation (TTA), ground state depletion or (reverse) ISC.^[139,153] PLDMR is therefore well-suited to detect long-lived triplets including non-geminate excitons and identify their molecular localization.^[22,24] Transient absorption (TA) spectroscopy and quantum-chemical calculations are further used to study excited state kinetics, including HT and ISC rates. With the combination of these powerful techniques, the following state-of-the-art donor and acceptor materials in different combinations are investigated: the

polymer PBDB-T and its fluorinated and chlorinated variants, PM6 and PM7, as well as the halogenated NFAs Y6 and Y7. The full molecule names and chemical structures are given in ch. 4.1.2, Figure 4.2 (donors) and Figure 4.3 (NFAs). This chapter will introduce the methods of cwPLDMR, trEPR and TA with their respective experimental results on PBDB-T:Y-series, followed by a short theoretical analysis of acceptor halogenation. Finally, the influence of halogenation will be discussed by combining the results of the respective methods. Given the large number of D:A combinations, experimental results in this chapter are presented only for acceptor Y6 in combination with PBDB-T, PM6, and PM7, with complementary results on Y7 given in the Appendix.

7.2 Probing Triplet Excitons with Magnetic Resonance

This chapter examines thoroughly the spin physics of triplet states using the complementary spin-sensitive methods of PLDMR and trEPR. The corresponding spin Hamiltonian of triplet states was already introduced in detail in ch. 3.2. The following summarizes the most important terms of the spin Hamiltonian together with the investigated spin states in regard to this chapter.

The Hamilton operator in the here used X-band regime (microwave frequency $\nu_{\text{MW}} \approx 9.4$ GHz and external magnetic field $B_0 \approx 340$ mT) can be reduced to mainly three contributions: Electron Zeeman (EZ) interaction \hat{H}_{EZ} , zero-field splitting (ZFS) \hat{H}_{ZFS} and exchange interaction \hat{H}_{EX} (other contributions, including hyperfine fields can be considered as negligible perturbations):^[52]

$$\hat{H} = \hat{H}_{\text{EZ}} + \hat{H}_{\text{ZFS}} + \hat{H}_{\text{EX}} = \mathbf{g}\mu_{\text{B}}\hat{\mathbf{S}}\vec{B} + \hat{\mathbf{S}}^{\text{T}}\mathbf{D}\hat{\mathbf{S}} + \hat{\mathbf{S}}_1^{\text{T}}\mathbf{J}\hat{\mathbf{S}}_2 \quad (7.1)$$

Here, $\hat{\mathbf{S}}$ is the total spin angular momentum operator (with $\hat{\mathbf{S}}_1$ and $\hat{\mathbf{S}}_2$ being the operators for the respective electron spins), \mathbf{g} the g-tensor (assumed to be isotropic due to a small spin-orbit coupling in these organic molecules) and μ_{B} the Bohr magneton, \mathbf{D} the ZFS tensor and \mathbf{J} the exchange-interaction tensor. The Zeeman interaction (see ch. 3.2.1) describes the quantized splitting of the paramagnetic states into their sublevels based on the interaction with the external magnetic field \vec{B} , i.e., the spin Hamiltonian eigenstates $|T_+\rangle$, $|T_0\rangle$, and $|T_-\rangle$.^[59] For nearby electron and hole (i.e., a locally excited state on a given molecule), the triplet sublevels are already energetically split in absence of an external magnetic field due to dipolar interactions between the spins of the unpaired electrons, referred to as ZFS (see ch. 3.2.2). This interaction is described by two important scalar parameters D and E of the corresponding ZFS tensor

D: The axial ZFS parameter D is related to the average inter-spin distance r (to first order approximation $D \sim r^{-3}$), whereby E describes the rhombicity, thus the deviation from axial symmetry.^[51,52,172] For CT states with longer spin-spin distances, spin conservation during charge separation generates spin-correlated radical pairs (SCRPs, eq. 3.6). The corresponding Hamiltonian eigenstates are represented in this chapter by pure $|^3\text{CT}_+\rangle$ and $|^3\text{CT}_-\rangle$ triplet states ($m_s = \pm 1$) and two mixed singlet-triplet states $|^3\text{CT}_0\rangle$ and $|^1\text{CT}_0\rangle$ ($m_s = 0$), where due to angular momentum conversion, only a spin mixing between the latter two can occur.

7.2.1 Detecting Triplet Excitons with Spin-Sensitive Photoluminescence

PLDMR Principle

Having clarified the spin physics of the system under consideration, we can now address their experimental detection with PLDMR and trEPR. Figure 7.1a depicts the PLDMR principle of probing the PL change of singlet states (either CT or molecular), which are coupled (via TTA, ISC, etc.) with paramagnetic states.^[169] Microwave irradiation induces transitions between the sublevels (purple arrows) leading to a change in PL intensity. In the case of ^3CT states, the comparatively large inter-spin distance results in negligible dipolar interaction (i.e., D value), which in turn induces a symmetrical splitting of triplet sublevels $|^3\text{CT}_+\rangle$, $|^3\text{CT}_0\rangle$ and $|^3\text{CT}_-\rangle$ in a magnetic field. Microwave irradiation of frequency ν_{MW} , resonant to the energetic sublevel splitting, induces allowed $\Delta m_s = \pm 1$ transitions at closely spaced magnetic field values. The result is a change of steady-state triplet population, leading to an increased ($\Delta\text{PL}/\text{PL} > 0$) or reduced ($\Delta\text{PL}/\text{PL} < 0$) PL yield under resonance conditions, referred to as full-field (FF) signal (see ch. 2.1.3). For the case of a localized molecular triplet states (T_{mol} in Figure 7.1a), the ZFS results in an asymmetric splitting of the triplet sublevels $|T_+\rangle$, $|T_0\rangle$, and $|T_-\rangle$ in the applied magnetic field. Thus, microwave irradiation induces transitions and PL changes at wider spaced magnetic field values, the distance of which depends linearly on the ZFS parameter D (see also ch. 3.3.1). In addition, there is a certain probability of $\Delta m_s = \pm 2$ transitions at half of the resonant magnetic field, referred to as half-field (HF) signal.^[51] The intensity of the HF signal increases with D (intensity $\sim r^{-6}$, see eq. 3.24) and is therefore detectable for molecular triplet excitons only.^[60] The total width of the spectrum in magnetic field units ($|2D|/g\mu_{\text{B}}$) together with the spectral position of the HF spectrum allows for the molecular localization of the triplet states involved in the PL generation process to be readily determined.^[22]

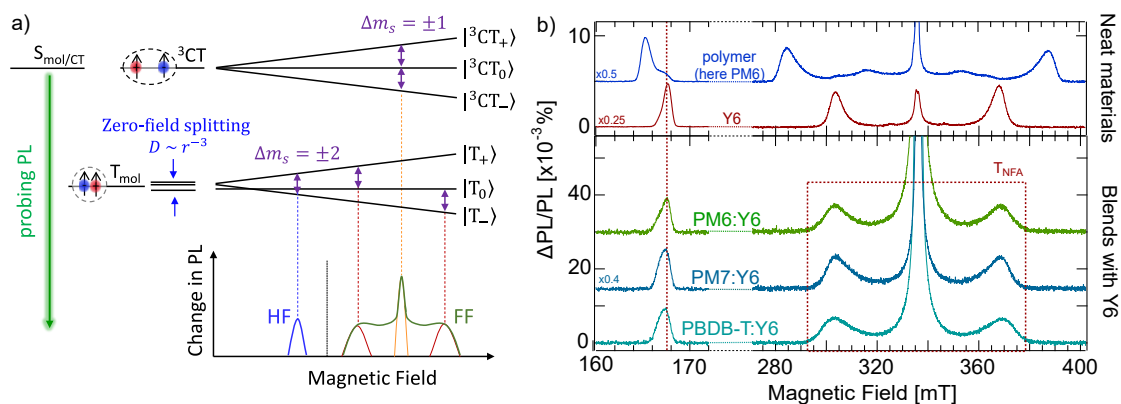


Figure 7.1: Photoluminescence detected magnetic resonance (PLDMR) of triplet excitons. a) PLDMR probes PL changes of singlet states ($S_{\text{mol/CT}}$), which are coupled to paramagnetic triplet states. CT and molecular triplet states (${}^3\text{CT}$, T_{mol}) are split due to Zeeman interaction and the ZFS parameter D : $|{}^3\text{CT}_{+,0,-}\rangle$, $|T_{+,0,-}\rangle$. Microwave irradiation induces $\Delta m_s = \pm 1$ transitions (purple), leading to a change in the PL yield detected as full field spectrum (FF). An additional signal is detected at half the magnetic field (HF) for $\Delta m_s = \pm 2$ transitions. b) PLDMR spectra for the neat materials PM6 and Y6 are shown together with the blends PBDB-T:Y6, PM6:Y6 and PM7:Y6. The spectral width of the FF signal and the position of the HF signal are determined by the material-dependent ZFS and therefore the triplet excitons in the blends can be assigned to the NFA Y6 (red dotted box). All PLDMR measurements were performed at $T = 10\text{K}$.

PLDMR of Neat Materials

Figure 7.1b presents PLDMR spectra of the neat materials PM6 and Y6 (top) as well as blends of Y6 with the polymer donors PBDB-T, PM6 and PM7 (bottom). The measurements were performed for thin-film samples produced by an optimized spin-coating recipe (given in experimental chapter, ch. 4.2.2) comparable to OSC device production.^[197,198] The PLDMR spectra of the neat polymers are almost identical; thus only PM6 is shown here and the spectra of PBDB-T and PM7 can be found in Figure 10.1 in the Appendix. All polymer spectra show a broad molecular triplet feature of 110 mT width, corresponding to a ZFS of $D/h = 1500\text{MHz}$. All ZFS parameters are derived by spectral simulation parameters using the MATLAB toolbox EasySpin^[58], whose simulation parameters are given in Table 10.2 in the Appendix. The PLDMR spectra additionally show a preferential alignment of the molecules on the substrates, represented by the 'wing-like' shape of the spectrum, as further discussed below. The HF signal is located at $B = 165.0\text{mT}$, whereby it possesses an additional shoulder, indicating a small fraction of molecules with different preferred orientation. Pristine NFA Y6 shows a molecular triplet signal with smaller width of around 70 mT, corresponding to $D/h = 940\text{MHz}$ and a HF signal at $B = 165.0\text{mT}$. Regarding the molecular triplet excitons of these neat materials, the distinct differences in ZFS parameters and HF signal positions between donor and acceptor materials give a favorable prerequisite to confi-

dently distinguish triplet excitons in blends. Furthermore, the materials show a central narrow peak, which has previously been assigned to spontaneously separated charge carriers, also called polaron pairs (PP), with a weak or no dipolar interaction.^[22,135,199] Pristine Y6 thereby possesses an additional broader central peak, most likely assigned to inter-CT states between Y6 moieties and will be discussed in the scope of a following project.^[200]

PLDMR of (Non-) Halogenated Blends

When blending Y6 with the donors PM6, PM7 and PBDB-T (lower PLDMR spectra in Figure 7.1b), the intensity of the central peak increases significantly due to the increased formation of separated polaron pairs, spectrally overlapping with CT states at the donor:acceptor. Since PLDMR is an optical technique on thin-films without electrodes, all formed CT states and polaron pairs do eventually recombine, increasing the impact of the central peak. Using trPLDMR, the previous chapter showed that the CT peak in PM6:NFA blends has a positive sign, which was assigned to triplet-polaron annihilation (TPA), being a central bimolecular interaction in these OSCs.^[49,135,173] As reminder, magnetic resonance conditions thereby convert triplet-polaron pairs from TPA allowed doublet state ($S = \frac{1}{2}$), where they can convert spin-allowed into the ground state with doublet manifold, into TPA forbidden quartet states ($S = \frac{3}{2}$), enhancing radiative recombination.^[174]

More importantly, all three blends show a broad triplet feature (300–370 mT), arising from long-lived molecular triplet excitons. The ZFS parameter D , related to the width of the FF spectra, and the positions of the HF signals at $B = 166.8$ mT (dotted vertical line in Figure 7.1b) clearly assign these PLDMR features to triplet excitons on the NFA Y6. The ZFS value in the blends is slightly larger with $D/h = 1020 - 1040$ MHz than in neat Y6 due to a marginally different molecular packing. However, the delocalization is not strongly affected according to the relation $D \sim r^{-3}$ (see eq. 3.18). Furthermore, the triplet features in all PLDMR spectra can only be simulated taking considerable molecular ordering into account, leading to the pronounced spectral 'wings'. The ordering factor λ gives information about the preferential orientation of the molecules, whereby Θ is the angle between the molecular z -axis and the applied magnetic field. Neat Y6 shows a clear preferential alignment of the molecules (Table 10.2) in direction of the applied magnetic field. This ordering is in line with intermolecular face-on stacking of Y6 to the substrate and enhanced crystallinity found for samples from chloroform (CF) solutions.^[201–203] When blending Y6 with the polymers, the ordering is maintained and comparable for the blends ($\lambda_{\Theta} = 4.5$ for PBDB-T:Y6 and $\lambda_{\Theta} = 5.5$ for PM6:Y6 and PM7:Y6). The similar ordering factor in the blends supports that the

backbone ordering known for neat Y6 remains present in the blends, as already confirmed for PM6:Y6 with GIWAXS measurements in literature.^[204] The PLDMR spectra also suggest similar preferential orientation of Y6 in PBDB-T:Y6 and PM7:Y6, whereby this face-on orientation in the blend is shown to be beneficial for charge transport in the direction normal to the substrate surface.^[205,206]

The detected triplet excitons on the NFA can be formed either by direct ISC, non-geminate HBT or by geminate HBT. While PLDMR is not able to distinguish between these pathways, its high sensitivity is crucial to reveal the presence of all long-lived triplet excitons. This sensitivity is achieved due to the optical detection and the continuous illumination, enhancing spin polarization due to annihilation effects, i.e., TTA in molecular triplet features, as discussed in more detail below and in the next chapter.^[26] The PLDMR measurements in blends with NFA Y7 also revealed long-living triplet excitons on the Y7 with all three (non-) halogenated donors (Figure 10.2 in Appendix). Thus, molecular triplet excitons are observed in all studied OPV blend, localized on the energetically low-lying NFA.

7.2.2 Probing Triplet Pathways with trEPR

While PLDMR probes steady-state populations due to continuous illumination, trEPR probes short-lived spin polarization generated by pulsed laser excitation. As already explained in ch. 3.3, trEPR is able to reveal generation pathways of geminate triplet excitons with distinct spin-polarization due to specific mechanisms, such as triplet states populated by ISC. As discussed below, the fraction of these geminate triplet excitons is very low in the studied blends. For the spin-coated samples, this yields a signal that is detectable but too weak to determine the spin polarization pattern with confidence (Figure 7.5). Therefore, trEPR measurements were additionally performed on drop-cast samples (Figure 7.2), giving a better signal-to-noise ratio to reliably identify the population mechanism. The comparison with spin-coated samples is further discussed below.

trEPR of (Non-) Halogenated Blends

Figure 7.2a shows the trEPR spectrum of Y6 and its blends with the three donor polymers (trEPR spectra of neat polymers and blends with Y7 shown in Figure 10.3). Neat Y6 shows a 70 mT wide spectrum, corresponding to $D/h = 945$ MHz, similar to the value obtained with PLDMR ($D/h = 940$ MHz). When blending Y6 with the polymers, all blends show an additional intense CT signal with narrow microwave emission/absorption feature ($B = 336.5$ mT), corresponding to a spin-correlated radical pair (see ch. 3.3.3). The width correlates with the width of PLDMR CT features in Figure 7.1b, assign-

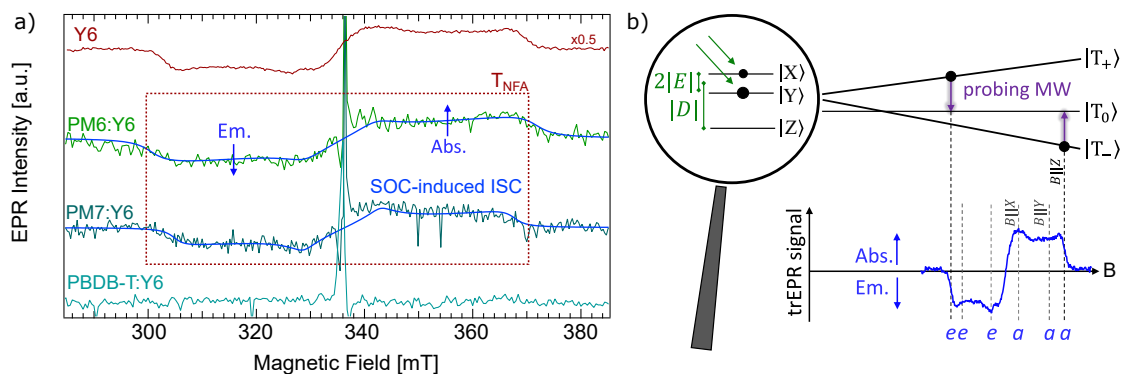


Figure 7.2: trEPR spectra of pristine Y6, PM6:Y6, PM7:Y6 and PBDB-T:Y6. a) trEPR spectra of blends with the halogenated donors (PM6 and PM7) have the same spectral fingerprint as triplets on pristine Y6 (red dotted box) as shown by the simulations (blue). The blend of PBDB-T:Y6 shows no detectable triplet formation. All trEPR measurements were performed at $T = 10$ K. b) Formation of polarized trEPR spectra for spin-orbit coupling (SOC) induced ISC triplets. ISC is sublevel selective and acts on the zero-field sublevels $|X\rangle, |Y\rangle$ and $|Z\rangle$. These populations are converted into populations of high-field triplet sublevels $|T_+\rangle, |T_0\rangle, |T_-\rangle$, depending on the principal axes orientation of the ZFS tensor \mathbf{D} with respect to magnetic field B . Microwave emission (e) or absorption (a) for $\Delta m_s = \pm 1$ transitions (purple) results in the shown Y6 trEPR pattern (blue). The $eeaaaa$ polarization pattern is due to SOC-induced ISC.

ing both to the same CT states. Regarding the molecular (broad) trEPR feature, almost identical spectral fingerprints are detected for the blends of PM6:Y6 and PM7:Y6. The same spectral width of the blends to neat Y6 (red frames box) proves that this feature is also arising from Y6 triplet excitons as already shown with PLDMR. In contrast to PLDMR, trEPR spectra can be simulated without considering molecular ordering. This is attributable to the fact that trEPR probes all (highly) spin-polarized triplet excitons, while PLDMR probes predominantly those triplets that are associated with luminescence, e.g., via TTA, mainly occurring in crystalline phases due to a higher diffusion length (more detailed comparison of the two methods will be given in the next chapter).^[26,207,208] More importantly, the pattern of the trEPR signal of PM6:Y6 and PM7:Y6 displays microwave emission (e) at lower fields and microwave absorption (a) at higher fields, consistent with triplet excitons populated by spin-orbit coupling (SOC) induced ISC, as further discussed below.

Regarding PBDB-T:Y6, molecular triplet excitons on Y6 are detected with PLDMR (Figure 7.1b), whereby no molecular triplet feature in trEPR is observed. While trEPR only probes geminate triplet excitons, PLDMR is also sensitive to triplet excitons by non-geminate recombination. This finding assigns the present triplet excitons in PBDB-T:Y6 detected by PLDMR (Figure 7.1b) to non-geminate hole back transfer (HBT). As also discussed below, non-geminate triplet excitons represent the main contribution

of energetically trapped triplet excitons. Thus, the triplet yield visible in trEPR is overall a very minor triplet channel but important to proof the present mechanism of SOC-induced ISC.

Triplet Excitons by SOC-induced ISC

Figure 7.2b depicts the formation mechanism of the broad spin-polarized Y6 triplet feature in the trEPR spectra of the neat materials and the blends, arising by selective population of the triplet sublevels by ISC from the excited singlet states.^[51] The formation of this pattern has already been explained in ch. 3.3.2 and is reviewed here with focus on Y6. The ISC mechanism for molecular excitons with small wave function extent (large D value) is based on SOC, which is the dominant ISC process for small electron-hole distances.^[38] At larger inter-spin distances, such as CT states, SOC is negligible and (reverse) ISC is driven by the intermixing of the SCRPs. Thus, triplet excitons formed via geminate HBT leads to a different trEPR spectral patterns, as discussed in ch. 3.3 and in the next chapter.^[26,49]

SOC-induced ISC acts on the zero-field triplet states, given by the eigenstates $|X\rangle, |Y\rangle$ and $|Z\rangle$ of the Hamiltonian (with X, Y and Z being the principal axis of the ZFS tensor \mathbf{D}), which are split due the ZFS parameters D and E .^[52,59] The ISC rate depends on the difference in the nature of the singlet and triplet excited states (ch. 2.2.2), whereby the population is spin selective, depending on the symmetries of the excited singlet and triplet wave functions.^[51,59,209] In the studied materials, SOC-induced ISC leads to a relative population p_i of zero-field triplet sublevels of $[p_x, p_y, p_z] = [0.34, 0.66, 0.00]$ in neat Y6 (Table 10.3). In a magnetic field, the population of the corresponding high-field sublevels $|T_+\rangle, |T_0\rangle, |T_-\rangle$ can be derived from the zero-field population, which depends on the orientation of the ZFS tensor with respect to the external magnetic field (here shown for $\vec{B} \parallel Z$, for further details see ch. 3.3.2).^[59] In this projection, the $|T_+\rangle$ and $|T_-\rangle$ states are more populated than $|T_0\rangle$, whereby resonant microwave irradiation drives this imbalance towards equal distributions. Together with the asymmetric splitting due to ZFS, microwave emission (e) at lower fields (negative intensity) and enhanced absorption (a) at higher fields can be detected with trEPR.^[51] In the present disordered organic samples, transitions from all orientations of \mathbf{D} with respect to B are superimposed as a characteristic spectrum with *eeea* pattern, which is indicative for triplet excitons populated by SOC-induced ISC.^[59] Returning to Figure 7.2a, the SOC-induced ISC pattern of Y6 triplets is also present in the blends of PM6:Y6 and PM7:Y6 with similar zero-field population (i.e., polarization pattern) of triplet sublevels as neat Y6. This result indicates that triplet states in the blends are also populated by SOC-induced ISC, with the comparable spin polarization indicating ISC on the NFA itself.

7.3 Studying Influence of Halogenation on Excited State Kinetics

The previous sections have unraveled the presence of triplet excitons on the NFA and demonstrated the pathway of SOC-induced ISC. The amount of triplet excitons entering this channel depends on different rates. After optical excitation of the blend, the singlet exciton can undergo different pathways: In the optimal case, it diffuses to the donor:acceptor interface to undergo charge transfer. Undissociated singlet excitons can make ISC to triplet states or relax back to the ground state. Halogenation alters the HOMO offset in the blends (Figure 4.4), which may affect the HT rate, important for the charge transfer in these blends.^[194] In addition, increasing halogenation could increase the ISC rate due to the heavier halogen atoms.^[195] To probe the effect of halogenation on the HT and ISC rates, transient absorption (TA) measurements and quantum chemical calculations are discussed below. Subsequently, the yields, i.e., the actual amount of excitons undergoing the respective pathway, are discussed based on TA and trEPR on spin-coated samples. Before beginning with the interpretation of TA data, the principle of TA spectroscopy will be explained.

7.3.1 Hole Transfer Kinetics by Transient Absorption

TA Spectroscopy Principle

Transient absorption (TA) spectroscopy is based on the transient pump-probe technique: A pump pulse generates short-lived excited states, while the time-dependent evolution of these states is probed by a second pulse after various time intervals.^[210] The investigation of these short-living states requires a short monochromatic pump pulse (≈ 100 fs) and a probe pulse covering a broader spectral wavelength range (visible wavelength range in this chapter and near infrared (NIR) range in the next chapter). The change in transmission ΔT of the probe beam sent through the sample is measured

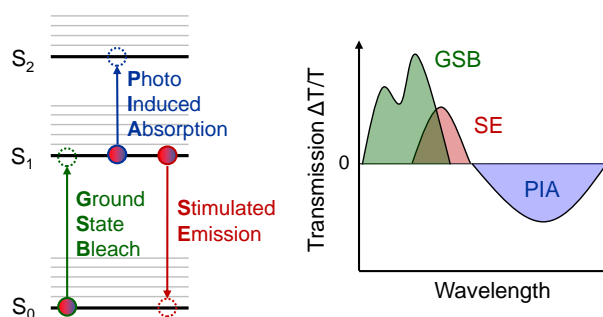


Figure 7.3: Principle of TA spectroscopy. GSB is caused by the depletion of the ground state after the pump pulse, SE is caused by the interaction of an excited state with the probe photon, and PIA is the absorption of an excited-state exciton into a higher state. TA spectra are measured by change of transmission ΔT of the probe pulse between pump on and pump off, normalized to transmission T when pump off.

change in transmission ΔT of the probe beam sent through the sample is measured

with respect to the system in the excited state (pump on) minus the transmission of the system in the ground state (pump off) for various time delays τ .^[103,210] The signal is typically normalized to the transmission of the system in the ground state (pump off), i.e., $\Delta T/T$.^[211] There are different important transitions to account for: If the pump pulse considerably depopulates the ground state and the molecules are in their excited states, the absorption of the ground state is reduced. Thus, an enhanced transmission $\Delta T/T > 0$ is observed in the respective wavelength range, also termed as *ground state bleach* (GSB), illustrated in Figure 7.3. The GSB can be easily identified as it is spectrally comparable to the steady-state absorption spectrum of the molecule. If photons from the probe beam interact with excited states of same energy, e.g., S_1 states, stimulated emission (SE) produces emission of the respective excited state.^[210] SE is spectrally similar to the fluorescence spectrum of the molecule (Stokes shifted to the GSB), and leads to an increased light intensity at the detector, i.e., positive $\Delta T/T > 0$ signal.^[210] Lastly, if the photons of the probe pulse are absorbed to further raise an excited state into a higher lying excited state (here shown for $S_1 \rightarrow S_2$, at longer time delays $T_1 \rightarrow T_n$ may also occur), the transmission is reduced $\Delta T/T < 0$, referred to as *photo-induced absorption* (PIA). If the singlet states have already dissociated into free charge carriers, PIA features can also be detected for electrons and holes. The time and spectral component of TA spectroscopy allows the investigation of excited state kinetics, e.g., hole transfer, but also the identification of triplet formation, as discussed in the next chapter.^[27,210]

Hole Transfer in PBDB-T:Y6

Having clarified the emergence of TA spectra, we can now turn to the application on the (non-) halogenated blends under consideration. Figure 7.4 shows the TA spectra and kinetics for Y6 blends with excitation wavelength of 800 nm for selective excitation of the NFA Y6. A low excitation fluence of $\sim 0.6 \mu\text{J cm}^{-2}$ is used to prevent excess bimolecular recombination in the first few nanoseconds from affecting the determination of the HT timescales. Figure 7.4a shows the time dependent TA spectra of PBDB-T:Y6, TA spectra for PM6:Y6 and PM7:Y6 are shown further below. The TA spectra reveal the Y6 GSB centered at 830 nm immediately after optical excitation, consistent with absorption spectra of Y6.^[201,212,213] Additionally, the PIA of Y6 singlet excitons at 910 nm is observed at the same timescales.^[200,214] More importantly, a clear GSB at 580 – 650 nm emerges in the TA spectra, consistent with the absorption spectrum of the polymer taken from literature.^[80,215] Since the excitation pump does not generate excitons on the PBDB-T (PM6, PM7 respectively), the appearance of the polymer GSB indicates fast dissociation of the Y6 exciton at the D:A interface. The presence of the polymer GSB

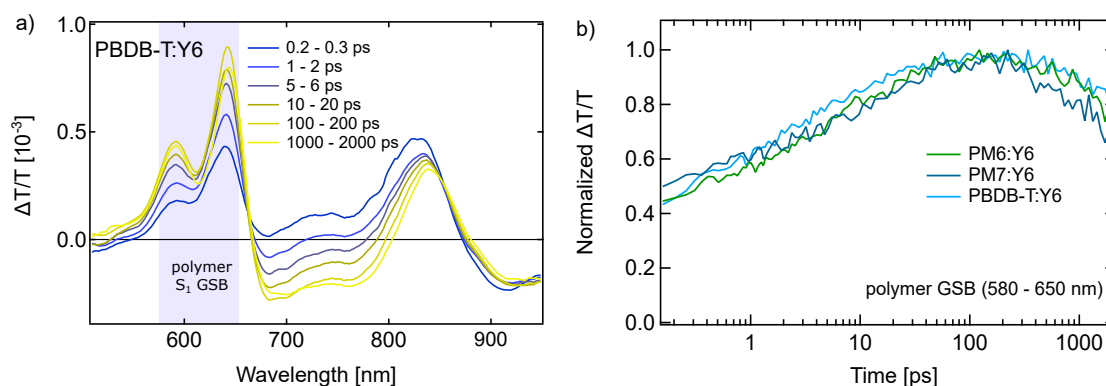


Figure 7.4: TA spectroscopy of PBDB-T:Y-series. a) TA spectra at different time delays for PBDB-T:Y6. b) HT kinetics extracted from polymer GSB (580 – 650 nm) for PM6:Y6, PM7:Y6 and PBDB-T:Y6. In all samples, hole transfer takes place on comparable timescales. All TA measurements used excitation wavelength of 800 nm for selective excitation of Y6 and were performed at $T = 293$ K. Measurements performed by A. J. Gillett.

already at 0.2 ps suggests that some HT occurs on ultrafast timescales.^[200,216] However, as the Y6 GSB falls, likely due to some spectral overlap with the negative sign PM6 hole polaron forming at 920 nm, the polymer GSB increases, peaking around 100 ps. This indicates a significant population of the NFA excitons require additional time to dissociate. On similar timescales, a broad negative band grows in between 680 and 800 nm. The feature from 680 to 730 nm can be assigned to the electro-absorption of the donor polymer, indicating the separation of bound interfacial CT states into free charges.^[49,200] It is overlapping with the PIA signal of Y6 anions at ≈ 780 nm, as already verified in blends with other donors.^[217] Summarized, all blends with NFA Y6 show a considerable HT yield whereby it decreases upon halogenation of the donor in these blends, as further discussed below.

HT Kinetics of (Non-) Halogenated Blends

Figure 7.4b shows the normalized HT kinetics from the polymer GSB between 580 and 650 nm. The hole transfer rate appears to be comparable for all donor combinations PBDB-T, PM6 and PM7 with Y6 (comparable HT kinetics were also extracted for NFA Y7). In addition to the ultrafast component already visible at 0.2 ps, the HT yield increases up to a peak at 100 ps, indicating that the HT is completed. The slower HT rate component is often attributed to diffusion limitations from excitons created far from the donor:acceptor interface.^[88,218,219] Zhong et al. performed measurements on 5:1 polymer:NFA blends to disentangle the ultrafast component, determined by intrinsic HT rates, from the morphology dependent exciton diffusion rates.^[215] However, the studied blends show similar kinetics in both components, reflecting that neither the small energetic shift in HOMO level (see Figure 4.4) nor probable morphology differ-

ences upon halogenation have a significant impact on the HT rates, which has been found to be largely governed by the interfacial morphology in PM6:Y6.^[200] However, despite initially generating a similar number of excitations on Y6 (as seen by the equal intensity of the Y6 GSB at 0.2 ps in all blends), the intensity of the polymer GSB reaches the highest value in PBDB-T, followed by PM6 and then PM7. This indicates, despite the comparable HT rate in all blends, a difference in the absolute HT yield, i.e., the number of exciton undergoing HT. A lower number of Y6 excitons reaching the D:A interface for HT could be owed to a larger domain size for the halogenated donor, as discussed below.

7.3.2 ISC Rates in (Non-) Halogenated Y-Series

Singlet excitons formed upon photoexcitation which do not reach the D:A interface for efficient HT may eventually undergo ISC to the respective triplet states. Quantum chemical calculations (performed by G. Londi and Y. Olivier, see end of the chapter) are thereby a practical tool to access possible differences in the ISC rates due to halogenation. The ISC rate k_{ISC} can be thereby determined by the semi-classical Marcus-Levich-Jortner expression, which treats high-frequency intramolecular vibrational modes, as described in ch. 2.2.2. The ISC rate can be expressed as the product of SOC matrix element $|\langle T_n | \hat{H}_{\text{SOC}} | S_1 \rangle|$ between initial state S_1 and end state T_n and the Franck-Condon weighted density of states FCWD (see eq. 2.11 for detailed description):^[38,39]

$$k_{\text{ISC}} = \frac{2\pi}{\hbar} |\langle T_n | \hat{H}_{\text{SOC}} | S_1 \rangle|^2 \text{FCWD} \quad (7.2)$$

According to El-Sayed's rule, the ISC rate depends on the nature of electronic transitions, i.e., higher ISC rate constant when the two states involved have different orbital types.^[220,221] The molecular orbitals involved in the S_1 excited state of Y6 (and Y7) as well as their respective contributions are very similar to those involved in their T_1 excited states, making SOC between these states negligible. For instance, in Y6, both S_1 and T_1 were calculated to have a dominant HOMO-to-LUMO transition (98% for S_1 and 90% for T_1), leading to a very small SOC value ($< 0.01 \text{ cm}^{-1}$). In contrast, the T_2 excited state (which is energetically also below S_1) shows a contribution of 75% of HOMO-to-LUMO+1 transition, involving a different localization of the electron wave function in comparison to S_1 . Consequently SOC between S_1 and T_2 is larger (on the order 0.05 cm^{-1}) compared to the SOC between S_1 and T_1 , enabling singlet-triplet conversion by ISC on the NFAs.

To study the influence of halogenation, the acceptors Y6 and Y7 were compared together with the non-halogenated version, called Y5 ("X = H" in Figure 4.3). In this manner, the natural transition orbitals (NTOs) were calculated, which provide a qualitative description of electronic excitations through an orbital representation in which each excited state is expressed as a single orbital pair, i.e., of electron (occupied) and hole (unoccupied).^[222] The same NTOs were found in all three cases, meaning that halogenation does not alter the nature of the low-lying excited states. In fact, the electron density on the halogen atoms in the NTO is thereby negligible, resulting in the SOC matrix element being almost insensitive to halogenation. As the respective singlet-triplet gap is also not changing considerably, the SOC-induced ISC kinetics can be assumed to be comparable for all (non-) halogenated acceptors.

7.3.3 Impact of Halogenation on ISC and HT Yield

While the HT and ISC kinetics are comparable for all PBDB-T:Y-series blends, the yields are determined to be different, i.e., the number of excitons undergoing these pathways varies. Figure 7.5 shows TA (top) and trEPR (bottom) measurements for Y6-based blends, i.e., PBDB-T:Y6 (left), PM6:Y6 (middle) and PM7:Y6 (right). Regarding the TA spectra, all samples show a comparable Y6 GSB at 830 nm, indicating the amount of created excitons being of the same magnitude. While a clear polymer GSB is visible in PBDB-T:Y6 and PM6:Y6 already after 0.2 ps, the polymer GSB in PM7:Y6 at 0.2 ps is very weakly pronounced. Comparing the intensity of polymer GSB when HT is completed at around 100 ps, the HT yield in PBDB-T:Y6 is the highest, followed by PM6:Y6 and PM7:Y6. In the same trend, the Y6 GSB is decaying slowest in PBDB-T:Y6, followed by PM6:Y6 and PM7:Y6. Since the HT kinetics are comparable in all three blends, the faster Y6 GSB decay is most likely due to undissociated Y6 S_1 excitons recombining to the ground state or undergoing ISC. Figure 7.5 (bottom) shows the trEPR measurements on the spin-coated substrates. PBDB-T:Y6 shows the highest CT peak, indicating the highest fraction of CT states in line with the higher HT yield from TA measurements in this blend. Regarding the molecular triplet excitons, trEPR of PBDB-T:Y6 shows a negligible broad triplet trEPR signal (inset), also consistent with the increased HT yield. In contrast, PM6:Y6 and PM7:Y6 show a small amount of molecular triplet excitons by ISC, as already seen in the drop-cast samples from Figure 7.2a. Thereby, the trEPR of PM6:Y6 and PM7:Y6 in the spin-coated substrates shows a smaller ISC yield in comparison to the drop-cast samples, arising from improved morphology enhancing the HT while reducing the ISC yield. Thus, the low ISC yields in these spin-coated samples indicate good HT efficiencies in all blends, although the presence of the molecular trEPR signal suggests incomplete charge carrier generation with halogenated donor.

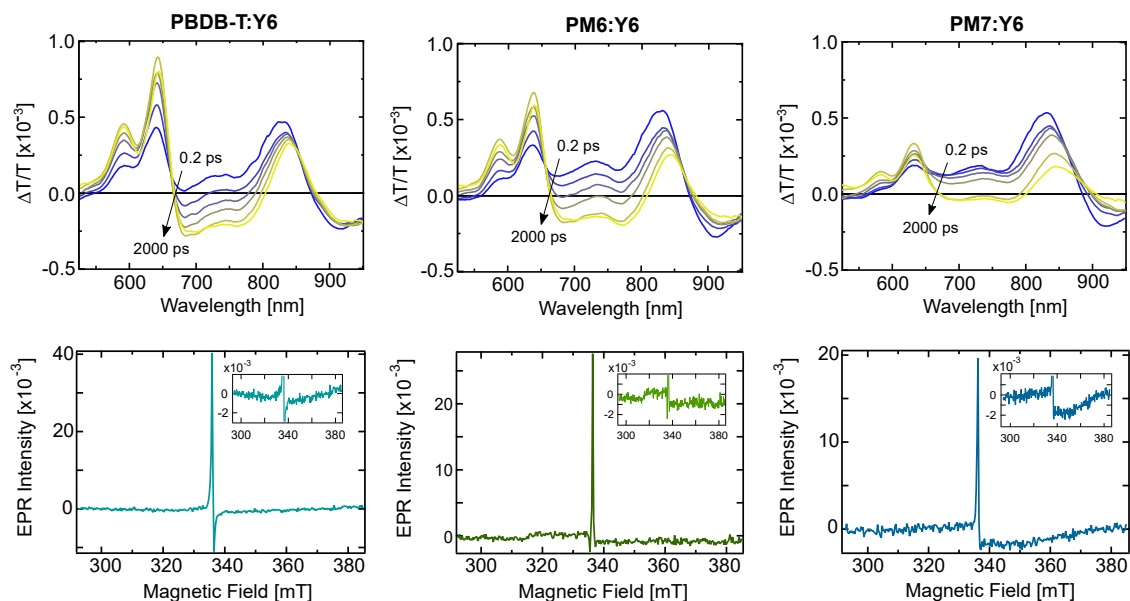


Figure 7.5: TA and trEPR measurements on spin-coated substrates with PBDB-T:Y6 (left), PM6:Y6 (middle) and PM7:Y6 (right). Top: TA spectra at different time delays from 0.2 ps (blue) to 2000 ps (yellow) after pump pulse. The decreasing polymer GSB (580 - 650 nm) upon increasing halogenation of the donor indicates decreasing HT yield. All TA measurements used excitation wavelength of 800 nm and were performed at $T = 293$ K. Measurements performed by A. J. Gillett. Bottom: trEPR spectra show the highest CT peak in PBDB-T:Y6, whilst decreasing upon halogenation of the donor. Inset: Molecular triplet excitons, i.e., present ISC yield, is detected in PM6:Y6 and PM7:Y6 while PBDB-T:Y6 exhibits no measurable molecular trEPR signal. Measurements performed at $T = 10$ K.

7.4 Discussion

Figure 7.6 shows the Jablonski diagram of the studied PBDB-T:Y-series blends, while Table 10.1 summarizes all corresponding energies and observed triplet formation mechanisms. The energies for singlet states S_1 and CT states are taken from literature, while triplet energies are determined by subtraction of calculated ΔE_{ST} . The investigated NFAs possess a low-lying singlet state with a small offset to CT energy, allowing small energy losses in comparison to fullerene-based solar cells.^[181,214] However, given the large ΔE_{ST} of the molecular states, the lowest NFA triplet states are energetically below the CT states and are not able to contribute to photocurrent, i.e., they are energetically trapped. Triplet excitons have small non-radiative decay rates and are long-lived, thus detectable with both PLDMR and trEPR. The following discussion addresses the individual triplet formation pathways and associated kinetics of Figure 7.6, based on the results and evaluations achieved from the measurements presented above. This analysis allows to identify the most important efficiency-limiting processes in the studied blends and unravel the impact of halogenation on these channels.

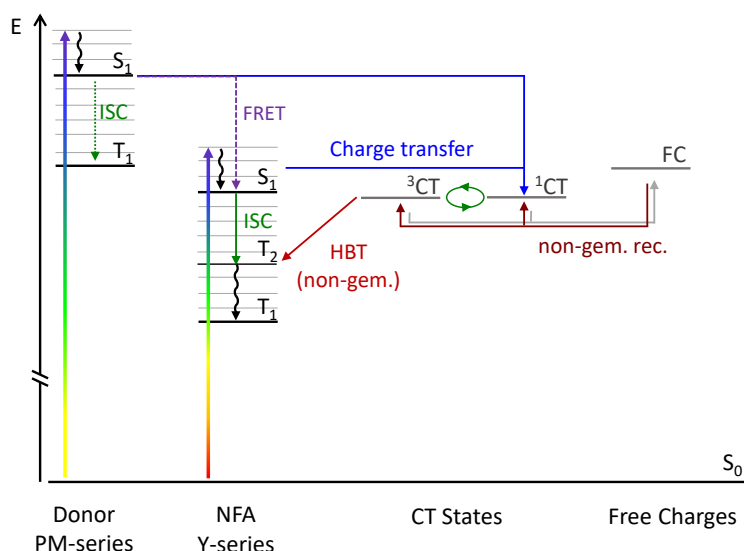


Figure 7.6: Energy diagram of the studied PBDB-T:Y-series blends. Optical excitation of donor or acceptor singlet is followed by interfacial charge transfer, FRET or direct ISC. NFA triplet states (T_1 , T_2) are energetically below the intermolecular CT states (^3CT , ^1CT) and therefore represent energetic trap states. NFA triplet states will be occupied by ISC from NFA S_1 state or by HBT from ^3CT , which itself is populated by non-geminate recombination of free charges (FC).

Geminate Pathways

Triplet excitons are detected in all PBDB-T:Y-series blends on the NFA triplet states (Figure 7.1b for Y6 blends and Figure 10.2 for Y7 blends). The polarization patterns in trEPR (Figure 7.2b for Y6 blends Figure 10.3 for Y7 blends) are consistent with polarization for SOC-induced ISC triplets (*eeea*). These polarization patterns of direct ISC can be readily distinguished from other processes, such as HBT from triplet CT states formed via geminate recombination.^[26,189] Geminate BCT is rather often observed in polymer:fullerene blends, as demonstrated in the next chapter. However, in the NFA-based blends investigated, no indication of geminate BCT, i.e., HBT to NFA triplet states could be observed, ruling out this triplet formation mechanism, as also reported in literature.^[49] The comparable zero-field populations of the blends and neat Y6 (Table 10.3) indicate ISC taking place on the NFA, e.g., in the center of NFA domains larger than the exciton diffusion length away from the donor:acceptor interface. The SOC-induced ISC rate is additionally increased through the presence of additional triplet states T_2 with larger change in their nature in regard to S_1 , increasing the SOC matrix element. As for the donor, ultrafast electron transfer quenches the singlet excitation in the sub-picosecond time range, with the possibility of Förster resonance energy transfer (FRET) to the NFA as another deactivation channel in these blends.^[185,186,218,223] Thus, the fast depopulation of the donor singlet states is kinet-

ically outcompeting slower ISC on the donor, suggesting the yield of excitons undergoing ISC on the polymers to be negligible (dotted arrow in Figure 7.6). Even if donor triplet states were populated with low yield, they would still be energetically above the CT and NFA states and could undergo charge or Dexter transfer. Thus, triplet excitons on the polymer donor are not energetically trapped in these blends and need not be considered as an efficient loss channel.

Non-Geminate Pathways

The NFA triplet yield in OSCs by SOC-induced ISC is assumed to be low due to a weak trEPR signal for the spin-coated substrates (Figure 7.5, bottom). Additionally, HBT from ^3CT states formed via non-geminate recombination of free charge carriers was confirmed, visible in all PLDMR spectra. Recombining free charge carriers with uncorrelated spin orientations will lead to the formation of 25% of ^1CT singlet and 75% ^3CT triplet states.^[63] The latter can relax spin-allowed to the lowest molecular triplet states via non-geminate HBT (dark red arrows in Figure 7.6).^[190] Thereby, the excitons initially occupy the three triplet sublevels equally due to spin statistics, but get redistributed within the spin-lattice relaxation time according to Boltzmann statistic. Additionally, continuous optical excitation, as in PLDMR, enhances the spin polarization due to accumulation of triplet excitons and subsequent spin-dependent annihilation processes. In combination with the high optical detection, this method proves to be very sensitive to non-geminate triplet excitons. Thus, trEPR alone could miss triplet excitons despite their significant presence as for the example of PBDB-T:Y6. Gillett et al. showed with transient absorption that in the blend PM6:Y6 around 90% of the non-geminately recombined CT states undergo HBT to the NFA triplet.^[49] In contrast, the ISC yield in neat Y6 is around 3%, further reduced in the blends due to a significant CT of 90% of the generated excitons.^[49] Regarding the similarity of ISC and HT rates between the blends, we assume a similar amount of triplet excitons in all PBDB-T:Y-series blends from non-geminate recombination. Since the rate of non-geminate HBT is shown to increase with temperature, the presence of non-geminate HBT triplet excitons even at 10K highlights the importance of this loss channel.^[49]

Excited States Kinetics of ISC and HT

The two most important rates affecting the population of triplet states upon excitation of the singlet states are HT and ISC rates. As differences in HT kinetics would give the singlet excitons more/less time to undergo ISC and vice versa, the impact of halogenation on these rates is of relevance. Regarding the halogenation of the acceptor, one could invoke an increase in SOC due to heavier halogen atoms, which would in-

crease the ISC rate, as has already been shown in literature for bromine or iodine.^[224] However, quantum-chemical calculations on NFA Y-series reveal that, starting from the non-halogenated acceptor Y5, the ISC rate does not change significantly upon fluorination and chlorination in these molecules due to the absence of significant weight of electron density on the halogen atoms. As for the HT kinetics, halogenation of PBDB-T is lowering the donor HOMO level (see Figure 4.4), leading to a higher V_{OC} in solar cells with PM6 and PM7.^[80,196] The smaller energy offset is desirable to minimize energy loss but one could consider a negative effect on the driving force due to a smaller HOMO offset.^[194,218] However, TA measurements (Figure 7.3b) showed a comparable HT rate with the three different (non-) halogenated donors. This outcome is not surprising, as the overall HT rate has been shown not being sensitive to the HOMO offset, especially in low-offset OSC: while the HT rate of NFA excitons generated in close proximity to the donor:acceptor interface occurs on sub-picosecond timescales, the overall HT process takes place on timescales of tens of picoseconds, dependent on exciton diffusion in the bulk morphology.^[216] Furthermore, Ma et al. showed that HT rates for PM6:Y6 are only weakly affected by temperature in the range from 15 to 300K, allowing the comparison with the low-temperature EPR measurements.^[225] Overall, the triplet population kinetics upon initial singlet excitation are shown to be comparable for (non-) halogenated donor and acceptor combinations.

Exciton Yield of ISC and HT

While the excited state kinetics are determined to be independent of halogenation, the HT and ISC yields, i.e., number of excitons undergoing HT and ISC, changes upon halogenation of the donor (Figure 7.5). The most probable reasons are differences in the morphology or domain sizes, depending on halogenation of donor/acceptor. Eastham et al. investigated different donor materials with NFA ITIC, demonstrating that efficient hole transfer depends strongly on the blend morphology rather than the energy level alignment.^[226] Comparing TA and trEPR in Figure 7.5, the HT yield decreases upon halogenation, while trEPR data show a detectable ISC yield in PM6:Y6 and PM7:Y6. These results could stem from an increased size and purity of domains due to fluorination and chlorination, i.e., due to reduced miscibility upon halogenation.^[225,227,228] These circumstances could decrease the number of excitons reaching the donor:acceptor interface, resulting in a decreased HT and increased ISC yield. However, domain sizes in the range of the exciton diffusion length are normally beneficial for dissociation of charge carriers, improving short-circuit current J_{SC} and fill factor FF of the solar cell.^[225,227] Thus, the key point for a good performing OSC is matching a good trade-off in bulk morphology between generation of charge transfer yield and

subsequent exciton dissociation.^[229] The higher efficiencies for PM6:Y6 and PM7:Y6 in comparison to PBDB-T:Y6 show that the positive impacts of the halogen, i.e., improved domain purity and higher V_{OC} upon halogenation of the donor, are more influential on solar cell performance.

Strategies for Next-Generation OPV

This chapter has shown by the application of complementary methods that halogenation, which has proven to be beneficial for device performance, does not avoid or eventually even enhances triplet formation. However, to further improve device efficiencies, the energetic trapping of triplet excitons must be reduced or completely prevented. There are different design strategies for next-generation OSCs to engineering out the triplet loss pathways: One approach is to reduce the BCT rate to molecular triplet states by hybridization between CT and local excitons or to outcompete triplet recombination by fast charge separation.^[49,230] Another approach is the combination of state-of-the-art OPV and OLED research by designing OSC acceptors with small singlet-triplet gap, e.g., intramolecular TADF emitters. This combination would prevent energetically trapped triplet excitons, as they can be thermally reactivated, while simultaneously preserve the small voltage losses. Thus, intramolecular TADF emitters with strong long-wavelength absorption and suitable HOMO/LUMO levels for efficient charge transfer could be promising candidates for OPV acceptors.

7.5 Conclusion

This chapter revealed loss processes to non-radiative long-lived triplet states by the application of triplet spin-sensitive techniques (PLDMR, trEPR) together with TA spectroscopy and quantum-chemical calculations. Using these complementary methods, all triplet excitons in the studied blends could be detected and distinguished, providing a complete picture of their generation pathways. The systems under consideration in this chapter were state-of-the-art donor:acceptor combinations employing the (non-) halogenated polymers PBDB-T, PM6, PM7 and the NFAs Y6 and Y7, with long-lived triplet excitons detected in all blends. These excitons are energetically trapped on the low-lying NFA triplet states, where they are unable to contribute to OSC performance due to a high energetic gap ΔE_{T-CT} to CT states. While the major contribution observed in all blends is non-geminate hole back transfer, in blends with halogenated donors there is also a triplet population pathway through SOC-induced ISC on the NFA. The impact of halogenation on the rates affecting the population of triplet states after excitation of the NFA singlet states, in particular ISC and hole transfer, is comparable

for all donor:acceptor combinations. Thus, shifting of HOMO levels or heavy halogen atoms has a minor influence on excited states kinetics. However, the increased triplet exciton yield by ISC with best performing PM6 and PM7 indicates an incomplete charge carrier generation, suggesting an adverse impact of domain aggregation through halogenation. While the benefits of halogenation still prevail in terms of overall device efficiency, the detection of energetically trapped triplet excitons in all these (non-) halogenated blends clearly shows that there is untapped potential to further improve plateauing OSC efficiencies.

7.6 Additional Information

Contribution to this chapter

This chapter is based on a collaborative work: A. J. Gillett¹ performed the TA measurements (Figure 7.3 and Figure 7.5, top). G. Londi² and Y. Olivier² performed the quantum chemical calculations (section 7.3.2). The TA measurements were performed in the Cavendish Laboratory at the University of Cambridge, the setup specifics can be found in the Experimentals (ch. 4.3.5). The quantum chemical calculations were calculated in the Laboratory for Computational Modeling of Functional Materials at the University of Namur, computational details can be found in Ref^[25].

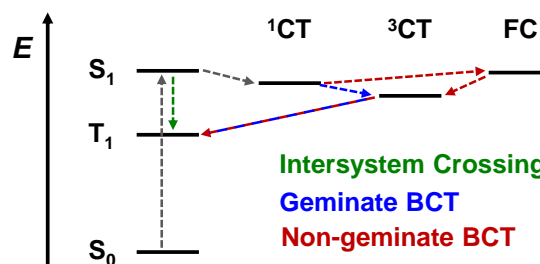
¹Cavendish Laboratory, University of Cambridge, JJ Thomson Avenue, Cambridge, UK

²Laboratory for Computational Modeling of Functional Materials, Namur Institute of Structured Matter, Université de Namur, Rue de Bruxelles, 61, 5000 Namur, Belgium

8 Experimental Framework for Probing Triplet Recombination Pathways in Organic Solar Cells

ABSTRACT

Non-radiative recombination to triplet states is not only observable in organic solar cells (OSCs) based on non-fullerene acceptors (NFAs), also OSCs based on fullerene acceptors exhibit strong triplet loss. In contrast to the more efficient NFA



systems that showed triplet states mostly formed via non-geminate recombination and a small amount of intersystem crossing (ISC), fullerene systems also reveal significant triplet formation via another geminate processes. Thereby, fullerene blends additionally exhibit contribution of geminate back charge transfer (BCT) to the energetically lower lying donor triplet. This chapter presents an experimental framework that combines time-resolved optical and magnetic resonance spectroscopy to detect triplet excitons and identify all three dominant formation mechanisms. This methodology enables to precisely disentangle the triplet formation pathways in the two well-studied polymer:fullerene systems PM6:PC₆₀BM and PTB7-Th:PC₆₀BM. The additional geminate BCT pathway is thereby suggested to enhance with electrons trapped in the isolated fullerenes sitting in the alkyl side chains of the donor polymers, highlighting the importance of engineering good donor and acceptor domain purity. By leveraging the strengths of three spin-sensitive techniques, already introduced in the previous chapter, the following analysis provides a complete picture of complex and overlapping triplet generation pathways in fullerene-based OSC blends.

This chapter is based on: A. Privitera¹, J. Grüne¹, A. Karki, W. K. Myers, V. Dyakonov, T.-Q. Nguyen, M. K. Riede, R. H. Friend, A. Sperlich and A. J. Gillett. Geminate and Nongeminate Pathways for Triplet Exciton Formation in Organic Solar Cells. *Adv. Energy Mater.*, 12, 16, 2103944 (2022).^[26]

¹contributed equally

8.1 Introduction

The timeline of organic solar cell (OSC) acceptors scales with their ability to achieve good power conversion efficiencies (PCEs) with suitable donors. While fullerene acceptors, e.g., PC₆₀BM and PC₇₀BM, were initially quite promising, non-fullerene acceptors (NFAs), such as ITIC and Y6 discussed in the previous chapters, have enabled further increase of PCEs.^[5,231,232] The reasons were already given in the previous chapter, lying primarily in their better absorption in the visible and near-infrared spectral regions and their better energy level tunability, driving efficiencies up to 19%.^[17,18] In contrast, fullerene acceptors only reveal absorption up to 500 nm, whereby the light harvesting can be improved up to 800 nm by choosing suitable donor as PTB7-Th.^[67] Besides the drawback of lower absorption in the visible wavelength range, fullerene systems also exhibit considerable voltage loss due to formation of triplet excitons, including an additional formation pathway of geminate back charge transfer (BCT).^[21,47,233] While the previous chapter focused on the impact of (non-) halogenated NFA systems on overall triplet formation, the following chapter will concentrate on the experimental opportunities to unravel all different triplet formation pathways utilizing two fullerene-based systems. Prior to the analysis of the spin-sensitive toolkit for triplet state detection in organic semiconductors, the necessity of the research goal of preventing triplet states in terms of device performance and stability will be elaborated.

Charge carrier recombination via molecular triplet states has been identified as a significant non-radiative voltage loss pathway, both in fullerene- and NFA-based OSCs.^[49,180,234,235] As already defined in the previous chapter, triplet states are especially responsible for the non-radiative voltage loss ΔV_{nr} . Thereby, non-radiative recombination in OSCs affects the open-circuit voltage V_{OC} by reducing the carrier lifetime from the intrinsic radiative limit.^[184,236] For instance, as noted in the last chapter, the fraction of charge carriers in PM6:Y6 that recombine via the NFA triplet is $\approx 90\%$, and similar triplet recombination proportions were found for fullerene acceptors.^[49,63,190] Non-radiative voltage losses can be quantified by the electroluminescence external quantum efficiency EQE_{EL} using the relation $\Delta V_{nr} = -\frac{k_B T}{e} \ln(\text{EQE}_{EL})$; where k_B is the Boltzmann constant, T the temperature and e the elementary charge. Since the EQE_{EL} depends on the fraction χ of radiative recombination events, the non-radiative triplet recombination reduces EQE_{EL} by a factor of 10 in these devices. The loss of V_{OC} due to triplet recombination can thus be estimated to be ≈ 60 meV in these OSCs.^[49] Hence, the detailed analysis and understanding of triplet formation pathways is necessary to prevent these crucial voltage losses.

In addition to a reduction in device performance, long-lived triplet excitons are detrimental to OSC stability, presenting a fundamental barrier for commercial applications. Thereby, the interaction with oxygen is one of the major issues.^[170,237,238] The presence of environmental molecular oxygen can either result in oxide radical formation (O_2^{\cdot}) by electron transfer from an excited molecule or, alternatively, in singlet oxygen (1O_2) formation by energy transfer from the excited triplet state to oxygen in its triplet ground state.^[22,237,239] Sudakov et al. investigated oxygen-related degradation in NFA-based OPV blends and found an increased production of O_2^{\cdot} due to mobile electrons on the NFA, destabilizing the donor polymer.^[22] Thus, preventing triplet exciton generation in OSCs is also a step towards reducing degradation and extending device lifetimes.

The reasons given require the elimination of triplet formation to be one of the key focuses in OSC research to further improve device performance and operational lifetime. Detecting and characterizing triplet states in organic semiconductors is generally an understudied topic in the field of OSC, as there are only a few techniques for probing triplet states accurately. This chapter presents an experimental framework combining triplet sensitive methods to uniquely identify triplet states and their respective formation pathways. The methods employed are photoluminescence detected magnetic resonance (PLDMR), transient electron paramagnetic resonance (trEPR), and transient absorption (TA). This combination of optical and magnetic resonance spectroscopies has already been applied in the previous chapter and has also been proven useful in literature to study triplet states in organic semiconductors.^[47,49,63,127,240] This chapter presents these three methods as a complementary set of techniques, including their strengths and limitations, enabling a thorough study of triplet excitons in OSCs. The demonstrated framework is thereby applied to two fullerene-based OSC systems, since they reveal all the major possible triplet formation pathways, as further described below.

8.2 Geminate and Non-Geminate Pathways for Triplet Exciton Formation

The two main pathways to populate T_1 states in NFA-based OSCs have already been introduced in the previous chapter. Fullerene-based OSC possess an additional considerable triplet formation pathway: geminate BCT. This supplemental population pathway therefore requires a more detailed analysis, which is accomplished by combining the triplet sensitivity techniques presented in this experimental framework, each of which addresses a specific (sub)set of triplet formation pathways to molecular T_1 . The

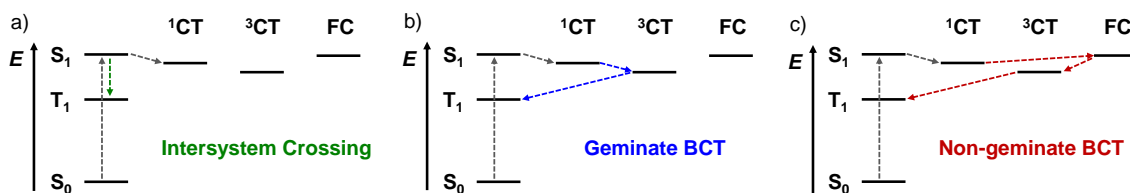


Figure 8.1: Formation pathways of molecular triplet states T_1 . a) Intersystem crossing (ISC): Population of T_1 via direct ISC after optical excitation of the singlet states S_1 . b) Geminate back charge transfer (BCT): Optical excitation of S_1 is followed by charge transfer to ^1CT . ^1CT states do not separate to free charges (FC), instead they undergo spin-mixing with ^3CT states and relax spin-allowed via geminate BCT to T_1 states. c) Non-geminate BCT: Optical excitation of S_1 is followed by charge transfer to ^1CT , which are separating into FC. Spin-statistical non-geminate recombination of FC leads to the formation of ^3CT states, which undergo BCT to molecular T_1 states.

three pathways are consolidated in Figure 8.1, which will be referred to throughout the chapter: a) Direct intersystem crossing (ISC) after optical excitation of S_1 states; b) Geminate BCT from triplet CT states (^3CT), formed by spin-mixing from singlet CT states (^1CT) states which do not separate into free charges (FC) carriers; c) BCT from ^3CT states, formed spin-statistically via non-geminate recombination from FC. As already discussed in ch. 2.3, long-living T_1 states are formed only if they are energetically below ^3CT states, whilst higher T_1 states relax spin-allowed to energetically lower triplet states.^[241,242] As ^3CT states can be readily converted into ^1CT due to their small energetic offset, their presence is also not expected to significantly impact device performance.^[49] Thus, T_1 states are only problematic if they are energetically below CT states. The offset between the CT states and the energetically lowest S_1 states (usually S_1 of the donor in fullerene-based blends and S_1 of the acceptor in NFA-based blends) is typically small ($< 0.2\text{ eV}$) to reduce the energy losses associated with charge generation.^[21,243,244] Given the large ΔE_{ST} energy gap of the molecular states in organic semiconductors, the T_1 states of the respective donor or acceptor are almost always below the CT states.^[178,179,245] Thereby, these low-lying T_1 states can be populated via any of the three pathways described above, forming energetically trapped triplet excitons on the respective molecule. Thus, the full understanding of the complex and overlapping population mechanisms is achieved by the application of multiple experimental techniques to unravel all present T_1 formation pathways.

The demonstrated experimental framework of PLDMR, trEPR and TA to study recombination via T_1 states is developed by employing two fullerene-based OSC model systems, both exhibiting comparable efficiencies: PM6:PC₆₀BM and PTB7-Th:PC₆₀BM.^[26] The full names and chemical structures are given in ch. 4.1.2. The polymers PM6 and

PTB7-Th have been chosen as they represent commonly used donor materials for efficient fullerene- and NFA-based OSCs.^[67,74,88,204,246] The selection of fullerene acceptors to demonstrate this experimental framework is motivated by two reasons: First, many NFA blends do not exhibit the geminate BCT pathway to T_1 states.^[49] Conversely, fullerene blends often exhibit geminate BCT T_1 formation, making the application of magnetic resonance even more important.^[47,189,233] Second, the fullerene component does not contribute significantly to the observed TA spectrum in the visible and near-infrared regions.^[16,47,186] Thus, the use of fullerene blends avoids the complex superposition of, e.g., polymer and NFA spectral features and dynamics, which simplifies the interpretation of the data. These reasons make fullerene acceptor blends an ideal model system to study the three main T_1 formation mechanisms and emphasize the complementarity of optical and magnetic resonance techniques. The following paragraphs first reveal strengths and limitations of the individual techniques, cooperated with experimental results of the detection and formation of T_1 . This analysis is followed by a discussion about the complementarity of all three triplet-sensitive techniques to give a full picture of generation pathways in OSCs.

8.2.1 Photoluminescence Detected Magnetic Resonance

As already mentioned in ch. 6, PLDMR spectroscopy can be employed as pulsed or steady-state technique with, in regard of both, optical and microwave excitation. In the investigation of organic semiconductors, continuous-wave PLDMR is most commonly applied, as employed in this and in the previous chapter.^[22,135,247] Continuous illumination can thereby also yield spin polarization of triplet sublevels by unequal recombination rates or triplet accumulation with subsequent annihilation processes, e.g., TTA. The enhanced spin polarization together with the exceptional optical detection significantly increases the experimental sensitivity of PLDMR. Thus, PLDMR is able to detect any triplet excitations that are coupled to the photoluminescence of the sample, probing triplet excitons formed by all three T_1 generation pathways described in Figure 8.1.^[247] The increased sensitivity allows PLDMR to resolve the half-field (HF) signal (see ch. 2.1.3), representing another major advantages of this method. As the probability of these HF transitions increases with the strength of dipolar coupling between localized electron spins (see eq. 3.24), and their magnetic field position depends on the strength of the ZFS parameters (see eq. 3.25), these signals provide an additional tool for determining the molecular location of a T_1 state.^[22,47,60] Thereby, even minor T_1 pathways can be probed, as further described below. Therefore, HF signals together with the analysis of the full-field (FF) signal provides a useful method to identify all triplet excitons and assign their molecular localization.

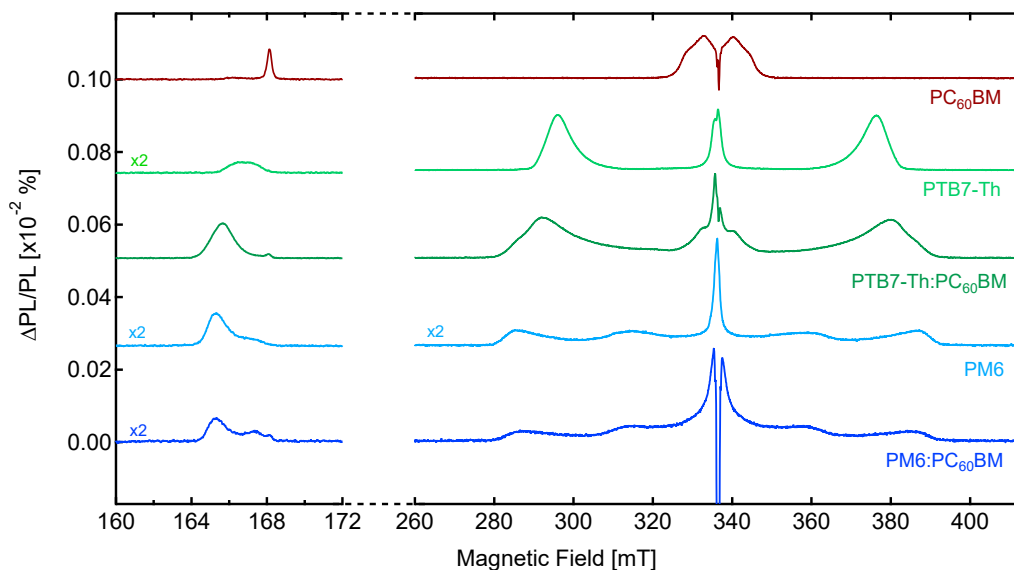


Figure 8.2: PLDMR spectra of the neat materials and blends with half-field (HF) and full-field (FF) signals. (Red) PLDMR spectrum of a neat PC₆₀BM film. The HF T₁ signal of PC₆₀BM is visible at 168.1 mT, whilst the FF T₁ and polaron features are present between 320 – 350 mT. (Light green) PLDMR spectrum of a neat PTB7-Th film. The HF T₁ signal of PTB7-Th is visible at 166.8 mT, whilst the FF T₁ manifests as the two spectral ‘wings’ at 296 and 376 mT. (Dark green) PLDMR spectrum of the PTB7-Th:PC₆₀BM blend film. The HF T₁ signal of PTB7-Th is visible at 165.6 mT, slightly shifted from the neat film due to the changes in the polymer chain ordering upon blending with PC₆₀BM. The HF signal of the PC₆₀BM T₁ is weakly visible at 168.1 mT. The FF PTB7-Th T₁ is visible between 280 – 390 mT with a small PC₆₀BM T₁ contribution from 320 – 350 mT. (Light blue) PLDMR spectrum of a neat PM6 film. The HF T₁ signal of PM6 is visible at 165.3 mT, whilst the FF T₁ is visible between 280 – 390 mT. (Dark blue) PLDMR spectrum of the PM6:PC₆₀BM blend film. The HF T₁ signals of PM6 and PC₆₀BM are visible at 165.3 mT and 168.1 mT, respectively. The FF PM6 T₁ is visible between 280 – 390 mT. All PLDMR spectra were acquired at $T = 10$ K.

Figure 8.2 displays the PLDMR spectra of neat films of PC₆₀BM (red), PTB7-Th (light green), PM6 (light blue) and the PTB7-Th:PC₆₀BM (dark green) and PM6:PC₆₀BM (dark blue) blends (EasySpin simulation parameters for each sample can be found in Table 10.4 in the Appendix). All spectra consist of a full-field (FF) region (260 – 410 mT, corresponding to $\Delta m_S = \pm 1$ transitions), and HF signals (160 – 172 mT, $\Delta m_S = \pm 2$ transitions). In the following, the individual spectra are described in more detail.

PLDMR of PC₆₀BM

PLDMR of neat PC₆₀BM (Figure 8.2, red) shows a relatively narrow T₁ feature in the FF spectrum between 320 – 350 mT, which can be described with the ZFS parameters $D/h = 360$ MHz and $E/h = 50$ MHz. In addition, a HF signal due to PC₆₀BM T₁ states is also detected at 168.1 mT, which can be easily distinguished from the HF signals of the polymer in the blends. Two additional features (sharp negative signals) are super-

imposed on the T_1 signal at 336.25 mT ($g = 2.0040$) and 336.65 mT ($g = 2.0012$), displayed enlarged in Figure 8.3 (left). These negative dips (marked with "+" and "-") can be assigned to the anion $\text{PC}_{60}\text{BM}^-$, as already known from literature, and the cation $\text{PC}_{60}\text{BM}^+$, respectively.^[248–250] The presence of these polarons indicate good charge carrier generation already in neat PC_{60}BM .

PLDMR of PTB7-Th: PC_{60}BM

Turning to the polymers, neat PTB7-Th (Figure 8.2, light green) shows a broader T_1 spectrum in the FF region between 290–380 mT, consistent with ZFS parameter $D/h = 1190$ MHz (high ordering prevents the determination of the ZFS parameter E). The higher D value leads to a shifted HF signal at 166.8 mT in contrast to PC_{60}BM (see eq. 3.25). Additionally, the spectrum reveals a large ordering factor, λ , as already seen in PLDMR spectra of the previous chapter. As a reminder, the ordering factor provides information about the orientational distribution of the molecules in the sample and is reflected by the outer ‘wings’ in the PLDMR spectra.^[52,58,251] The ordering factor λ is extracted here for Θ and ϕ , where Θ is the angle between the molecular z -axis and the applied magnetic field, and ϕ is the in-plane angle. If λ is zero, all molecular orientations occur with the same probability. For PTB7-Th, the ordering for Θ is $\lambda_{\Theta} = 11$, corresponding to an extremely narrow orientational distribution of the molecules in the direction of the applied magnetic field. Upon blending PTB7-Th with PC_{60}BM (Figure 8.2, dark green), a broad T_1 feature of the polymer is again clearly visible in the FF and HF signals of the blend. However, the ZFS parameter D increases from $D/h = 1190$ MHz in pristine PTB7-Th to $D/h = 1310$ MHz in the blend, while the ordering factor decreases to $\lambda_{\Theta} = 7.5$. The variation in ZFS parameter also induces a change in the HF position to neat PTB7-Th. The change in these values suggest that blending PTB7-Th with PC_{60}BM affects the polymer chain ordering in the PTB7-Th domains. This is probably given due to fullerene intercalation within the polymer sidechains as known for these blends, which will be further discussed below.^[252] Additionally, the blend shows a positive ($\Delta \text{PL}/\text{PL} > 0$) CT peak with two negative signals at $g = 2.0012$ and $g = 2.0037$, displayed enlarged in Figure 8.3 (middle). The lower g value is identical to the negative polaron $\text{PC}_{60}\text{BM}^-$, as detected in neat PC_{60}BM , whilst the higher g value likely represents the positive polaron PTB7-Th⁺ on the polymer ($\text{PC}_{60}\text{BM}^-$ marked as "-" and PTB7-Th⁺ marked as "+").^[253]

PLDMR of PM6: PC_{60}BM

Regarding the other polymer PM6 (Figure 8.2, light blue), the PLDMR spectrum reveals a broad T_1 feature between 280–390 mT, corresponding to ZFS parameters $D/h =$

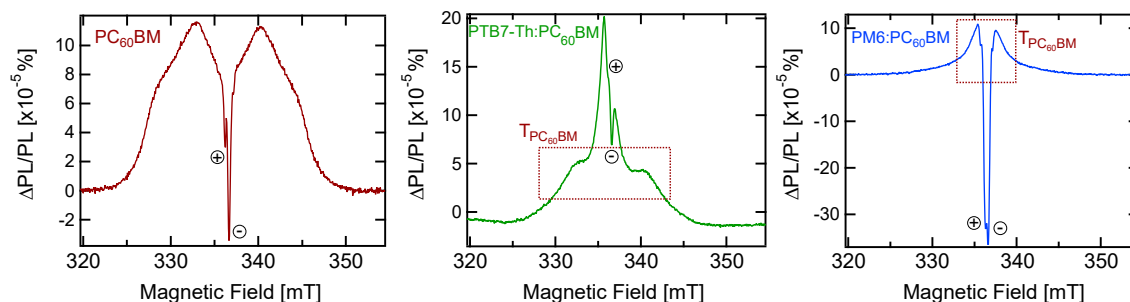


Figure 8.3: Enlarged PLDMR spectra (320–350 mT) of neat PC₆₀BM (left), PTB7-Th:PC₆₀BM (middle) and PM6:PC₆₀BM (right). Neat PC₆₀BM shows two sharp negative signals, corresponding to the cation PC₆₀BM⁺ and the anion PC₆₀BM⁻ (marked as "+" and "-" respectively). The blends show a positive ($\Delta\text{PL}/\text{PL} > 0$) peak with two negative signals of different strengths. The peak at higher magnetic field (lower g value) corresponds to PC₆₀BM⁻, whilst the peak at lower magnetic field (higher g value) corresponds to the positive polaron PTB7-Th⁺ and PM6⁺, respectively. The blends also show a contribution of PC₆₀BM T₁ in the FF spectrum, implying undissociated charge carriers in fullerene rich domains.

1500 MHz and $E/h = 70$ MHz. This polymer also shows a preferential orientation of the molecules, whereby a reduced ordering of $\lambda_{\Theta} = 5.5$ is observed in contrast to PTB7-Th. When blending PM6 with PC₆₀BM (Figure 8.2, dark blue), the broader polymer triplet is again clearly visible in the FF and HF signals. Thereby, the PM6 T₁ ZFS parameters remain the same before and after blending with PC₆₀BM and the ordering factors reduces only slightly to $\lambda_{\Theta} = 5.0$. This is in clear contrast to PTB7-Th:PC₆₀BM, where the ZFS parameters and ordering factors of PTB7-Th change significantly upon blending. Thus, the ordering of the polymer chains in PM6 is less disrupted upon mixing with PC₆₀BM, when compared to PTB7-Th. As the previous blend, the PLDMR spectrum shows a positive CT peak with two negative signals at $g = 2.0012$ and $g = 2.0034$, displayed enlarged in Figure 8.3 (right). The lower g value is again identical to the negative polaron PC₆₀BM⁻, whilst the higher g value is similar to PTB7-Th⁺ and most likely represents the positive polaron PM6⁺ on the PM6 (PC₆₀BM⁻ marked as "-" and PM6⁺ marked as "+").^[253]

Detecting Minor Triplet Formation Pathway on PC₆₀BM

Minor triplet channels are difficult to detect even with triplet sensitive measurements. However, the high experimental sensitivity of PLDMR enables to resolve a weak PC₆₀BM T₁ contribution in the HF signal at 168.1 mT for both blends PTB7-Th:PC₆₀BM and PM6:PC₆₀BM (Figure 8.2). Additionally, the enlarged PLDMR spectra in Figure 8.3 show a contribution of PC₆₀BM T₁ in the FF region (320–350 mT), as also verified by EasySpin simulations (see Table 10.4 in Appendix). Thus, without PLDMR, minority T₁ generation pathways could easily be missed. When considering the formation mechanism for

PC₆₀BM T₁ states in the blends, they are energetically too high ($E_{T_1} \approx 1.5$ eV) to be populated by BCT from the CT states, especially in these low band gap polymer:fullerene systems with large S₁ – CT energetic offset to the acceptor.^[241] Furthermore, as the PC₆₀BM T₁ will be higher in energy than the T₁ states of PM6 and PTB7-Th, any PC₆₀BM T₁ states formed near the donor:acceptor interface would be expected to relax into the lower lying polymer T₁ states or ³CT states.^[245] However, fullerene rich domains or agglomerates are often found in polymer:fullerene bulk heterojunction blends.^[252,254] Thus, the PC₆₀BM T₁ states observed must be located in isolated PC₆₀BM domains and populated by S₁ states not reaching the donor:acceptor interface. This observation reinforces the importance of ensuring that domain sizes are on the order of the exciton diffusion length to enable efficient charge generation and suppress T₁ formation via direct SOC-induced ISC from undissociated S₁ states.^[255]

8.2.2 Transient Electron Paramagnetic Resonance

While PLDMR is an extremely sensitive method to detect all present triplet excitons, it has its limitations in differentiating between T₁ triplet formation mechanisms. In contrast, trEPR is not employed as a steady-state technique but instead uses short laser pulses to generate characteristic spin polarization on the triplet sublevels. trEPR typically has time resolutions in the order of hundreds of nanoseconds and can probe spin polarizations up to several microseconds.^[51,256] Thereby, trEPR is as PLDMR sensitive to all states with unpaired spins, including molecular T₁ states, spin-correlated radical pairs (or CT states), and free charge carriers.^[47,189,233] The spin polarization of trEPR signals additionally provides information about the formation of geminate T₁ states, i.e., SOC-induced ISC and geminate BCT (pathways in Figure 8.1a and b).^[51,256] As already explained in ch. 3.3.2 and in the previous chapter, direct ISC mediated by SOC from S₁ states result in a spin-selective population of the zero-field triplet sublevels $|X\rangle$, $|Y\rangle$ and $|Z\rangle$, manifesting as a characteristic polarization pattern of *aaaeee*, *eeea*, *eeaeaa*, *aaeae*, *aeaeae* or *eaeaea* when probing the high-field triplet levels $|T_{-}\rangle$, $|T_0\rangle$ and $|T_{+}\rangle$. In contrast to that, geminate BCT from ³CT to T₁ states, which has not been visible in the NFA-based blends in the previous chapter, is obtained by selective population of the high-field spin states and results in a characteristic pattern of *aeaeae* or *eaeeae* (see ch. 3.3.3).

Contrary to PLDMR, non-geminate recombination does not produce spin polarization high enough to be measured in trEPR. The spin-statistical recombination of uncorrelated free charge carriers to T₁ via ³CT first results in an equal population of the $|T_{-}\rangle$, $|T_0\rangle$ and $|T_{+}\rangle$ sublevel. The equal population will rearrange in a Boltzmann distribution within the spin-lattice relaxation time, but in the low-field (~ 330 mT) regime,

as explored here with X-band EPR, the established spin polarization is too low for the reduced sensitivity of microwave detection.^[52]

To access the pathways of geminate triplet excitons present in the studied polymer: fullerene blends, Figure 8.4 and Figure 8.5 display the trEPR spectra for PM6:PC₆₀BM and PTB7-Th:PC₆₀BM, respectively, with EasySpin parameters given in Table 10.5 of the Appendix. Thereby, the spectra are obtained at 1 μ s and 5 μ s after the laser pulse to account for the time-dependent changes in spin polarization.

trEPR of PM6:PC₆₀BM

The trEPR spectrum of PM6:PC₆₀BM at 1 μ s (Figure 8.4a) shows a clear response of the blend to resonance conditions between 290 – 400 mT (trEPR spectra shifted in contrast to PLDMR spectra in Figure 8.2 due to the use of a cavity with a different microwave resonant frequency ν_{MW}). Here, the ZFS parameters $D/h = 1300$ MHz and $E/h = 140$ MHz are comparable to neat PM6 (Table 10.5) and the ZFS parameters obtained from PLDMR measurements, assigning this feature to the T₁ states of PM6. The minor differences in D values between the two magnetic resonance techniques are addressed below. In contrast to PLDMR, the minor pathway of the PC₆₀BM T₁ states is not observed in trEPR spectra owing to the lower sensitivity of this method, as also

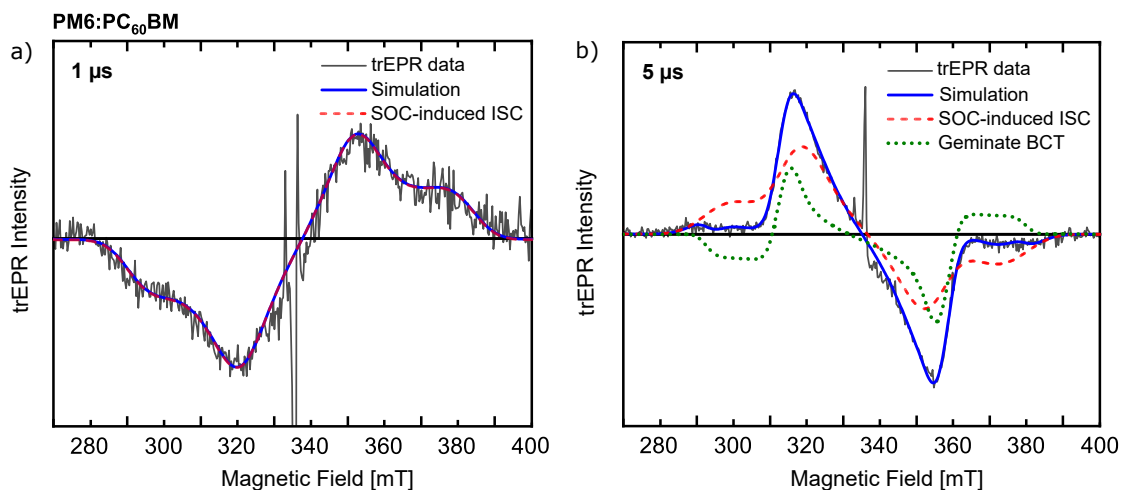


Figure 8.4: trEPR spectra of PM6:PC₆₀BM blends studied. a) trEPR spectrum at 1 μ s. PM6 T₁ feature visible between 290–400 mT with a single *eeeeea* component (red dashed line, equal to overall simulation), indicating T₁ formation via direct ISC from undissociated S₁ states. The central *aeae* feature is assigned to CT states. b) trEPR spectrum at 5 μ s. The PM6 T₁ feature possesses two contributions: First, a component with *aeaeae* pattern, representing the inverted ISC contribution from the 1 μ s spectrum (red dashed line). Second, a component with *eaeeea* pattern, characteristic of T₁ states formed via geminate BCT (green dotted line). All trEPR spectra were acquired at $T = 80$ K and excitation of 532 nm. Measurements and evaluation performed by A. Privitera.

discussed below. However, trEPR can derive the formation pathways of the occupied PM6 T_1 states: Spectral simulations of the T_1 triplet signal yield a ZFS population of $[p_x, p_y, p_z]_{1\mu s} = [0.14, 0.52, 0.34]$, corresponding to an *eeaaaa* polarization pattern (red dashed line in Figure 8.4a). This spin polarization can be attributed to photogenerated S_1 states that do not reach the donor:acceptor interface but instead undergo SOC-induced ISC to the PM6 T_1 state. In addition, the spectrum shows an intense, spectrally narrow central feature ($B \approx 346$ mT) with an *aeae* polarization corresponding to CT states in the blend (see ch. 3.3.3).

Figure 8.4b shows the trEPR spectrum of PM6:PC₆₀BM at 5 μ s after the laser pulse. A clear evolution of the polarization pattern can be observed, with the structure becoming more complex. The ZFS parameters of $D/h = 1220$ MHz and $E/h = 40$ MHz still correspond to T_1 on PM6. However, in addition to the SOC-induced ISC visible at 1 μ s, there is an additional contribution from geminate BCT as frequently observed in polymer:fullerene blends.^[189] The contribution of SOC-induced ISC changes the ZFS population to $[p_x, p_y, p_z]_{5\mu s} = [0.39, 0.20, 0.41]$ at 5 μ s, corresponding to an *aeae* polarization pattern (red dashed line in Figure 8.4b). This spectral inversion in contrast to 1 μ s can be attributed to an unequal decay rate of the three high-field triplet sublevels.^[49,257] However, a reliable fit can only be obtained with an additional polarization pattern (green dotted line in Figure 8.4b). This result can be attributed to the population of PM6 T_1 -states by geminate BCT and thus contrasts with the NFA-based donor:acceptor blends from the previous chapter, as described below. Similar to 1 μ s, the trEPR spectrum at 5 μ s shows an intense and narrow central peak, whereby the pure absorption feature indicates free charges absorbing microwaves.^[256]

trEPR of PTB7-Th:PC₆₀BM

Turning to the polymer PTB7-Th, Figure 8.5a and b show the trEPR spectra of PTB7-Th:PC₆₀BM at 1 μ s and 5 μ s after laser pulse with triplet signals between 300 – 390 mT. The T_1 ZFS parameters $D/h = 1050$ MHz and $E/h = 200$ MHz are consistent with the neat PTB7-Th (Table 10.5) and comparable to values obtained from PLDMR, with deviations discussed below. Hence, this feature is also attributable to the T_1 states on the polymer. Both trEPR spectra cannot be well described by a SOC-induced ISC contribution only, requiring the consideration of geminate BCT. Therefore, both spectra are simulated with two species: The first contribution is described by SOC-induced ISC with similar ZFS population of $[p_x, p_y, p_z]_{1\mu s} = [0.37, 0.33, 0.30]$ and $[p_x, p_y, p_z]_{5\mu s} = [0.35, 0.33, 0.32]$, corresponding to an *aaaeee* polarization pattern (red dashed lines in Figure 8.5). The second contribution with an *eaaeaa* polarization pattern confirms the presence of geminate BCT in the T_1 formation pathways in PTB7-Th:PC₆₀BM (green

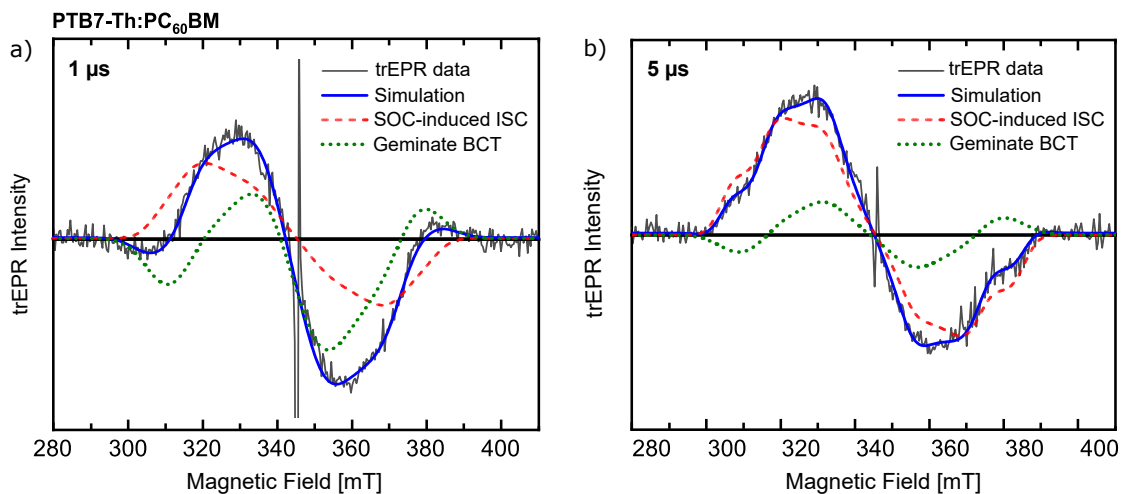


Figure 8.5: trEPR spectra of PTB7-Th:PC₆₀BM blends studied. a) trEPR spectrum at 1 μ s. The PTB7-Th T₁ feature visible between 300 – 390 mT with two contributions: First, a component with *aaaaee* pattern, indicating T₁ formation via direct ISC from undissociated S₁ states (red dashed line). Second, a component with *eaaeaa* pattern, characteristic of T₁ states formed via geminate BCT (green dotted line). The central *ae* feature is assigned to CT states. b) trEPR spectrum at 5 μ s. PTB7-Th T₁ feature possesses the same two contributions: First component with *aeaeae* pattern from ISC to T₁ states (red dashed line), second component with *eaaeaa* pattern from T₁ states formed via geminate BCT (green dotted line). All trEPR spectra were acquired at 80 K and excitation of 532 nm. Measurements and evaluation performed by A. Privitera.

dotted line in Figure 8.5). In addition, both trEPR spectra exhibit a strong, narrow central peak with *ea* feature associated with CT states.^[256]

Comparing the trEPR spectra of the fullerene-based blends, geminate BCT is found to occur in PTB7-Th:PC₆₀BM at both 1 μ s and 5 μ s. In contrast, in PM6:PC₆₀BM, this pathway is observed only at 5 μ s, whereby simultaneously the CT states visible at 1 μ s turn into free charges by 5 μ s. Since the spin mixing between $|^1\text{CT}\rangle$ and $|^3\text{CT}_0\rangle$ of the SCRPs occurs on timescales of tens of nanoseconds, faster than the time resolution of the trEPR measurements, the observed CT states can be considered as an admixture of both states. The eventual appearance of free charges in PM6:PC₆₀BM suggests that the CT states are on average more weakly bound than in PTB7-Th:PC₆₀BM. Figure 8.3 already showed that the polaron signals (positive and negative free charges) in PLDMR are much more intense in PM6:PC₆₀BM in contrast to PTB7-Th:PC₆₀BM, indicating a larger fraction of electrons and holes are far enough apart to no longer interact magnetically. The geminate BCT rate strongly decreases with electron-hole distance, while more separated charge carriers are also expected to reach the donor-acceptor interface less frequently. Thus, more weakly bound CT states with larger average electron-hole separation can result in a slower geminate BCT process in PM6:PC₆₀BM.

Comparison of Fullerene- and NFA-based OSC Systems

The NFA-based OSC systems studied in the previous chapter only exhibited SOC-induced ISC to T_1 states as geminate formation pathways. Conversely, the described trEPR measurements reveal the presence of T_1 states occupied by geminate BCT in fullerene-based OSC blends, as also reported in literature.^[47,189,233,235] The PLDMR measurements already suggested intercalation of fullerene molecules within the alkyl side chains of the donor polymer, resulting in mixed polymer/fullerene regions.^[254,258–261] In addition, PLDMR revealed local fullerene domains, which are known to increase solar cell efficiency by driving charge separation in the mixed regions to pure fullerene domains.^[254,262,263] However, if the fullerene concentration in these mixed regions falls below the percolation threshold for efficient electron transport, charge separation is hindered and geminate recombination will result.^[262–265] Therefore, poorly-connected fullerene domains provide the possibility for geminate 3CT formation from 1CT states on nanosecond timescales, followed by BCT to T_1 states.^[266,267] In contrast, many efficient NFA OSCs have been shown to possess good phase purity, which has previously been shown to facilitate CT state dissociation and reduce BCT T_1 formation.^[205,268–270] Thus, the engineering of good phase purity in the donor:acceptor bulk heterojunction appears to be beneficial for reducing BCT T_1 generation pathways in OSCs.

8.2.3 Transient Absorption Spectroscopy

Analysis of trEPR spectra enables the distinction between geminate T_1 formation pathways, i.e., SOC-induced ISCs and geminate BCT. To also explore T_1 formation via non-geminate BCT (pathways in Figure 8.1c), TA spectroscopy is a valuable method that is widely employed to study photophysical processes in OSCs.^[49,186,190,271] In contrast to the other two methods described, TA is not intended to manipulate paramagnetic spin states, but instead provides insight into the evolution of optically bright and dark states on time scales from femtoseconds to milliseconds. Therefore, TA is also well suited to probe optically dark T_1 states in OSC, i.e., by using photoinduced absorption (PIA) signatures (see Figure 7.3) typically located in the near-infrared (NIR), as a unique fingerprint for the presence and localization of these states on the respective molecules.^[49,63,180,190,234]

Theoretically, TA can distinguish between the presence of T_1 formation pathways by direct ISC and geminate BCT (i.e., monomolecular processes), and non-geminate BCT (i.e., bimolecular processes). While monomolecular T_1 generation pathways ex-

hibit no fluence dependence on the optical excitation power, bimolecular events show strong fluence dependence.^[49,63,190] However, in the presence of significant bimolecular pathways, i.e., non-geminate BCT, the fluence dependent T_1 formation dominates the monomolecular processes, making the latter invisible. Nevertheless, many fullerene- and NFA-based OSCs possess a dominant amount of non-geminate BCT (as discussed in the previous chapter), making TA an important technique to reliably detect the presence of this process.^[49,63,180,190,234]

TA of PM6:PC₆₀BM

Figure 8.6a presents the time-dependent TA spectra of PM6:PC₆₀BM in the NIR region up to 1800 ps after photoexcitation at 600 nm. At 0.2 – 0.3 ps, the TA spectra show a PIA feature centered around 1175 nm which decays on picosecond timescales. Since this PIA feature is also observed in neat PM6 films, it can be attributed to S_1 states in PM6. The rapid quenching of this S_1 PIA signal indicates ultrafast electron transfer to the acceptor PC₆₀BM. Within hundreds of picoseconds, the TA spectra show the formation of a new PIA band between 1500 and 1650 nm. This feature can be attributed to photo-induced absorption of formed T_1 on these timescales. Since the T_1 PIA signature for PC₆₀BM is found at 720 nm, this PIA feature can be assigned to T_1 states on the donor PM6.^[272,273]

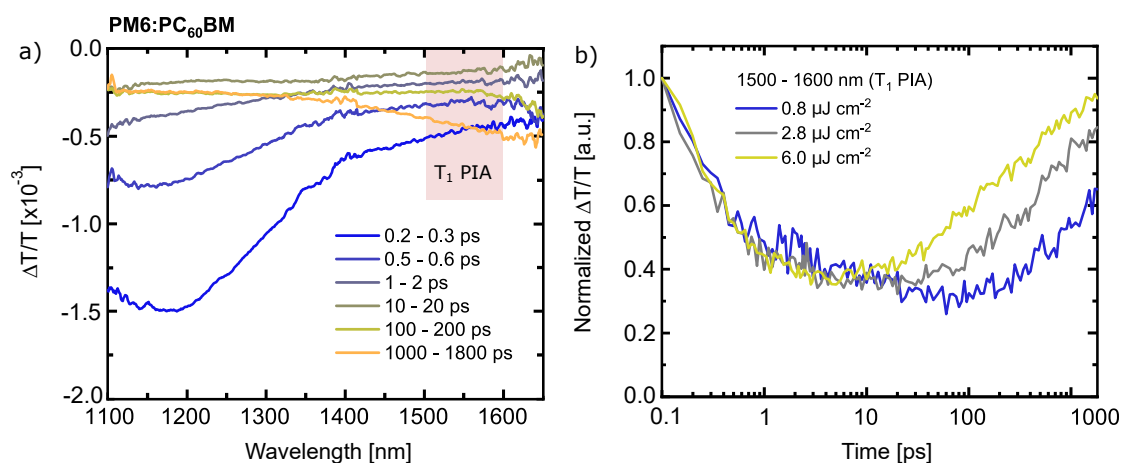


Figure 8.6: TA spectroscopy of PM6:PC₆₀BM. a) Time-dependent TA spectra in the NIR region after photoexcitation at 600 nm with a fluence of $2.8 \mu\text{J cm}^{-2}$. At early timescales, PM6 S_1 PIA is centered at at 1175 nm, decaying within picoseconds due to electron transfer. At hundreds of picoseconds, formation of a new PIA band between 1500 – 1650 nm indicates recombination into PM6 T_1 states. b) TA kinetics extracted between 1500 – 1650 nm for different fluences. The fluence dependence of the T_1 PIA reveals T_1 formation via bimolecular recombination, i.e., non-geminate BCT. Measurements and evaluation performed by A. J. Gillett.

To investigate whether these T_1 states are populated by bimolecular recombination, i.e., non-geminate BCT, Figure 8.6b depicts the kinetics between 1500 – 1600 nm (T_1 PIA) for three different fluences of $0.8 \mu\text{J cm}^{-2}$, $2.8 \mu\text{J cm}^{-2}$, and $6.0 \mu\text{J cm}^{-2}$. The formation of this PM6 T_1 PIA signature shows a strong fluence dependence, indicating that non-geminate BCT plays a large part in PM6 triplet population. Combined with the results of magnetic resonance techniques, a full picture of T_1 formation pathways, including SOC-induced ISC, geminate BCT, and non-geminate BCT, can be drawn for PM6:PC₆₀BM blends.

As already addressed in the previous chapters, triplet-polaron annihilation (TPA), also often called triplet-charge annihilation (TCA), is a central bimolecular process in OSC.^[49,135,173] It is a primary non-radiative quenching pathway of T_1 and thus, directly responsible for increased non-radiative voltage loss ΔV_{nr} in OSCs with significant T_1 formation.^[49,179,235] The TA spectra show that the rise in T_1 PIA begins to flatten out towards $2 \mu\text{s}$ in the highest fluence measurement of $6.0 \mu\text{J cm}^{-2}$, attributable to a competing impact of TPA. This effect is especially expected to be more pronounced under higher excitation fluences in the sub-nanosecond range, since the TPA rate depends on the charge carrier density and mobility in the film.^[49,63,190]

TA of PTB7-Th:PC₆₀BM

Having verified the bimolecular formation process in PM6:PC₆₀BM, we can now address the eventual appearance of non-geminate BCT in the second blend PTB7-Th:PC₆₀BM. Figure 8.7a shows the time-dependent TA spectra of PTB7-Th:PC₆₀BM in the NIR region up to 1900 ps after photoexcitation at 700 nm. The TA spectra show two PIA signatures at 0.1 – 0.15 ps: One PIA feature peaking at 1125 nm and one broader PIA band extending towards 1450 nm. Since this also occurs in neat donor PTB7-Th films^[26], it can be attributed to S_1 states on the PTB7-Th. As in PM6:PC₆₀BM, the rapid quenching of the PTB7-Th S_1 PIA within picoseconds indicates ultrafast electron transfer from the polymer to the fullerene. The earlier PIA signature at 1125 nm can be attributed to formed hole polarons located on the PTB7-Th.^[274]

In contrast to PM6:PC₆₀BM, the T_1 formation here is noticeable by a broadening of the low energy edge of the hole polaron PIA (1250 – 1300 nm), which increases within hundreds of picoseconds. Figure 8.7b shows the kinetics, extracted between 1250 – 1300 nm, for different fluences ($0.6 \mu\text{J cm}^{-2}$, $1.2 \mu\text{J cm}^{-2}$ and $3.6 \mu\text{J cm}^{-2}$). The clearly visible fluence dependence for later timescales indicates a bimolecular formation mechanism. This result suggests that the extracted signature corresponds to the PIA of PTB7-Th T_1 states, which is consistent with literature reports, and overlaps with the PIA of hole polarons.^[274]

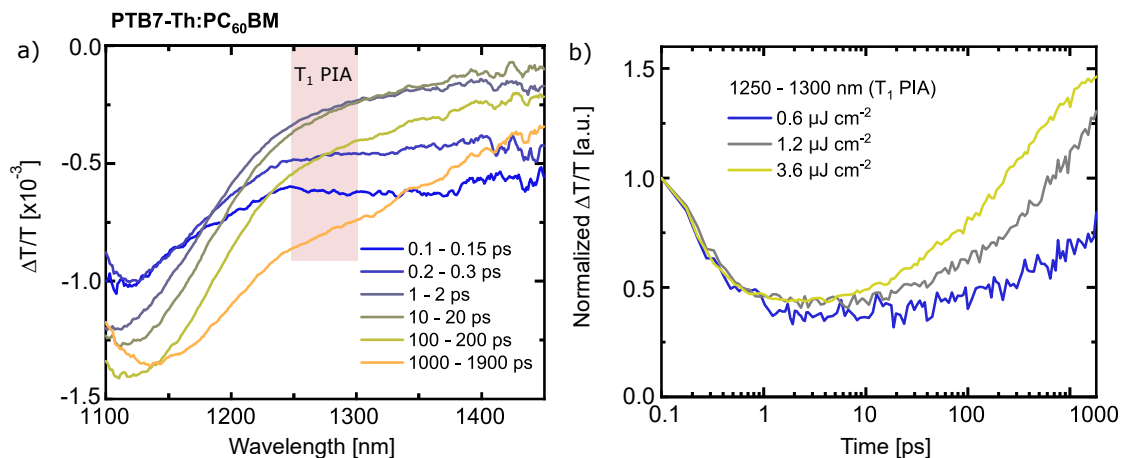


Figure 8.7: TA spectroscopy of PTB7-Th:PC₆₀BM blend studied. a) Time-dependent TA spectra in the NIR region after photoexcitation at 700 nm with a fluence of $3.6 \mu\text{J cm}^{-2}$. The PTB7-Th S_1 PIA band around 1400 nm decays within the first picoseconds due to electron transfer to PC₆₀BM, leaving behind the PTB7-Th hole polaron PIA at 1125 nm. Over hundreds of picoseconds, a new PIA band on the low energy edge of the hole polaron around 1300 nm begins to grow in, indicating recombination into PTB7-Th T_1 states. b) TA kinetics extracted between 1250 – 1300 nm for different fluences. The fluence dependence of the T_1 PIA region growth shows that T_1 formation occurs following the bimolecular recombination of free charge carriers. All TA measurements were performed at $T = 293\text{ K}$. Measurements and evaluation performed by A. J. Gillett.

8.3 Complementarity of PLDMR, trEPR and TA

The analysis showed that by leveraging the strengths of the three techniques, a complete picture of T_1 -formation pathways in OSCs can be obtained, which are summarized in Table 8.1. The following section discusses concluding the complementarity and important differences of the three techniques presented by comparing their individual characteristics.

Beginning with a comparison of the magnetic resonance techniques, both PLDMR and trEPR provide a direct way for the study of T_1 states. Both methods are typically performed at cryogenic temperatures to slow exciton kinetics and enhance spin polarization. In trEPR, sample excitation is provided by nanosecond laser pulses, giving the technique, depending on the Q factor of the resonator (see ch. 4.3.1), a time resolution of hundreds of nanoseconds up to microseconds. In contrast, PLDMR is based on continuous optical excitation, enabling only steady-state populations to be probed. While trEPR produces a characteristic spin polarization on the T_1 states after the short laser pulse, allowing to distinguish between population mechanisms, the T_1 formation pathways in PLDMR cannot be easily resolved. However, the higher energy of optical

photons compared to microwave photons allows for higher sensitivity of optical detection, making PLDMR sensitive to all T_1 states that are coupled to luminescence, including minor pathways.^[247] Additionally, steady-state conditions can enhance spin polarization on the T_1 state due to unequal recombination rates or accumulation, leading to annihilation effects such as TTA. The resulting exceptional sensitivity of this method thus allows the detection of usually low spin polarized pathways, such as non-geminate BCT.

The comparison between PLDMR spectra and trEPR spectra showed slight differences in the ordering and ZFS parameters. The reason being that trEPR studies all (highly) spin-polarized triplet states via detection of microwave absorption and emission, while PLDMR studies only the triplet states associated with luminescence, e.g. via TTA or (reverse) ISC.^[139,153] The higher ordering parameter in PLDMR suggests that the PLDMR signal primarily stems from ordered (crystalline) polymer domains, where TTA is efficient^[207,208], rather than from amorphous domains, which are also probed by trEPR. The same effect is visible upon mixing PTB7-Th with PC₆₀BM: while PLDMR shows an extreme change in order and ZFS parameters upon blending, trEPR exhibits only minor changes, allowing the conclusion that crystalline domains are most affected when mixed with PC₆₀BM.

In order to reliably assign bimolecular processes, TA spectroscopy is a valuable technique. Since this ultrafast optical spectroscopy method is not dependent on spin polarization, its strength lies here in the detection of non-geminate BCT and is able to assign this process by fluence-dependent measurements. TA spectroscopy can track the formation of T_1 with excellent time resolution from femtoseconds to milliseconds, allowing the study of photophysical processes up to room temperature. As a result, this method is most comparable to real devices, in contrast to magnetic resonance, which is performed at cryogenic temperatures. The combination of all three spin-sensitive measurement techniques provides a detailed insight into the exciton pathways in fullerene-based blends (Table 8.1): While TA detects non-geminate BCT in both fullerene blends, trEPR detects SOC-induced ISC and BCT of geminate triplet excitons. PLDMR confirms triplet excitons produced by all three pathways due to its high sensitivity, while additionally detecting minor PC₆₀BM pathways. All three measurement methods confirmed that the long-lived triplet states are formed on the polymer by determining PIAs, ZFS parameters, or positions of HF signals. Given the energy difference to CT states, these polymer triplet states are unable to contribute to the device performance, increasing the crucial voltage loss and presenting a target for device degradation.

Table 8.1: Summary of T_1 formation pathways detected by each technique in PM6:PC₆₀BM and PBT7-Th:PC₆₀BM. While PLDMR detects T_1 states by all formation pathways, trEPR can distinguish between geminate pathways, i.e., geminate BCT and SOC-induced ISC. TA confirms the presence of non-geminate BCT. All techniques identify T_1 states on the donor (D), while PLDMR detects also weak signatures of T_1 states on the acceptor (A). ZFS parameters are given for trEPR and PLDMR for the dominant donor triplet signal.

Blend	Non-geminate BCT	Geminate BCT	SOC-induced ISC	D/h, E/h [MHz]	T_1 location
PM6:PC ₆₀ BM	TA	-	trEPR (1 μ s)	1300, 140	D
		trEPR (5 μ s)	trEPR (5 μ s)	1220, 40	
	PLDMR			1500, 70	D, A (weak)
PTB7-Th:PC ₆₀ BM	TA	trEPR (1 μ s)	trEPR (1 μ s)	1050, 200	D
		trEPR (5 μ s)	trEPR (5 μ s)	1143, 164	
	PLDMR			1470, 180	D, A (weak)

8.4 Conclusion

This chapter showed that the application of the complementary techniques of PLDMR, trEPR, and TA spectroscopy can generate a complete picture of triplet T_1 formation pathways in OSCs. By applying this approach to two fullerene-based OSC model systems, the ability to unravel the role of triplet states in OSCs has been demonstrated by identifying both, the molecular localization and the formation mechanism for the broad spectrum of T_1 states in these systems. Thus, in addition to exhibiting the non-geminate pathway and SOC-induced ISC to T_1 states, the measurements have shown that fullerene-based blends frequently exhibit also the geminate BCT mechanism.^[47,235] This is in clear contrast to the more efficient NFA-based OSC systems from the previous chapter, whose geminate BCT pathway appears to be absent, consistent with their improved performance.^[49] The geminate BCT mechanism is thereby attributed to isolated fullerene molecules trapped in the alkyl side chains of the donor polymers, suggesting that good purity of the donor and acceptor phases is key to suppressing this process.^[254,258,259,261] The previous and this chapter have shown that the presented experimental framework is applicable to both fullerene and NFA blends and will be valuable for the future research task of engineering out recombination pathways via T_1 states in OSCs.

8.5 Additional Information

Contribution to this chapter

This chapter is based on a collaborative work: A. J. Gillett¹ performed and evaluated the TA measurements (section 8.2.3, Figure 8.6, Figure 8.7). A. Privitera^{2,3} and W. K. Mayers⁴ conducted, evaluated and fitted the trEPR measurements (section 8.2.2, Figure 8.4, Figure 8.5). The samples for TA and magnetic resonance measurements were prepared by A. J. Gillett¹. The TA measurements were performed in the Cavendish Laboratory at the University of Cambridge, the setup specifics can be found in the Experimentals (ch. 4.3.5). The trEPR measurements were performed at the Centre for Advanced ESR at the University of Oxford. The setup principle is comparable to trEPR setup given in the Experimentals (ch. 4.3.1) with specific components given in Ref. [26].

¹Cavendish Laboratory, University of Cambridge, JJ Thomson Avenue, Cambridge, UK

²Clarendon Laboratory, University of Oxford, Parks Road, Oxford, UK

³Department of Chemistry, University of Torino, Via Giuria, Torino, IT

⁴Centre for Advanced ESR, Inorganic Chemistry Laboratory, University of Oxford, South Parks Road, Oxford, UK

Copyright Clearance

Content in this chapter is adapted from 'Privitera, A., Grüne, J., Karki, A., Myers, W. K., Dyakonov, V., Nguyen, T.-Q., Riede, M. K., Friend, R. H., Sperlich, A., Gillett, A. J., Geminat and Nongeminate Pathways for Triplet Exciton Formation in Organic Solar Cells. *Adv. Energy Mater.* 2022, 2103944. <https://doi.org/10.1002/aenm.202103944>'. Published under the terms of the Creative Commons CC BY license. Copyright 2022. Advanced Energy Materials published by Wiley-VCH GmbH.

9 Summary

The present thesis addressed the identification and characterization of spin states in optoelectronic materials and devices using multiple spin-sensitive techniques. For this purpose, a systematic study with focus on triplet states as well as associated loss pathways and excited state kinetics was carried out. The research was based on comparing a range of donor:acceptor systems, reaching from organic light emitting diodes (OLEDs) based on thermally activated delayed fluorescence (TADF) to organic photovoltaics (OPV) employing fullerene and multiple non-fullerene acceptors (NFAs). By developing new strategies, e.g., appropriate modeling, new magnetic resonance techniques and experimental frameworks, the influence of spin states in the fundamental processes of organic semiconductors could be investigated. Thereby, the combination of techniques based on the principle of electron paramagnetic resonance (EPR), in particular transient EPR (trEPR) and optically detected magnetic resonance (ODMR), with all-optical methods, such as transient electroluminescence (trEL) and transient absorption (TA), have been employed. As a result, excited spin states, in particular molecular and charge transfer (CT) states, were investigated in terms of kinetic behavior and associated pathways, which revealed a significant impact of triplet states on efficiency-limiting processes in both optoelectronic applications.

First, the characterization of the excited state kinetics in exciplex-based OLEDs was carried out by trEL on the model system of m-MTDATA:3TPYMB. For the analysis, a new suitable kinetic model for electrically driven TADF OLEDs including second order effects was developed. This model is especially useful for trEL on exciplex-based TADF OLEDs, as the non-absorbing exciplex states render the rates extraction in trPL infeasible and the higher triplet density in electrical excitation additionally enhances the probability of annihilation effects. A suitable fit procedure was developed for the application of this kinetic model to investigate the influence of efficiency-limiting effects in operational OLEDs, whereby a thorough analysis revealed triplet-triplet annihilation (TTA) to be the dominant second-order effect. Remarkably, TTA accounts for a significant part to triplet depopulation in these exciplex-based TADF OLEDs as a result of a moderate reverse intersystem crossing (RISC) rate and high triplet density, leading to TTA depopulating the triplet states by 50% at room temperature. Since TTA is a less efficient triplet harvesting mechanism in contrast to the TADF characteristic RISC process, these results revealed an important efficiency-limiting loss channel.

To get a deeper insight into the role of the triplet states in donor:acceptor systems, magnetic resonant conditions were applied. Therefore, a technique of transient optically detected magnetic resonance (trODMR) was developed, presenting a spectral and time-resolved method that directly probes spin-states associated with photoluminescence (trPLDMR) or electroluminescence (trELDMR). The advantages of the technique lie in the direct PL or EL detection and additional temporal component in contrast to continuous-wave (cw) ODMR application, allowing to precisely determine the different signals' spectral contributions with absolute sign and amplitude. Noteworthy, the previously investigated electrically driven devices revealed significant differences in intermediate triplet states in comparison to optically excited thin films. Optical excitation must therefore be treated with special caution, since additional spin states could be studied, although the emitting final state may be identical in devices and thin films. Thereby, this method has proven its usefulness in donor:acceptor systems not only on TADF-based OLEDs and thin films, but also on OPV materials employing state-of-the-art NFAs, where the involvement of even molecular triplet excitons in luminescence has been evidenced.

To extend the studies on OPV systems, further spin-sensitive techniques, in particular cwPLDMR and trEPR, corroborated with TA measurements, have been applied to provide a strong insight into molecular triplet states and associated efficiency-limiting processes. These complementary methods were applied on the one hand to state-of-the-art donor:acceptor combinations employing (non-) halogenated donors PBDB-T, PM6 and PM7 and acceptors Y6 and Y7 to identify long-lived triplet states and their generation pathways to the NFA in all blends. Thereby, the major contributions evidenced in all blends was hole back transfer (HBT) from CT states, formed via non-geminate recombination of free charge carriers. Remarkably, the blends with best performing halogenated donors also yielded a geminate triplet pathway by spin-orbit coupling (SOC) induced intersystem crossing (ISC). Regarding the impact of halogenation on excited state kinetics, in particular the competing singlet depopulating ISC and hole transfer (HT) rates, shifting HOMO levels or heavier halogen atoms were determined to have a minor influence. However, increased ISC yield with halogenated donors indicate incomplete charge carrier generation in these blends, suggesting an adverse impact of domain aggregation. Thus, halogenation of OPV materials may show better device performance but not avoid or eventually even enhances triplet generation.

To compare state-of-the-art NFA acceptors with traditionally used fullerene acceptors, the spin-sensitive methods were additionally applied to fullerene-based OSCs, PTB7-Th:PCBM and PM6:PCBM. Furthermore, the focus was concluding on the complementarity of the spin-sensitive methods PLDMR, trEPR and TA, as each of these

methods is suitable for investigating a specific (sub)set of triplet formation pathways. While PLDMR is able to detect all triplet states with high sensitivity, including minor triplet pathways, trEPR reveals spin dynamics of geminate pathways. TA pursues the experimental framework through assigning non-geminate back charge transfer (BCT), giving the opportunity to disentangle all present pathways in OPV materials. Consequently, geminate BCT could be identified and assigned in fullerene-based blends in addition to the non-geminate pathway and SOC-induced ISC, standing in clear contrast to better performing NFA-based blends. The presence of this geminate BCT is suggested to be caused by isolated fullerene molecules trapped in the alkyl side chains of the donor polymer.

The results of the fullerene- and NFA-based studies both indicate that, in addition to photophysical properties, morphology plays an important role, whereby good purity of the donor and acceptor phases in the diffusion length exciton size could reduce or even suppress triplet loss processes. Furthermore, they pay attention that the future research goal should lie in preventing the triplet formation pathways in state-of-the-art donor:acceptor combinations to make a sizable efficiency step in plateauing OSC efficiencies.

To conclude, this thesis contributed to the deeper understanding of optoelectronic materials and devices by investigating involved spin states, excited state kinetics and associated efficiency-limiting pathways. The extensive studies on different materials and devices for application in OLEDs and OPVs revealed the necessity for both systems to prevent the identified loss processes, especially represented by accumulation or formation of triplet excitons. The powerful toolbox of spin-sensitive techniques and evaluation methods developed in this thesis was thereby able to provide an insight and solution approaches to the important future research goal of increasing the efficiency of organic optoelectronic devices.

Zusammenfassung

Die vorliegende Arbeit befasste sich mit der Identifizierung und Charakterisierung von Spinzuständen in optoelektronischen Materialien und Bauelementen unter Verwendung mehrerer spinsensitiver Techniken. Dazu wurde eine systematische Studie mit Schwerpunkt auf Triplet-Zuständen sowie den damit verbundenen Verlustpfaden und der Kinetik der zugehörigen angeregten Zustände durchgeführt. Der Schwerpunkt lag auf dem Vergleich einer Reihe von Donor:Akzeptor-Systemen, die von organischen Leuchtdioden (engl. *organic light emitting diodes*, OLEDs), basierend auf thermisch aktivierter verzögerter Fluoreszenz (engl. *thermally activated delayed fluorescence*, TADF), bis hin zu organischer Photovoltaik (OPV), unter Verwendung von Fulleren und mehreren Nicht-Fulleren Akzeptoren (NFAs), reichten. Durch die Entwicklung neuer Strategien, z.B. adäquater Modellierung, neuer Techniken im Bereich der Magnetresonanz und experimenteller Konzepte, konnte der Einfluss von Spinzuständen auf die grundlegenden Prozesse organischer Halbleiter untersucht werden. Dabei wurden Techniken, die auf dem Prinzip der Elektronenspinresonanz (engl. *electron paramagnetic resonance*, EPR) basieren, insbesondere transientes EPR (trEPR) und optisch detektierte Magnetresonanz (ODMR), mit rein optischen Methoden, wie transienter Elektrolumineszenz (trEL) und transienter Absorption (TA), kombiniert. Resultierend wurden angeregte Spinzustände, insbesondere molekulare und Ladungstransfer (engl. *charge transfer*, CT) Zustände, im Hinblick auf das kinetische Verhalten und assoziierten Exzitonpfaden untersucht, wobei ein bedeutender Einfluss von Triplet-Zuständen auf effizienzlimitierende Prozesse in beiden optoelektronischen Anwendungen aufgezeigt wurde.

Zunächst wurde die Kinetik der angeregten Zustände in Exciplex-basierten OLEDs anhand trEL am Modellsystem m-MTDATA:3TPYMB charakterisiert. Für die Analyse wurde ein neues kinetisches Modell für elektrisch betriebene TADF-OLEDs entwickelt, das Effekte zweiter Ordnung berücksichtigt. Dieses Modell ist besonders nützlich für trEL an Exciplex-basierten TADF-OLEDs, da die nicht absorbierenden Exciplex-Zustände die Ratenextraktion in trPL unpraktikabel machen und die höhere Triplettdichte bei elektrischer Anregung zusätzlich die Wahrscheinlichkeit von Annihilationseffekten erhöht. Für die Anwendung dieses kinetischen Modells wurde ein geeignetes Fit-Verfahren entwickelt, um den Einfluss von effizienzlimitierenden Effekten in betriebsfähigen OLEDs zu untersuchen. Dabei zeigte eine ausführliche Analyse,

dass Triplett-Triplett-Annihilation (TTA) der dominierende Effekt zweiter Ordnung ist. Bemerkenswerterweise trägt TTA in diesen Exciplex-basierten TADF-OLEDs aufgrund einer moderaten RISC-Rate (engl. *reverse intersystem crossing*) und einer hohen Triplett-dichte zu einem erheblichen Teil zur Triplettdepopulation bei, wobei der TTA Anteil bei Raumtemperatur bis zu 50% erreicht. Da TTA im Gegensatz zu dem für TADF charakteristischen RISC-Prozess ein weniger effizienter Triplett-Erntemechanismus ist, zeigten diese Ergebnisse einen wichtigen effizienzlimitierenden Verlustweg auf.

Um einen detaillierteren Einblick in die Rolle der Triplett-Zustände in Donor:Akzeptor-Systemen zu erhalten, wurden die optoelektronischen Materialsysteme mit Magnetresonanzmethoden untersucht. Dazu wurde die Technik der transienten optisch detektierten Magnetresonanz (trODMR) entwickelt, die eine spektrale und zeitaufgelöste Methode darstellt, mit der Spinzustände in Verbindung mit Photolumineszenz (trPLDMR) oder Elektrolumineszenz (trELDMR) direkt untersucht werden können. Die Vorteile der Technik liegen in der direkten PL- oder EL-Detektion und der zusätzlichen zeitlichen Komponente, wodurch die spektralen Beiträge der verschiedenen Zustände mit absolutem Vorzeichen und Amplitude genau bestimmt werden können. Interessanterweise zeigten die zuvor untersuchten elektrisch betriebenen OLEDs signifikante Unterschiede in den intermediären Triplett-Zuständen im Vergleich zu optisch angeregten Dünnschichten. Optische Anregung muss daher mit besonderer Vorsicht behandelt werden, da trotz identisch emittierendem Endzustand von OLEDs und Dünnschichten zusätzliche Spinzustände untersucht werden könnten. Die entwickelte Methode hat ihre Nützlichkeit in Donor:Akzeptor-Systemen nicht nur an TADF-basierten OLEDs und Dünnschichten bewiesen, sondern auch an auf modernsten NFA basierenden OPV-Materialien, wobei hier auch die Beteiligung von molekularen Triplett-Exzitonen an der Lumineszenz nachgewiesen werden konnte.

Zur Erweiterung der Forschung an OPV-Systemen wurden weitere spinsensitive Techniken, insbesondere cwPLDMR und trEPR, in Verbindung mit TA-Messungen angewendet, um einen detaillierten Einblick in molekulare Triplett-Zustände und damit verbundene effizienzlimitierende Prozesse zu erhalten. Diese komplementären Methoden wurden einerseits auf die neuesten Donor:Akzeptor-Kombinationen mit den (nicht-) halogenierten Donoren PBDB-T, PM6 und PM7 und den NFAs Y6 und Y7 angewandt, um langlebige Triplett-Zustände und ihre Entstehungspfade zum NFA zu untersuchen. Dabei ergab den Hauptbeitrag in allen Mischungen der Lochrücktransfer von CT-Zuständen, die durch Rekombination von freien Ladungsträgern entstehen (engl. *non-geminate recombination*). Die Mischungen mit den vielversprechenden halogenierten Donoren ergaben sogar zusätzlich einen Übergang vom angeregten Singulett zum Triplett-Zustand (engl. *intersystem crossing*, ISC), induziert durch

Spin-Bahn Kopplung (engl. *spin-orbit coupling*, SOC). Hinsichtlich der Auswirkungen der Halogenierung auf die Kinetik der angeregten Zustände, insbesondere auf die konkurrierenden Singulett-depopulierenden ISC- und Lochtransferraten, wurde ein vernachlässigbarer Einfluss der Verschiebung von HOMO-Niveaus oder schwereren Halogenatomen festgestellt. Die erhöhte ISC-Ausbeute mit halogeniertem Donor weist jedoch auf eine unvollständige Ladungsträgergenerierung in diesen Mischungen hin, was auf einen konkurrierenden negativen Einfluss der Domänenaggregation hindeutet. Somit wurde gezeigt, dass Halogenierung die allgemeine Leistung zwar erhöht, die Bildung von Triplett-Exzitonen aber nicht verhindert oder eventuell sogar verstärkt.

Um die modernen NFA-Akzeptoren mit den traditionell verwendeten Fulleren-Akzeptoren zu vergleichen, wurden die spinsensitiven Methoden zusätzlich auf Fulleren-basierte OSCs, PTB7-Th:PCBM und PM6:PCBM, angewendet. Darüber hinaus lag der Schwerpunkt auf der Komplementarität der spinsensitiven Methoden PLDMR, trEPR und TA, da jede dieser Methoden für die Untersuchung eines bestimmten (Teil-) Bereichs von Triplettbildungswegen geeignet ist. Während PLDMR sämtliche Triplett-Zustände mit hoher Empfindlichkeit nachweisen kann, einschließlich schwach beteiligter Triplettpfade, ermöglicht trEPR die Untersuchung der Spindynamik von Triplettexzitonen, die aus einer gepaarten Photoanregung (engl. *geminate pair*) stammen. TA erweitert das experimentelle Konzept durch die Zuweisung von Ladungsrücktransfer aus Rekombination von freien Ladungsträgern, wodurch alle vorhandenen Pfade in OPV-Materialien entschlüsselt werden können. Folglich konnte gepaarter Ladungsrücktransfer in Fulleren-basierten Kombinationen zusätzlich zum nicht-gepaarten Pfad und SOC-induzierter ISC identifiziert und zugeordnet werden, was in deutlichem Gegensatz zu den effizienteren NFA-basierten Mischungen steht. Das Auftreten dieses gepaarten Rücktransfers wird auf isolierte Fullerenmoleküle zurückgeführt, die in den Alkylseitenketten des Donorpolymers gefangen sind. Die Ergebnisse der Fulleren- und NFA-basierten Studien deuten darauf hin, dass neben den photophysikalischen Eigenschaften auch die Morphologie eine wichtige Rolle spielt, wobei eine gute Reinheit der Donor- und Akzeptorphasen in der Größe der Exzitonsdiffusionslänge Triplett-Verlustprozesse reduzieren oder sogar unterdrücken könnte. Darüber hinaus sollte das Hauptziel der weiteren Forschung darin bestehen, die Pfade zur Triplettbildung in modernen Donor:Akzeptor-Kombinationen zu unterbinden, um einen beträchtlichen Effizienzsprung bei den momentan sättigenden OSC-Effizienzen zu erreichen.

Zusammenfassend hat diese Arbeit zu einem tieferen Verständnis von optoelektronischen Materialien und Bauelementen beigetragen, indem sie die beteiligten Spinzustände, die Kinetik der angeregten Zustände und die damit verbundenen Ver-

lustpfade untersuchte. Anhand der umfangreichen Studien zu verschiedenen Materialien und Bauelementen für die Anwendung in OLEDs und OPVs konnte für beide Forschungsbereiche die Notwendigkeit aufgezeigt werden, die identifizierten effizientlimitierenden Prozesse zu verhindern. Das in dieser Arbeit vorgestellte leistungsstarke Portfolio an spinsensitiven Techniken und Evaluierungsmethoden konnte einen Einblick und Lösungsansätze für das weitere Forschungsziel liefern, die Effizienz von organischen optoelektronischen Bauelementen zu steigern.

10 Appendix

Appendix to ch. 5: Kinetic Modeling of Transient Electroluminescence reveals Efficiency-Limiting Process in Exciplex-Based TADF OLEDs

Python-Script for Fitting trEL Data:

For fitting the transient EL measurements from Figure 5.2, an iterative procedure (forward Euler method) was used, in which the rate equations are solved by stepwise integration with a timestep Δt , small enough to properly model the data. The fitting was realized by a standard Levenberg-Marquardt algorithm, implemented in the Scipy library (v. 1.1.0) in Python (v. 3.7.6), using the simulated rate equation model as fitting function. The script used for the iterative solution of the rate equations including calculation of loss processes and contribution to EL looks as follows:

```
def trEL(x,kr,knr,kT,kisc,krisc,kTP,kTT,kST,kSP,j,T,E):

    Input parameter:
    x                -> time vector
    kr, knr, kT, kisc, krisc -> direct transition rates
    kTP, KTT, kST, kSP -> 2nd order transitions
    j                -> operating current
    T                -> temperature
    E                -> energy

    y = 6.86e-11      # epsilon_r=2.9 (in cm)
    e = 1.6e-19       # elementary charge
    d = 70e-7         # OLED emission layer thickness (in cm)
    dt = 0.0000001   # time step

    n = int(0.01/dt)  # steps in simulated time interval
    n1 = int(n/2)     # turn-off point

    # State vectors
    S1 = np.zeros(n)  # Singlet population
    T1 = np.zeros(n)  # Triplet population
    m = np.zeros(n)   # Polaron population
    tim = np.zeros(n) # Time vector population
    tim[0] = -n1*dt
```

```

EL = np.zeros(n)          # EL-signal from Singlet
dEL = np.zeros(n)        # normalized EL

# Loss processes
TTA_loss = np.zeros(n)   # non-radiative TTA loss
TTA_sing = np.zeros(n)   # TTA singlet repopulation
RISC_loss = np.zeros(n)  # Triplet depopulation by RISC
kT_loss = np.zeros(n)    # non-radiation Triplet decay

# Contributions to EL
n_TTA = np.zeros(n)      # TTA recombination
n_RISC = np.zeros(n)     # RISC
n_pol = np.zeros(n)      # Polaron contribution
n_TTA_norm = np.zeros(n)
n_RISC_norm = np.zeros(n)
n_pol_norm = np.zeros(n)

# Scaling krisc with Boltzmann factor:
z = ((1/200)-(1/T))*(1/8.61733e-5)
krisc = krisc*math.exp(z*E)

# Iterative simulation on complete time vector
for i in range(1,n):
    if i<n1:              #Time interval with OLED on
        tim[i] = tim[i-1]+dt
        m[i] = m[i-1] + (j/(e*d) - y*m[i-1]*m[i-1])*dt
        S1[i] = S1[i-1]+(-(kr+knr)*S1[i-1]+krisc*T1[i-1]-kisc*S1[i-1]
            +(1/4)*kTT*T1[i-1]*T1[i-1]-kST*T1[i-1]*S1[i-1]
            -2*kSP*m[i-1]*S1[i-1]+0.25*y*m[i-1]*m[i-1])*dt
        T1[i] = T1[i-1]+(-kT*T1[i-1]-krisc*T1[i-1]+kisc*S1[i-1]
            -2*kTP*m[i-1]*T1[i-1]-(5/4)*kTT*T1[i-1]*T1[i-1]
            +0.75*y*m[i-1]*m[i-1])*dt
        EL[i] = kr*S1[i]

#Loss processes of Triplet States
TTA_loss[i] = (5/4)*kTT*T1[i]*T1[i]
TTA_sing[i] = (1/4)*kTT*T1[i]*T1[i]
RISC_loss[i] = krisc*T1[i]
kT_loss[i] = kT*T1[i]

#Contribution to EL
n_TTA[i] = n_TTA[i-1]+((1/4)*kTT*T1[i-1]*T1[i-1]
    -(kr+knr+kisc)*n_TTA[i-1])*dt
n_RISC[i] = n_RISC[i-1]+(krisc*T1[i-1]
    -(kr+knr+kisc)*n_RISC[i-1])*dt
n_pol[i] = n_pol[i-1]+(0.25*y*m[i-1]*m[i-1]

```

```

-(kr+knr+kisc)*n_pol[i-1])*dt

if n1<=i and i<n: # Time interval after turnoff, transient decay
    tim[i] = tim[i-1]+dt
    m[i] = m[i-1] +(- y*m[i-1]*m[i-1])*dt
    S1[i] = S1[i-1]+(-(kr+knr)*S1[i-1]+krisc*T1[i-1]-kisc*S1[i-1]
        +(1/4)*kTT*T1[i-1]*T1[i-1]-kST*T1[i-1]*S1[i-1]
        -2*kSP*m[i-1]*S1[i-1]+0.25*y*m[i-1]*m[i-1])*dt
    T1[i] = T1[i-1]+(-kT*T1[i-1]-krisc*T1[i-1]
        +kisc*S1[i-1]-2*kTP*m[i-1]*T1[i-1]
        -(5/4)*kTT*T1[i-1]*T1[i-1]+0.75*y*m[i-1]*m[i-1])*dt
    EL[i] = kr*S1[i]

#Loss processes of Triplet States
TTA_loss[i] = (5/4)*kTT*T1[i]*T1[i]
TTA_sing[i] = (1/4)*kTT*T1[i]*T1[i]
RISC_loss[i] = krisc*T1[i]
kT_loss[i] = kT*T1[i]

#Contribution to EL
n_TTA[i] = n_TTA[i-1]+((1/4)*kTT*T1[i-1]*T1[i-1]
    -(kr+knr+kisc)*n_TTA[i-1])*dt
n_RISC[i] = n_RISC[i-1]+(krisc*T1[i-1]
    -(kr+knr+kisc)*n_RISC[i-1])*dt
n_pol[i] = n_pol[i-1]+(0.25*y*m[i-1]*m[i-1]
    -(kr+knr+kisc)*n_pol[i-1])*dt

# normalize contribution to EL on steady-state singlet population
n_TTA_norm = n_TTA/(S1[n1-100])*100
n_RISC_norm = n_RISC/(S1[n1-100])*100
n_pol_norm = n_pol/(S1[n1-100])*100

# normalize simulation
for i in range(1,n):
    dEL[i] = EL[i]/EL[n1-100]

# interpolate dEL output on x-vector (to allow fitting)
dEL_out = np.interp(x,tim,dEL)

# Outputs
return dEL_out, tim, TTA_loss, TTA_sing, RISC_loss, kT_loss, n_TTA, n_RISC, n_pol,
n_TTA_norm, n_RISC_norm, n_pol_norm

```

Transformation of TTA rate

The TTA process is split up into three parts, either forming a quintet, triplet or the singlet state. Hence, the individual loss-rates with respect to the original triplet population are given by the probability of the transition multiplied with the number of lost triplets (0 for quintet, 1 for triplet and 2 for singlet) or transferred to the singlet state (0 for quintet, 0 for triplet and 1 for singlet) in the process. This results in rates of $\frac{5}{9} k'_{TT}$ for the depopulation of the triplet state and $\frac{1}{9} k'_{TT}$ for the population of the singlet state through TTA. Defining $k_{TT} = \frac{9}{4} k'_{TT}$, these rates can be transformed to the following:

$$\begin{aligned} \frac{dT_1}{dt} &= \dots - \left(0 \cdot \frac{5}{9} + 1 \cdot \frac{3}{9} + 2 \cdot \frac{1}{9} \right) = \dots - \frac{5}{9} k'_{TT} \stackrel{k_{TT} = \frac{9}{4} k'_{TT}}{=} \dots - \frac{5}{4} k_{TT} \\ \frac{dS_1}{dt} &= \dots + \left(0 \cdot \frac{5}{9} + 0 \cdot \frac{3}{9} + 1 \cdot \frac{1}{9} \right) = \dots + \frac{1}{9} k'_{TT} \stackrel{k_{TT} = \frac{9}{4} k'_{TT}}{=} \dots + \frac{1}{4} k_{TT} \end{aligned} \quad (10.1)$$

Appendix to ch. 7: Triplet States and their Generation Pathways in (Non-) Halogenated PBDB-T:Y-Series

Table 10.1: Energy values for donor polymers PBDB-T, PM6, PM7 and acceptors Y6, Y7. S_1 and CT energies of experimentally determined values are taken from given references (Averaged values). Triplet energies are determined by subtraction of calculated ΔE_{ST} from S_1 . CT singlet and triplet energies are treated as isoenergetic. Triplets in blends are localized on acceptor molecules populated by different formation mechanisms (ng = non-geminate). The CT value for PM7:Y7 is assumed to be identical with PM6:Y6 because PM6 and PM7 have identical energy levels.

Material	T_1 [eV]	ΔE_{ST} [eV]	T_1, T_2 [eV]	CT [eV]	Triplets	Mechanism	Ref.
PBDB-T	1.85	0.40	1.45			ISC	[175,275]
PM6	1.92	0.41	1.51			ISC	[191,276]
PM7	1.92	0.41	1.51			ISC	[277]
Y6	1.39	0.56, 0.35	0.83, 1.04			ISC	[71,200,205,275,276,278]
Y7	1.40	0.55, 0.34	0.85, 1.06			ISC	[279]
PBDB-T:Y6				1.35	Y6	HBT (ng)	[214]
PM6:Y6				1.37	Y6	ISC, HBT (ng)	[49,88,205,275,278]
PM7:Y6				1.37	Y6	ISC, HBT (ng)	[193]
PBDB-T:Y7				1.36	Y7	HBT (ng)	[193]
PM6:Y7				1.38	Y7	ISC, HBT (ng)	[214]
PM7:Y7				1.38	Y7	ISC, HBT (ng)	n.a.

EasySpin Simulation Parameter

Table 10.2: Parameter for PLDMR spectral simulations using the MATLAB tool EasySpin for spin-coated substrates of Figure 7.1 and Figure 10.1. Parameters given are the ZFS parameters D and E , ordering factors $\lambda_\theta, \lambda_\phi$, the spectral linewidth with Gaussian and Lorentzian contributions [Gaussian Lorentzian] and the weight of the signal. *: E value cannot be determined due to high ordering.

Film	Donor				Acceptor				CT-state	
	D/h, E/h [MHz]	$\lambda_\theta, \lambda_\phi$	LW [mT]	Weight	D/h, E/h [MHz]	$\lambda_\theta, \lambda_\phi$	LW [mT]	Weight	LW [mT]	Weight
Y6					940, 200*	11.0, 0	[6.8 0]	0.7	[0 2.5] [0 0.9]	0.30 -0.19
PBDB-T	1500, 120	7.1, 0	[4.5 0]	0.37					[1 1.4]	0.36
	1500, 120	-1.5, 4.0	[0 8.9]	0.27						
PM6	1500, 120	11.4, 0	[4 0]	0.40						
	1500, 120	-2.0, 8.0	[0 8]	0.12					[0 1]	0.20
	1500, 75	-1.0, -5.0	[0 5]	0.28						
PM7	1510, 120	8.0 0	[4 0]	0.48						
	1510, 120	-2.0 7.0	[0 8]	0.20					[0 1.4]	0.12
	1510, 50	-2.0 0	[0 7]	0.20						
PBDB-T:Y6					1040, 200*	4.5, 0	[7 0]	0.20	[0.8 1.8]	0.80
PM6:Y6					1020, 200*	5.5, 0	[7 0]	0.15	[0.8 2.2]	0.85
PM7:Y6					1000, 200*	5.5, 0	[7 0]	0.38	[0.9 2.5]	0.62

Table 10.3: Parameter for trEPR spectral simulations using the Matlab tool EasySpin for dropcasted samples from Figure 7.2 and Figure 10.3. Parameters given are the ZFS parameters D and E , ordering factors $\lambda_\theta, \lambda_\phi$, relative zero-field populations, and the spectral linewidth with Gaussian and Lorentzian contributions [Gaussian Lorentzian].

Film	Donor				Acceptor			
	D/h, E/h [MHz]	$\lambda_\theta, \lambda_\phi$	[$p_x p_y p_z$]	Lw [mT]	D/h, E/h [MHz]	$\lambda_\theta, \lambda_\phi$	[$p_x p_y p_z$]	Lw [mT]
Y6					945, 215	0, 0	[0.00 0.66 0.34]	[0 2]
Y7					850, 240	0, 0	[0.00 0.62 0.42]	[0 1.5]
PBDB-T	1460, 95	0.68, 0.44	[0.00 0.51 0.49]	[0 2.3]				
PM6	1455, 100	0.42, -0.1	[0.00 0.56 0.44]	[0 2.7]				
PM7	1510, 120	0.35, 0.1	[0.00 0.53 0.47]	[0 2.0]				
PM6:Y6					995, 210	0.42, -0.1	[0.00 0.66 0.34]	[0 3.2]
PM7:Y6					880, 160	0.35, 0.1	[0.00 0.66 0.34]	[0 2.0]
PM6:Y7					900, 200	0.42, -0.1	[0.00 0.60 0.40]	[0 4]
PM7:Y7					925, 200	0.35, -1.0	[0.00 0.60 0.40]	[0 2.1]

Additional PLDMR and trEPR spectra

PLDMR for donors PBDB-T, PM6, and PM7

Figure 10.1 shows PLDMR spectra of neat PBDB-T, PM6, and PM7 on spin-coated substrates. The position of the HF signal and the width of the FF signal are similar (see Table 10.2). All donors show a preferential molecular ordering on the substrate, whereby they exhibit, in contrast to NFAs, a coexistence of edge-on and face-on orientation.^[202,203]

The additional orientation leads to a shoulder in the HF signals and wings in the FF signal at 315 and 360 mT.

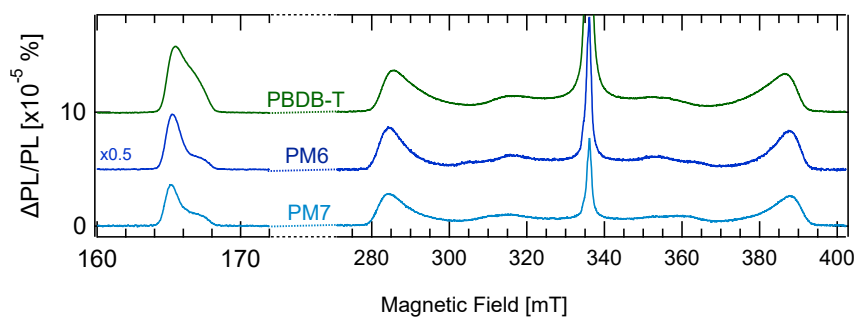


Figure 10.1: PLDMR spectra of the neat PBDB-T, PM6, and PM7 on spin-coated substrates. The position of the HF signal and the width of the FF signal are similar. Additionally, all PLDMR spectra show a considerable ordering.

PLDMR for donor:Y7 blended thin films

Figure 10.2 shows PLDMR spectra of neat NFA Y7 and donors PBDB-T, PM6 and PM7 and their blends PBDB-T:Y7, PM6:Y7 and PM7:Y7. The same presence of NFA triplet excitons can be found, whereby the width of the spectra are almost identical for Y6 blends in ch. 7. The measurements were performed on drop-cast samples, whereby only the ordering factor is higher for spin-coated substrates, as the molecules show preferential orientation on the substrate (face-on or edge-on orientation).

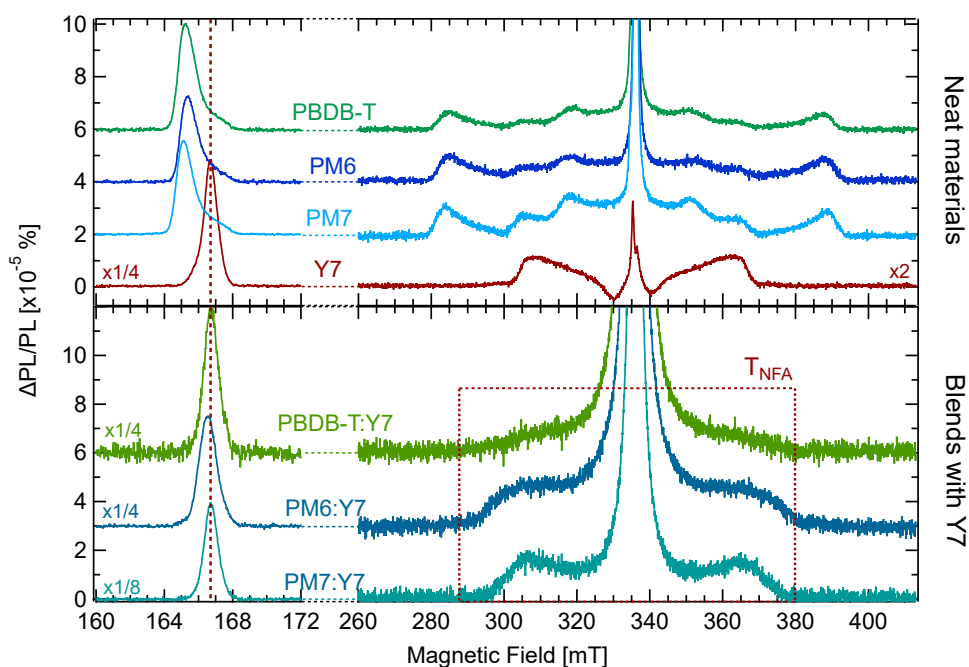


Figure 10.2: PLDMR spectra of neat materials Y7, PBDB-T, PM6, and PM7 as well as their blends PBDB-T:Y7, PM6:Y7 and PM7:Y7 on drop-cast samples. The position of the HF signal and the width of the FF signal reveal Y7 triplet excitons in all blends.

trEPR for neat polymer, Y7 and donor:y7 blends

Figure 10.3 shows the trEPR spectra for neat polymers (left, recorded with Amplitude Minilite II, see sec. 4.3.1) and donor:Y7 blends (right, recorded with Ekspla PL2210, see sec. 4.3.1) with simulation parameters given in Table 10.3. Analogous to Figure 7.2, blends with donor PM6 and PM7 show ISC yield, while there is no visible trEPR signal in PBDB-T:Y7. Signal reduced in Y7 blends due to lower laser excitation power.

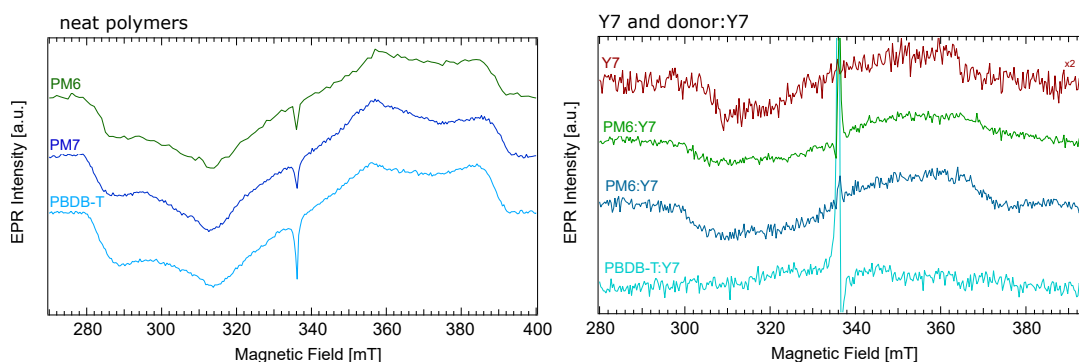


Figure 10.3: trEPR spectra of neat PBDB-T, PM6, PM7 (left) and their blends PBDB-T:Y7, PM6:Y7 and PM7:Y7 (right) on dropcasted samples. The width of the FF signal reveal Y7 triplet excitons in blends PM6:Y7 and PM7:Y7.

Appendix to ch. 8: Experimental Framework for Probing Triplet Recombination Pathways in Organic Solar Cells

Table 10.4: Results of EasySpin simulations with axial (D) and rhombic (E) zero-field splitting parameters, ordering factors for distribution along Θ and ϕ (λ_Θ , λ_ϕ), spectral linewidth with Gaussian and Lorentzian contributions [Gaussian Lorentzian], weight (according to normalized spectra) and g-factor. PC₆₀BM shows two negative signals, likely corresponding to PC₆₀BM anion and cation. *: E value is determined from dropcast samples due to high ordering of spin-coated samples. **: E value can not be determined due to high ordering.

Film	Donor				Acceptor				CT-state		
	D/h, E/h [MHz]	$\lambda_\Theta, \lambda_\phi$	LW / mT	Weight	D/h, E/h [MHz]	$\lambda_\Theta, \lambda_\phi$	LW / mT	Weight	LW / mT	Weight	g
PC ₆₀ BM					360, 50	-1, 0	[2.5, 0]	1.00	[0 0.3] [0 0.2]	-0.03 -0.07	2.0012 2.004
PTB7-TH	1190, 180*	11, 0	[5 0]	0.78					[0 2] [0 0.8]	0.22 -0.43	2.0042 2.0047
PTB7-TH: PC ₆₀ BM	1310, 180** 1470, 180**	7.5, -4 3, -4	[6 0] [5 0]	0.0037 0.0064	320, 30	-1, 0	[2.5 0]	0.52	[0 1.8] [0 0.35] [0 0.6]	0.48 -0.03 -0.06	2.0044 2.0012 2.0037
PM6	1500, 70	1, 2 5.5, 3	[9 0] [5 0]	0.52 0.30					[0 1.5]	0.18	2.0045
PM6:PC ₆₀ BM	1500, 70	0.5, 3 5, 3	[9 0] [5 0]	0.42 0.11	360, 50		[0 4]	0.10	[0 2.8] [0 0.5] [0 0.4]	0.37 -0.15 -0.09	2.0025 2.0012 2.0034

Table 10.5: Results of EasySpin simulations with axial (D) and rhombic (E) zero-field splitting parameters, with assignment to triplets on donor (D) and acceptor (A). Two different populating mechanisms have been considered: SOC-induced ISC and geminate BCT with populations of zero-field states ($[p_1 p_2 p_3]$) and for high-field levels ($[p_+ p_0 p_-]$) Only Lorentzian broadening was considered to avoid over-parameterizing the fitting; the linewidth is reported in units of mT. Last column reports the normalized root-mean-square-deviation (NRMSD) of the fit. Evaluation performed by A. Privitera.

Film	D/h, E/h [MHz]	T_1	ISC triplet			Geminate BCT triplet			NRMSD
			$[p_1 p_2 p_3]$	LW [mT]	Weight	$[p_+ p_0 p_-]$	LW /mT	Weight	
PC ₆₀ BM 1 μ s	-237, 39	A	[0.34 0.40 0.26]	1.59	0.66	[0 1 0]	2.08	0.34	0.02
PC ₆₀ BM 5 μ s	-256, 35	A	[0.40 0.38 0.22]	2.04	0.78	[0 1 0]	3.11	0.22	0.01
PM6 1 μ s	1410, 125	D	[0.28 0.36 0.36]	8					0.08
PM6 5 μ s	135, 0	D	[0.34 0.43 0.23]	5					0.10
PTB7-TH 1 μ s	1100, 160	D	[0.12 0.43 0.23]	11					0.03
PTB7-TH 5 μ s	1050, 160	D	[0.47 0.28 0.25]	8					0.04
PM6:PC ₆₀ BM 1 μ s	1300, 140	D	[0.14 0.52 0.34]	12					0.16
PM6:PC ₆₀ BM 5 μ s	1220, 40	D	[0.39 0.2 0.41]	13	0.57	[0 1 0]	5	0.43	0.04
PTB7-Th:PC ₆₀ BM 1 μ s	1050, 200	D	[0.37 0.33 0.30]	9	0.63	[0 1 0]	13	0.37	0.03
PTB7-Th:PC ₆₀ BM 5 μ s	[1143 164]	D	[0.35 0.33 0.32]	7	0.78	[0 1 0]	11	0.22	0.04

Bibliography

- [1] N. Pasachoff. *Marie Curie: And the science of radioactivity*. Oxford University Press (1996).
- [2] G. Destriau. Recherches sur les scintillations des sulfures de zinc aux rayons α . *Journal de Chimie Physique*, **33**, 587 (1936). doi: [10.1051/jcp/1936330587](https://doi.org/10.1051/jcp/1936330587).
- [3] M. Pope, H. Kallmann and P. Magnante. Electroluminescence in organic crystals. *The Journal of Chemical Physics*, **38**, 8, 2042 (1963). doi: [10.1063/1.1733929](https://doi.org/10.1063/1.1733929).
- [4] K. Goushi and C. Adachi. Efficient organic light-emitting diodes through up-conversion from triplet to singlet excited states of exciplexes. *Applied Physics Letters*, **101**, 2, 023306 (2012). doi: [10.1063/1.4737006](https://doi.org/10.1063/1.4737006).
- [5] Q. Liu, Y. Jiang, K. Jin, J. Qin, J. Xu, W. Li, J. Xiong, J. Liu, Z. Xiao, K. Sun, S. Yang, X. Zhang and L. Ding. 18% efficiency organic solar cells. *Science Bulletin*, **65**, 4, 272 (2020). doi: [10.1016/j.scib.2020.01.001](https://doi.org/10.1016/j.scib.2020.01.001).
- [6] G. Horowitz. Organic field-effect transistors. *Advanced Materials*, **10**, 5, 365 (1998). doi: [10.1002/\(sici\)1521-4095\(199803\)10:5<365::aid-adma365>3.0.co;2-u](https://doi.org/10.1002/(sici)1521-4095(199803)10:5<365::aid-adma365>3.0.co;2-u).
- [7] C. W. Tang and S. A. VanSlyke. Organic electroluminescent diodes. *Applied Physics Letters*, **51**, 12, 913 (1987). doi: [10.1007/978-3-642-93430-8_71](https://doi.org/10.1007/978-3-642-93430-8_71).
- [8] J. H. Burroughes, D. D. Bradley, A. Brown, R. Marks, K. Mackay, R. H. Friend, P. L. Burns and A. B. Holmes. Light-emitting diodes based on conjugated polymers. *Nature*, **347**, 6293, 539 (1990). doi: [10.1038/347539a0](https://doi.org/10.1038/347539a0).
- [9] M. A. Baldo, D. F. O'Brien, Y. You, A. Shoustikov, S. Sibley, M. E. Thompson and S. R. Forrest. Highly efficient phosphorescent emission from organic electroluminescent devices. *Nature*, **395**, 6698, 151 (1998). doi: [10.1038/25954](https://doi.org/10.1038/25954).
- [10] A. Endo, M. Ogasawara, A. Takahashi, D. Yokoyama, Y. Kato and C. Adachi. Thermally activated delayed fluorescence from Sn⁴⁺-porphyrin complexes and their application to organic light emitting diodes—a novel mechanism for electroluminescence. *Advanced Materials*, **21**, 47, 4802 (2009). doi: [10.1002/adma.200900983](https://doi.org/10.1002/adma.200900983).

- [11] C. W. Tang. Two-layer organic photovoltaic cell. *Applied Physics Letters*, **48**, 2, 183 (1986). doi: [10.1063/1.96937](https://doi.org/10.1063/1.96937).
- [12] N. S. Sariciftci, L. Smilowitz, A. J. Heeger and F. Wudl. Photoinduced electron transfer from a conducting polymer to buckminsterfullerene. *Science*, **258**, 5087, 1474 (1992). doi: [10.1126/science.258.5087.1474](https://doi.org/10.1126/science.258.5087.1474).
- [13] G. Yu, J. Gao, J. C. Hummelen, F. Wudl and A. J. Heeger. Polymer photovoltaic cells: enhanced efficiencies via a network of internal donor-acceptor heterojunctions. *Science*, **270**, 5243, 1789 (1995). doi: [10.1126/science.270.5243.1789](https://doi.org/10.1126/science.270.5243.1789).
- [14] J. C. Hummelen, B. W. Knight, F. LePeq, F. Wudl, J. Yao and C. L. Wilkins. Preparation and characterization of fulleroid and methanofullerene derivatives. *The Journal of Organic Chemistry*, **60**, 3, 532 (1995). doi: [10.1021/jo00108a012](https://doi.org/10.1021/jo00108a012).
- [15] G. Bernardo, T. Lopes, D. G. Lidzey and A. Mendes. Progress in upscaling organic photovoltaic devices. *Advanced Energy Materials*, **11**, 23, 2100342 (2021). doi: [10.1002/aenm.202100342](https://doi.org/10.1002/aenm.202100342).
- [16] A. Karki, J. Vollbrecht, A. J. Gillett, P. Selter, J. Lee, Z. Peng, N. Schopp, A. L. Dixon, M. Schrock, V. Nádaždy et al. Unifying charge generation, recombination, and extraction in low-offset non-fullerene acceptor organic solar cells. *Advanced Energy Materials*, **10**, 29, 2001203 (2020). doi: [10.1002/aenm.202001203](https://doi.org/10.1002/aenm.202001203).
- [17] Y. Lin, J. Wang, Z. Zhang, H. Bai, Y. Li, D. Zhu and X. Zhan. An electron acceptor challenging fullerenes for efficient polymer solar cells. *Advanced Materials*, **27**, 7, 1170 (2015). doi: [10.1002/adma.201404317](https://doi.org/10.1002/adma.201404317).
- [18] Y. Cui, Y. Xu, H. Yao, P. Bi, L. Hong, J. Zhang, Y. Zu, T. Zhang, J. Qin and J. Ren. Single-junction organic photovoltaic cell with 19% efficiency. *Advanced Materials*, **33**, 41, 2102420 (2021). doi: [10.1002/adma.202102420](https://doi.org/10.1002/adma.202102420).
- [19] S. Ullbrich, J. Benduhn, X. Jia, V. C. Nikolis, K. Tvingstedt, F. Piersimoni, S. Roland, Y. Liu, J. Wu, A. Fischer et al. Emissive and charge-generating donor-acceptor interfaces for organic optoelectronics with low voltage losses. *Nature Materials*, **18**, 5, 459 (2019). doi: [10.1038/s41563-019-0324-5](https://doi.org/10.1038/s41563-019-0324-5).
- [20] D. Kasemann, R. Brückner, H. Fröb and K. Leo. Organic light-emitting diodes under high currents explored by transient electroluminescence on the nanosecond scale. *Physical Review B*, **84**, 11, 115208 (2011). doi: [10.1103/physrevb.84.115208](https://doi.org/10.1103/physrevb.84.115208).

- [21] J. Benduhn, K. Tvingstedt, F. Piersimoni, S. Ullbrich, Y. Fan, M. Tropicano, K. A. McGarry, O. Zeika, M. K. Riede, C. J. Douglas et al. Intrinsic non-radiative voltage losses in fullerene-based organic solar cells. *Nature Energy*, **2**, 6, 1 (2017). doi: [10.1038/nenergy.2017.53](https://doi.org/10.1038/nenergy.2017.53).
- [22] I. Sudakov, M. Van Landeghem, R. Lenaerts, W. Maes, S. Van Doorslaer and E. Goovaerts. The interplay of stability between donor and acceptor materials in a fullerene-free bulk heterojunction solar cell blend. *Advanced Energy Materials*, **10**, 46, 2002095 (2020). doi: [10.1002/aenm.202002095](https://doi.org/10.1002/aenm.202002095).
- [23] J. Grüne, N. Bunzmann, M. Meinecke, V. Dyakonov and A. Sperlich. Kinetic modeling of transient electroluminescence reveals TTA as an efficiency-limiting process in exciplex-based TADF OLEDs. *The Journal of Physical Chemistry C*, **124**, 47, 25667 (2020). doi: [10.1021/acs.jpcc.0c06528](https://doi.org/10.1021/acs.jpcc.0c06528).
- [24] J. Grüne, V. Dyakonov and A. Sperlich. Detecting triplet states in opto-electronic and photovoltaic materials and devices by transient optically detected magnetic resonance. *Materials Horizons*, **8**, 9, 2569 (2021). doi: [10.1039/d1mh00999k](https://doi.org/10.1039/d1mh00999k).
- [25] J. Grüne, G. Londi, A. J. Gillett, B. Stähly, S. Lulei, M. Kotova, Y. Olivier, V. Dyakonov and A. Sperlich. Energetically trapped triplet excitons and their generation pathways in (non-) halogenated PBDB-T:Y-series. *arXiv preprint* (2022). doi: [10.48550/arXiv.2204.14088](https://doi.org/10.48550/arXiv.2204.14088).
- [26] A. Privitera, J. Grüne, A. Karki, W. K. Myers, V. Dyakonov, T.-Q. Nguyen, M. K. Riede, R. H. Friend, A. Sperlich and A. J. Gillett. Geminate and nongeminate pathways for triplet exciton formation in organic solar cells. *Advanced Energy Materials*, **12**, 16, 2103944 (2022). doi: [10.1002/aenm.202103944](https://doi.org/10.1002/aenm.202103944).
- [27] A. Köhler and H. Bässler. *Electronic processes in organic semiconductors: An introduction*. John Wiley & Sons (2015). doi: [10.1002/9783527685172](https://doi.org/10.1002/9783527685172).
- [28] W. Tress. *Organic solar cells*. Springer (2014). doi: [10.1007/978-3-319-10097-5](https://doi.org/10.1007/978-3-319-10097-5).
- [29] W. Brütting. *Physics of Organic Semiconductors*. John Wiley & Sons (2005). doi: [10.1002/3527606637.ch](https://doi.org/10.1002/3527606637.ch).
- [30] M. J. Griffith, S. Cottam, J. Stamenkovic, J. A. Posar and M. Petasecca. Printable organic semiconductors for radiation detection: from fundamentals to fabrication and functionality. *Frontiers in Physics*, **8**, 22 (2020). doi: [10.3389/fphy.2020.00022](https://doi.org/10.3389/fphy.2020.00022).

- [31] C. Deibel and V. Dyakonov. Polymer–fullerene bulk heterojunction solar cells. *Reports on Progress in Physics*, **73**, 9, 096401 (2010). doi: [10.1088/0034-4885/73/9/096401](https://doi.org/10.1088/0034-4885/73/9/096401).
- [32] W. Brütting, J. Frischeisen, T. D. Schmidt, B. J. Scholz and C. Mayr. Device efficiency of organic light-emitting diodes: Progress by improved light outcoupling. *physica status solidi (a)*, **210**, 1, 44 (2013). doi: [10.1002/pssa.201228320](https://doi.org/10.1002/pssa.201228320).
- [33] M. Brustolon and E. Giamello. *Electron Paramagnetic Resonance: A Practitioners Toolkit*. John Wiley & Sons (2009). ISBN 9780470432235.
- [34] J. A. Weil and J. R. Bolton. *Electron paramagnetic resonance: elementary theory and practical applications*. John Wiley & Sons (2007). ISBN 9780470084984.
- [35] R. Ernstorfer. Spectroscopic investigation of photoinduced heterogeneous electron transfer. Ph.D. thesis, University of Berlin (2004).
- [36] V. May and O. Kühn. *Charge and energy transfer dynamics in molecular systems*. John Wiley & Sons (2008). doi: [10.1002/9783527633791](https://doi.org/10.1002/9783527633791).
- [37] P. G. Baranov, H. J. von Bardeleben, F. Jelezko and J. Wrachtrup. *Magnetic Resonance of Semiconductors and Their Nanostructures*. Springer (2017). doi: [10.1007/978-3-7091-1157-4](https://doi.org/10.1007/978-3-7091-1157-4).
- [38] D. Beljonne, Z. Shuai, G. Pourtois and J. Bredas. Spin-orbit coupling and intersystem crossing in conjugated polymers: a configuration interaction description. *The Journal of Physical Chemistry A*, **105**, 15, 3899 (2001). doi: [10.1021/jp010187w](https://doi.org/10.1021/jp010187w).
- [39] G. Pourtois, D. Beljonne, J. Cornil, M. Ratner and J. Brédas. Photoinduced electron-transfer processes along molecular wires based on phenylenevinylene oligomers: a quantum-chemical insight. *Journal of the American Chemical Society*, **124**, 16, 4436 (2002). doi: [10.1021/ja017150](https://doi.org/10.1021/ja017150).
- [40] X.-K. Chen, D. Kim and J.-L. Brédas. Thermally activated delayed fluorescence (TADF) path toward efficient electroluminescence in purely organic materials: molecular level insight. *Accounts of Chemical Research*, **51**, 9, 2215 (2018). doi: [10.1021/acs.accounts.8b00174](https://doi.org/10.1021/acs.accounts.8b00174).
- [41] P. K. Samanta, D. Kim, V. Coropceanu and J.-L. Brédas. Up-conversion intersystem crossing rates in organic emitters for thermally activated delayed fluorescence: impact of the nature of singlet vs triplet excited states. *Journal of the American Chemical Society*, **139**, 11, 4042 (2017). doi: [10.1021/jacs.6b12124](https://doi.org/10.1021/jacs.6b12124).

- [42] H. Yersin. *Highly efficient OLEDs: Materials based on thermally activated delayed fluorescence*. John Wiley & Sons (2019). ISBN 9783527339006.
- [43] R. H. Fowler and L. Nordheim. Electron emission in intense electric fields. *Proceedings of the Royal Society of London. Series A, Containing Papers of a Mathematical and Physical Character*, **119**, 781, 173 (1928). doi: [10.1142/9789814503464_0087](https://doi.org/10.1142/9789814503464_0087).
- [44] J. Simmons. Richardson-schottky effect in solids. *Physical Review Letters*, **15**, 25, 967 (1965). doi: [10.1103/physrevlett.15.967](https://doi.org/10.1103/physrevlett.15.967).
- [45] B. Riedel. *Effizienzsteigerung in organischen Leuchtdioden*. KIT Scientific Publishing (2011).
- [46] F. Kraffert and J. Behrends. Spin-correlated doublet pairs as intermediate states in charge separation processes. *Molecular Physics*, **115**, 19, 2373 (2017). doi: [10.1080/00268976.2016.1278479](https://doi.org/10.1080/00268976.2016.1278479).
- [47] F. Kraffert, R. Steyrlleuthner, S. Albrecht, D. Neher, M. C. Scharber, R. Bittl and J. Behrends. Charge separation in PCPDTBT:PCBM blends from an EPR perspective. *The Journal of Physical Chemistry C*, **118**, 49, 28482 (2014). doi: [10.1021/jp509650v](https://doi.org/10.1021/jp509650v).
- [48] C. L. Braun. Electric field assisted dissociation of charge transfer states as a mechanism of photocarrier production. *The Journal of Chemical Physics*, **80**, 9, 4157 (1984). doi: [10.1063/1.447243](https://doi.org/10.1063/1.447243).
- [49] A. J. Gillett, A. Privitera, R. Dilmurat, A. Karki, D. Qian, A. Pershin, G. Londi, W. K. Myers, J. Lee and J. Yuan. The role of charge recombination to triplet excitons in organic solar cells. *Nature*, **597**, 7878, 666 (2021). doi: [10.1038/s41586-021-03840-5](https://doi.org/10.1038/s41586-021-03840-5).
- [50] D. Goldfarb and S. Stoll. *EPR spectroscopy: fundamentals and methods*. John Wiley & Sons (2018). ISBN 9781119162995.
- [51] S. Richert, C. E. Tait and C. R. Timmel. Delocalisation of photoexcited triplet states probed by transient EPR and hyperfine spectroscopy. *Journal of Magnetic Resonance*, **280**, 103 (2017). doi: [10.1016/j.jmr.2017.01.005](https://doi.org/10.1016/j.jmr.2017.01.005).
- [52] T. Biskup. Structure–function relationship of organic semiconductors: Detailed insights from time-resolved EPR spectroscopy. *Frontiers in Chemistry*, **7**, 10 (2019). doi: [10.3389/fchem.2019.00010](https://doi.org/10.3389/fchem.2019.00010).

- [53] C. Buckley, D. Hunter, P. Hore and K. McLauchlan. Electron spin resonance of spin-correlated radical pairs. *Chemical Physics Letters*, **135**, 3, 307 (1987). doi: [10.1016/0009-2614\(87\)85162-x](https://doi.org/10.1016/0009-2614(87)85162-x).
- [54] P. Hore, D. Hunter, C. McKie and A. Hoff. Electron paramagnetic resonance of spin-correlated radical pairs in photosynthetic reactions. *Chemical Physics Letters*, **137**, 6, 495 (1987). doi: [10.1016/0009-2614\(87\)80617-6](https://doi.org/10.1016/0009-2614(87)80617-6).
- [55] S. Stoll. Easyspin online documentation. <http://easyspin.org/easyspin/documentation/hamiltonian.html>.
- [56] A. Bencini and D. Gatteschi. Exchange and superexchange. In *Electron Paramagnetic Resonance of Exchange Coupled Systems*, 1–19. Springer (1990). doi: [10.1007/978-3-642-74599-7_1](https://doi.org/10.1007/978-3-642-74599-7_1).
- [57] Y. Hou, X. Zhang, K. Chen, D. Liu, Z. Wang, Q. Liu, J. Zhao and A. Barbon. Charge separation, charge recombination, long-lived charge transfer state formation and intersystem crossing in organic electron donor/acceptor dyads. *Journal of Materials Chemistry C*, **7**, 39, 12048 (2019). doi: [10.1039/c9tc04285g](https://doi.org/10.1039/c9tc04285g).
- [58] S. Stoll and A. Schweiger. Easyspin, a comprehensive software package for spectral simulation and analysis in EPR. *Journal of Magnetic Resonance*, **178**, 1, 42 (2006). doi: [10.1016/j.jmr.2005.08.013](https://doi.org/10.1016/j.jmr.2005.08.013).
- [59] S. Weber. Transient EPR (2017). doi: [10.1002/9780470034590.emrstm1509](https://doi.org/10.1002/9780470034590.emrstm1509).
- [60] S. S. Eaton, K. M. More, B. M. Sawant and G. R. Eaton. Use of the esr half-field transition to determine the interspin distance and the orientation of the interspin vector in systems with two unpaired electrons. *Journal of the American Chemical Society*, **105**, 22, 6560 (1983). doi: [10.1021/ja00360a005](https://doi.org/10.1021/ja00360a005).
- [61] J. Svorec, M. Valko, J. Moncol, M. Mazúr, M. Melník and J. Telser. Determination of intermolecular copper–copper distances from the EPR half-field transitions and their comparison with distances from x-ray structures: applications to copper (ii) complexes with biologically important ligands. *Transition Metal Chemistry*, **34**, 2, 129 (2009). doi: [10.1007/s11243-008-9168-6](https://doi.org/10.1007/s11243-008-9168-6).
- [62] F. Laquai, D. Andrienko, C. Deibel and D. Neher. Charge carrier generation, recombination, and extraction in polymer–fullerene bulk heterojunction organic solar cells. *Elementary Processes in Organic Photovoltaics*, 267–291 (2017). doi: [DOI: 10.1007/978-3-319-28338-8_1](https://doi.org/10.1007/978-3-319-28338-8_1).

- [63] S. M. Menke, A. Sadhanala, M. Nikolka, N. A. Ran, M. K. Ravva, S. Abdel-Azeim, H. L. Stern, M. Wang, H. Sirringhaus, T.-Q. Nguyen et al. Limits for recombination in a low energy loss organic heterojunction. *ACS Nano*, **10**, 12, 10736 (2016). doi: [10.1021/acsnano.6b06211](https://doi.org/10.1021/acsnano.6b06211).
- [64] Z. Zheng, H. Yao, L. Ye, Y. Xu, S. Zhang and J. Hou. PBDB-T and its derivatives: A family of polymer donors enables over 17% efficiency in organic photovoltaics. *Materials Today*, **35**, 115 (2020). doi: [10.1016/j.mattod.2019.10.023](https://doi.org/10.1016/j.mattod.2019.10.023).
- [65] X. Li, R. Ma, T. Liu, Y. Xiao, G. Chai, X. Lu, H. Yan and Y. Li. Fine-tuning homo energy levels between PM6 and PBDB-T polymer donors via ternary copolymerization. *Science China Chemistry*, **63**, 9, 1256 (2020). doi: [10.1007/s11426-020-9805-7](https://doi.org/10.1007/s11426-020-9805-7).
- [66] Q. Fan, U. A. Méndez-Romero, X. Guo, E. Wang, M. Zhang and Y. Li. Fluorinated photovoltaic materials for high-performance organic solar cells. *Chemistry–An Asian Journal*, **14**, 18, 3085 (2019). doi: [10.1002/asia.201900795](https://doi.org/10.1002/asia.201900795).
- [67] S.-H. Liao, H.-J. Jhuo, Y.-S. Cheng and S.-A. Chen. Fullerene derivative-doped zinc oxide nanofilm as the cathode of inverted polymer solar cells with low-bandgap polymer (PTB7-Th) for high performance. *Advanced Materials*, **25**, 34, 4766 (2013). doi: [10.1002/adma.201301476](https://doi.org/10.1002/adma.201301476).
- [68] S. Kim, M. A. M. Rashid, T. Ko, K. Ahn, Y. Shin, S. Nah, M. H. Kim, B. Kim, K. Kwak and M. Cho. New insights into the photodegradation mechanism of the PTB7-Th film: Photooxidation of π -conjugated backbone upon sunlight illumination. *The Journal of Physical Chemistry C*, **124**, 5, 2762 (2020). doi: [10.1021/acs.jpcc.9b09954](https://doi.org/10.1021/acs.jpcc.9b09954).
- [69] Q. Liu, J. Toudert, F. Liu, P. Mantilla-Perez, M. M. Bajo, T. P. Russell and J. Martorell. Circumventing uv light induced nanomorphology disorder to achieve long lifetime PTB7-Th:PCBM based solar cells. *Advanced Energy Materials*, **7**, 21, 1701201 (2017). doi: [10.1002/aenm.201701201](https://doi.org/10.1002/aenm.201701201).
- [70] W. Zhao, D. Qian, S. Zhang, S. Li, O. Inganäs, F. Gao and J. Hou. Fullerene-free polymer solar cells with over 11% efficiency and excellent thermal stability. *Advanced Materials*, **28**, 23, 4734 (2016). doi: [10.1002/adma.201600281](https://doi.org/10.1002/adma.201600281).
- [71] G. Li, X. Zhang, L. O. Jones, J. M. Alzola, S. Mukherjee, L.-w. Feng, W. Zhu, C. L. Stern, W. Huang, J. Yu, V. K. Sangwan, D. M. DeLongchamp, K. L. Kohlstedt, M. R. Wasielewski, M. C. Hersam, G. C. Schatz, A. Facchetti and T. J. Marks. Systematic

- merging of nonfullerene acceptor π -extension and tetrafluorination strategies affords polymer solar cells with > 16% efficiency. *Journal of the American Chemical Society*, **143**, 16, 6123 (2021). doi: [10.1021/jacs.1c00211](https://doi.org/10.1021/jacs.1c00211).
- [72] H. Wang, Y. He, Y. Li and H. Su. Photophysical and electronic properties of five PCBM-like C₆₀ derivatives: spectral and quantum chemical view. *The Journal of Physical Chemistry A*, **116**, 1, 255 (2012). doi: [10.1021/jp208520v](https://doi.org/10.1021/jp208520v).
- [73] H. W. Kroto, J. R. Heath, S. C. O'Brien, R. F. Curl and R. E. Smalley. C₆₀: Buckminsterfullerene. *Nature*, **318**, 6042, 162 (1985). doi: [10.1038/318162a0](https://doi.org/10.1038/318162a0).
- [74] M.-A. Pan, T.-K. Lau, Y. Tang, Y.-C. Wu, T. Liu, K. Li, M.-C. Chen, X. Lu, W. Ma and C. Zhan. 16.7%-efficiency ternary blended organic photovoltaic cells with PCBM as the acceptor additive to increase the open-circuit voltage and phase purity. *Journal of Materials Chemistry A*, **7**, 36, 20713 (2019). doi: [10.1039/c9ta06929a](https://doi.org/10.1039/c9ta06929a).
- [75] A. Seitkhan, M. Neophytou, R. K. Hallani, J. Troughton, N. Gasparini, H. Faber, E. Abou-Hamad, M. N. Hedhili, G. T. Harrison, D. Baran et al. A multilayered electron extracting system for efficient perovskite solar cells. *Advanced Functional Materials*, **30**, 43, 2004273 (2020). doi: [10.1002/adfm.202004273](https://doi.org/10.1002/adfm.202004273).
- [76] Y. Chen, C. Xu, J. Xiong, Z. Zhang, X. Zhang, J. Yang, X. Xue, D. Yang and J. Zhang. Benefits of fullerene/SnO₂ bilayers as electron transport layer for efficient planar perovskite solar cells. *Organic Electronics*, **58**, 294 (2018). doi: [10.1016/j.orgel.2018.03.041](https://doi.org/10.1016/j.orgel.2018.03.041).
- [77] Y. Bai, B. Yang, X. Chen, F. Wang, T. Hayat, A. Alsaedi and Z. Tan. Constructing desired vertical component distribution within a PBDB-T:ITIC-M photoactive layer via fine-tuning the surface free energy of a titanium chelate cathode buffer layer. *Frontiers in Chemistry*, **6**, 292 (2018). doi: [10.3389/fchem.2018.00292](https://doi.org/10.3389/fchem.2018.00292).
- [78] Y.-J. Xue, F.-Y. Cao, P.-K. Huang, Y.-C. Su and Y.-J. Cheng. Isomeric effect of fluorene-based fused-ring electron acceptors to achieve high-efficiency organic solar cells. *Journal of Materials Chemistry A*, **8**, 10, 5315 (2020). doi: [10.1039/c9ta14040a](https://doi.org/10.1039/c9ta14040a).
- [79] Y. Zhang, H. Feng, L. Meng, Y. Wang, M. Chang, S. Li, Z. Guo, C. Li, N. Zheng, Z. Xie et al. High performance thick-film nonfullerene organic solar cells with efficiency over 10% and active layer thickness of 600 nm. *Advanced Energy Materials*, **9**, 45, 1902688 (2019). doi: [10.1002/aenm.201902688](https://doi.org/10.1002/aenm.201902688).

- [80] R. Ma, T. Liu, Z. Luo, Q. Guo, Y. Xiao, Y. Chen, X. Li, S. Luo, X. Lu and M. Zhang. Improving open-circuit voltage by a chlorinated polymer donor endows binary organic solar cells efficiencies over 17%. *Science China: Chemistry*, **63**, 3, 325 (2020). doi: [10.1007/s11426-019-9669-3](https://doi.org/10.1007/s11426-019-9669-3).
- [81] J. Zhang, Y. Han, W. Zhang, J. Ge, L. Xie, Z. Xia, W. Song, D. Yang, X. Zhang and Z. Ge. High-efficiency thermal-annealing-free organic solar cells based on an asymmetric acceptor with improved thermal and air stability. *ACS Applied Materials & Interfaces*, **12**, 51, 57271 (2020). doi: [10.1021/acsami.0c17423](https://doi.org/10.1021/acsami.0c17423).
- [82] C.-K. Wang, B.-H. Jiang, J.-H. Lu, M.-T. Cheng, R.-J. Jeng, Y.-W. Lu, C.-P. Chen and K.-T. Wong. A near-infrared absorption small molecule acceptor for high-performance semitransparent and colorful binary and ternary organic photovoltaics. *ChemSusChem*, **13**, 5, 903 (2020). doi: [10.1002/cssc.201903087](https://doi.org/10.1002/cssc.201903087).
- [83] J. Fang, Q. Liu, J. Zhang, L. Ye, J. Wu, Z. Wei, X. Guo, M. Zhang and Y. Li. Efficient as-cast polymer solar cells with high and stabilized fill factor. *Solar RRL*, **4**, 10, 2000275 (2020). doi: [10.1002/solr.202000275](https://doi.org/10.1002/solr.202000275).
- [84] C. Li, Q. Yue, H. Wu, B. Li, H. Fan and X. Zhu. Small bandgap non-fullerene acceptor enables efficient PTB7-Th solar cell with near 0 eV HOMO offset. *Journal of Energy Chemistry*, **52**, 60 (2021). doi: [10.1016/j.jechem.2020.03.058](https://doi.org/10.1016/j.jechem.2020.03.058).
- [85] Y. Li, W. Su, F. Wu, Z. Xu, Y.-K. Wang, M. Zhang, Z.-Q. Jiang and L.-S. Liao. Near-infrared non-fullerene acceptors based on dithienyl [1, 2-b: 4, 5-b'] benzodithiophene core for high performance PTB7-Th-based polymer solar cells. *Organic Electronics*, **65**, 63 (2019). doi: [10.1016/j.orgel.2018.10.042](https://doi.org/10.1016/j.orgel.2018.10.042).
- [86] J. Lee, S.-J. Ko, M. Seifrid, H. Lee, B. R. Luginbuhl, A. Karki, M. Ford, K. Rosenthal, K. Cho, T.-Q. Nguyen et al. Bandgap narrowing in non-fullerene acceptors: single atom substitution leads to high optoelectronic response beyond 1000 nm. *Advanced Energy Materials*, **8**, 24, 1801212 (2018). doi: [10.1002/aenm.201801212](https://doi.org/10.1002/aenm.201801212).
- [87] R. Zhao, C. Dou, Z. Xie, J. Liu and L. Wang. Polymer acceptor based on b \leftarrow n units with enhanced electron mobility for efficient all-polymer solar cells. *Angewandte Chemie International Edition*, **55**, 17, 5313 (2016). doi: [10.1002/ange.201601305](https://doi.org/10.1002/ange.201601305).
- [88] M. Zhang, L. Zhu, G. Zhou, T. Hao, C. Qiu, Z. Zhao, Q. Hu, B. W. Larson, H. Zhu, Z. Ma et al. Single-layered organic photovoltaics with double cascading charge transport pathways: 18% efficiencies. *Nature Communications*, **12**, 1, 1 (2021). doi: [10.1038/s41467-020-20580-8](https://doi.org/10.1038/s41467-020-20580-8).

- [89] T. Liu, R. Ma, Z. Luo, Y. Guo, G. Zhang, Y. Xiao, T. Yang, Y. Chen, G. Li, Y. Yi et al. Concurrent improvement in jsc and voc in high-efficiency ternary organic solar cells enabled by a red-absorbing small-molecule acceptor with a high lumo level. *Energy & Environmental Science*, **13**, 7, 2115 (2020). doi: [10.1039/D0EE00662A](https://doi.org/10.1039/D0EE00662A).
- [90] W. Tang, W. Peng, M. Zhu, H. Jiang, W. Wang, H. Xia, R. Yang, O. Inganäs, H. Tan, Q. Bian et al. 17.25% high efficiency ternary solar cells with increased open-circuit voltage using a high homo level small molecule guest donor in a PM6:Y6 blend. *Journal of Materials Chemistry A*, **9**, 36, 20493 (2021). doi: [10.1039/D1TA05284E](https://doi.org/10.1039/D1TA05284E).
- [91] Y. Chen, T. Liu, L.-K. Ma, W. Xue, R. Ma, J. Zhang, C. Ma, H. K. Kim, H. Yu, F. Bai et al. Alkoxy substitution on IDT-series and Y-series non-fullerene acceptors yielding highly efficient organic solar cells. *Journal of Materials Chemistry A*, **9**, 12, 7481 (2021). doi: [10.1039/D0TA10953C](https://doi.org/10.1039/D0TA10953C).
- [92] X. Xu, K. Feng, Z. Bi, W. Ma, G. Zhang and Q. Peng. Single-junction polymer solar cells with 16.35% efficiency enabled by a platinum (ii) complexation strategy. *Advanced Materials*, **31**, 29, 1901872 (2019). doi: [10.1002/adma.201901872](https://doi.org/10.1002/adma.201901872).
- [93] H.-C. Wang, C.-H. Chen, R.-H. Li, Y.-C. Lin, C.-S. Tsao, B. Chang, S. Tan, Y. Yang and K.-H. Wei. Engineering the core units of small-molecule acceptors to enhance the performance of organic photovoltaics. *Solar RRL*, **4**, 10, 2000253 (2020). doi: [10.1002/solr.202000253](https://doi.org/10.1002/solr.202000253).
- [94] T. Gokulnath, J. Choi, H.-Y. Park, K. Sung, Y. Do, H. Park, J. Kim, S. S. Reddy, J. Kim and M. Song. A wide-bandgap -conjugated polymer for high-performance ternary organic solar cells with an efficiency of 17.40 *Nano Energy*, **89**, 106323 (2021). doi: [10.1016/j.nanoen.2021.106323](https://doi.org/10.1016/j.nanoen.2021.106323).
- [95] Y. Wang, J. Chen, H. D. Kim, B. Wang, R. Iriguchi and H. Ohkita. Ternary blend solar cells based on a conjugated polymer with diketopyrrolopyrrole and carbazole units. *Frontiers in Energy Research*, 113 (2018). doi: [10.3389/fenrg.2018.00113](https://doi.org/10.3389/fenrg.2018.00113).
- [96] H. K. Yoo, H. Lee, K. Lee, C. Kang, C.-S. Kee, I.-W. Hwang and J. W. Lee. Conditions for optimal efficiency of PCBM-based terahertz modulators. *AIP Advances*, **7**, 10, 105008 (2017). doi: [10.1063/1.5001561](https://doi.org/10.1063/1.5001561).
- [97] G. Sharma, T. Shanap, K. Patel and M. El-Mansy. Photovoltaic properties of bulk heterojunction devices based on CuI-PVA as electron donor and PCBM and

- modified PCBM as electron acceptor. *Materials Science-Poland*, **30**, 1, 10 (2012). doi: [10.2478/s13536-012-0003-6](https://doi.org/10.2478/s13536-012-0003-6).
- [98] P. P. Khlyabich, B. Burkhart, A. E. Rudenko and B. C. Thompson. Optimization and simplification of polymer–fullerene solar cells through polymer and active layer design. *Polymer*, **54**, 20, 5267 (2013). doi: [10.1016/j.polymer.2013.07.053](https://doi.org/10.1016/j.polymer.2013.07.053).
- [99] G. L. Schulz, M. Urdanpilleta, R. Fitzner, E. Brier, E. Mena-Osteritz, E. Reinold and P. Bäuerle. Optimization of solution-processed oligothiophene: fullerene based organic solar cells by using solvent additives. *Beilstein Journal of Nanotechnology*, **4**, 1, 680 (2013). doi: [10.3762/bjnano.4.77](https://doi.org/10.3762/bjnano.4.77).
- [100] H. Kim, a. C. Gilmore, A. Pique, J. Horwitz, H. Mattoussi, H. Murata, Z. Kafafi and D. Chrisey. Electrical, optical, and structural properties of indium–tin–oxide thin films for organic light-emitting devices. *Journal of Applied Physics*, **86**, 11, 6451 (1999). doi: [10.1063/1.371708](https://doi.org/10.1063/1.371708).
- [101] Z. Z. You and J. Y. Dong. Oxygen plasma treatment effects of indium-tin oxide in organic light-emitting devices. *Vacuum*, **81**, 7, 819 (2007). doi: [10.1016/j.vacuum.2006.09.004](https://doi.org/10.1016/j.vacuum.2006.09.004).
- [102] I. Irfan, S. Graber, F. So and Y. Gao. Interplay of cleaning and de-doping in oxygen plasma treated high work function indium tin oxide (ITO). *Organic Electronics*, **13**, 10, 2028 (2012). doi: [10.1016/j.orgel.2012.05.036](https://doi.org/10.1016/j.orgel.2012.05.036).
- [103] A. J. Gillett. Removing the spin-triplet loss pathway in organic solar cells: A strategy to enhance radiative efficiency and minimise energy loss. Ph.D. thesis, University of Cambridge (2019).
- [104] K. Goushi, K. Yoshida, K. Sato and C. Adachi. Organic light-emitting diodes employing efficient reverse intersystem crossing for triplet-to-singlet state conversion. *Nature Photonics*, **6**, 4, 253 (2012). doi: [10.1038/nphoton.2012.31](https://doi.org/10.1038/nphoton.2012.31).
- [105] Y. Tao, K. Yuan, T. Chen, P. Xu, H. Li, R. Chen, C. Zheng, L. Zhang and W. Huang. Thermally activated delayed fluorescence materials towards the breakthrough of organoelectronics. *Advanced Materials*, **26**, 47, 7931 (2014). doi: [10.1002/adma.201402532](https://doi.org/10.1002/adma.201402532).
- [106] A. Endo, K. Sato, K. Yoshimura, T. Kai, A. Kawada, H. Miyazaki and C. Adachi. Efficient up-conversion of triplet excitons into a singlet state and its application for organic light emitting diodes. *Applied Physics Letters*, **98**, 8, 42 (2011). doi: [10.1063/1.3558906](https://doi.org/10.1063/1.3558906).

- [107] H. Uoyama, K. Goushi, K. Shizu, H. Nomura and C. Adachi. Highly efficient organic light-emitting diodes from delayed fluorescence. *Nature*, **492**, 7428, 234 (2012). doi: [10.1038/nature11687](https://doi.org/10.1038/nature11687).
- [108] Q. Zhang, B. Li, S. Huang, H. Nomura, H. Tanaka and C. Adachi. Efficient blue organic light-emitting diodes employing thermally activated delayed fluorescence. *Nature Photonics*, **8**, 4, 326 (2014). doi: [10.1038/nphoton.2014.12](https://doi.org/10.1038/nphoton.2014.12).
- [109] H. Nakanotani, K. Masui, J. Nishide, T. Shibata and C. Adachi. Promising operational stability of high-efficiency organic light-emitting diodes based on thermally activated delayed fluorescence. *Scientific Reports*, **3**, 1, 1 (2013). doi: [10.1038/srep02127](https://doi.org/10.1038/srep02127).
- [110] N. Haase, A. Danos, C. Pflumm, A. Morherr, P. Stachelek, A. Mekic, W. Brutting and A. P. Monkman. Kinetic modeling of transient photoluminescence from thermally activated delayed fluorescence. *The Journal of Physical Chemistry C*, **122**, 51, 29173 (2018). doi: [10.1021/acs.jpcc.8b11020](https://doi.org/10.1021/acs.jpcc.8b11020).
- [111] P. Yuan, X. Qiao, D. Yan and D. Ma. Magnetic field effects on the quenching of triplet excitons in exciplex-based organic light emitting diodes. *Journal of Materials Chemistry C*, **6**, 21, 5721 (2018). doi: [10.1039/c8tc01260a](https://doi.org/10.1039/c8tc01260a).
- [112] N. Bunzmann, S. Weissenseel, L. Kudriashova, J. Gruene, B. Krugmann, J. V. Grazulevicius, A. Sperlich and V. Dyakonov. Optically and electrically excited intermediate electronic states in donor: acceptor based OLEDs. *Materials Horizons*, **7**, 4, 1126 (2020). doi: [10.1039/c9mh01475f](https://doi.org/10.1039/c9mh01475f).
- [113] Q. Huang, S. Zhao, P. Wang, Z. Qin, Z. Xu, D. Song, B. Qiao and X. Xu. Investigating the evolution of exciplex states in thermally activated delayed fluorescence organic light-emitting diodes by transient measurement. *Journal of Luminescence*, **201**, 38 (2018). doi: [10.1016/j.jlumin.2018.03.094](https://doi.org/10.1016/j.jlumin.2018.03.094).
- [114] H. A. Al Attar and A. P. Monkman. Electric field induce blue shift and intensity enhancement in 2D exciplex organic light emitting diodes; controlling electron-hole separation. *Advanced Materials*, **28**, 36, 8014 (2016). doi: [10.1002/adma.201600965](https://doi.org/10.1002/adma.201600965).
- [115] N. A. Drigo, L. G. Kudriashova, S. Weissenseel, A. Sperlich, A. J. Huckaba, M. K. Nazeeruddin and V. Dyakonov. Photophysics of deep blue acridane- and benzonitrile-based emitter employing thermally activated delayed fluorescence. *The Journal of Physical Chemistry C*, **122**, 39, 22796 (2018). doi: [10.1021/acs.jpcc.8b08716](https://doi.org/10.1021/acs.jpcc.8b08716).

- [116] T. Kobayashi, D. Kawate, A. Niwa, T. Nagase, K. Goushi, C. Adachi and H. Naito. Intersystem crossing rate in thermally activated delayed fluorescence emitters. *physica status solidi (a)*, **217**, 3, 1900616 (2020). doi: [10.1002/pssa.201900616](https://doi.org/10.1002/pssa.201900616).
- [117] S. Weissenseel, N. A. Drigo, L. G. Kudriashova, M. Schmid, T. Morgenstern, K.-H. Lin, A. Prlj, C. Corminboeuf, A. Sperlich, W. Brütting et al. Getting the right twist: influence of donor–acceptor dihedral angle on exciton kinetics and singlet–triplet gap in deep blue thermally activated delayed fluorescence emitter. *The Journal of Physical Chemistry C*, **123**, 45, 27778 (2019). doi: [10.1021/acs.jpcc.9b08269](https://doi.org/10.1021/acs.jpcc.9b08269).
- [118] M. A. Baldo, C. Adachi and S. R. Forrest. Transient analysis of organic electrophosphorescence. II. Transient analysis of triplet–triplet annihilation. *Physical Review B*, **62**, 16, 10967 (2000). doi: [10.1103/physrevb.62.10967](https://doi.org/10.1103/physrevb.62.10967).
- [119] B. Ruhstaller, S. Carter, S. Barth, H. Riel, W. Riess and J. Scott. Transient and steady-state behavior of space charges in multilayer organic light-emitting diodes. *Journal of Applied Physics*, **89**, 8, 4575 (2001). doi: [10.1063/1.1352027](https://doi.org/10.1063/1.1352027).
- [120] Y. Zhang, M. Whited, M. E. Thompson and S. R. Forrest. Singlet–triplet quenching in high intensity fluorescent organic light emitting diodes. *Chemical Physics Letters*, **495**, 4-6, 161 (2010). doi: [10.1016/j.cplett.2010.06.079](https://doi.org/10.1016/j.cplett.2010.06.079).
- [121] C. Li, Y. Xu, Y. Liu, Z. Ren, Y. Ma and S. Yan. Highly efficient white-emitting thermally activated delayed fluorescence polymers: Synthesis, non-doped white OLEDs and electroluminescent mechanism. *Nano Energy*, **65**, 104057 (2019). doi: [10.1016/j.nanoen.2019.104057](https://doi.org/10.1016/j.nanoen.2019.104057).
- [122] C. Murawski, K. Leo and M. C. Gather. Efficiency roll-off in organic light-emitting diodes. *Advanced Materials*, **25**, 47, 6801 (2013). doi: [10.1002/adma.201301603](https://doi.org/10.1002/adma.201301603).
- [123] H. Yersin, A. F. Rausch, R. Czerwieniec, T. Hofbeck and T. Fischer. The triplet state of organo-transition metal compounds. Triplet harvesting and singlet harvesting for efficient OLEDs. *Coordination Chemistry Reviews*, **255**, 21-22, 2622 (2011). doi: [10.1016/j.ccr.2011.01.042](https://doi.org/10.1016/j.ccr.2011.01.042).
- [124] R. Czerwieniec, M. J. Leitzl, H. H. Homeier and H. Yersin. Cu (I) complexes–thermally activated delayed fluorescence. photophysical approach and material design. *Coordination Chemistry Reviews*, **325**, 2 (2016). doi: [10.1016/j.ccr.2016.06.016](https://doi.org/10.1016/j.ccr.2016.06.016).

- [125] J. M. Choi, W. Lee, K. K. Kim and J. Y. Lee. Exciton management by co-doping of blue triplet emitter as a lifetime improving method of blue thermally activated delayed fluorescent devices. *Organic Electronics*, **45**, 104 (2017). doi: [10.1016/j.orgel.2017.03.003](https://doi.org/10.1016/j.orgel.2017.03.003).
- [126] A. Niwa, S. Haseyama, T. Kobayashi, T. Nagase, K. Goushi, C. Adachi and H. Naito. Triplet-triplet annihilation in a thermally activated delayed fluorescence emitter lightly doped in a host. *Applied Physics Letters*, **113**, 8, 083301 (2018). doi: [10.1063/1.5025870](https://doi.org/10.1063/1.5025870).
- [127] V. Dyakonov, G. Rösler, M. Schwoerer and E. Frankevich. Evidence for triplet interchain polaron pairs and their transformations in polyphenylenevinylene. *Physical Review B*, **56**, 7, 3852 (1997). doi: [10.1103/physrevb.56.3852](https://doi.org/10.1103/physrevb.56.3852).
- [128] D. Stich, F. Späth, H. Kraus, A. Sperlich, V. Dyakonov and T. Hertel. Triplet-triplet exciton dynamics in single-walled carbon nanotubes. *Nature Photonics*, **8**, 2, 139 (2014). doi: [10.1038/nphoton.2013.316](https://doi.org/10.1038/nphoton.2013.316).
- [129] S. Reineke, K. Walzer and K. Leo. Triplet-exciton quenching in organic phosphorescent light-emitting diodes with Ir-based emitters. *Physical Review B*, **75**, 12, 125328 (2007). doi: [10.1103/physrevb.75.125328](https://doi.org/10.1103/physrevb.75.125328).
- [130] M. Baldo, R. Holmes and S. Forrest. Prospects for electrically pumped organic lasers. *Physical Review B*, **66**, 3, 035321 (2002). doi: [10.1103/physrevb.66.035321](https://doi.org/10.1103/physrevb.66.035321).
- [131] D. Tanaka, T. Takeda, T. Chiba, S. Watanabe and J. Kido. Novel electron-transport material containing boron atom with a high triplet excited energy level. *Chemistry Letters*, **36**, 2, 262 (2007). doi: [10.1246/cl.2007.262](https://doi.org/10.1246/cl.2007.262).
- [132] T. Jiang, Y. Liu, Z. Ren and S. Yan. The design, synthesis and performance of thermally activated delayed fluorescence macromolecules. *Polymer Chemistry*, **11**, 9, 1555 (2020). doi: [10.1039/d0py00096e](https://doi.org/10.1039/d0py00096e).
- [133] E. Hontz, W. Chang, D. N. Congreve, V. Bulovic, M. A. Baldo and T. Van Voorhis. The role of electron-hole separation in thermally activated delayed fluorescence in donor-acceptor blends. *The Journal of Physical Chemistry C*, **119**, 45, 25591 (2015). doi: [10.1021/acs.jpcc.5b07340](https://doi.org/10.1021/acs.jpcc.5b07340).
- [134] F. B. Dias, J. Santos, D. R. Graves, P. Data, R. S. Nobuyasu, M. A. Fox, A. S. Batsanov, T. Palmeira, M. N. Berberan-Santos, M. R. Bryce et al. The role of local triplet

- excited states and d-a relative orientation in thermally activated delayed fluorescence: photophysics and devices. *Advanced Science*, **3**, 12, 1600080 (2016). doi: [10.1002/advs.201600080](https://doi.org/10.1002/advs.201600080).
- [135] J. Shinar. Optically detected magnetic resonance studies of luminescence-quenching processes in π -conjugated materials and organic light-emitting devices. *Laser & Photonics Reviews*, **6**, 6, 767 (2012). doi: [10.1002/lpor.201100026](https://doi.org/10.1002/lpor.201100026).
- [136] R. Liu, Y. Zhang, Y. Lei, P. Chen and Z. Xiong. Magnetic field dependent triplet-triplet annihilation in Alq₃-based organic light emitting diodes at different temperatures. *Journal of Applied Physics*, **105**, 9, 093719 (2009). doi: [10.1063/1.3125507](https://doi.org/10.1063/1.3125507).
- [137] J. Xiang, Y. Chen, W. Jia, L. Chen, Y. Lei, Q. Zhang and Z. Xiong. Realization of triplet-triplet annihilation in planar heterojunction exciplex-based organic light-emitting diodes. *Organic Electronics*, **28**, 94 (2016). doi: [10.1016/j.orgel.2015.10.017](https://doi.org/10.1016/j.orgel.2015.10.017).
- [138] R. Scholz, P. Kleine, R. Lygaitis, L. Popp, S. Lenk, M. K. Etherington, A. P. Monkman and S. Reineke. Investigation of thermally activated delayed fluorescence from a donor-acceptor compound with time-resolved fluorescence and density functional theory applying an optimally tuned range-separated hybrid functional. *The Journal of Physical Chemistry A*, **124**, 8, 1535 (2020). doi: [10.1021/acs.jpca.9b11083](https://doi.org/10.1021/acs.jpca.9b11083).
- [139] E. Goovaerts. Optically detected magnetic resonance (ODMR). *eMagRes*, 343–358 (2007). doi: [10.1002/9780470034590.emrstm1524](https://doi.org/10.1002/9780470034590.emrstm1524).
- [140] A. van der Est. Continuous-wave EPR. *eMagRes*, 1411–1422 (2007). doi: [10.1002/9780470034590.emrstm1508](https://doi.org/10.1002/9780470034590.emrstm1508).
- [141] D. Kaplan, M. Browne and J. Cowen. Pulsed x-band EPR spectrometer. *Review of Scientific Instruments*, **32**, 11, 1182 (1961). doi: [10.1063/1.1717202](https://doi.org/10.1063/1.1717202).
- [142] G. Jeschke, M. Sajid, M. Schulte and A. Godt. Three-spin correlations in double electron-electron resonance. *Physical Chemistry Chemical Physics*, **11**, 31, 6580 (2009). doi: [10.1039/b905724b](https://doi.org/10.1039/b905724b).
- [143] A. Milov, A. Maryasov and Y. D. Tsvetkov. Pulsed electron double resonance (peldor) and its applications in free-radicals research. *Applied Magnetic Resonance*, **15**, 1, 107 (1998). doi: [10.1007/bf03161886](https://doi.org/10.1007/bf03161886).

- [144] A. Kastler. Quelques suggestions concernant la production optique et la détection optique d'une inégalité de population des niveaux de quantification spatiale des atomes. Application à l'expérience de stern et gerlach et à la résonance magnétique. *Journal de Physique et Le Radium*, **11**, 6, 255 (1950). doi: [10.1051/j-physrad:01950001106025500](https://doi.org/10.1051/j-physrad:01950001106025500).
- [145] V. Dyakonov, N. Gauss, G. Rösler, S. Karg, W. Rieß and M. Schwoerer. Electron spin resonance in PPV-photodiodes: detection via photoinduced current. *Chemical Physics*, **189**, 3, 687 (1994). doi: [10.1016/0301-0104\(94\)00340-8](https://doi.org/10.1016/0301-0104(94)00340-8).
- [146] A. L. Kwiram. Optical detection of paramagnetic resonance in phosphorescent triplet states. *Chemical Physics Letters*, **1**, 7, 272 (1967). doi: [10.1016/0009-2614\(67\)80017-4](https://doi.org/10.1016/0009-2614(67)80017-4).
- [147] J. Schmidt, I. Hesselmann, M. De Groot and J. Van der Waals. Optical detection of electron resonance transitions in phosphorescent quinoxaline. *Chemical Physics Letters*, **1**, 10, 434 (1967). doi: [10.1016/0009-2614\(67\)85066-8](https://doi.org/10.1016/0009-2614(67)85066-8).
- [148] M. Sharnoff. Esr-produced modulation of triplet phosphorescence. *The Journal of Chemical Physics*, **46**, 8, 3263 (1967). doi: [10.1063/1.1841199](https://doi.org/10.1063/1.1841199).
- [149] P. Lane, X. Wei, Z. Vardeny, J. Partee and J. Shinar. Optically detected magnetic-resonance study of triplet-state dynamics in C₇₀. *Physical Review B*, **53**, 12, R7580 (1996). doi: [10.1103/PhysRevB.53.R7580](https://doi.org/10.1103/PhysRevB.53.R7580).
- [150] G. Li, J. Shinar and G. Jabbour. Electroluminescence-detected magnetic resonance studies of Pt octaethyl porphyrin-based phosphorescent organic light-emitting devices. *Physical Review B*, **71**, 23, 235211 (2005). doi: [10.1103/physrevb.71.235211](https://doi.org/10.1103/physrevb.71.235211).
- [151] M. W. Doherty, N. B. Manson, P. Delaney, F. Jelezko, J. Wrachtrup and L. C. Hollenberg. The nitrogen-vacancy colour centre in diamond. *Physics Reports*, **528**, 1, 1 (2013). doi: [10.1016/j.physrep.2013.02.001](https://doi.org/10.1016/j.physrep.2013.02.001).
- [152] M. Scharber, N. Schultz, N. Sariciftci and C. Brabec. Optical-and photocurrent-detected magnetic resonance studies on conjugated polymer/fullerene composites. *Physical Review B*, **67**, 8, 085202 (2003). doi: [10.1103/physrevb.67.085202](https://doi.org/10.1103/physrevb.67.085202).
- [153] S. Vāth, K. Tvingstedt, M. Auth, A. Sperlich, A. Dabuliene, J. V. Grazulevicius, P. Stakhira, V. Cherpak and V. Dyakonov. Direct observation of spin states involved in organic electroluminescence based on thermally activated

- delayed fluorescence. *Advanced Optical Materials*, **5**, 3, 1600926 (2017). doi: [10.1002/adom.201600926](https://doi.org/10.1002/adom.201600926).
- [154] M.-K. Lee, M. Segal, Z. Soos, J. Shinar and M. Baldo. Yield of singlet excitons in organic light-emitting devices: A double modulation photoluminescence-detected magnetic resonance study. *Physical Review Letters*, **94**, 13, 137403 (2005). doi: [10.1103/physrevlett.94.137403](https://doi.org/10.1103/physrevlett.94.137403).
- [155] M. Huisjen and J. S. Hyde. A pulsed EPR spectrometer. *Review of Scientific Instruments*, **45**, 5, 669 (1974). doi: [10.1063/1.1686710](https://doi.org/10.1063/1.1686710).
- [156] P. Dawson, B. Cavenett and G. Sowersby. Pulsed optically detected resonance in semiconductors. *Solid-State Electronics*, **21**, 11-12, 1451 (1978). doi: [10.1016/0038-1101\(78\)90223-x](https://doi.org/10.1016/0038-1101(78)90223-x).
- [157] S. Stoll. Pulse EPR. *eMagRes*, 23–38 (2007). doi: [10.1002/9780470034590.emrstm1510](https://doi.org/10.1002/9780470034590.emrstm1510).
- [158] X. Liu, H. Popli, O. Kwon, H. Malissa, X. Pan, B. Park, B. Choi, S. Kim, E. Ehrenfreund and C. Boehme. Isotope effect in the magneto-optoelectronic response of organic light-emitting diodes based on donor–acceptor exciplexes. *Advanced Materials*, **32**, 48, 2004421 (2020). doi: [10.1002/adma.202004421](https://doi.org/10.1002/adma.202004421).
- [159] Y. Sheng, T. Nguyen, G. Veeraraghavan, . Mermer, M. Wohlgenannt, S. Qiu and U. Scherf. Hyperfine interaction and magnetoresistance in organic semiconductors. *Physical Review B*, **74**, 4, 045213 (2006). doi: [10.1103/physrevb.74.045213](https://doi.org/10.1103/physrevb.74.045213).
- [160] W. Baker, D. McCamey, K. Van Schooten, J. M. Lupton and C. Boehme. Differentiation between polaron-pair and triplet-exciton polaron spin-dependent mechanisms in organic light-emitting diodes by coherent spin beating. *Physical Review B*, **84**, 16, 165205 (2011). doi: [10.1103/physrevb.84.165205](https://doi.org/10.1103/physrevb.84.165205).
- [161] W. Baker, T. Keevers, J. Lupton, D. McCamey and C. Boehme. Slow hopping and spin dephasing of coulombically bound polaron pairs in an organic semiconductor at room temperature. *Physical Review Letters*, **108**, 26, 267601 (2012). doi: [10.1103/physrevlett.108.267601](https://doi.org/10.1103/physrevlett.108.267601).
- [162] D. Dunstan and J. Davies. The behaviour of donor-acceptor recombination emission in II-VI crystals subjected to magnetic resonance. *Journal of Physics C: Solid State Physics*, **12**, 14, 2927 (1979). doi: [10.1088/0022-3719/12/14/027](https://doi.org/10.1088/0022-3719/12/14/027).

- [163] R. Street. Recombination in a-Si: H: spin-dependent effects. *Physical Review B*, **26**, 7, 3588 (1982). doi: [10.1103/PhysRevB.26.3588](https://doi.org/10.1103/PhysRevB.26.3588).
- [164] F. Koschnick, T. Hangleiter, K. Song and J. Spaeth. Optically detected magnetic resonance study of an oxygen-vacancy complex in bafbr. *Journal of Physics: Condensed Matter*, **7**, 34, 6925 (1995). doi: [10.1088/0953-8984/7/34/015](https://doi.org/10.1088/0953-8984/7/34/015).
- [165] L. Langof, E. Ehrenfreund, E. Lifshitz, O. Micic and A. Nozik. Continuous-wave and time-resolved optically detected magnetic resonance studies of nonetched/etched inp nanocrystals. *The Journal of Physical Chemistry B*, **106**, 7, 1606 (2002). doi: [10.1021/jp013720g](https://doi.org/10.1021/jp013720g).
- [166] E. H. Fooks and R. A. Zakarevicius. *Microwave engineering using microstrip circuits*. Prentice-Hall, Inc. (1990).
- [167] S.-Y. Lee, S. Paik, D. R. McCamey and C. Boehme. Modulation frequency dependence of continuous-wave optically/electrically detected magnetic resonance. *Physical Review B*, **86**, 11, 115204 (2012). doi: [10.1103/physrevb.86.115204](https://doi.org/10.1103/physrevb.86.115204).
- [168] J. Shinar. Trapped polarons, free polarons and triplet excitons in π -conjugated polymer films and light-emitting diodes. *Synthetic Metals*, **78**, 3, 277 (1996). doi: [10.1016/0379-6779\(96\)80150-0](https://doi.org/10.1016/0379-6779(96)80150-0).
- [169] H. Kraus, M. C. Heiber, S. V ath, J. Kern, C. Deibel, A. Sperlich and V. Dyakonov. Analysis of triplet exciton loss pathways in PTB7:PC₇₁BM bulk heterojunction solar cells. *Scientific Reports*, **6**, 1, 1 (2016). doi: [10.1038/srep29158](https://doi.org/10.1038/srep29158).
- [170] P. Cheng and X. Zhan. Stability of organic solar cells: challenges and strategies. *Chemical Society Reviews*, **45**, 9, 2544 (2016). doi: [10.1039/c5cs00593k](https://doi.org/10.1039/c5cs00593k).
- [171] L. Duan, Y. Zhang, M. He, R. Deng, H. Yi, Q. Wei, Y. Zou and A. Uddin. Burn-in degradation mechanism identified for small molecular acceptor-based high-efficiency nonfullerene organic solar cells. *ACS Applied Materials Interfaces*, **12**, 24, 27433 (2020). doi: [10.1021/acsami.0c05978](https://doi.org/10.1021/acsami.0c05978).
- [172] G. Jeschke. Determination of the nanostructure of polymer materials by electron paramagnetic resonance spectroscopy. *Macromolecular Rapid Communications*, **23**, 4, 227 (2002). doi: [10.1002/1521-3927\(20020301\)23:4<227::aid-marc227>3.0.co;2-d](https://doi.org/10.1002/1521-3927(20020301)23:4<227::aid-marc227>3.0.co;2-d).

- [173] B. Z. Tedlla, F. Zhu, M. Cox, B. Koopmans and E. Goovaerts. Spin-dependent photophysics in polymers lightly doped with fullerene derivatives: Photoluminescence and electrically detected magnetic resonance. *Physical Review B*, **91**, 8, 085309 (2015). doi: [10.1103/physrevb.91.085309](https://doi.org/10.1103/physrevb.91.085309).
- [174] T. Keevers, W. Baker and D. McCamey. Theory of exciton-polaron complexes in pulsed electrically detected magnetic resonance. *Physical Review B*, **91**, 20, 205206 (2015). doi: [10.1103/physrevb.91.205206](https://doi.org/10.1103/physrevb.91.205206).
- [175] M. S. Kotova, G. Londi, J. Junker, S. Dietz, A. Privitera, K. Tvingstedt, D. Beljonne, A. Sperlich and V. Dyakonov. On the absence of triplet exciton loss pathways in non-fullerene acceptor based organic solar cells. *Materials Horizons*, **7**, 6, 1641 (2020). doi: [10.1039/d0mh00286k](https://doi.org/10.1039/d0mh00286k).
- [176] P. Deotare, W. Chang, E. Hontz, D. Congreve, L. Shi, P. Reuswig, B. Modtland, M. Bahlke, C. Lee and A. Willard. Nanoscale transport of charge-transfer states in organic donor-acceptor blends. *Nature Materials*, **14**, 11, 1130 (2015). doi: [10.1038/nmat4424](https://doi.org/10.1038/nmat4424).
- [177] Y. Wang, K. Sahin-Tiras, N. J. Harmon, M. Wohlgenannt and M. E. Flatté. Immense magnetic response of exciplex light emission due to correlated spin-charge dynamics. *Physical Review X*, **6**, 1, 011011 (2016). doi: [10.1103/physrevx.6.011011](https://doi.org/10.1103/physrevx.6.011011).
- [178] A. J. Gillett, C. Tonnelé, G. Londi, G. Ricci, M. Catherin, D. M. Unson, D. Casanova, F. Castet, Y. Olivier, W. M. Chen et al. Spontaneous exciton dissociation enables spin state interconversion in delayed fluorescence organic semiconductors. *Nature Communications*, **12**, 1, 1 (2021). doi: [10.1038/s41467-021-26689-8](https://doi.org/10.1038/s41467-021-26689-8).
- [179] J. Benduhn, F. Piersimoni, G. Londi, A. Kirch, J. Widmer, C. Koerner, D. Beljonne, D. Neher, D. Spoltore and K. Vandewal. Impact of triplet excited states on the open-circuit voltage of organic solar cells. *Advanced Energy Materials*, **8**, 21, 1800451 (2018). doi: [10.1002/aenm.201800451](https://doi.org/10.1002/aenm.201800451).
- [180] Z. Chen, X. Chen, Z. Jia, G. Zhou, J. Xu, Y. Wu, X. Xia, X. Li, X. Zhang and C. Deng. Triplet exciton formation for non-radiative voltage loss in high-efficiency non-fullerene organic solar cells. *Joule* (2021). doi: [10.1016/j.joule.2021.04.002](https://doi.org/10.1016/j.joule.2021.04.002).
- [181] J. Hofinger, C. Putz, F. Mayr, K. Gugujonovic, D. Wielend and M. C. Scharber. Understanding the low voltage losses in high-performance non-fullerene acceptor-based organic solar cells. *Materials Advances* (2021). doi: [10.1039/d1ma00293g](https://doi.org/10.1039/d1ma00293g).

- [182] V. C. Nikolis, J. Benduhn, F. Holzmueller, F. Piersimoni, M. Lau, O. Zeika, D. Neher, C. Koerner, D. Spoltore and K. Vandewal. Reducing voltage losses in cascade organic solar cells while maintaining high external quantum efficiencies. *Advanced Energy Materials*, **7**, 21, 1700855 (2017). doi: [10.1002/aenm.201700855](https://doi.org/10.1002/aenm.201700855).
- [183] W. Shockley and H. J. Queisser. Detailed balance limit of efficiency of p-n junction solar cells. *Journal of Applied Physics*, **32**, 3, 510 (1961). doi: [10.4324/9781315793245-44](https://doi.org/10.4324/9781315793245-44).
- [184] U. Rau. Reciprocity relation between photovoltaic quantum efficiency and electroluminescent emission of solar cells. *Physical Review B*, **76**, 8, 085303 (2007). doi: [10.1103/physrevb.76.085303](https://doi.org/10.1103/physrevb.76.085303).
- [185] X. Wan, C. Li, M. Zhang and Y. Chen. Acceptor–donor–acceptor type molecules for high performance organic photovoltaics—chemistry and mechanism. *Chemical Society Reviews*, **49**, 9, 2828 (2020). doi: [10.1039/d0cs00084a](https://doi.org/10.1039/d0cs00084a).
- [186] S. Karuthedath, J. Gorenflot, Y. Firdaus, N. Chaturvedi, C. S. De Castro, G. T. Harrison, J. I. Khan, A. Markina, A. H. Balawi, T. A. D. Peña et al. Intrinsic efficiency limits in low-bandgap non-fullerene acceptor organic solar cells. *Nature Materials*, **20**, 3, 378 (2021). doi: [10.1038/s41563-020-00835-x](https://doi.org/10.1038/s41563-020-00835-x).
- [187] W. Chang, D. N. Congreve, E. Hontz, M. E. Bahlke, D. P. McMahon, S. Reineke, T. C. Wu, V. Bulović, T. Van Voorhis and M. A. Baldo. Spin-dependent charge transfer state design rules in organic photovoltaics. *Nature communications*, **6**, 1, 1 (2015). doi: [10.1038/ncomms7415](https://doi.org/10.1038/ncomms7415).
- [188] I. Ramirez, A. Privitera, S. Karuthedath, A. Jungbluth, J. Benduhn, A. Sperlich, D. Spoltore, K. Vandewal, F. Laquai and M. Riede. The role of spin in the degradation of organic photovoltaics. *Nature Communications*, **12**, 1, 1 (2021). doi: [10.1038/s41467-020-20601-6](https://doi.org/10.1038/s41467-020-20601-6).
- [189] S. A. Thomson, J. Niklas, K. L. Mardis, C. Mallares, I. D. Samuel and O. G. Poluektov. Charge separation and triplet exciton formation pathways in small-molecule solar cells as studied by time-resolved EPR spectroscopy. *The Journal of Physical Chemistry C*, **121**, 41, 22707 (2017). doi: [10.1021/acs.jpcc.7b08217](https://doi.org/10.1021/acs.jpcc.7b08217).
- [190] A. Rao, P. C. Chow, S. Gélinas, C. W. Schlenker, C.-Z. Li, H.-L. Yip, A. K.-Y. Jen, D. S. Ginger and R. H. Friend. The role of spin in the kinetic control of recombination in organic photovoltaics. *Nature*, **500**, 7463, 435 (2013). doi: [10.1038/nature12339](https://doi.org/10.1038/nature12339).

- [191] K. Wang, H. Chen, J. Zhang, Y. Zou and Y. Yang. Intrachain and interchain exciton–exciton annihilation in donor–acceptor copolymers. *The Journal of Physical Chemistry Letters*, **12**, 16, 3928 (2021). doi: [10.1021/acs.jpcclett.1c00369](https://doi.org/10.1021/acs.jpcclett.1c00369).
- [192] J. Han, X. Wang, D. Huang, C. Yang, R. Yang and X. Bao. Employing asymmetrical thieno [3, 4-d] pyridazin-1 (2 H)-one block enables efficient ternary polymer solar cells with improved light-harvesting and morphological properties. *Macromolecules*, **53**, 15, 6619 (2020). doi: [10.1021/acs.macromol.0c00459](https://doi.org/10.1021/acs.macromol.0c00459).
- [193] L. Ma, H. Yao, J. Wang, Y. Xu, M. Gao, Y. Zu, Y. Cui, S. Zhang, L. Ye and J. Hou. Impact of electrostatic interaction on bulk morphology in efficient donor–acceptor photovoltaic blends. *Angewandte Chemie* (2021). doi: [10.1002/ange.202102622](https://doi.org/10.1002/ange.202102622).
- [194] R. Wang, J. Yuan, R. Wang, G. Han, T. Huang, W. Huang, J. Xue, H. Wang, C. Zhang and C. Zhu. Rational tuning of molecular interaction and energy level alignment enables high-performance organic photovoltaics. *Advanced Materials*, **31**, 43, 1904215 (2019). doi: [10.1002/adma.201904215](https://doi.org/10.1002/adma.201904215).
- [195] Y. Xiang, Y. Zhao, N. Xu, S. Gong, F. Ni, K. Wu, J. Luo, G. Xie, Z.-H. Lu and C. Yang. Halogen-induced internal heavy-atom effect shortening the emissive lifetime and improving the fluorescence efficiency of thermally activated delayed fluorescence emitters. *Journal of Materials Chemistry C*, **5**, 46, 12204 (2017). doi: [10.1039/c7tc04181k](https://doi.org/10.1039/c7tc04181k).
- [196] Q. Fan, T. Liu, W. Gao, Y. Xiao, J. Wu, W. Su, X. Guo, X. Lu, C. Yang and H. Yan. Overcoming the energy loss in asymmetrical non-fullerene acceptor-based polymer solar cells by halogenation of polymer donors. *Journal of Materials Chemistry A*, **7**, 25, 15404 (2019). doi: [10.1039/c9ta02243k](https://doi.org/10.1039/c9ta02243k).
- [197] R. Ma, T. Yang, Y. Xiao, T. Liu, G. Zhang, Z. Luo, G. Li, X. Lu, H. Yan and B. Tang. Air-processed efficient organic solar cells from aromatic hydrocarbon solvent without solvent additive or post-treatment: Insights into solvent effect on morphology. *Energy Environmental Materials* (2021). doi: [10.1002/eem2.12226](https://doi.org/10.1002/eem2.12226).
- [198] F. D. Eisner, M. Azzouzi, Z. Fei, X. Hou, T. D. Anthopoulos, T. J. S. Dennis, M. Heeney and J. Nelson. Hybridization of local exciton and charge-transfer states reduces nonradiative voltage losses in organic solar cells. *Journal of the American Chemical Society*, **141**, 15, 6362 (2019). doi: [10.29363/nanoge.nfm.2019.227](https://doi.org/10.29363/nanoge.nfm.2019.227).

- [199] J. De Ceuster, E. Goovaerts, A. Bouwen and V. Dyakonov. Recombination of triplet excitons and polaron pairs in a derived paraphenylene vinylene pentamer. *Physical Review B*, **68**, 12, 125202 (2003). doi: [10.1103/physrevb.68.125202](https://doi.org/10.1103/physrevb.68.125202).
- [200] R. Wang, C. Zhang, Q. Li, Z. Zhang, X. Wang and M. Xiao. Charge separation from an intra-moiety intermediate state in the high-performance PM6:Y6 organic photovoltaic blend. *Journal of the American Chemical Society*, **142**, 29, 12751 (2020). doi: [10.1021/jacs.0c04890](https://doi.org/10.1021/jacs.0c04890).
- [201] L. Zhu, M. Zhang, G. Zhou, T. Hao, J. Xu, J. Wang, C. Qiu, N. Prine, J. Ali and W. Feng. Efficient organic solar cell with 16.88% efficiency enabled by refined acceptor crystallization and morphology with improved charge transfer and transport properties. *Advanced Energy Materials*, **10**, 18, 1904234 (2020). doi: [10.1002/aenm.201904234](https://doi.org/10.1002/aenm.201904234).
- [202] G. Zhang, X.-K. Chen, J. Xiao, P. C. Chow, M. Ren, G. Kupgan, X. Jiao, C. Chan, X. Du, R. Xia et al. Delocalization of exciton and electron wavefunction in non-fullerene acceptor molecules enables efficient organic solar cells. *Nature Communications*, **11**, 1, 1 (2020). doi: [10.1038/s41467-020-17867-1](https://doi.org/10.1038/s41467-020-17867-1).
- [203] Y. Li, H. Meng, J. Huang and C. Zhan. Structural cutting of non-fullerene acceptors by chlorination: effects of substituent number on device performance. *ACS Applied Materials Interfaces*, **12**, 45, 50541 (2020). doi: [10.1021/acsami.0c16389](https://doi.org/10.1021/acsami.0c16389).
- [204] J. Yuan, Y. Zhang, L. Zhou, G. Zhang, H.-L. Yip, T.-K. Lau, X. Lu, C. Zhu, H. Peng, P. A. Johnson et al. Single-junction organic solar cell with over 15% efficiency using fused-ring acceptor with electron-deficient core. *Joule*, **3**, 4, 1140 (2019). doi: [10.1016/j.joule.2019.01.004](https://doi.org/10.1016/j.joule.2019.01.004).
- [205] A. Karki, J. Vollbrecht, A. L. Dixon, N. Schopp, M. Schrock, G. M. Reddy and T. Nguyen. Understanding the high performance of over 15% efficiency in single-junction bulk heterojunction organic solar cells. *Advanced Materials*, **31**, 48, 1903868 (2019). doi: [10.1002/adma.201903868](https://doi.org/10.1002/adma.201903868).
- [206] V. Vohra, K. Kawashima, T. Kakara, T. Koganezawa, I. Osaka, K. Takimiya and H. Murata. Efficient inverted polymer solar cells employing favourable molecular orientation. *Nature Photonics*, **9**, 6, 403 (2015). doi: [10.1038/nphoton.2015.84](https://doi.org/10.1038/nphoton.2015.84).
- [207] C. Grieco, G. S. Doucette, R. D. Pensack, M. M. Payne, A. Rimshaw, G. D. Scholes, J. E. Anthony and J. B. Asbury. Dynamic exchange during triplet transport in

- nanocrystalline tips-pentacene films. *Journal of the American Chemical Society*, **138**, 49, 16069 (2016). doi: [10.1021/jacs.6b10010](https://doi.org/10.1021/jacs.6b10010).
- [208] Y. Zhang and S. R. Forrest. Triplet diffusion leads to triplet–triplet annihilation in organic phosphorescent emitters. *Chemical Physics Letters*, **590**, 106 (2013). doi: [10.1016/j.cplett.2013.10.048](https://doi.org/10.1016/j.cplett.2013.10.048).
- [209] E. W. Evans, Y. Olivier, Y. Puttison, W. K. Myers, T. J. Hele, S. M. Menke, T. H. Thomas, D. Credgington, D. Beljonne, R. H. Friend et al. Vibrationally assisted intersystem crossing in benchmark thermally activated delayed fluorescence molecules. *The Journal of Physical Chemistry Letters*, **9**, 14, 4053 (2018). doi: [10.1021/acs.jpcllett.8b01556](https://doi.org/10.1021/acs.jpcllett.8b01556).
- [210] R. Berera, R. van Grondelle and J. Kennis. Ultrafast transient absorption spectroscopy: principles and application to photosynthetic systems. *Photosynthesis Research*, **101**, 2, 105 (2009). doi: [10.1007/s11120-009-9454-y](https://doi.org/10.1007/s11120-009-9454-y).
- [211] K. E. Knowles, M. D. Koch and J. L. Shelton. Three applications of ultrafast transient absorption spectroscopy of semiconductor thin films: spectroelectrochemistry, microscopy, and identification of thermal contributions. *Journal of Materials Chemistry C*, **6**, 44, 11853 (2018). doi: [10.1039/c8tc02977f](https://doi.org/10.1039/c8tc02977f).
- [212] R. Yu, H. Yao, Y. Cui, L. Hong, C. He and J. Hou. Improved charge transport and reduced nonradiative energy loss enable over 16% efficiency in ternary polymer solar cells. *Advanced Materials*, **31**, 36, 1902302 (2019). doi: [10.1002/adma.201902302](https://doi.org/10.1002/adma.201902302).
- [213] S. Li, L. Zhan, Y. Jin, G. Zhou, T. Lau, R. Qin, M. Shi, C. Li, H. Zhu and X. Lu. Asymmetric electron acceptors for high-efficiency and low-energy-loss organic photovoltaics. *Advanced Materials*, **32**, 24, 2001160 (2020). doi: [10.1002/adma.202001160](https://doi.org/10.1002/adma.202001160).
- [214] L. Qin, X. Liu, X. Zhang, J. Yu, L. Yang, F. Zhao, M. Huang, K. Wang, X. Wu and Y. Li. Triplet acceptors with a d-a structure and twisted conformation for efficient organic solar cells. *Angewandte Chemie International Edition*, **59**, 35, 15043 (2020). doi: [10.1002/ange.202006081](https://doi.org/10.1002/ange.202006081).
- [215] Y. Zhong, M. Causa, G. J. Moore, P. Krauspe, B. Xiao, F. Günther, J. Kublitski, R. Shivhare, J. Benduhn and E. BarOr. Sub-picosecond charge-transfer at near-zero driving force in polymer: non-fullerene acceptor blends and bilayers. *Nature Communications*, **11**, 1, 1 (2020). doi: [10.1038/s41467-020-14549-w](https://doi.org/10.1038/s41467-020-14549-w).

- [216] S. Refaely-Abramson, S. Sharifzadeh, N. Govind, J. Autschbach, J. B. Neaton, R. Baer and L. Kronik. Quasiparticle spectra from a nonempirical optimally tuned range-separated hybrid density functional. *Physical Review Letters*, **109**, 22, 226405 (2012). doi: [10.1103/physrevlett.109.226405](https://doi.org/10.1103/physrevlett.109.226405).
- [217] S.-i. Natsuda, T. Saito, R. Shirouchi, Y. Sakamoto, T. Takeyama, Y. Tamai and H. Ohkita. Cascaded energy landscape as a key driver for slow yet efficient charge separation with small energy offset in organic solar cells. *Energy Environmental Science* (2022). doi: [10.1039/d1ee03565g](https://doi.org/10.1039/d1ee03565g).
- [218] J. Wu, J. Lee, Y.-C. Chin, H. Yao, H. Cha, J. Luke, J. Hou, J.-S. Kim and J. R. Durrant. Exceptionally low charge trapping enables highly efficient organic bulk heterojunction solar cells. *Energy Environmental Science*, **13**, 8, 2422 (2020). doi: [10.1039/d0ee01338b](https://doi.org/10.1039/d0ee01338b).
- [219] F. Liu, L. Zhou, W. Liu, Z. Zhou, Q. Yue, W. Zheng, R. Sun, W. Liu, S. Xu, H. Fan et al. Organic solar cells with 18% efficiency enabled by an alloy acceptor: a two-in-one strategy. *Advanced Materials*, **33**, 27, 2100830 (2021). doi: [https://10.1002/adma.202100830](https://doi.org/10.1002/adma.202100830).
- [220] M. A. El-Sayed. Triplet state. its radiative and nonradiative properties. *Accounts of Chemical Research*, **1**, 1, 8 (1968). doi: [10.1021/ar50001a002](https://doi.org/10.1021/ar50001a002).
- [221] E. Y.-T. Li, T.-Y. Jiang, Y. Chi and P.-T. Chou. Semi-quantitative assessment of the intersystem crossing rate: an extension of the El-Sayed rule to the emissive transition metal complexes. *Physical Chemistry Chemical Physics*, **16**, 47, 26184 (2014). doi: [10.1039/c4cp03540b](https://doi.org/10.1039/c4cp03540b).
- [222] R. L. Martin. Natural transition orbitals. *The Journal of Chemical Physics*, **118**, 11, 4775 (2003). doi: [10.1002/0470845015.cu0028](https://doi.org/10.1002/0470845015.cu0028).
- [223] C. Ma, C. C. Chan, X. Zou, H. Yu, J. Zhang, H. Yan, K. S. Wong and P. C. Chow. Unraveling the temperature dependence of exciton dissociation and free charge generation in nonfullerene organic solar cells. *Solar RRL*, **5**, 4, 2000789 (2021). doi: [10.1002/solr.202000789](https://doi.org/10.1002/solr.202000789).
- [224] J. Wang, L. Yu, L. Hu, G. Chen, H. Xin and X. Feng. Ambient ammonia synthesis via palladium-catalyzed electrohydrogenation of dinitrogen at low overpotential. *Nature Communications*, **9**, 1, 1 (2018). doi: [10.1038/s41467-018-04213-9](https://doi.org/10.1038/s41467-018-04213-9).
- [225] R. Ma, G. Li, D. Li, T. Liu, Z. Luo, G. Zhang, M. Zhang, Z. Wang, S. Luo and T. Yang. Understanding the effect of end group halogenation in tuning miscibility and

- morphology of high-performance small molecular acceptors. *Solar RRL*, **4**, 9, 2000250 (2020). doi: [10.1002/solr.202000250](https://doi.org/10.1002/solr.202000250).
- [226] N. D. Eastham, J. L. Logsdon, E. F. Manley, T. J. Aldrich, M. J. Leonardi, G. Wang, N. E. Powers-Riggs, R. M. Young, L. X. Chen and M. R. Wasielewski. Hole-transfer dependence on blend morphology and energy level alignment in polymer: Itic photovoltaic materials. *Advanced Materials*, **30**, 3, 1704263 (2018). doi: [10.1002/adma.201704263](https://doi.org/10.1002/adma.201704263).
- [227] Q. Fan, Q. Zhu, Z. Xu, W. Su, J. Chen, J. Wu, X. Guo, W. Ma, M. Zhang and Y. Li. Chlorine substituted 2D-conjugated polymer for high-performance polymer solar cells with 13.1%. *Nano Energy*, **48**, 413 (2018). doi: [10.1016/j.nanoen.2018.04.002](https://doi.org/10.1016/j.nanoen.2018.04.002).
- [228] Z. Liu, Y. Gao, J. Dong, M. Yang, M. Liu, Y. Zhang, J. Wen, H. Ma, X. Gao and W. Chen. Chlorinated wide-bandgap donor polymer enabling annealing free nonfullerene solar cells with the efficiency of 11.5%. *The Journal of Physical Chemistry Letters*, **9**, 24, 6955 (2018). doi: [10.1021/acs.jpcllett.8b03247](https://doi.org/10.1021/acs.jpcllett.8b03247).
- [229] G. Dennler, M. C. Scharber and C. J. Brabec. Polymer-fullerene bulk-heterojunction solar cells. *Advanced Materials*, **21**, 13, 1323 (2009). doi: [10.1002/adma.200801283](https://doi.org/10.1002/adma.200801283).
- [230] P. C. Chow, C. C. Chan, C. Ma, X. Zou, H. Yan and K. S. Wong. Factors that prevent spin-triplet recombination in non-fullerene organic photovoltaics. *The Journal of Physical Chemistry Letters*, **12**, 21, 5045 (2021). doi: [10.1021/acs.jpcllett.1c01214](https://doi.org/10.1021/acs.jpcllett.1c01214).
- [231] L. Zhou, J. Chang, Z. Liu, X. Sun, Z. Lin, D. Chen, C. Zhang, J. Zhang and Y. Hao. Enhanced planar perovskite solar cell efficiency and stability using a perovskite/PCBM heterojunction formed in one step. *Nanoscale*, **10**, 6, 3053 (2018). doi: [10.1039/c7nr07753j](https://doi.org/10.1039/c7nr07753j).
- [232] S. Zhang, Y. Qin, J. Zhu and J. Hou. Over 14% efficiency in polymer solar cells enabled by a chlorinated polymer donor. *Advanced Materials*, **30**, 20, 1800868 (2018). doi: [10.1002/adma.201800868](https://doi.org/10.1002/adma.201800868).
- [233] L. Franco, A. Toffoletti, M. Ruzzi, L. Montanari, C. Carati, L. Bonoldi and R. Po'. Time-resolved EPR of photoinduced excited states in a semiconducting polymer/PCBM blend. *The Journal of Physical Chemistry C*, **117**, 4, 1554 (2013). doi: [10.1021/jp306278v](https://doi.org/10.1021/jp306278v).

- [234] R. Wang, J. Xu, L. Fu, C. Zhang, Q. Li, J. Yao, X. Li, C. Sun, Z.-G. Zhang, X. Wang et al. Nonradiative triplet loss suppressed in organic photovoltaic blends with fluoridated nonfullerene acceptors. *Journal of the American Chemical Society*, **143**, 11, 4359 (2021). doi: [10.1021/jacs.0c13352](https://doi.org/10.1021/jacs.0c13352).
- [235] J. M. Marin-Beloqui, D. T. Toolan, N. A. Panjwani, S. Limbu, J.-S. Kim and T. M. Clarke. Triplet-charge annihilation in a small molecule donor: Acceptor blend as a major loss mechanism in organic photovoltaics. *Advanced Energy Materials*, **11**, 24, 2100539 (2021). doi: [10.1002/aenm.202100539](https://doi.org/10.1002/aenm.202100539).
- [236] R. T. Ross. Some thermodynamics of photochemical systems. *The Journal of Chemical Physics*, **46**, 12, 4590 (1967). doi: [10.1063/1.1840606](https://doi.org/10.1063/1.1840606).
- [237] A. Sperlich, H. Kraus, C. Deibel, H. Blok, J. Schmidt and V. Dyakonov. Reversible and irreversible interactions of poly (3-hexylthiophene) with oxygen studied by spin-sensitive methods. *The Journal of Physical Chemistry B*, **115**, 46, 13513 (2011). doi: [10.1021/jp2077215](https://doi.org/10.1021/jp2077215).
- [238] M. Jørgensen, K. Norrman and F. C. Krebs. Stability/degradation of polymer solar cells. *Solar Energy Materials and Solar Cells*, **92**, 7, 686 (2008). doi: [10.1016/j.solmat.2008.01.005](https://doi.org/10.1016/j.solmat.2008.01.005).
- [239] K. Kawaoka, A. Khan and D. R. Kearns. Role of singlet excited states of molecular oxygen in the quenching of organic triplet states. *The Journal of Chemical Physics*, **46**, 5, 1842 (1967). doi: [10.1063/1.1840943](https://doi.org/10.1063/1.1840943).
- [240] A. A. Bakulin, S. D. Dimitrov, A. Rao, P. C. Chow, C. B. Nielsen, B. C. Schroeder, I. McCulloch, H. J. Bakker, J. R. Durrant and R. H. Friend. Charge-transfer state dynamics following hole and electron transfer in organic photovoltaic devices. *The Journal of Physical Chemistry Letters*, **4**, 1, 209 (2013). doi: [10.1021/jz301883y](https://doi.org/10.1021/jz301883y).
- [241] C. W. Schlenker, K.-S. Chen, H.-L. Yip, C.-Z. Li, L. R. Bradshaw, S. T. Ochsenbein, F. Ding, X. S. Li, D. R. Gamelin, A. K.-Y. Jen and J. Ginger. Polymer triplet energy levels need not limit photocurrent collection in organic solar cells. *Journal of the American Chemical Society*, **134**, 48, 19661 (2012). doi: [10.1021/ja306110b](https://doi.org/10.1021/ja306110b).
- [242] M. Liedtke, A. Sperlich, H. Kraus, A. Baumann, C. Deibel, M. J. Wirix, J. Loos, C. M. Cardona and V. Dyakonov. Triplet exciton generation in bulk-heterojunction solar cells based on endohedral fullerenes. *Journal of the American Chemical Society*, **133**, 23, 9088 (2011). doi: [10.1021/ja2025432](https://doi.org/10.1021/ja2025432).

- [243] X.-K. Chen, D. Qian, Y. Wang, T. Kirchartz, W. Tress, H. Yao, J. Yuan, M. Hülsbeck, M. Zhang, Y. Zou et al. A unified description of non-radiative voltage losses in organic solar cells. *Nature Energy*, **6**, 8, 799 (2021). doi: [10.1038/s41560-021-00843-4](https://doi.org/10.1038/s41560-021-00843-4).
- [244] D. Qian, Z. Zheng, H. Yao, W. Tress, T. R. Hopper, S. Chen, S. Li, J. Liu, S. Chen, J. Zhang et al. Design rules for minimizing voltage losses in high-efficiency organic solar cells. *Nature Materials*, **17**, 8, 703 (2018). doi: [10.1038/s41563-018-0128-z](https://doi.org/10.1038/s41563-018-0128-z).
- [245] A. Köhler and D. Beljonne. The singlet–triplet exchange energy in conjugated polymers. *Advanced Functional Materials*, **14**, 1, 11 (2004). doi: [10.1002/adfm.200305032](https://doi.org/10.1002/adfm.200305032).
- [246] Y.-J. Hsieh, Y.-C. Huang, W.-S. Liu, Y.-A. Su, C.-S. Tsao, S.-P. Rwei and L. Wang. Insights into the morphological instability of bulk heterojunction PTB7-Th/PCBM solar cells upon high-temperature aging. *ACS Applied Materials & Interfaces*, **9**, 17, 14808 (2017). doi: [10.1021/acsami.7b01296](https://doi.org/10.1021/acsami.7b01296).
- [247] D. Carbonera. Optically detected magnetic resonance (ODMR) of photoexcited triplet states. *Photosynthesis Research*, **102**, 2, 403 (2009). doi: [10.1007/s11120-009-9407-5](https://doi.org/10.1007/s11120-009-9407-5).
- [248] O. G. Poluektov, S. Filippone, N. Martín, A. Sperlich, C. Deibel and V. Dyakonov. Spin signatures of photogenerated radical anions in polymer-[70] fullerene bulk heterojunctions: high frequency pulsed EPR spectroscopy. *The Journal of Physical Chemistry B*, **114**, 45, 14426 (2010). doi: [10.1021/jp1012347](https://doi.org/10.1021/jp1012347).
- [249] O. G. Poluektov, J. Niklas, K. L. Mardis, S. Beaupré, M. Leclerc, C. Villegas, S. Erten-Ela, J. L. Delgado, N. Martín, A. Sperlich et al. Electronic structure of fullerene heterodimer in bulk-heterojunction blends. *Advanced Energy Materials*, **4**, 7, 1301517 (2014). doi: [10.1002/aenm.201301517](https://doi.org/10.1002/aenm.201301517).
- [250] C. A. Reed and R. D. Bolskar. Discrete fulleride anions and fullerenium cations. *Chemical Reviews*, **100**, 3, 1075 (2000). doi: [10.1021/cr980017o](https://doi.org/10.1021/cr980017o).
- [251] T. Biskup, M. Sommer, S. Rein, D. L. Meyer, M. Kohlstädt, U. Würfel and S. Weber. Ordering of pcdtbt revealed by time-resolved electron paramagnetic resonance spectroscopy of its triplet excitons. *Angewandte Chemie International Edition*, **54**, 26, 7707 (2015). doi: [10.1002/anie.201502241](https://doi.org/10.1002/anie.201502241).

- [252] W. Chen, T. Xu, F. He, W. Wang, C. Wang, J. Strzalka, Y. Liu, J. Wen, D. J. Miller, J. Chen et al. Hierarchical nanomorphologies promote exciton dissociation in polymer/fullerene bulk heterojunction solar cells. *Nano Letters*, **11**, 9, 3707 (2011). doi: [10.1021/nl201715q](https://doi.org/10.1021/nl201715q).
- [253] J. Niklas, K. L. Mardis, B. P. Banks, G. M. Grooms, A. Sperlich, V. Dyakonov, S. Beaupré, M. Leclerc, T. Xu, L. Yu et al. Highly-efficient charge separation and polaron delocalization in polymer–fullerene bulk-heterojunctions: A comparative multi-frequency EPR and DFT study. *Physical Chemistry Chemical Physics*, **15**, 24, 9562 (2013). doi: [10.1039/c3cp51477c](https://doi.org/10.1039/c3cp51477c).
- [254] B. A. Collins, Z. Li, J. R. Tumbleston, E. Gann, C. R. McNeill and H. Ade. Absolute measurement of domain composition and nanoscale size distribution explains performance in PTB7:PC₇₁BM solar cells. *Advanced Energy Materials*, **3**, 1, 65 (2013). doi: [10.1002/aenm.201200377](https://doi.org/10.1002/aenm.201200377).
- [255] Y. Firdaus, V. M. Le Corre, S. Karuthedath, W. Liu, A. Markina, W. Huang, S. Chattopadhyay, M. M. Nahid, M. I. Nugraha, Y. Lin et al. Long-range exciton diffusion in molecular non-fullerene acceptors. *Nature Communications*, **11**, 1, 1 (2020). doi: [10.1038/s41467-020-19029-9](https://doi.org/10.1038/s41467-020-19029-9).
- [256] J. Niklas, S. Beaupre, M. Leclerc, T. Xu, L. Yu, A. Sperlich, V. Dyakonov and O. G. Poluektov. Photoinduced dynamics of charge separation: from photosynthesis to polymer–fullerene bulk heterojunctions. *The Journal of Physical Chemistry B*, **119**, 24, 7407 (2015). doi: [10.1021/jp511021v](https://doi.org/10.1021/jp511021v).
- [257] C. Hintze, U. E. Steiner and M. Drescher. Photoexcited triplet state kinetics studied by electron paramagnetic resonance spectroscopy. *ChemPhysChem*, **18**, 1, 6 (2017). doi: [10.1002/cphc.201600868](https://doi.org/10.1002/cphc.201600868).
- [258] P. Kohn, Z. Rong, K. H. Scherer, A. Sepe, M. Sommer, P. Muller-Buschbaum, R. H. Friend, U. Steiner and S. Huttner. Crystallization-induced 10-nm structure formation in P3HT/PCBM blends. *Macromolecules*, **46**, 10, 4002 (2013). doi: [10.1021/ma400403c](https://doi.org/10.1021/ma400403c).
- [259] N. D. Treat, A. Varotto, C. J. Takacs, N. Batara, M. Al-Hashimi, M. J. Heeney, A. J. Heeger, F. Wudl, C. J. Hawker and M. L. Chabynyc. Polymer-fullerene miscibility: a metric for screening new materials for high-performance organic solar cells. *Journal of the American Chemical Society*, **134**, 38, 15869 (2012). doi: [10.1021/ja305875u](https://doi.org/10.1021/ja305875u).

- [260] E. Buchaca-Domingo, A. Ferguson, F. Jamieson, T. McCarthy-Ward, S. Shoaee, J. Tumbleston, O. Reid, L. Yu, M.-B. Madec, M. Pfannmüller et al. Additive-assisted supramolecular manipulation of polymer:fullerene blend phase morphologies and its influence on photophysical processes. *Materials Horizons*, **1**, 2, 270 (2014). doi: [10.1039/c3mh00125c](https://doi.org/10.1039/c3mh00125c).
- [261] N. C. Cates, R. Gysel, Z. Beiley, C. E. Miller, M. F. Toney, M. Heeney, I. McCulloch and M. D. McGehee. Tuning the properties of polymer bulk heterojunction solar cells by adjusting fullerene size to control intercalation. *Nano Letters*, **9**, 12, 4153 (2009). doi: [10.1021/nl9023808](https://doi.org/10.1021/nl9023808).
- [262] H. Utzat, S. D. Dimitrov, S. Wheeler, E. Collado-Fregoso, P. S. Tuladhar, B. C. Schroeder, I. McCulloch and J. R. Durrant. Charge separation in intermixed polymer:PC₇₀BM photovoltaic blends: correlating structural and photophysical length scales as a function of blend composition. *The Journal of Physical Chemistry C*, **121**, 18, 9790 (2017). doi: [10.1021/acs.jpcc.7b02898](https://doi.org/10.1021/acs.jpcc.7b02898).
- [263] F. C. Jamieson, E. B. Domingo, T. McCarthy-Ward, M. Heeney, N. Stingelin and J. R. Durrant. Fullerene crystallisation as a key driver of charge separation in polymer/fullerene bulk heterojunction solar cells. *Chemical Science*, **3**, 2, 485 (2012). doi: [10.1039/c1sc00674f](https://doi.org/10.1039/c1sc00674f).
- [264] D. W. Gehrig, I. A. Howard, S. Sweetnam, T. M. Burke, M. D. McGehee and F. Laquai. The impact of donor–acceptor phase separation on the charge carrier dynamics in PBTTT:PCBM photovoltaic blends. *Macromolecular Rapid Communications*, **36**, 11, 1054 (2015). doi: [10.1002/marc.201500112](https://doi.org/10.1002/marc.201500112).
- [265] J. A. Bartelt, Z. M. Beiley, E. T. Hoke, W. R. Mateker, J. D. Douglas, B. A. Collins, J. R. Tumbleston, K. R. Graham, A. Amassian, H. Ade et al. The importance of fullerene percolation in the mixed regions of polymer–fullerene bulk heterojunction solar cells. *Advanced Energy Materials*, **3**, 3, 364 (2013). doi: [10.1002/aenm.201200637](https://doi.org/10.1002/aenm.201200637).
- [266] S. D. Dimitrov, S. Wheeler, D. Niedzialek, B. C. Schroeder, H. Utzat, J. M. Frost, J. Yao, A. Gillett, P. S. Tuladhar, I. McCulloch et al. Polaron pair mediated triplet generation in polymer/fullerene blends. *Nature Communications*, **6**, 1, 1 (2015). doi: [10.1038/ncomms7501](https://doi.org/10.1038/ncomms7501).
- [267] E. Salvadori, N. Luke, J. Shaikh, A. Leventis, H. Bronstein, C. W. Kay and T. M. Clarke. Ultra-fast spin-mixing in a diketopyrrolopyrrole monomer/fullerene

- blend charge transfer state. *Journal of Materials Chemistry A*, **5**, 46, 24335 (2017). doi: [10.1039/c7ta07381j](https://doi.org/10.1039/c7ta07381j).
- [268] D. Di Nuzzo, A. Aguirre, M. Shahid, V. S. Gevaerts, S. C. Meskers and R. A. Janssen. Improved film morphology reduces charge carrier recombination into the triplet excited state in a small bandgap polymer-fullerene photovoltaic cell. *Advanced Materials*, **22**, 38, 4321 (2010). doi: [10.1002/adma.201001452](https://doi.org/10.1002/adma.201001452).
- [269] G. Zhou, H. Ding, L. Zhu, C. Qiu, M. Zhang, T. Hao, W. Feng, Y. Zhang, H. Zhu and F. Liu. Photophysics, morphology and device performances correlation on non-fullerene acceptor based binary and ternary solar cells. *Journal of Energy Chemistry*, **47**, 180 (2020). doi: [10.1016/j.jechem.2019.12.007](https://doi.org/10.1016/j.jechem.2019.12.007).
- [270] L. Ye, H. Hu, M. Ghasemi, T. Wang, B. A. Collins, J.-H. Kim, K. Jiang, J. H. Carpenter, H. Li, Z. Li et al. Quantitative relations between interaction parameter, miscibility and function in organic solar cells. *Nature Materials*, **17**, 3, 253 (2018). doi: [10.1038/s41563-017-0005-1](https://doi.org/10.1038/s41563-017-0005-1).
- [271] A. Karki, J. Vollbrecht, A. J. Gillett, S. S. Xiao, Y. Yang, Z. Peng, N. Schopp, A. L. Dixon, S. Yoon and M. Schrock. The role of bulk and interfacial morphology in charge generation, recombination, and extraction in non-fullerene acceptor organic solar cells. *Energy Environmental Science*, **13**, 10, 3679 (2020). doi: [10.1039/d0ee01896a](https://doi.org/10.1039/d0ee01896a).
- [272] C. Keiderling, S. Dimitrov and J. R. Durrant. Exciton and charge generation in PC₆₀BM thin films. *The Journal of Physical Chemistry C*, **121**, 27, 14470 (2017). doi: [10.1021/acs.jpcc.7b03962](https://doi.org/10.1021/acs.jpcc.7b03962).
- [273] P. C. Chow, S. Albert-Seifried, S. Gélinas and R. H. Friend. Nanosecond intersystem crossing times in fullerene acceptors: implications for organic photovoltaic diodes. *Advanced Materials*, **26**, 28, 4851 (2014). doi: [10.1002/adma.201400846](https://doi.org/10.1002/adma.201400846).
- [274] Y. Tamai, Y. Fan, V. O. Kim, K. Ziabrev, A. Rao, S. Barlow, S. R. Marder, R. H. Friend and S. M. Menke. Ultrafast long-range charge separation in nonfullerene organic solar cells. *ACS Nano*, **11**, 12, 12473 (2017). doi: [10.1021/acsnano.7b06575](https://doi.org/10.1021/acsnano.7b06575).
- [275] G. Han, T. Hu and Y. Yi. Reducing the singlet triplet energy gap by end-group stacking toward high-efficiency organic photovoltaics. *Advanced Materials*, **32**, 22, 2000975 (2020). doi: [10.1002/adma.202000975](https://doi.org/10.1002/adma.202000975).
- [276] L. Perdigón-Toro, H. Zhang, A. Markina, J. Yuan, S. M. Hosseini, C. M. Wolff, G. Zuo, M. Stolterfoht, Y. Zou and F. Gao. Barrierless free charge generation in

- the high-performance PM6:Y6 bulk heterojunction non-fullerene solar cell. *Advanced Materials*, **32**, 9, 1906763 (2020). doi: [10.1002/adma.201906763](https://doi.org/10.1002/adma.201906763).
- [277] K. Zhou, Y. Liu, A. Alotaibi, J. Yuan, C. Jiang, J. Xin, X. Liu, B. A. Collins, F. Zhang and W. Ma. Molecular and energetic order dominate the photocurrent generation process in organic solar cells with small energetic offsets. *ACS Energy Letters*, **5**, 2, 589 (2020). doi: [10.1021/acseenergylett.0c00029](https://doi.org/10.1021/acseenergylett.0c00029).
- [278] S. Li, C.-Z. Li, M. Shi and H. Chen. New phase for organic solar cell research: emergence of Y-series electron acceptors and their perspectives. *ACS Energy Letters*, **5**, 5, 1554 (2020). doi: [10.1021/acseenergylett.0c00537](https://doi.org/10.1021/acseenergylett.0c00537).
- [279] Y. Cui, H. Yao, J. Zhang, T. Zhang, Y. Wang, L. Hong, K. Xian, B. Xu, S. Zhang and J. Peng. Over 16% efficiency organic photovoltaic cells enabled by a chlorinated acceptor with increased open-circuit voltages. *Nature Communications*, **10**, 1, 1 (2019). doi: [10.1038/s41467-019-10351-5](https://doi.org/10.1038/s41467-019-10351-5).

Publications

- J. Grüne, N. Bunzmann, M. Meinecke, V. Dyakonov and A. Sperlich. Kinetic Modeling of Transient Electroluminescence reveals TTA as Efficiency-Limiting Process in Exciplex-Based TADF OLEDs. *J. Phys. Chem. C*, **124**, 47, 25667-25674 (2020). doi: [10.1021/acs.jpcc.0c06528](https://doi.org/10.1021/acs.jpcc.0c06528)
- J. Grüne, V. Dyakonov and A. Sperlich. Detecting triplet states in opto-electronic and photovoltaic materials and devices by transient optically detected magnetic resonance. *Mater. Horiz.*, **8**, 9, 2569-2575 (2021). doi: [10.1039/D1MH00999K](https://doi.org/10.1039/D1MH00999K)
This article has been specially selected to feature in Horizons Community Board Collection: Optical and Photonic Materials and Devices
- A. Privitera¹, J. Grüne¹, A. Karki, W. K. Myers, V. Dyakonov, T.-Q. Nguyen, M. K. Riede, R. H. Friend, A. Sperlich and A. J. Gillett. Geminate and Nongeminate Pathways for Triplet Exciton Formation in Organic Solar Cells. *Adv. Energy Mater.*, **12**, 16, 2103944 (2022). doi: [10.1002/aenm.202103944](https://doi.org/10.1002/aenm.202103944)
- J. Grüne, G. Londi, A. J. Gillett, B. Stähly, S. Lulei, M. Kotova, Y. Olivier, V. Dyakonov and A. Sperlich. Energetically Trapped Triplet Excitons and their Generation Pathways in (Non-) Halogenated PBDB-T:Y-Series. *under review*. Preprint on arXiv: [10.48550/arXiv.2204.14088](https://arxiv.org/abs/10.48550/arXiv.2204.14088)
- N. Bunzmann, N., S. Weissenseel, L. Kudriashova, J. Grüne, B. Krugmann, J. V. Grazulevicius, A. Sperlich and V. Dyakonov. Optically and electrically excited intermediate electronic states in donor:acceptor based OLEDs. *Mater. Horiz.*, **7**, 4, 1126-1137 (2020). doi: [10.1039/C9MH01475F](https://doi.org/10.1039/C9MH01475F)
- L. Ress, D. Kaiser, J. Grüne, M. Gerlach, R. Engelbert, T. Brixner, A. Sperlich, B. Engels and I. Fischer. Femtosecond dynamics of diphenylpropynylidene in ethanol and dichloromethane. *Spectrochimica Acta Part A: Molecular and Biomolecular Spectroscopy*, **254**, 119606 (2021). doi: [10.1016/j.saa.2021.119606](https://doi.org/10.1016/j.saa.2021.119606)

¹contributed equally

- A. Hochgesang, S. Biberger, J. Grüne, J. Mohanraj, F.-J. Kahle, V. Dyakonov, A. Köhler and M. Thelakkat. Intricacies and Mechanism of p-Doping Spiro-MeOTAD Using Cu(TFSI)₂. *Adv. Electron. Mater.*, **8**, 10, 2200113 (2022). doi: [10.1002/aelm.202200113](https://doi.org/10.1002/aelm.202200113)

Danksagung

Zuletzt möchte ich einen großen Dank an alle Personen aussprechen, die mich in den letzten Jahren unterstützt und zum Gelingen dieser Doktorarbeit beigetragen haben:

- Zunächst geht ein herzlicher Dank an Prof. Dr. Vladimir Dyakonov für die Aufnahme in den Lehrstuhl und die Möglichkeit zur Durchführung meiner Doktorarbeit. Danke für die hilfreichen Diskussionen, guten Ratschläge und die Möglichkeiten auch meine eigenen Ideen umsetzen zu können. Die Zeit hat mir eine sehr gute Vorbereitung für den wissenschaftlichen Alltag gebracht.
- Außerdem geht ein besonderer Dank an meinen Betreuer PD Dr. Andreas Sperlich. Vielen Dank für deinen wissenschaftlichen Input und viele Diskussionen sowie für hilfreiche Tipps bei Papern und Vorträgen. Danke außerdem für das Vertrauen in meine Arbeit, dass du auch mein selbstständiges Arbeiten immer gefördert hast, aber trotzdem mit Rat und Tat zur Seite standest.
- Weiterhin vielen Dank an meine ehemaligen OLED PhD Kollegen Nikolai Bunzmann und Sebastian Weißenseel: Ihr habt mich schon in meiner Bachelorarbeit herzlich aufgenommen, mich in die Setups eingelernt und hattet immer ein offenes Ohr. Danke für unsere gemeinsame Zeit der OLED Gruppe, für produktive Meetings und schöne Konferenzen, es hat mit euch viel Spaß gemacht.
- Ein besonderer Dank geht auch an meine OPV Masteranden Basil Stähly und Sebastian Lulei. Es hat super Spaß gemacht, mit euch Setups aufzubauen, zu brainstormen, zu diskutieren und tolle Wissenschaft zu betreiben. Danke Sebastian, dass du die Laune mit deinen Witzen immer hochgehalten hast und danke Basil für die lustige Zeit im Büro. Und danke, dass ihr mich immer mit Süßigkeiten versorgt habt.
- Herzlichen Dank auch an alle anderen Bachelor- und Masterstudenten, für eure produktive Mitarbeit in OLEDs bauen, Setups aufbauen und Messen.
- Another special thanks to Alex Gillett for performing the TA measurements, for the scientific input on OPV and TA und for the opportunity for further interesting collaborations.

- Also a great thanks to Alberto Privitera for providing trEPR measurements and for interesting and always nice discussions.
- Besonderer Dank auch an Sara Wirsing und Bernd Engels für die Zusammenarbeit an den OLED Systemen und vielen netten Meetings, ich habe viel von euch lernen dürfen.
- Dann möchte ich Andreas Gottscholl danken, für das ganze gemeinsame Troubleshooting an den Setups, v.a. an einem gewissen EPR Spektrometer, das der Beginn unserer Freundschaft war. Danke für die Gesellschaft auch an Wochenevende und Feiertagen und natürlich für die morgendlichen Kaffeegespräche.
- Ein besonderer Dank auch an Büro E08, meine zweite Heimat. Besonders an meine PhD Kollegen Melina Armer und Patrick Dörflinger, ihr seid von Kollegen zu echten Freunden geworden.
- Vielen Dank weiterhin an André Thiem-Riebe und Detlev Kranl, mit eurem technischen Wissen habt ihr unzählige Probleme im Labor gelöst.
- Außerdem vielen Dank an Diep Phan für die Hilfe zwecks allen verwaltungstechnischen Angelegenheiten.
- Insgesamt allen, die mich über die Zeit in der EP6 (zeitweise) begleitet haben. Wir hatten immer eine super Arbeitsatmosphäre und haben tolle Dinge auch außerhalb der Uni zusammen erlebt.
- Zu guter Letzt möchte ich herzlich meinem privaten Umfeld danken: Meiner Familie, meinen Eltern und meinem Bruder Marvin, die mich schon immer unterstützt haben und bei denen ich weiß, dass sie immer für mich da waren und sein werden! Und natürlich Philipp, der immer bedingungslos an meiner Seite steht und auch verständnisvoll war, wenn ich nachts oder wochenends am arbeiten war (und es war auch schnell kein Geheimnis mehr, dass ich ohne deine Kochkünste wahrscheinlich verhungert wäre). Weiterhin auch einen Dank an Anna, auf Marvin und dich konnte man sich immer verlassen und ich freue mich, meine Nichte bald begrüßen zu dürfen.

Acknowledgement

This thesis was funded by the Deutsche Forschungsgemeinschaft (DFG, German Research Foundation) within the Research Training School “Molecular biradicals: Structure, properties and reactivity” (GRK2112).